ΕΘΝΙΚΟ ΜΕΤΣΟΒΙΟ ΠΟΛΥΤΕΧΝΕΙΟ

ΣΧΟΛΗ ΗΛΕΚΤΡΟΛΟΓΩΝ ΜΗΧΑΝΙΚΩΝ & ΜΗΧΑΝΙΚΩΝ ΥΠΟΛΟΓΙΣΤΩΝ

ΤΟΜΕΑΣ ΣΥΣΤΗΜΑΤΩΝ ΜΕΤΑΔΟΣΗΣ ΠΛΗΡΟΦΟΡΙΑΣ ΚΑΙ ΤΕΧΝΟΛΟΓΙΑΣ

Design and realization of photonic structures and control for interferometric hybridly integrated sensors

ΔΙΔΑΚΤΟΡΙΚΗ ΔΙΑΤΡΙΒΗ

Ελευθέριος Χαρ. Γουναρίδης

Αθήνα, Μάιος 2021

ΕΘΝΙΚΟ ΜΕΤΣΟΒΙΟ ΠΟΛΥΤΕΧΝΕΙΟ
ΣΧΟΛΗ ΗΛΕΚΤΡΟΛΟΓΩΝ ΜΗΧΑΝΙΚΩΝ & ΜΗΧΑΝΙΚΩΝ ΥΠΟΛΟΓΙΣΤΩΝ
ΤΟΜΕΑΣ ΣΥΣΤΗΜΑΤΩΝ ΜΕΤΑΔΟΣΗΣ ΠΛΗΡΟΦΟΡΙΑΣ ΚΑΙ ΤΕΧΝΟΛΟΓΙΑΣ

Design and realization of photonic structures and control for interferometric hybridly integrated sensors

ΔΙΔΑΚΤΟΡΙΚΗ ΔΙΑΤΡΙΒΗ

Ελευθέριος Χαρ. Γουναρίδης

Συμβουλευτική Επιτροπή: Ηρακλής Αβραμόπουλος
Νικόλαος Ουζούνογλου
Ιωάννα Ζεργιώτη

Εγκρίθηκε από την επταμελή εξεταστική επιτροπή την 14η Μαΐου 2021

....	....	....
Ηρακλής Αβραμόπουλος Καθηγητής Ε.Μ.Π.	Ιωάννα Ζεργιώτη Καθηγήτρια Ε.Μ.Π.	Γεώργιος Ματσόπουλος Καθηγητής Ε.Μ.Π.
....	....	....
Κωνσταντίνα Νικήτα Καθηγήτρια Ε.Μ.Π.	Κωνσταντίνος Δέρβος Καθηγητής Ε.Μ.Π.	Απόστολος Κλινάκης Ερευνητής Α' Ι.Ι.Β.Ε.Α.Α.
	....	
	Νεκτάριος Κοζύρης Καθηγητής Ε.Μ.Π.	

Αθήνα, Μάιος 2021

. . . .

Ελευθέριος Χαρ. Γουναρίδης
Διδάκτωρ Μηχανικός Σχολής Ηλεκτρολόγων Μηχανικών και Μηχανικών Υπολογιστών Ε.Μ.Π.

Contents

Acknowledgements

Καλοκαίρι του 2013, ίσως οι πιο αγχωτικοί μήνες της μέχρι τότε ζωής μου. Κάθε μέρα, η κύρια σκέψη μου ήταν το ενδεχόμενο για ένα διαφορετικό επαγγελματικό βήμα, που θα έφερνε τελικά τούμπα όλη μου τη ζωή. Έτσι και έγινε. Από το Σεπτέμβρη του ίδιου έτους, ένας τελείως διαφορετικός κόσμος βρέθηκε μπροστά μου. Βρισκόμουν πια στο Εργαστήριο Φωτονικών Επικοινωνιών του Ε.Μ.Π. Είχε ανοίξει η πόρτα για να γίνω μέλος μιας από τις πιο δυνατές ερευνητικές ομάδες στην Ελλάδα, ίσως η πιο δυνατή στον τομέα της. Από τότε μέχρι σήμερα μοιάζει να έχει περάσει μια ζωή. Μια ζωή γεμάτη εμπειρίες, χαρές, λύπες, επιτυχίες, αποτυχίες, προσπάθεια, απογοήτευση, ικανοποίηση και ξανά από την αρχή.

Αυτό το ταξίδι δε θα μπορούσα να το ζήσω αλλιώς, αν δε μου έδινε την ευκαιρία ο επικεφαλής του Ε.Φ.Ε. κύριος Ηρακλής Αβραμόπουλος. Από τη πρώτη μας συνάντηση θυμάμαι την παρότρυνσή του να ασχοληθώ με τις δραστηριότητες του εργαστηρίου. Να ψάχνει και να επιδιώκει τη θέληση και την έμπνευση σε καθέναν που θεωρεί ικανό, να γίνει μέλος της ομάδας του. Όλα αυτά τα χρόνια, στάθηκε δίπλα μου, καθοδηγώντας με οποιαδήποτε στιγμή χρειάστηκε. Οι γνώσεις του, το πάθος του για τη φωτονική και η διαίσθησή του είναι χαρακτηριστικά αδιαμφισβήτητα και εντυπωσιακά. Αυτή η στήριξη όμως δεν έμεινε μόνο σε επαγγελματικό επίπεδο. Ήταν εκεί, να με υποστηρίξει και να με βοηθήσει τόσο με λόγια όσο και με πράξεις και σε προσωπικό επίπεδο. Τον εκτιμώ και τον ευχαριστώ πολύ για αυτό.

Θέλω να αναφερθώ προσωπικά και στην κυρία Ιωάννα Ζεργιώτη. Το ταξίδι στον κόσμο των αισθητήρων και των εντυπωσιακών εφαρμογών τους, ξεκίνησε από κοινή προσπάθεια των δύο ερευνητικών ομάδων του Ε.Μ.Π. με συμπληρωματικές δραστηριότητες. Οι συμβουλές της και η στάση της αποτέλεσαν παράδειγμα για την προσωπική μου πορεία. Θέλω επίσης να τονίσω την ανθρώπινη πλευρά και βοήθεια τόσο της ίδιας, όπως και αυτή του κύριου Απόστολου Κλινάκη και Νικόλαου Ουζούνογλου, που απλόχερα και ανιδιοτελώς πρόσφεραν. Το «ευχαριστώ» από πλευράς μου είναι το ελάχιστο.

Ένα μεγάλο ευχαριστώ χρωστάω και στους στενούς συνεργάτες και συναδέλφους μου. Ξεκινώντας από τον διδάκτορα Χρήστο Κουλουμέντα, τον οποίο και ευχαριστώ για την πολύτιμη καθοδήγησή του και την υπομονή του όλα αυτά τα χρόνια. Αποτελεί παράδειγμα η επιστημονική του κατάρτιση, η μεθοδικότητα και ο σχεδιασμός του, στοιχεία που πάντα οδηγούν προς το βέλτιστο αποτέλεσμα. Τον διδάκτορα Πάνο Γκρούμα, που από την πρώτη στιγμή στάθηκε δίπλα μου, βοηθώντας με σε όλες τις δραστηριότητες. Τον διδάκτορα Βασίλη Κατοπώδη, που έστω για μικρό χρονικό διάστημα, έδωσε το παράδειγμα στησίματος και περάτωσης πειραμάτων. Επίσης ευχαριστώ τον Χρήστο Τσώκο, για τις εποικοδομητικές συζητήσεις και συμβουλές. Τέλος, ευχαριστώ τον Αδάμ Ραπτάκη για την εξαιρετική έως τώρα συνεργασία. Εύχομαι και θα προσπαθήσω να προοδεύσουμε.

Θα ήθελα επίσης να ευχαριστήσω τα υπόλοιπα μέλη του εργαστηρίου, παλαιά και νέα, για τις κοινές μας εμπειρίες και συζητήσεις που αποτελούν μαθήματα ζωής.

Θέλω ξεχωριστά να ευχαριστήσω τους στενούς μου φίλους, που τόσα χρόνια υπήρξαν δίπλα μου και με στήριξαν, πολλές φορές εν αγνοία τους, σε όλες τις φάσεις της επαγγελματικής και προσωπικής μου πορείας.

Τέλος, θέλω να πω το μεγαλύτερο ευχαριστώ στους γονείς μου. Για τη διαπαιδαγώγηση, τη στήριξη, τις θυσίες, την καθοδήγηση, τις συμβουλές, την προσπάθεια, το κίνητρο, την αγάπη, το πείσμα, τη φροντίδα, το παράδειγμα, τις γνώσεις, για όλα. Τώρα ο πατέρας μου δε θα μπορεί πια να μου λέει «κάτσε τελείωσε το διδακτορικό σου». Θα πρέπει να βάλουμε νέους στόχους. Είμαι επίσης σίγουρος ότι η μάμμυ θα φούσκωνε από χαρά!

Στους γονείς μου

List of abbreviations

ADC	Analog to Digital
APF	All Pass Filter
BOR	Bodies of Revolution
BPM	Beam Propagation Method
CAD	Computer-aided Design
CMOS	Complementary Metal Oxide Semiconductor
CMP	Chemical Mechanical Polishing
CW	Continuous Wave
DAC	Digital to Analog
DC	Duty Cycle
DD	Double Distilled
DL	Detection Limit
DS	Double Stripe
ELV	Extra-Low Voltage
EM	Electromagnetic
EME	Eigen Mode Expansion
EU	European Union
FAU	Fiber Array Unit
FDTD	Finite Difference Time Domain
FEM	Finite Element Method
FF	Fill Factor
FFT	Fast Fourier Transform
FPGA	Field Programmable Gate Array
FSM	Finite State Machines
FSR	Free Spectral Range
FTP	File Transfer Protocol
HDD	Hard Disk Drive
HDMI	High-Definition Multimedia Interface
HPLC	High Performance Liquid Chromatography

IoT	Internet of Things
LCD	Liquid Crystal Display
LIFT	Laser Induced Forward Transfer Technique
LoC	Lab on a Chip
LPCVD	Low Pressure Chemical Vapor Deposition
LS	Lower Stripe
MFD	Mode Field Diameter
$MgCl_2$	Magnesium Chloride
MMI	Multimode Interference coupler
MPA	Mode Propagation Analysis
MRR	Micro-ring Resonator
MS	Mass Spectrometry
MZI	Mach-Zehnder Interferometer
ORP	Optical Ring Resonator
OTA	Ochratoxin A
PBC	Periodic Boundary Conditions
PCB	Printed Circuit Board
PD	Photodiode
PDL	Polarization Dependent Loss
PEC	Perfect Electrical Conductor
PIC	Photonic Integrated Circuit
PML	Perfectly Matched Layer
PPW	Points per Wavelength
Q-factor	Quality factor
RAM	Random Access Memory
RI	Refractive Index
RIU	Refractive Index Unit
RT	Real Time
Si	Silicon
Si_3N_4	Silicon Nitride
SiO_2	Silicon Oxide

SMF	Single Mode Fibers
SNR	Signal to Noise Ratio
SOI	Silicon on Insulator
SPR	Surface Plasmon Resonance
SS	Single Stripe
SSD	Solid State Disk
TBC	Transparent Boundary Condition
TE	Transverse Electric
TEOS	Tetraethylorthosilicate
TF	Transfer Function
TIA	Transimpedance Amplifier
TLC	Thin Layer Chromatography
TM	Transverse Magnetic
UART	Universal Asynchronous Receiver Transmitter
USB	Universal Serial Bus
UTF	Unicode Transformation Format
VCSEL	Vertical Cavity Surface Emitting Laser
WHO	World Health Organization

Abstract in English

In the last two decades, we have witnessed a remarkable progress in the development of biophotonic sensor devices and their application in areas such as environmental monitoring, biotechnology, medical diagnostics, drug screening, food safety, and security, among others. The technology of optical biosensors has reached a high degree of maturity and several commercial products are on the market. But problems of stability, sensitivity, and size have prevented the general use of optical biosensors for real field applications. Integrated photonic biosensors based on silicon technology could solve such drawbacks, offering early diagnostic tools with better sensitivity, specificity, and reliability, which could improve the effectiveness of in-vivo and in-vitro diagnostics.

In this thesis, the development of the refractive index photonic sensor will be shown, mainly related to the design photonic structures towards to miniaturization by the hybrid integration of the photonic sensor, the development of the algorithm for processing the data which will lead to enhanced sensitivity and limit of detection and the requisite control electronics.

Firstly, in chapter 1, the state-of-the-art of the sensors in different competitive platforms is presented. The advancement and the potential of the integrated lab-on-a-chip photonic sensors in terms of sensitivity and compactness is briefly described. In more detail, the waveguide photonic platform on which the passive photonic structures have been designed as well as the principle of operation of the refractive index sensor is presented.

In chapter 2, three different simulation methods have been described. Each one of them is being used for a different stage of the photonic component design. Moreover, the designs of three main structures are presented, which are intended to increase the compactness of the photonic sensor through the hybrid integration that could offer. In more detail, three monolithic structures are described, which are the keys for the effectiveness of the power budget and the proper operation of the optical circuit. The first kind of structures is the multimode interference couplers (MMIs) which is responsible for accurately splitting the light from the single VCSEL into 8 equal parts that feed the on-chip integrated interferometers with insertion loss and power imbalance lower than 0.5 dB. The second kind of structures is the grating coupler which is responsible for the vertical coupling of light from the flip-chip bonded VCSEL into the TriPleX waveguide, having coupling efficiency almost 30%. The third kind of structure is a polarization rotator which enables the rotation of the perpendicular waveguide symmetry and thus, leads to indirect spatial rotation of the propagation axis causing the excitation of two hybrid modes, supporting both TE and TM polarization. These photonic structures provide true potential for sensor compactness and miniaturization.

In chapter 3, a method for the processing of the measurement data and the calculation of the resonance shift based on the well-known Fast Fourier Transform (FFT) is presented. For the first time the FFT-based method is being studied as an alternative to the peak-search method for high performance lab-on-a-chip bio-photonic systems, based on resonant cavities and wavelength scanning lasers. An extensive set of numerical studies comparing the two methods is presented, under an improved noise model, and is demonstrated that the FFT method can improve the resolution and the detection limit of the system by 2-3 order of magnitude. It is also shown that for practical scanning steps and realistic levels of loss inside the cavity, Q-factor values around 10^4 can maximize the performance with resolution close to 0.01 pm and detection limit close to 10^{-7} nm/RIU. In order to extend the benchmarking of the FFT method, it is also compared against a more sophisticated and resource consuming peak-search variant, which is widely used in practical systems and is based on Lorentzian fitting. Through this comparison, it is found that the FFT method has still a major advantage, as it can achieve the same level of accuracy in the estimation of the resonance shift using a scanning step that is almost 270 times larger than the necessary step in the Lorentzian fitting process.

In chapter 4, the general architecture of the electronic platform that controls the individual parts of the sensor system is presented. This 2-layer architecture has at the lower layer subunits for the control of the internal pretreatment unit, the control of the microfluidic structures on the microfluidic chip, the control of the optoelectronic components on the optoelectronic platform and the collection, organization and further transmission of the raw results. At the upper layer of the architecture, there is the microcontroller that orchestrates and synchronizes the individual electronic boards ensuring their proper operation and interaction. In the second part of this chapter, experimental results are presented, which are in a perfect alignment and agreement with the trends of the numerical studies that have been presented in chapter 3. Moreover, experiments with real samples are presented, using biomodified sensing MRRs and having as target the detection and capture the specific binding of the mycotoxin OTA and copper target molecules to the aptamers targeting OTA and copper, respectively as well as the effect of the $MgCl_2$ presence on the molecules binding.

In the last chapter of this thesis, some general and interesting conclusions are drawn and presented and finally, some ideas for future work based on the models and the results of this thesis are mentioned.

Keywords: Photonic sensors, hybrid integration, refractive index, multi-mode interference couplers, grating couplers, polarization rotator, micro-ring resonators, Fast Fourier Transform, SiN (TriPleX) platform, photonic integrated circuits.

Περίληψη στα Ελληνικά

Τις τελευταίες δύο δεκαετίες, έχουμε παρατηρήσει μια αξιοσημείωτη πρόοδο στην ανάπτυξη συσκευών βιο-φωτονικών αισθητήρων και την εφαρμογή τους σε τομείς όπως η παρακολούθηση του περιβάλλοντος, η βιοτεχνολογία, η ιατρική διαγνωστική, ο έλεγχος φαρμάκων, ο έλεγχος ποιότητας των τροφίμων και η γενικότερη ασφάλεια. Η τεχνολογία των οπτικών βιο-αισθητήρων έχει φτάσει σε μεγάλο βαθμό ωριμότητας και πολλά εμπορικά προϊόντα κυκλοφορούν στην αγορά. Ωστόσο, προβλήματα σταθερότητας, ευαισθησίας και μεγέθους έχουν αποτρέψει τη γενική χρήση οπτικών βιο-αισθητήρων για εφαρμογές στο πραγματικό πεδίο δράσης. Ολοκληρωμένοι φωτονικοί βιο-αισθητήρες που βασίζονται στην τεχνολογία πυριτίου θα μπορούσαν να λύσουν τέτοια μειονεκτήματα, προσφέροντας εργαλεία πρώιμης διάγνωσης με καλύτερη ευαισθησία, επιλεκτικότητα και αξιοπιστία, τα οποία θα μπορούσαν να βελτιώσουν την αποτελεσματικότητα των in-vivo και in-vitro διαγνωστικών διεργασιών.

Σε αυτή τη διατριβή, παρουσιάζεται η ανάπτυξη του φωτονικού αισθητήρα ανίχνευσης της αλλαγής του δείκτη διάθλασης του δείγματος, υπό το πρίσμα κυρίως του σχεδιασμού φωτονικών δομών με σκοπό την επιπλέον σμίκρυνσή του αξιοποιώντας την υβριδική ολοκλήρωση του φωτονικού αισθητήρα, την ανάπτυξη του αλγορίθμου για την επεξεργασία των δεδομένων με σκοπό να οδηγήσει σε αυξημένη ευαισθησία, βελτίωση του ορίου ανίχνευσης καθώς και την παρουσίαση των απαραίτητων ηλεκτρονικών ελέγχου του αισθητήρα.

Αρχικά, στο κεφάλαιο 1, παρουσιάζεται η τελευταία λέξη της τεχνολογίας των αισθητήρων σε διάφορες ανταγωνιστικές πλατφόρμες. Περιγράφεται εν συντομία η εξέλιξη και η δυνατότητα των ολοκληρωμένων φωτονικών αισθητήρων (lab-on-a-chip) όσον αφορά την ευαισθησία και το μέγεθος. Αναλυτικότερα, παρουσιάζεται η φωτονική πλατφόρμα κυματοδηγού στην οποία έχουν σχεδιαστεί οι παθητικές φωτονικές δομές, καθώς και η αρχή λειτουργίας του αισθητήρα ανίχνευσης αλλαγής του δείκτη διάθλασης.

Στο κεφάλαιο 2, έχουν περιγραφεί τρεις διαφορετικές μέθοδοι προσομοίωσης. Κάθε μία από αυτές χρησιμοποιείται σε ένα διαφορετικό στάδιο του σχεδιασμού των φωτονικών δομών. Επιπλέον, παρουσιάζονται τα σχέδια τριών κύριων τύπων φωτονικών δομών, που αποσκοπούν στην περαιτέρω μείωση των διαστάσεων του φωτονικού αισθητήρα μέσω της υβριδικής ολοκλήρωσης που θα μπορούσαν να προσφέρουν. Αναλυτικότερα, περιγράφονται τρεις μονολιθικές φωτονικές δομές, οι οποίες είναι το κλειδί για την αποτελεσματικότερη μείωση προϋπολογισμού ισχύος και τη βελτίωση της λειτουργίας του οπτικού κυκλώματος. Το πρώτο είδος δομών είναι οι συζεύκτες πολλών ρυθμών (MMIs) που είναι υπεύθυνοι για την ακριβή αναπαραγωγή πολλαπλών απεικονίσεων του φωτός εισόδου τους, από τη συγκεκριμένη πηγή φωτός που χρησιμοποιούμε (VCSEL), σε 8 όμοιες εικόνες ώστε να τροφοδοτούν τα ενσωματωμένα στο ολοκληρωμένο τσιπ συμβολόμετρα, με συνολικές απώλειες και ανισορροπία ισχύος στους κυματοδηγούς εξόδου τους, μικρότερη από 0.5 dB. Το δεύτερο είδος δομών είναι ο ζεύκτης φράγματος περίθλασης (grating coupler) που είναι υπεύθυνος για την κατακόρυφη σύζευξη φωτός από το VCSEL προς τον κυματοδηγό TriPleX, με συντελεστή ζεύξης σχεδόν 30%. Το τρίτο είδος δομής είναι ένας περιστροφικός πολωτής που επιτρέπει την περιστροφή της κάθετης συμμετρίας κυματοδηγού και έτσι, οδηγεί σε

έμμεση χωρική περιστροφή του άξονα διάδοσης προκαλώντας την διέγερση δύο υβριδικών ρυθμών, υποστηρίζοντας τόσο την πόλωση TE όσο και TM. Αυτές οι φωτονικές δομές παρέχουν πραγματική προοπτική για έναν πιο συμπαγή και μικρών διαστάσεων αισθητήρα.

Στο κεφάλαιο 3, παρουσιάζεται η μέθοδος που αναπτύχθηκε για την επεξεργασία των πειραματικών δεδομένων και τον υπολογισμό της μετατόπισης του μήκους κύματος συντονισμού, η οποία βασίζεται στη γνωστή πλέον Fourier Transform (FT) θεωρία. Για πρώτη φορά, η μέθοδος Fast Fourier Transform (FFT) που βασίζεται στην ομώνυμη θεωρία, μελετάται ως εναλλακτική της μεθόδου αναζήτησης τοπικού μεγίστου (peak-search method) για βιο-φωτονικά συστήματα υψηλής απόδοσης, βασισμένα σε κοιλότητες συντονισμού και λέιζερ με δυνατότητα σάρωσης του μήκους κύματος λειτουργίας τους. Παρουσιάζεται ένα εκτεταμένο σύνολο αριθμητικών μελετών που συγκρίνουν τις δύο μεθόδους, με ένα βελτιωμένο μοντέλο θορύβου σε σύγκριση με και αποδεικνύεται ότι η FFT μέθοδος που αναπτύχθηκε στα πλαίσια αυτής της διατριβής και βασίζεται στη FT θεωρία, μπορεί να βελτιώσει την ανάλυση και το όριο ανίχνευσης του συστήματος κατά 2-3 τάξεις μεγέθους. Αποδεικνύεται επίσης ότι για πρακτικά βήματα σάρωσης και ρεαλιστικά επίπεδα απώλειας εντός της κοιλότητας, οι τιμές συντελεστή ποιότητας των κοιλοτήτων συντονισμού Q-factor περίπου 10^4 μπορούν να μεγιστοποιήσουν την απόδοση με ανάλυση κοντά στο 0.01 pm και όριο ανίχνευσης κοντά στα 10^{-7} nm/RIU. Προκειμένου να επεκταθεί η συγκριτική αξιολόγηση της μεθόδου FFT, συγκρίνεται επίσης με μια πιο εξελιγμένη και μικρότερης κατανάλωσης πόρων παραλλαγή της μεθόδου αναζήτησης τοπικού μεγίστου, η οποία χρησιμοποιείται ευρέως σε πρακτικά συστήματα και βασίζεται στην προσαρμογή Lorentzian. Μέσω αυτής της σύγκρισης, διαπιστώνεται ότι η μέθοδος FFT εξακολουθεί να έχει ένα σημαντικό πλεονέκτημα, καθώς μπορεί να επιτύχει το ίδιο επίπεδο ακρίβειας στην εκτίμηση της μετατόπισης του μήκους κύματος συντονισμού χρησιμοποιώντας ένα βήμα σάρωσης που είναι σχεδόν 270 φορές μεγαλύτερο από το απαραίτητο βήμα στην περίπτωση της μεθόδου που βασίζεται στην προσαρμογή Lorentzian.

Στο κεφάλαιο 4, παρουσιάζεται η γενική αρχιτεκτονική της ηλεκτρονικής πλατφόρμας που ελέγχει τα μεμονωμένα μέρη του συστήματος του αισθητήρα. Αυτή η αρχιτεκτονική είναι δύο επιπέδων. Στο πρώτο επίπεδο έχει στις υπομονάδες για τον έλεγχο της εσωτερικής μονάδας προ-επεξεργασίας του δείγματος, τον έλεγχο των μικροροϊκών δομών στο μικροροϊκό τσιπ, τον έλεγχο των οπτο-ηλεκτρονικών εξαρτημάτων στην οπτο-ηλεκτρονική πλατφόρμα και τη συλλογή, οργάνωση και περαιτέρω μετάδοση των ακατέργαστων αποτελεσμάτων. Στο ανώτερο επίπεδο της αρχιτεκτονικής, υπάρχει ο μικροελεγκτής που ενορχηστρώνει και συγχρονίζει τις μεμονωμένες ηλεκτρονικές πλακέτες διασφαλίζοντας τη σωστή λειτουργία και αλληλεπίδραση μεταξύ τους. Στο δεύτερο μέρος αυτού του κεφαλαίου παρουσιάζονται πειραματικά αποτελέσματα, τα οποία βρίσκονται σε τέλεια ευθυγράμμιση και συμφωνούν με τις τάσεις των αριθμητικών μελετών που έχουν παρουσιαστεί στο κεφάλαιο 3. Επιπλέον, παρουσιάζονται πειράματα με πραγματικά δείγματα, χρησιμοποιώντας βιο-τροποποιημένους μικροδακτυλίους συντονισμού (MRR) και έχοντας ως στόχο την ανίχνευση και τη δέσμευση των μορίων μυκοτοξίνης OTA και χαλκού στα αντίστοιχα απταμερή, καθώς και την επίδραση της παρουσίας $MgCl_2$ στη διαδικασία μέτρησης.

Στο τελευταίο κεφάλαιο αυτής της διατριβής, συγκεντρώνονται και παρουσιάζονται ορισμένα γενικά και ενδιαφέροντα συμπεράσματα και τέλος, αναφέρονται μερικές ιδέες για μελλοντική εργασία με βάση τα μοντέλα και τα αποτελέσματα αυτής.

Λέξεις κλειδιά: Φωτονικοί αισθητήρες, υβριδική ολοκλήρωση, δείκτης διάθλασης, συζεύκτες πολλών ρυθμών, ζεύκτης φράγματος περίθλασης, περιστροφικός πολωτής, μικροδακτύλιοι συντονισμού, Fast Fourier Transform, πλατφόρμα νιτριδίου του πυριτίου (TriPleX), φωτονικά ολοκληρωμένα κυκλώματα.

Εκτεταμένη περίληψη

Αυτή η διατριβή, προχωρά στην παροχή σαφών λύσεων για την ανάπτυξη ενός φωτονικού αισθητήρα ανίχνευσης αλλαγής του δείκτη διάθλασης, με στόχο την επιπλέον σμίκρυνσή του και την υβριδική ολοκλήρωσή του. Έτσι, το αποτέλεσμα αυτής της διατριβής είναι η παρουσίαση παραδείγματος ανάπτυξης ενός ολοκληρωμένου, φορητού, με εξαιρετική ευαισθησία και ακρίβεια αισθητήρα για διάφορες εφαρμογές.

Τα δύο κύρια σημεία στα οποία δόθηκε έμφαση κατά τη διάρκεια της ανάπτυξής του είναι:

Η ευαισθησία: η ευαισθησία εξαρτάται τόσο από τη φυσική λειτουργία του αισθητήρα όσο και από τα μόρια που είναι προς ανίχνευση με την αντίστοιχη και κατάλληλη βιοχημεία. Η ευαισθησία των αισθητήρων συμβολής, ειδικά των ολοκληρωμένων σε φωτονικά chips, είναι ακόμη μέτρια και μάλιστα 2-3 τάξεις μεγέθους χαμηλότερα από το θεωρητικό όριο [Link Pythia]. Μεταφράζοντας αυτήν την ευαισθησία στο όριο αλλαγής του δείκτη διάθλασης που μπορεί να ανιχνευτεί, είναι μεταξύ 10^{-6} – 10^{-7} μονάδων δείκτη διάθλασης (RIU), τη στιγμή που το θεωρητικό όριο είναι στη 10^{-9} τάξη μεγέθους και το αντίστοιχο όριο ανίχνευσης σε πιο σύνθετους και ογκώδεις Surface Plasmon Resonance (SPR) αισθητήρες είναι $< 10^{-7}$ [Herold2009], [Link BIOFOS]. Όσο αφορά τους βιομετατροπείς που χρησιμοποιούνται για την αναγνώριση των αναλυτών, τα αντισώματα και τα απταμερή είναι τα πιο κοινά στοιχεία και έχουν επιδείξει την ικανότητά τους για υψηλή ευαισθησία (χαμηλά όρια ανίχνευσης) σε διάφορους τύπους βιοαισθητήρων [Yurii2012].

Συμπάγεια και ευκολία στη χρήση: Παρά την εντυπωσιακή πρόοδο στη φωτονική ολοκλήρωση που βασίζεται σε εφαρμογές τηλεπικοινωνιών [Deisingh2004], η συμπάγεια του φωτονικού μέρους των αισθητήρων είναι ακόμη περιορισμένη, καθώς οι οπτικές πηγές και τα στοιχεία ανίχνευσης τοποθετούνται εκτός του φωτονικού chip και συνδέονται με αυτό με τη χρήση οπτικών ινών και άλλων ογκωδών οπτικών στοιχείων. Με αυτόν τον τρόπο, οι αισθητήρες γίνονται πιο περίπλοκοι, δύσκολοι στη χρήση και δαπανηροί, ειδικά αν λαμβάνεται υπόψιν η αποτελεσματικότητα της ζεύξης του φωτός στο φωτονικό chip καθώς και η πόλωση του φωτός εισόδου.

Το φωτονικό μέρος του συστήματος βασίζεται στη χρήση πολλαπλών μικροδακτυλίων συντονισμού (Micro-Ring Resonators-MRRs) ως στοιχεία οπτικών συμβολόμετρων. Τα MRRs θα ενσωματωθούν μονολιθικά σε φωτονικό chip, το οποίο είναι συμβατό με την τεχνολογία CMOS, και βασίζεται στην πλατφόρμα ολοκλήρωσης TriPleX, η οποία χρησιμοποιεί στρώματα νιτριδίου του πυριτίου σαν κυματοδηγούς και οξειδίου του πυριτίου σαν περίβλημα [De Vos2007]. Αξιοποιώντας τον υψηλό παράγοντα ποιότητας (Q-factor) των MRRs ως οπτικών κοιλοτήτων (10^4), την εξαιρετικά χαμηλή απώλεια διάδοσης της πλατφόρμας TriPleX (<0.01 dB/cm) και τη λειτουργία του συστήματος στα 850 nm, το σύστημα είναι σε θέση να παράσχει λύση για θέματα χαμηλής ευαισθησίας των ολοκληρωμένων συστημάτων (Lab-on-a-Chip – LoC), καθώς είναι ικανά να ανιχνεύσουν πολλαπλούς αναλύτες με όριο ανίχνευσης κοντά στο $8.5 \cdot 10^{-7}$ RIU. Επιπλέον, προκειμένου να αντιμετωπιστεί η περιορισμένη συμπάγεια του οπτικού μέρους του αισθητήρα καθώς επίσης και οι σχετικές δυσκολίες που προκύπτουν από το χειρισμό του φωτός στην είσοδο και στην έξοδο του φωτονικού chip, θα σχεδιαστούν φωτονικά παθητικά στοιχεία με στόχο την υβριδική ολοκλήρωση του λέιζερ επιφανειακής εκπομπής κάθετου οπτικού αντηχείου (Vertical - Cavity Surface - Emitting Laser - VCSEL) και της συστοιχίας των φωτοδιόδων μαζί με τα μονολιθικά ενσωματωμένα MRRs και το υπόλοιπο φωτονικό κύκλωμα σε όσο το δυνατόν μικρότερου αποτυπώματος φωτονικό chip. Επιπλέον, ο αλγόριθμος που θα αναπτυχθεί για την επεξεργασία των δεδομένων του αισθητήρα, τον καθιστά πολύ ανθεκτικό σε διαφορετικά είδη θορύβου. Τα ηλεκτρονικά συστήματα ελέγχου και οδήγησης θα παρέχουν μια φιλική προς το χρήστη διεπαφή. Τελικά, ο αισθητήρας που θα παρουσιαστεί στα πλαίσια της παρούσας διατριβής, θα είναι αυτόνομος και φορητός.

Τρία είναι τα κύρια συμβολομετρικά σχήματα που ερευνώνται εντατικά σήμερα: το συμβολόμετρο του Young, το συμβολόμετρο του Mach-Zehnder (Mach-Zehnder interferometer – MZI) και ο μικροδακτύλιος συντονισμού (Micro-Ring resonator – MRR). Το πρώτο χρησιμοποιεί μία πηγή φωτός της οποίας η δέσμη χωρίζεται σε δύο. Η μία χρησιμοποιείται ως δέσμη αναφοράς και η δεύτερη «ανιχνεύει» το δείγμα. Οι δύο δέσμες, συνδυάζονται και δημιουργούν ένα μοτίβο συμβολής το οποίο ανιχνεύεται από έναν, δύο διαστάσεων ανιχνευτή. Το MZI βασίζεται σε παρόμοια αρχή. Το φως εισόδου, χωρίζεται σε δύο μέρη, τα οποία συνδυάζονται ξανά, αφότου το ένα από τα δύο περάσει από την περιοχή ανίχνευσης. Το τελικό φως στην έξοδο, ανιχνεύεται είτε από μία φωτοδίοδο είτε από ένα φασματόμετρο, ανάλογα με το αν η πηγή που χρησιμοποιήθηκε ήταν μονοχρωματική ή πηγή ευρείας ζώνης.

Οι MRRs πρέπει να θεωρηθούν ως το επόμενο λογικό βήμα στην εξέλιξη των συμβολομετρικών βιο-φωτονικών αισθητήρων. Σε σύγκριση με τα MZI, έχουν το πλεονέκτημα ότι είναι εξαιρετικά συμπαγή, επιτρέποντας έτσι την επιπλέον σμίκρυνση και την ταυτόχρονη χρήση των αισθητήρων. Επιπλέον, όπως κάνουν και οι MZI, έτσι και τα MRRs αντιπροσωπεύουν περιοδικά οπτικά φίλτρα αλλά με πολύ υψηλότερη λεπταισθησία και οξύτητα της κορυφής συντονισμού, το οποίο έχει ως αποτέλεσμα υψηλότερη την ευαισθησία του συστήματος. Το θεωρητικό όριο για την ανίχνευση αλλαγής του δείκτη διάθλασης αισθητήρων που βασίζονται σε MRRs είναι 10^{-9} RIU [Link Pythia], αν και στην πράξη το όριο είναι αρκετά υψηλότερο κατά μερικές τάξεις μεγέθους. Οι βιοαισθητήρες που βασίζονται σε MRRs έχουν ήδη επιδειχθεί σε πολυμερική πλατφόρμα με διαμέτρους 60 μm [Kitsara2010] και σε πλατφόρμα Silicon-on-insulator (SOI) με διαμέτρους μόλις 10 μm [Krioukov2003]. Το όριο ανίχνευσης των SOI MRRs είναι της τάξης των 10^{-4} – 10^{-5} RIU. Για να μειωθεί ακόμη περισσότερο αυτό το όριο, έχουν αναπτυχθεί MRRs που βασίζονται σε κυματοδηγούς υποδοχής και όχι σε κυματοδηγούς ράχης, που επιτρέπουν ισχυρότερη αλληλεπίδραση μεταξύ του δείγματος προς ανίχνευση και του πεδίου διάδοσης και τη μείωση του ορίου ανίχνευσης κατά έναν παράγοντα 3.5 [Chao2006]. Επιπλέον, τα MRRs έχουν ήδη δειχθεί στην TriPleX πλατφόρμα σαν δοκιμαστικές δομές για βιοαισθητήρα με διαμέτρους 100 μm [Vos2007], οι οποίες είναι ήδη αρκετά μικρές ώστε να συμμορφώνονται με το ελάχιστο διαθέσιμο και εφικτό μέγεθος των περιοχών στην επιφάνεια του αισθητήρα, και επιτρέπουν την υλοποίηση εξαιρετικά συμπαγών συστοιχιών αισθητήρων. Το όριο ανίχνευσης που έχει επιτευχθεί είναι χαμηλότερο από 10^{-6} RIU σαν αποτέλεσμα του συνολικού δυναμικού της TriPleX πλατφόρμας για MRRs με υψηλές τιμές του Q-factor και της διαφάνειας της πλατφόρμα στα 850 nm μήκος κύματος.

Η πλατφόρμα TriPleX [De Vos2007] θα χρησιμοποιηθεί για το φωτονικό κομμάτι του αισθητήρα. Στην τυπική της γεωμετρία, για εφαρμογές αισθητήρων, η πλατφόρμα TriPleX αποτελείται από ένα στρώμα πυρήνα νιτριδίου του πυριτίου (Si_3N_4) ως κυματοδηγό με περίβλημα οξείδιο του πυριτίου (SiO_2) το οποίο μπορεί να αφαιρεθεί τοπικά στην περιοχή ανίχνευσης των MRRs προκειμένου να επιτραπεί η αλληλεπίδραση μεταξύ του κυματοδηγούμενου φωτός μέσα στην κοιλότητα συντονισμού με τα στοχευμένα μόρια προς ανίχνευση του δείγματος όπως φαίνεται στην **Figure *1***. Σε αυτήν την γεωμετρία, η TriPleX πλατφόρμα διαθέτει ισχυρή πολική διπλοθλαστικότητα που αποτρέπει την απόσβεση του σήματος σε εφαρμογές συμβολομετρικών αισθητήρων. Επιπλέον, ο κυματοδηγός, παραμένει διαφανής και με εξαιρετικά χαμηλή απώλεια διάδοσης (<0.01 dB/cm) στα 850 nm, όπου η απορρόφηση από τα υδατικά διαλύματα (ή ισοδύναμα από προ επεξεργασμένα υδατικά διαλύματα) είναι χαμηλή και το κόστος των διαθέσιμων VCSELs μικρό. Η ελαχιστοποίηση της απορρόφησης του φωτός από το δείγμα, καθώς επίσης και της απώλειας διάδοσης εντός του κυματοδηγού, είναι εξαιρετικά επιθυμητή για δύο λόγους: πρώτον επιτρέπει να λαμβάνονται υπόψιν μόνο φαινόμενα συμβολών που βασίζονται στις αλλαγές του (πραγματικού μέρους τού) δείκτη διάθλασης εντός της κοιλότητας, καθιστώντας έτσι τη βαθμονόμηση και την τελική επεξεργασία δεδομένων απλή και αξιόπιστη. Δεύτερον, επιτρέπει τον σχεδιασμό κοιλοτήτων με υψηλό Q-factor (>10.000) που οδηγούν με τη σειρά τους σε εξαιρετικά ευαίσθητους αισθητήρες με πολύ χαμηλά όρια στην ανίχνευση αλλαγών του δείκτη διάθλασης [Link Pythia].

Στα πλαίσια αυτής της διατριβής, θα μελετηθούν περαιτέρω οι ιδιότητες και η λειτουργία των MRRs, με αποτέλεσμα τη βέλτιστη διατομή του κυματοδηγού, το σχήμα και τον παράγοντας ζεύξης με τους δύο κυματοδηγούς με σκοπό να επιτευχθούν όρια ανίχνευσης χαμηλότερα από 10^{-7} RIU. Η ελεύθερη φασματική περιοχή (Free Spectral Range – FSR) των MRRs, καθορίζεται από τη συνολικό μήκος της κοιλότητας, και θα είναι εντός του εύρους 0.5 – 1.0 nm. Για να επιτευχθεί αυτό το εύρος, η ακτίνα του καμπύλου τμήματος της κοιλότητας θα πρέπει να είναι μικρότερη από 75 μm και το μήκος του ευθύ τομέα της κοιλότητας, μικρότερο από 150 μm. Η χρήση των MRRs θα συνδυαστεί με ένα VCSEL με εύρος συντονισμού άνω του 1.5 nm, με πλάτος γραμμής (linewidth) μικρότερο των 0.05 nm και κατανάλωση ισχύος μικρότερη από 50 cW. Αυτό το ευρύ φάσμα συντονισμού θα επιτευχθεί μέσω κατάλληλου συνδυασμού θερμοκρασίας και ρύθμισης του ρεύματος οδήγησης του VCSEL [La Pera2002, De Vos2007]. Δεδομένου ότι η ακρίβεια ανίχνευσης του συστήματος θα είναι χαμηλότερη από 10^{-6} nm και το συνολικό εύρος σάρωσης υψηλότερο από 1.5 nm, το στοχευμένο δυναμικό εύρος της μέτρησης θα είναι τουλάχιστον 5 τάξεις μεγέθους.

Ο φωτονικός αισθητήρας θα ενσωματώσει μονολιθικά σε ένα κύκλωμα βασιζόμενο στην πλατφόρμα TriPleX, κύρια στοιχεία όπως έναν συζεύκτη πολλών ρυθμών (MMI) [Claes2009] και μία οκταπλή συστοιχία MRRs, και θα επιτρέψει την ταυτόχρονη ανίχνευση αλλαγών του δείκτη διάθλασης σε έξι διαφορετικά MRRs. Ο συζεύκτης MMI θα χωρίζει το φως του VCSEL σε οκτώ όμοια και ίσα μέρη τα οποία θα οδηγηθούν στις εισόδους των επιμέρους MRRs. Οι απώλειες παρεμβολής του MMI θα είναι μικρότερη από 1 dB και η ανισορροπία ισχύος μεταξύ των οκτώ κυματοδηγών εξόδου θα είναι μικρότερη από 0.5 dB. Ένα από τα MRRs δε θα λειτουργεί ως αισθητήρας αλλαγής του δείκτη διάθλασης στην επιφάνειά του ώστε να χρησιμοποιείται ως αναφορά προκειμένου να ληφθούν υπόψιν τυχόν μεταβολές του VCSEL. Ένα ασύμμετρο συμβολόμετρο MZI (asymmetric Mach Zehnder Interferometer – aMZI) θα χρησιμοποιηθεί για σκοπούς βαθμονόμησης ενώ τα υπόλοιπα έξι MRRs θα χρησιμοποιηθούν για την πραγματική ανίχνευση. Η στοχευμένη απώλειας συμβολής εντός του οπτικού chip θα είναι <12 dB συμπεριλαμβανομένης της ανελαστικής απώλειας του συζεύκτη MMI (9dB) λόγω του διαχωρισμού της ισχύος σε οκτώ μέρη.

Αυτή η διατριβή θα κάνει ένα αποφασιστικό βήμα για την υιοθέτηση εννοιών υβριδικής ολοκλήρωσης που χρησιμοποιούνται ευρέως σήμερα για την κατασκευή φωτονικών ολοκληρωμένων κυκλωμάτων στον τομέα των τηλεπικοινωνιών και θα τα εφαρμόσει με σκοπό την ανάπτυξη εξαιρετικά συμπαγών, λειτουργικών οπτικών κυκλωμάτων για εφαρμογές αισθητήρων. Πιο συγκεκριμένα, τεχνικές ανάστροφης επαφής στο chip (flip-chip bonding), οι οποίες βασίζονται σε συστήματα συγκόλλησης Indium ή AuSn [Iga2000], θα εφαρμοστούν για την ενσωμάτωση του VCSEL με λειτουργία στα 850 nm καθώς και της συστοιχίας των οκτώ φωτοδιόδων πυριτίου στο TriPleX chip. Το μέγεθος της συστοιχίας των φωτοδιόδων θα είναι όσο το μέγεθος της συστοιχίας των MRRs έτσι ώστε να παρακολουθεί και να απεικονίζει τη θύρα «πτώσης» (drop port) κάθε MRR αυξάνοντας με αυτόν τον τρόπο τον ευαισθησία και την αξιοπιστία του συστήματος (**Figure *2***). Στην περίπτωση του VCSEL, ένας ζεύκτης φράγματος περίθλασης (grating coupler) δύο θυρών θα ενσωματωθεί στον πυρήνα του κυματοδηγού με σκοπό να συζεύξει το φως από το VCSEL στον κυματοδηγό και στην δεύτερη περίπτωση ένας ζεύκτης φράγματος περίθλασης μονής θύρας ώστε να συζεύξει το φως από τον κυματοδηγό στις φωτοδιόδους. Οι μικρότερες απώλειες σύζευξης του φωτός που επετεύχθησαν είναι 2-3 dB. (συντελεστής σύζευξης 54%) Αυτό έχει ως αποτέλεσμα συνολικές απώλειες <17 dB για το οπτικό παθητικό κύκλωμα. Αυτή η τιμή αναμένεται να επιτρέψει επαρκή λόγο σήματος - θορύβου (Signal-to-Noise Ratio – SNR) και ανάλυση μέτρησης. Το τελικό οπτικό chip θα διευκολύνει τη λειτουργία των οκτώ στοιχείων ανίχνευσης με δύο από αυτά να έχουν σκοπό αναφοράς και βαθμονόμησης και θα έχει αποτύπωμα 10x5 mm^2. Η **Figure *3*** παρουσιάζει μια απεικόνιση του οπτικού chip του φωτονικού συστήματος.

Στη συνέχεια της διατριβής παρουσιάζεται ο σχεδιασμός των φωτονικών δομών, βασισμένες στην πλατφόρμα TriPleX. Οι μέθοδοι προσομοίωσης που χρησιμοποιήθηκαν, παρουσιάζονται αναλυτικά. Συγκεκριμένα είναι η μέθοδος πεπερασμένου στοιχείου (Finite Element Method – FEM), η μέθοδος διάδοσης της δέσμης (Beam Propagation Method – BPM) και η μέθοδος πεπερασμένων διαφορών στο πεδίο του χρόνου (Finite Difference Time Domain – FDTD).

Αναλυτικότερα, η μέθοδος FEM είναι σε πλεονεκτική θέση για σύνθετες γεωμετρίες ή/και για υλικά με υψηλή αντίθεση του δείκτη διάθλασης. Παρουσιάζεται το βασικό θεωρητικό υπόβαθρο της μεθόδου FEM και το πως αυτή εφαρμόζεται στο συγκεκριμένο λογισμικό που χρησιμοποιήθηκε για τις προσομοιώσεις. Είναι μια εφαρμογή που λαμβάνει υπόψιν το πλήρες διάνυσμα είτε για κυματοδηγούμενους είτε για διαρρέοντες ρυθμούς, καθώς επίσης για ρυθμούς κοιλότητας σε ένα ή σε δύο διαστάσεων καρτεσιανό επίπεδο και τριών διαστάσεων για σώματα περιστροφής σε κυλινδρικές συντεταγμένες. Επίσης, η μέθοδος χρησιμοποιεί υπερσύγχρονα υβριδικά άκρα/στοιχεία του κόμβου που επιτρέπουν τον αποτελεσματικό διαχωρισμό των πλαστών από τους φυσικούς ρυθμούς. Πρώτης και δεύτερης τάξης παρεμβολή παρέχεται τόσο για τα ορθογώνια όσο και για τα τρίγωνα σχήματα. Οι οριακές συνθήκες του τέλειου ηλεκτρικού αγωγού (Perfect Electrical Conductor – PEC) ή του τέλειου αντιστοιχισμένου στρώματος (Perfectly Matched Layer – PML) μπορούν να επιλεγούν ανεξάρτητα για κάθε κατεύθυνση. Μπορεί επίσης να χρησιμοποιηθεί για την εύρεση όλων ή μιας υποομάδας ρυθμών για ένα συγκεκριμένο μήκος κύματος λειτουργίας.

Η δεύτερη μέθοδος που χρησιμοποιήθηκε είναι η BPM, η οποία έχει στόχο την παροχή ενός γενικού πακέτου προσομοίωσης για τον υπολογισμό διάδοσης των κυμάτων φωτός σε αυθαίρετες γεωμετρίες κυματοδηγού. Στην αρχή της προσομοίωσης γίνονται πολλές παραδοχές και παρότι πολλές εξ αυτών στη συνέχεια χαλαρώνουν η BPM μέθοδος παραμένει ένα δύσκολο πρόβλημα. Ο υπολογιστικός πυρήνας του προγράμματος ο οποίος βασίζεται σε διαδικασία πεπερασμένων διαφορών στην κυματοδήγηση της δέσμης, περιγράφεται λεπτομερώς στις παραπομπές [Scarmozzino2000, Scarmozzino1991]. Η τεχνική αυτή, χρησιμοποιεί μεθόδους πεπερασμένων διαφορών για την επίλυση της γνωστής παραβολικής ή παραξιακής προσέγγισης της εξίσωσης Helmholtz. Επίσης, η μέθοδος BPM χρησιμοποιεί «διαφανείς» συνοριακές συνθήκες όπως περιγράφεται στην παραπομπή [Hadley1992].

Η τρίτη και τελευταία μέθοδος είναι η FDTD η οποία αποτελεί μια αυστηρή λύση των εξισώσεων του Maxwell και δεν έχει προσεγγίσεις ή θεωρητικούς περιορισμούς. Η μέθοδος αυτή χρησιμοποιείται ευρέως ως τεχνική διάδοσης κυμάτων σε ολοκληρωμένα οπτικά, ειδικά σε καταστάσεις όπου οι λύσεις που παρέχονται από άλλες μεθόδους όπως π.χ. από την BPM, δεν είναι πραγματικές με φυσικό νόημα ή δεν μπορούν να αντιμετωπίσουν τη γεωμετρία της δομής. Δεδομένου ότι η μέθοδος FDTD αποτελεί μια άμεση λύση των εξισώσεων του Maxwell, είναι επόμενο να περιλαμβάνει πολλές περισσότερες παραμέτρους και εφέ σε σχέση με άλλες μεθόδους.

Χρησιμοποιώντας τις κατάλληλες μεθόδους προσομοίωσης στο λογισμικό Rsoft, η βασική δομή κυματοδήγησης έχει βελτιστοποιηθεί όσο αφορά τις απώλειες διάδοσης (0.01 dB/cm) και τη δυνατότητα για ακόμη πιο συμπαγές δομές, διατηρώντας παράλληλα τη μονορυθμική λειτουργία της στα 850 nm. Στα πλαίσια αυτής της διατριβής, τρεις φωτονικές δομές έχουν σχεδιαστεί. Η πρώτη είναι ο συζεύκτης πολλών ρυθμών (Multimode Interference Coupler – MMI) με σκοπό τον ομοιόμορφο και ισόποσο διαχωρισμό της ισχύος. Η δεύτερη είναι ο συζεύκτης φράγματος περίθλασης (Grating Coupler) με σκοπό την ανακατεύθυνση του φωτός από την οριζόντια κυματοδηγούμενη κατεύθυνση στην κάθετη, εκτός φωτονικού chip και αντίστροφα, και ο περιστροφικός πολωτής, με σκοπό τη διέγερση και εμφάνιση δύο υβριδικών ρυθμών με στόχο την εκμετάλλευση της πληροφορίας τόσο από τον εγκάρσιο ηλεκτρικό (Transverse Electric – TE) όσο και από τον εγκάρσιο μαγνητικό (Transverse Magnetic – TM) ρυθμό.

Η αυτό-απεικόνιση περιοδικών αντικειμένων που φωτίζονται από σύμφωνο φως, περιεγράφηκε για πρώτη φορά πριν 170 χρόνια [Talbot1836]. Οι κυματοδηγοί αυτό-εστίασης μπορούν επίσης να γεννήσουν περιοδικές, πραγματικές εικόνες ενός αντικειμένου όπως περιγράφεται στην παραπομπή [Marcuse1972]. Στις παραπομπές [Ulrich1975-1], [Ulrich1975-2], εξηγήθηκε λεπτομερώς η δυνατότητα επίτευξης της αυτό-απεικόνισης σε ομοιογενή κυματοδηγό. Η αρχή μπορεί να δηλωθεί ως εξής: Η αυτο-απεικόνιση είναι μια ιδιότητα των κυματοδηγών που υποστηρίζουν πολλαπλούς ρυθμούς, με τους οποίους ένα προφίλ πεδίου εισόδου αναπαράγεται σε μεμονωμένες ή πολλαπλές εικόνες, ανά περιοδικά διαστήματα κατά την κατεύθυνση διάδοσης του οδηγού. Ένα παράδειγμα τέτοιου κυματοδηγού εμφανίζεται στην **Figure *15***.

Ο συζεύκτης MMI, σε σύγκριση με τη φωτονική παθητική δομή Y-junction, προσφέρει σημαντικά πλεονεκτήματα όσον αφορά τη συμπάγεια και τις οπτικές απώλειες. Ο σχεδιασμός του ζεύκτη MMI έχει γίνει λαμβάνοντας υπόψη τις τιμές του δείκτη διάθλασης του πυρήνα αλλά και του περιβλήματος όπως επίσης και την απώλεια διάδοσης στην πλατφόρμα TriPleX, καθώς και τους περιορισμούς της τεχνολογίας που σχετίζονται με την ομοιογένεια φυσικού πλάτους της δομής τόσο σε σχεδιαστικό όσο και σε κατασκευαστικό επίπεδο. Η βελτιστοποίηση του σχεδιασμού συζεύκτη MMI στοχεύει σε χαμηλές συνολικές απώλειες εντός του chip (<1 dB) και σε χαμηλή ανισορροπία ισχύος μεταξύ των κυματοδηγών εξόδου (<0.5 dB). Η **Figure *19*** απεικονίζει μία τέτοια δομή στο μικροσκόπιο. Μελετήθηκαν τόσο απλοί, όσο και πιο περίπλοκοι σχεδιασμοί MMI δομών όπως για παράδειγμα με κωνικά τμήματα στους κυματοδηγούς εισόδου και εξόδου για την καλύτερη κυματοδήγηση του φωτός σε σχέση με τις απώλειες, καθώς επίσης με πρισματικές και καμπύλες περιοχές.

Ο συζεύκτης φράγματος περίθλασης, είναι μια δομή κυματοδηγού η οποία έχει περιοδικές κυματοειδείς ζεύξεις και χρησιμοποιείται για τη ζεύξη του φωτός από μία θέση εκτός του επιπέδου του φωτονικού chip προς και από αυτό εκμεταλλευόμενο το φαινόμενο της περίθλασης.

Ο συζεύκτης φράγματος περίθλασης έχει ενσωματωθεί μονολιθικά στο στρώμα πυρήνα του κυματοδηγού, επιτρέποντας έτσι την κατακόρυφη σύζευξη του εκπεμπόμενου φωτός από το VCSEL προς τον κυματοδηγό και από τον κυματοδηγό προς τις φωτοδιόδους. Αυτή η κατακόρυφη διάταξη, μπορεί να οδηγήσει σε ανακλάσεις οι οποίες μπορούν να βλάψουν το VCSEL αλλά και να προσθέσουν σφάλμα στις μετρήσεις του αισθητήρα. Για το λόγο αυτό, ένα ασύμμετρο φράγμα περίθλασης υιοθετήθηκε ώστε να ρυθμίζει σωστά τη γωνία του ανακλώμενου φωτός. Οι κύριες παράμετροι σχεδιασμού του φράγματος περίθλασης είναι το βάθος εισχώρησης της δέσμης στο φωτονικό chip, το μήκος και η περίοδος του συζεύκτη. Όλες βελτιστοποιήθηκαν χρησιμοποιώντας τη κατάλληλη κάθε φορά μέθοδο προσομοίωσης, λαμβάνοντας υπόψιν τη διάμετρο του πεδίου της δέσμης λειτουργίας του VCSEL, το μήκος κύματος εκπομπής του (850 nm) καθώς και τις πρακτικές ανοχές της διαδικασίας κατασκευής της πλατφόρμας TriPleX με στόχο η απώλεια σύζευξης να είναι χαμηλότερη από 1.5 dB. Στην **Figure *37*** παρουσιάζεται ένα σχηματικό του συζεύκτη φράγματος περίθλασης καθώς και η τοποθέτησή του στο φωτονικό chip.

Επιπλέον, έχει σχεδιαστεί μια νέα δομή που ονομάζεται συζεύκτης φράγματος περίθλασης «δύο θυρών» (**Figure *45***) [Gounaridis2019], με σκοπό τη μέγιστη ανακατεύθυνση του φωτός από το VCSEL μέσα στο φωτονικό chip, αξιοποιώντας και τις δύο πλευρές του. Δεδομένου ότι ο συζεύκτης φράγματος περίθλασης μία θύρας που σχεδιάστηκε έχει συντελεστή ζεύξης άνω του 25%, και λαμβάνοντας υπόψιν ότι η ίδια ποσότητας φωτός κυματοδηγείται και προς την άλλη κατεύθυνση, αυτός ο νέος σχεδιασμός αναμενόταν να έχει απόδοση 50-55%.

Λαμβάνοντας υπόψιν και τη συμβολή του κύματος εκπομπής από το VCSEL με το ανακλώμενο κύμα από τη διεπιφάνεια Si-SiO_2, τέτοια ώστε να είναι ενισχυτική, μετρήθηκε πειραματικά ο συντελεστής ζεύξης του να φτάνει το 54%.

Το VCSEL που έχει τοποθετηθεί πάνω από το φωτονικό chip με τη μέθοδο flip-chip, εκπέμπει φως με TE ρυθμό. Αυτός είναι και ο λόγος που ο συζεύκτης φράγματος περίθλασης που σχεδιάστηκε, λειτουργεί μόνο για αυτόν το ρυθμό. Το χαρακτηριστικό που εκμεταλλευόμαστε είναι η φθίνουσα ουρά του κυματοδηγούμενου φωτός, η οποία μπορεί και αλληλοεπιδρά με το δείγμα και ανιχνεύει τυχόν αλλαγές στο δείκτη διάθλασης που λαμβάνουν χώρα στο πάνω μέρος του κυματοδηγού, μέσα στα παράθυρα ανίχνευσης του MRR. Δεδομένου ότι είναι γνωστό πως η φθίνουσα ουρά του TM ρυθμού είναι μεγαλύτερη από αυτή του TE και άρα μπορεί να οδηγήσει σε μεγαλύτερη διείσδυση του φωτός μέσα στο δείγμα, αυξάνοντας την ευαισθησία του αισθητήρα, και οι δύο ρυθμοί πρέπει να είναι παρόντες στο φωτονικό chip. Η ύπαρξη και των δύο αυτών ρυθμών θα μπορούσε να γίνει με την περιστροφή του VCSEL κατά 45^0 στην κορυφή του κυματοδηγού. Αλλά τότε, μία περίπλοκη δομή ζεύξης φράγματος περίθλασης θα έπρεπε να σχεδιαστεί, η οποία θα υποστήριζε και τους δύο ρυθμούς. Αρχικές προσπάθειες και μελέτες προσομοίωσης έδειξαν πως μια τέτοια περίπλοκη δομή δεν είναι εύκολο να σχεδιαστεί και να έχει εγγυημένα την επιθυμητή λειτουργία. Για το λόγο αυτό, πραγματοποιήθηκε μία μελέτη προσομοίωσης ενός παθητικού φωτονικού στοιχείου που εξάγει το TM ρυθμό από τη λειτουργία του TE. Ένας μερικός περιστροφικός πολωτής μελετήθηκε ως η θεωρητική δομή που θα επιτρέψει την εν μέρει μετατροπή του TE σε TM κυματοδηγούμενο ρυθμό. Το συγκεκριμένο παθητικό στοιχείο, επιλέχθηκε λόγω της απλότητας λειτουργίας του. Λέγοντας «μερικός περιστροφικός πολωτής» θέλουμε να αναφέρουμε πως και οι δύο ρυθμοί (TE και TM) θα είναι παρόντες στο φωτονικό chip έτσι ώστε να εξάγουμε τις πληροφορίες ανίχνευσης και από τους δύο ταυτόχρονα. Με άλλα λόγια, και οι δύο ρυθμοί θα πρέπει να διαδοθούν στο φωτονικό κύκλωμα και να περάσουν από τα αισθητήρια στοιχεία MRRs. Ο μερικός περιστροφικός πολωτής, δε χρειάζεται να έχει την καλύτερη απόδοση μετατροπής, μιας και δεν είναι απαραίτητη η ακριβής αναλογία του 50% μεταξύ των δύο ρυθμών κυματοδήγησης. Έπειτα, όπως φαίνεται και στην **Figure *54***, δύο διαφορετικοί συζεύκτες φράγματος περίθλασης θα χρησιμοποιούνταν, ένας για κάθε ρυθμό, με σκοπό την οδήγηση του φωτός προς τις φωτοδιόδους.

Στην **Figure *55*** παρουσιάζεται ο μερικός περιστροφικός πολωτής με τις κύριες παραμέτρους σχεδίασής του για τη σωστή λειτουργία του, οι οποίες έχουν μελετηθεί θεωρητικά κατά τη διάρκεια των προσομοιώσεων.

Το κύριο μέρος του μερικού περιστροφικού πολωτή είναι ένας τραπεζοειδής κυματοδηγός. Η τοπολογία αυτού του κυματοδηγού επιτρέπει την περιστροφή της κάθετης συμμετρίας του, η οποία οδηγεί σε έμμεση χωρική περιστροφή του άξονα διάδοσης, προκαλώντας έτσι τη διέγερση των δύο υβριδικών ρυθμών TE και TM. Έτσι, αν το μήκος ασυμφωνίας (beating length) επιλεγεί προσεκτικά, η κατάσταση πόλωσης του κυματοδηγούμενου φωτός μπορεί να περιστραφεί από τον TE στον TM ρυθμό στο επιθυμητό ποσοστό. Για αυτήν τη θεωρητική μελέτη, χρησιμοποιήθηκε τόσο το λειτουργικό Rsoft όσο και το Lumerical.

Στη συνέχεια, παρουσιάζεται λεπτομερώς η αλγοριθμική μέθοδος που αναπτύχθηκε για την ακριβή εκτίμηση της μετατόπισης μήκους κύματος συντονισμού λόγω της αλλαγής του δείκτη διάθλασης στην επιφάνεια ανίχνευσης των MRRs στα φωτονικά chips. Πιο συγκεκριμένα, παρουσιάζεται πρώτα θεωρία των φωτονικών δομών MMRs. Γενικά, ένας συντονιστής μικροδακτυλίου αποτελείται από έναν κυκλικό οπτικό κυματοδηγό και έναν μηχανισμό ζεύξης για πρόσβαση του φωτός στον οπτικό βρόχο. Όταν τα κύματα στον βρόχο δημιουργούν μια μετατόπιση φάσης που ισούται με ακέραια πολλαπλάσια του 2π, τα κύματα συμβάλουν ενισχυτικά και η κοιλότητα είναι συντονισμένη. Δύο κύριοι τύποι MRR παρουσιάζονται στις ακόλουθες παραγράφους, ο all-pass (**Figure *60***) και ο add-drop (**Figure *61***) MRR.

Ένας all-pass τύπος MRR δημιουργείται λαμβάνοντας μια έξοδο ενός κατευθυντικού ζεύκτη και τροφοδοτώντας τον ξανά στην είσοδο. Μια τέτοια συσκευή παρουσιάζει συντονισμό περιοδικής κοιλότητας όταν το φως που διασχίζει τον δακτύλιο αποκτά μετατόπιση φάσης που αντιστοιχεί σε ακέραιο πολλαπλάσιο των 2π ακτινίων. Ο συντονιστής σχηματίζεται μαθηματικά από δύο παραμέτρους: τη δύναμη ζεύξης και τη διαδρομή ανατροφοδότησης.

Η άμεση αναλογία κυματοδηγού ενός ελεύθερου χώρου Fabry-Perot επιτυγχάνεται με την προσθήκη ενός δεύτερου οδηγού, παράλληλο στον πρώτο, από την απέναντι μεριά του μικροδακτυλίου συντονισμού. Αυτή η τοπολογία συμπεριφέρεται ως φίλτρο πλάτους στενής ζώνης που μπορεί να προσθέσει ή να αφαιρέσει μια ζώνη συχνοτήτων από ένα εισερχόμενο σήμα, και ονομάζεται add-drop φίλτρο. Επειδή αυτή η διαμόρφωση είναι μαθηματικά ισοδύναμη με το εκτενώς μελετημένο κλασικό ιντερφερόμετρο Fabry-Perot, οι εξισώσεις από τους συντελεστές μετάδοσης αναφέρονται απλώς: ο συντελεστής απόδοσης έντασης που αντιστοιχεί στο φως παρακάμπτοντας τον κυματοδηγό χαμηλότερης διέγερσης παρουσιάζεται στην εξίσωση 77. Αυτό αντιστοιχεί σε ένα μεταδιδόμενο σήμα τροποποιημένο έτσι ώστε να έχει εξαχθεί μια στενή ζώνη συχνοτήτων. Η εξαγόμενη ζώνη υπάρχει στη θύρα drop με τον συντελεστή μετάδοσης να εμφανίζεται ξανά στην εξίσωση 78. Αν και υπάρχουν παρόμοιες βελτιώσεις όπως στο all-pass filter όσο αφορά στην αποτελεσματική μετατόπιση φάσης στις δύο θύρες, συνδυάζονται με τα κυρίαρχα φαινόμενα πλάτους. Ως εκ τούτου, αν και η απόκριση φάσης δεν πρέπει να αγνοηθεί, εφαρμόζεται σπάνια για τις ιδιότητές της.

Στο δεύτερο μέρος, περιγράφεται η μοντελοποίηση και ο ποσοτικός προσδιορισμός απόδοσης των αισθητήρων που βασίζονται σε MRR. Το κύριο κριτήριο είναι το όριο ανίχνευσης (Detection Limit – DL), το οποίο ορίζεται ως η ελάχιστη αλλαγή του δείκτη διάθλασης που μπορεί να ανιχνευθεί αξιόπιστα από το σύστημα, στην ανώτερη επιφάνεια του MRR. Ανάλογα με το μέγεθος των μορίων-στόχων και τον τρόπο με τον οποίο συλλαμβάνονται κοντά στην επιφάνεια του MRR, το όριο ανίχνευσης μπορεί να μεταφραστεί στην ελάχιστη ποσότητα των μορίων που μπορούν να ανιχνευθούν και να ποσοτικοποιηθούν. Όπως αναφέρθηκε, το DL σχετίζεται με την ανάλυση R και την ευαισθησία S του συστήματος μέσω της σχέσης 86.

Η ευαισθησία περιγράφει το επίπεδο μετατόπισης συντονισμού ανά αλλαγή RIU. Για όλους τους τύπους κοιλοτήτων, η ευαισθησία εξαρτάται από το επίπεδο αλληλεπίδρασης μεταξύ του οπτικού κύματος και του δείγματος. Στα MRR γενικά και στα TriPleX MRRs συγκεκριμένα, αυτή η αλληλεπίδραση είναι μέτρια και οδηγεί σε μέτρια επίπεδα ευαισθησίας (100 nm/RIU). Η ανάλυση από την άλλη πλευρά, περιγράφει την ελάχιστη μετατόπιση συντονισμού που είναι ανιχνεύσιμη από το σύστημα χρησιμοποιώντας τη διαδικασία σάρωσης μήκους κύματος. Στην ιδανική περίπτωση, είναι ένας απείρως μικρός αριθμός, αλλά στην πραγματικότητα, έχει συγκεκριμένους περιορισμούς που προέρχονται από το θόρυβο πλάτους, τον φασματικό θόρυβο και το θόρυβο λόγω της θερμοκρασίας του συστήματος μέτρησης, καθώς και από τους εγγενείς περιορισμούς της μεθόδου που χρησιμοποιείται για την επεξεργασία των δεδομένων της μέτρησης. Χωρίς να εξετάσουμε τη μέθοδο επεξεργασίας σε αυτό το σημείο, η ανάλυση μπορεί να καθοριστεί ως η τυπική απόκλιση 3σ της μετρούμενης θέσης συντονισμού ($3\sigma_{\text{meas-n}}$), η οποία αντιπροσωπεύει τον συνολικό θόρυβο μέτρησης που περιγράφεται στη σχέση 87 και σχετίζεται με τα είδη θορύβων που προηγήθηκαν.

Ο θόρυβος πλάτους προστίθεται στο σήμα, επηρεάζοντας μόνο την κατακόρυφη θέση του κάθε σημείου μέτρησης. Σχετίζεται με το σχετικό θόρυβο έντασης του λέιζερ σάρωσης, το θόρυβο της φωτοδιόδου και το σφάλμα κβαντοποίησης στη μονάδα ανίχνευσης του συστήματος [White2008]. Για τα τυπικά συστήματα με χαμηλά επίπεδα οπτικής ισχύος στη φωτοδίοδο/φωτοανιχνευτή, φαίνεται πως κυριαρχεί ο θόρυβος λήψης [Misiakos2014, Agrawal2002]. Ο θόρυβος πλάτους κάθε σημείου, μπορεί να αναπαραχθεί με τη κατανομή Poisson, η οποία προσεγγίζει πολύ καλά την κανονική κατανομή [Agrawal2002].

Ο φασματικός θόρυβος στη συνάρτηση μεταφοράς είναι εξαιρετικά όμοιος με τον θόρυβο πλάτους. Η διαταραχή σε αυτήν την περίπτωση, συμβαίνει στην οριζόντια θέση του κάθε σημείου κατά μήκος του άξονα των μηκών κύματος. Οι στατιστικές ιδιότητες το φασματικού θορύβου ποικίλλουν μεταξύ των διαφορετικών συστημάτων και εξαρτώνται από τον τύπο, την ακρίβεια και τη σταθερότητα του μηχανισμού σάρωσης του μήκους κύματος του λέιζερ. Ωστόσο, για βήματα μέτριου μεγέθους, τα οποία είναι αρκετά μεγαλύτερα από το πλάτος γραμμής του λέιζερ, είναι λογικό να αναμένεται ότι η κατανομή του μήκους κύματος κάθε σημείου, ακολουθεί ξανά την κανονική κατανομή γύρω από την ονομαστική της τιμή.

Ο θόρυβος λόγω της θερμοκρασίας σχετίζεται με τις διακυμάνσεις της θερμοκρασίας περιβάλλοντος που αλλάζουν με τη σειρά τους το δείκτη διάθλασης του πυρήνα και του περιβλήματος του κυματοδηγού του MRR μέσα του θερμο-οπτικού φαινομένου. Αυτές οι αλλαγές επηρεάζουν τον ενεργό δείκτη διάθλασης του κυματοδηγούμενου ρυθμού με τυχαίες μετατοπίσεις του μήκους κύματος συντονισμού, οι οποίες προστίθενται στο πραγματικό σήμα του αισθητήρα. Με την προϋπόθεση ότι η διάρκεια σάρωσης είναι αρκετά μικρή (χαμηλότερη του ενός δευτερολέπτου), ο θόρυβος θερμοκρασίας επηρεάζει το σύνολο των σημείων της συνάρτησης μεταφοράς με ομογενή τρόπο και αντιστοιχεί σε μετατόπιση της μέτρησης η οποία πρέπει είτε να αποφεύγεται, είτε να λαμβάνεται υπόψιν κατά τη διάρκεια της μέτρησης. Προσπάθειες προς αυτήν την κατεύθυνση περιλαμβάνουν την ανάπτυξη MRRs με ανοχή στις μεταβολές της θερμοκρασίας [Han2007, Djordjevic2013], την ενσωμάτωση ενεργού ελέγχου της θερμοκρασίας του συστήματος, και τη χρήση ενός MRR αναφοράς πάνω στο chip ώστε να προσδιορίζεται και να αντισταθμίζεται αυτή η μεταβολή μέσω διαφορικών μετρήσεων [Heideman2012, Zhu2007].

Οι μελέτες προσομοίωσης συνέκριναν τη μέθοδο Fast Fourier Transform – FFT σε σχέση με τη μέθοδο αναζήτησης τοπικού μεγίστου και απέδειξαν ότι οι κοιλότητες συντονισμού με πολύ υψηλό Q-factor δεν είναι απαραίτητες για την επίτευξη χαμηλών ορίων ανίχνευσης. Η μέθοδος FFT αποδίδει καλύτερα για κοιλότητες συντονισμού με μέτριες τιμές του Q-factor που απαιτούν χαλαρές ανοχές στην κατασκευή. Η μέθοδος που έχει διερευνηθεί σε αυτή τη διατριβή χρησιμοποιεί τη μέθοδο FFT για τον υπολογισμό της σχετικής καθυστέρησης μεταξύ δύο πανομοιότυπων κυματομορφών. Βασίζεται στην πολύ γνωστή ιδιότητα του μετασχηματισμού Fourier που μεταφράζει οποιαδήποτε καθυστέρηση μεταξύ δύο συναρτήσεων από το πεδίο του χρόνου σε διαφορά φάσης στο πεδίο της συχνότητας. Επομένως, εάν είναι δυνατόν να εκτιμηθεί με ακρίβεια αυτή η διαφορά φάσης, είναι επίσης δυνατό να εκτιμηθεί και η καθυστέρηση. Αυτή η ιδιότητα δεν περιορίζεται μόνο σε συναρτήσεις του χρόνου, αλλά αφορά οποιαδήποτε φυσική λειτουργία, συμπεριλαμβανομένου του ενδιαφέροντός μας για αυτή τη διατριβή, της οπτικής μετάδοσης στη θύρα πτώσης με συνάρτηση μεταφοράς $T_d(\lambda)$, συναρτήσει του μήκους κύματος. Σε αυτήν την περίπτωση, η καθυστέρηση στο «χρονικό πεδίο» μεταξύ δύο συναρτήσεων μεταφοράς $T_{d1}(\lambda)$ και $T_{d2}(\lambda)$ μεταφράζεται άμεσα στην επιθυμητή μετατόπιση συντονισμού.

Επίσης, παρουσιάζεται ο πυρήνας του αλγορίθμου Fast Fourier Transform (FFT). Επιπλέον, πραγματοποιήθηκαν μελέτες προσομοίωσης για να περιγραφεί η επίδραση του θορύβου πλάτους και του φασματικού θορύβου, ο αριθμός κορυφών συντονισμού εντός του παραθύρου σάρωσης μήκους κύματος, η επίδραση της εξάρτησης ισχύος της πηγής λέιζερ στο μήκος κύματος και το αποτέλεσμα της θέσης των συναρτήσεων μεταφοράς μέσα στο παράθυρο σάρωσης. Τα κύρια συμπεράσματα είναι ότι η παρουσία πρόσθετων κορυφών συντονισμού στο παράθυρο επεξεργασίας και μέτρησης μπορεί να μειώσει τον θόρυβο και να βελτιώσει την ακρίβεια σε ένα θορυβώδες περιβάλλον. Η μέθοδος FFT είναι πολύ ανεκτική ακόμα και όταν υπάρχει εξάρτηση ισχύος από το μήκος κύματος, η θέση των συναρτήσεων μεταφοράς μέσα στο παράθυρο σάρωσης πρέπει να είναι τέτοια ώστε η ισχύς σήματος στην άκρη του παραθύρου να είναι ελάχιστη για να αποφευχθούν ασυμμετρίες στο περιοδικό σήμα της μεθόδου.

Μελετώντας το θόρυβο πλάτους και χρησιμοποιώντας MRRs με ρεαλιστικές τιμές του συντελεστή εξασθένησης ισχύος α ($\alpha<1$), καταλήγουμε στο ότι η μέθοδος FFT βελτιώνει την ανάλυση του αισθητήρα σε σχέση με τη μέθοδο ανίχνευσης τοπικού μεγίστου, αρκετές τάξεις μεγέθους. Συγκεκριμένα, η μέθοδος ανίχνευσης τοπικού μεγίστου έχει ανάλυση 1 – 10 pm. Από την άλλη μεριά, η μέθοδος FFT επιτρέπει ανάλυση της τάξης του 1 pm για εξαιρετικά χαμηλές τιμές του SNR, και για ανάλυση μεταξύ του 0.001 και 0.01 pm για τιμές SNR 60 dB. Η εικόνα παραμένει η ίδια για ιδανικά MRRs με $\alpha=1$. Σε αυτήν την περίπτωση, η ανάλυση που παρέχει η μέθοδος αναζήτησης τοπικού μεγίστου περιορίζεται από το βήμα σάρωσης, το οποίο στην μελέτη που πραγματοποιήθηκε παραμένει ίσο ή μεγαλύτερο από 0.0625 pm. Ωστόσο, ακόμη και αν αυτός ο περιορισμός δεν υπήρχε, τα αποτελέσματα δείχνουν πως η μέθοδος FFT προσφέρει βελτίωση στην ανάλυση κατά δύο τάξεις μεγέθους.

Η χρήση της FFT μεθόδου, προσφέρει σημαντική βελτίωση στην ανάλυση του συστήματος ακόμη και για φασματικό θόρυβο χαμηλότερο από την τιμή $3\sigma_\lambda$. Από την άλλη μεριά, ενώ ο Q-factor φαίνεται να μην έχει κάποιο πρακτικό αποτέλεσμα στην περίπτωση της μεθόδου ανίχνευσης τοπικού μεγίστου, δε συμβαίνει το ίδιο και για τη μέθοδο FFT. Συγκεκριμένα, η ανάλυση του συστήματος είναι μέτρια για υψηλούς Q-factors αλλά βελτιώνεται αξιοσημείωτα για χαμηλότερους συντελεστές, όπου ένας μεγάλος αριθμός σημείων βρίσκεται εντός του φάσματος συντονισμού και συμμετέχουν στον υπολογισμό της μεθόδου FFT. Για τιμή του Q-factor ίση με 10^4, το κέρδος της FFT μεθόδου σε σχέση με τη μέθοδο αναζήτησης τοπικού μεγίστου, κυμαίνεται μεταξύ 10 και 100 για όλα τα βήματα σάρωσης του λέιζερ και όλα τα επίπεδα φασματικού θορύβου.

Ο αριθμός των επιπλέον κορυφών συντονισμού μέσα στο παράθυρο σάρωσης και επεξεργασίας μπορεί να οδηγήσει στη μείωση του θορύβου της μέτρησης και να βελτιώσει την ακρίβεια της FFT μεθόδου. Καθώς η μέση τιμή σφάλματος παραμένει αμελητέα σε όλες τις περιπτώσεις διαφορετικών αριθμών κορυφών συντονισμού μέσα στο παράθυρο σάρωσης, είναι εμφανής η βελτίωση που συμβαίνει στην τυπική απόκλιση 3σ κατά περίπου έναν παράγοντα δύο, για όλα τα βήματα σάρωσης όταν λαμβάνουμε υπόψιν τέσσερις αντί μίας κορυφής. Σημειώνεται ωστόσο ότι αυτή η βελτίωση συμβαίνει σε βάρος ενός μεγαλύτερου εύρους σάρωσης, το οποίο συνεπάγεται μεγαλύτερη πολυπλοκότητα του λέιζερ, των ηλεκτρονικών οδήγησης καθώς και της διάρκειας της μέτρησης.

Η εξάρτηση από την ισχύ τού λέιζερ φαίνεται να μην έχει πρακτικά καμία επίδραση στην περίπτωση που λαμβάνεται υπόψιν μία κορυφή συντονισμού μέσα στο παράθυρο σάρωσης, να έχει μια ασθενή επίπτωση στην περίπτωση των δύο κορυφών και επίσης μικρή επίδραση στην περίπτωση των τεσσάρων κορυφών. Ο μηχανισμός αυτού του φαινομένου, δε σχετίζεται με τις θεμελιώδης ιδιότητες της FFT μεθόδου, αλλά με τα χαμηλότερα επίπεδα ισχύος του αριστερού μέρους του παραθύρου σάρωσης. Από τη στιγμή που η μέθοδος χρησιμοποιεί σημεία από όλα τα μέρη των συναρτήσεων μεταφοράς των MRRs ώστε να εξάγει τη μετατόπιση του μήκους κύματος συντονισμού, αυτά τα μέρη χαμηλότερης ισχύος κάνουν τη μέτρηση πιο θορυβώδη, αυξάνοντας ουσιαστικά την τιμή της τυπικής απόκλισης 3σ.

Η ασυμμετρία των συναρτήσεων μεταφοράς των MRRs μέσα στο παράθυρο σάρωσης που προέρχεται από τη θέση τους, δεν επηρεάζει την τυπική απόκλιση 3σ των μετρήσεων σημαντικά. Από την άλλη μεριά όμως, η μέση τιμή του σφάλματος αυξάνεται μαζί με την αύξηση της ασυνέχειας των συναρτήσεων και σχεδόν ανεξάρτητα με το βήμα σάρωσης. Δεδομένου ότι η χρήση παραθύρων σάρωσης που βασίζονται σε παράθυρα Gauss, κωνικού συνημίτονου και παραθύρων Chebyshev, και επεξεργασίας των σημείων μέτρησης όπως αυτά που περιγράφονται στην παραπομπή [Harris1978], δεν μπορεί να επιλύσει επαρκώς αυτό το πρόβλημα, είναι προφανές ότι η εξάλειψη των άκρων ασυνέχειας των συναρτήσεων μεταφοράς είναι απαραίτητα για να επιτευχθούν αξιόπιστες μετρήσεις. Στην πράξη, αυτό μπορεί να συμβεί χρησιμοποιώντας ένα μεγαλύτερο παράθυρο σάρωσης και επιλέγοντας έπειτα, ένα παράθυρο επεξεργασίας των σημείων, μικρότερο από το αρχικό, το οποίο θα περιέχει ακέραια πολλαπλάσια του FSR των MRRs και θα είναι συμμετρικό σε σχέση με τις κορυφές συντονισμού των συναρτήσεων μεταφοράς.

Κλείνοντας με την μελέτη της FFT μεθόδου, έγινε η σύγκρισή της με τη μέθοδο της Lorentzian προσαρμογής. Παρότι προκύπτει πως οι τιμές των τυπικών αποκλίσεων των δύο μεθόδων είναι συγκρίσιμες και πολύ καλές, σημειώνεται πως για μεγαλύτερα βήματα σάρωσης που μελετήθηκαν στην παρούσα διατριβή, η μέση τιμή του σφάλματος στην εκτίμηση της μεταβολής του μήκους κύματος συντονισμού με τη μέθοδο της Lorentzian προσαρμογής είναι αρκετά μεγάλη. Σε συνδυασμό με την πολύ μικρή τυπική απόκλιση της μεθόδου, μπορεί να οδηγήσει σε αποτυχία μέτρησης της πραγματικής αλλαγής του δείκτη διάθλασης. Από την άλλη μεριά, για μικρά βήματα σάρωσης (<0.015 pm), η απόδοση της μεθόδου της Lorentzian προσαρμογής είναι πράγματι πολύ υψηλή, το οποίο όμως δεν είναι πρακτικό για LoC συστήματα όπως αυτό που πραγματεύεται η παρούσα διατριβή. Αξίζει να σημειωθεί πως η μέθοδος FFT έχει πλεονέκτημα σε σχέση με τη μέθοδο Lorentzian προσαρμογής ακόμη και στο χρόνο υλοποίησης των μετρήσεων εκτίμησης της μεταβολής του μήκους κύματος συντονισμού, κατά έναν παράγοντα 60, όπως έδειξαν οι μελέτες που πραγματοποιήθηκαν στο περιβάλλον της MATLAB.

Στη συνέχεια της διατριβής, παρέχεται μια λεπτομερής περιγραφή της ηλεκτρονικής πλατφόρμας, καθώς και η πλατφόρμα λογισμικού και η διεπαφή μεταξύ του χρήστη και του φωτονικού βιοαισθητήρα και η λεπτομερής περιγραφή ενός αντιπροσωπευτικού πειράματος με στόχο την ανίχνευση συγκεκριμένων πρωτεϊνών.

Δίνεται η περιγραφή της αρχιτεκτονικής της πλατφόρμας ηλεκτρονικών και περιγράφονται λεπτομερώς τα διάφορα εξαρτήματα που αποτελούν την πλατφόρμα αυτήν. Συγκεκριμένα, τα εξαρτήματα που περιλαμβάνονται στην πλατφόρμα είναι η κύρια μονάδα ελέγχου, η μονάδα προεπεξεργασίας, η μονάδα ανίχνευσης (με τη σειρά της αποτελείται από τις μονάδες ελέγχου οπτικό-ηλεκτρονικής και μικροροϊκών) και το δίκτυο διανομής ισχύος καθώς επίσης και οι προδιαγραφές των εξαρτημάτων που χρησιμοποιήθηκαν. Στο φυσικό επίπεδο, η κύρια μονάδα ελέγχου θα συνδεθεί μέσω Ethernet με την οπτοηλεκτρονική και τις μονάδες προεπεξεργασίας (άμεσες συνδέσεις). Οι μονάδες μικροροϊκών και κύριου ελέγχου θα συνδεθούν μέσω USB σε σειριακή επικοινωνία (απλή UART επικοινωνία).

Στο δεύτερο μέρος αυτού του κεφαλαίου, η εστίαση στρέφεται στην πλατφόρμα λογισμικού και στις διεπαφές ανάμεσα στο χρήστη και τον βιοαισθητήρα, περιγράφοντας λεπτομερώς τον προγραμματισμό των ηλεκτρονικών. Η κύρια γλώσσα προγραμματισμού που χρησιμοποιείται είναι το LabVIEW της National Instruments. Το LabVIEW είναι μια γραφική γλώσσα, που διευκολύνει τον προγραμματισμό, επιτρέποντας στον προγραμματιστή να επικεντρωθεί περισσότερο στην εφαρμογή και προσφέρει επίσης ένα απλό εργαλείο σχεδίασης διεπαφής του χρήστη με τα γραφικά. Τα προγράμματα LabVIEW αποτελούνται από δύο μέρη που επικοινωνούν διμερώς, δηλαδή τα διαγράμματα “block”, όπου βρίσκεται ο κώδικας και πραγματοποιείται όλη η επεξεργασία, και τα μπροστινά panel όπου ο χρήστης αλληλοεπιδρά με το πρόγραμμα, αλλάζοντας τις τιμές των μεταβλητών και οπτικοποιώντας τα αποτελέσματα. Ένα κεντρικό πρόγραμμα που εκτελείται στην κύρια μονάδα ελέγχου θα ελέγχει τις μονάδες οπτικοηλεκτρονικής, μικροροϊκών και προεπεξεργασίας. Στο επίπεδο εφαρμογής, η προεπεξεργασία και ο κύριος έλεγχος θα επικοινωνούν και θα αναλύουν αρχεία xml που περιέχουν τις εντολές και τα μηνύματα, μέσω ζευγών διακομιστή/πελάτη FTP, τα μικροροϊκά και ο κύριος έλεγχος θα επικοινωνούν ανταλλάσσοντας χαρακτήρες UTF-8, η οπτοηλεκτρονική και η κύρια μονάδα ελέγχου θα επικοινωνούν χρησιμοποιώντας κοινόχρηστες μεταβλητές δικτύου, μια ιδιόκτητη τεχνολογία LabVIEW που θεωρείται ως ένα μαύρο κουτί για τον προγραμματιστή, αλλά προσφέρει απρόσκοπτη επικοινωνία μεταξύ των δύο συσκευών δημιουργώντας ξανά κοινόχρηστα και μεταβαλλόμενα ζεύγη διακομιστών/πελατών.

Το σύστημα που έχει αναπτυχθεί στοχεύει να είναι ένα εξελιγμένο, αυτόνομο, φορητό σύστημα βιο-φωτονικού αισθητήρα, ικανό να ανιχνεύει σε σύντομο χρονικό διάστημα και με ακρίβεια, διαφορετικούς αναλύτες σε ελαιόλαδο, σε ξηρούς καρπούς και σε γάλα στα πλαίσια του ευρωπαϊκού έργου BIOFOS. Έχοντας υπόψη αυτές τις προϋποθέσεις, ο βιο-αισθητήρας σχεδιάστηκε από την αρχή της ως το τέλος της ανάπτυξής του, έχοντας τη δυνατότητα να εκτελεί όλες τις απαραίτητες ενέργειες, δηλαδή προεπεξεργασία δειγμάτων, διανομή δειγμάτων και έλεγχο ροής, απόκτηση δεδομένων και ανίχνευση σε μία μόνο συσκευή.

Το σχέδιο χρήσης φορητού υπολογιστή ως συνοδευτικής μονάδας για τον έλεγχο του αισθητήρα και την παρουσίαση των αποτελεσμάτων απορρίφθηκε κατά τη διάρκεια της διατριβής και επιλέχθηκε ένας ενσωματωμένος υπολογιστής με οθόνη LCD, παρέχοντας αυτονομία και ένα περισσότερο συμπαγές σύστημα. Αυτό το σύστημα βιοαισθητήρα σχεδιάστηκε για να λειτουργεί στην περιοχή εξαιρετικά χαμηλής τάσης (Extra-Low Voltage – ELV) που απαιτεί μόνο 12V DC, έτσι ώστε να είναι απολύτως ασφαλές για τον χρήστη.

Η αρχιτεκτονική του hardware του συστήματος βιοαισθητήρα ακολουθεί ένα ιεραρχικό σχήμα όπως θα περιγράφεται λεπτομερώς στο τέταρτο κεφάλαιο. Τα εξαρτήματα του hardware επιλέχθηκαν προσεκτικά για υψηλή απόδοση, συμβατότητα, χαμηλή κατανάλωση ενέργειας και ευκολία προγραμματισμού.

Στο τελευταίο μέρος της διατριβής, παρουσιάζεται ένα πείραμα επαλήθευσης με χρήση διαλυμάτων σουκρόζης, των θεωρητικών μελετών που περιγράφηκαν στα προηγούμενα κεφάλαια. Ακολουθεί επίσης ένα πείραμα αξιολόγησης του αισθητήρα για τη συγκεκριμένη δέσμευση των μορίων-στόχων μυκοτοξίνης OTA και χαλκού στα απταμερή που στοχεύουν OTA και χαλκό, αντίστοιχα. Επιπλέον, έχει διερευνηθεί η επίδραση της παρουσίας $MgCl_2$ στην πρόσδεση αυτών των μορίων στα αντίστοιχα απταμερή. Κατά τη διάρκεια αυτών των πειραμάτων χρησιμοποιήθηκαν διαφορετικά είδη ρυθμιστικών διαλυμάτων.

Chapter 1. Introduction

Over the past years, significant efforts have been placed on optical lab-on-a-chip technology based on optical interferometers [Centi2009]. The interferometric photonic sensors are label-free, do not suffer from electromagnetic interference and can really deliver on the vision for miniaturized optofluidic sensors, as a result of the revolution in photonic integration technology since early 2000s [Deisingh2004, Iqbal2010]. As summarized in **Table 1**, they appear to have significant overall advantage over competitive platforms such as fluorescence-based [Di Stefano2012], surface plasmon resonance (SPR)-based [Hua2012] electrochemical [Zhang2012], surface acoustic waves-based [Guo2012].

***Table 1** Qualitative benchmarking of LoC-based optical interferometric biosensors against competitive technologies.*

Type of biosensors	Use of labels	Integration potential	EM interference	Sensitivity
Fluorescence-based	Yes	Medium	No	Very high
Surface plasmon resonance-based	No	Low	No	High
Electrochemical	No	High	High sensitivity	High
Surface acoustic waves-based	No	Low	High sensitivity	Medium
Surface stress-based	No	Low	High sensitivity	Medium
Optical interferometric	No	High	No	Very high (in principle)

Nevertheless, even in the case of the interferometric sensors, significant challenges are yet to be addressed so as to exploit the full potential of the sensing mechanism and of the photonic integration technology. In more detail:

Sensitivity: The sensitivity depends both on the physics of the sensing mechanism and the targeted molecules that should be detected with the corresponding, suitable biochemistry. The sensitivity of the interferometric LoC-based sensors is specifically concerned, it is still moderate and 2-3 orders of magnitude lower than the theoretical limit [Link Pythia]. Translated into the limit of the refractive index (RI) change that can be detected, it is between 10^{-6} - 10^{-7} RI units (RIU), while the theoretical limit is 10^{-9} RIU and the corresponding detection limit of the (more complex and bulkier) SPR sensors is $<10^{-7}$ RIU [Herold2009], [Link BIOFOS]. Regarding the biotransducer elements utilized for the recognition of the analytes, antibodies and aptamers are the most common elements having demonstrated their ability for high sensitivity (low detection limits) in various types of biosensors [Yurii2012].

Compactness and ease in use: Despite the impressive progress on photonic integration driven by telecom applications [Deisingh2004], the compactness of the photonic part of the sensors is still limited, as the optical sources and the detection elements are placed off-chip and are connected with the photonic chip through optical fibers and bulk optical elements. In this way, the sensor devices become more complex and their use difficult and expensive, especially as far the efficiency of the coupling light and the handling of the polarization of the input light are concerned.

Other challenges towards the sensing mechanism are the specificity, the reliability, the reusability and low cost. The specificity issues that all types of label-free photonic sensors still face today are related to their biochemical part. It is common to have a system capable of detecting an analyte with high sensitivity but at the same time not being able to distinguish between the analyte and closely related biomolecules [Holford2012]. Obtaining reproducible results with bio-photonic sensors is hampered by the limitations in the methods of surface functionalization and biotransducer immobilization on the sensor surfaces. These are not stable enough and can result in large variations in the number of active biotransducer molecules on these surfaces [Boutopoulos2008, Trilling2013]. Moreover, in the common case of antibodies as biotransducers, the reliability is also affected by the low reproducibility of the antibodies themselves and their large batch-to-batch variation [Ruigrok2011]. The development of ultra-low-cost, disposable devices has been the dominant model for the development and commercialization of all types of LoC sensors so far. The adoption of this model has been mandatory due to the limited durability and reusability of the antibodies as biorecognition elements, as well as due to the difficulty in the design of efficient cleansing cycles for the fluidics of the sensors.

This thesis, steps in to provide clear-cut solutions and to address the first two above mentioned points which have been so far the actual roadblocks for the uptake of LoC technology. The outcome of this work will provide a paradigm shift in the development of LoC sensors by providing solutions towards the developing of a portable, integrated and high-added value sensor system for various applications.

The photonic part of the system will rely on the use of multiple micro-ring resonators (MRRs) as the optical interference elements. The MRRs will be monolithically integrated on a CMOS compatible photonic chip based on the TriPleX integration technology, which employs silicon-nitride and silicon-oxide layers [De Vos2007]. Exploiting the high quality (Q-factor) of the MRRs as optical cavities, the ultra-low propagation loss of the TriPleX platform (<0.01 dB/cm) and the operation of the system at 850 nm, the system will be able to provide a convincing solution for the low-sensitivity issues of current LoC systems, as it will be capable of multi-analyte detection with record detection limit towards $8.5\cdot10^{-7}$ RIU. Furthermore, in order to address the limited compactness of the optical part and the related difficulties in the handling of the input and output light, photonic passive components will be designed for the hybrid integration of the 850 nm vertical cavity surface emitting laser (VCSEL) and the photodetector array together with the monolithic MRRs and the rest of the passive circuitry on a low-footprint photonic chip. Moreover, the algorithm which will be used for processing the data making the sensor very tolerant to different kinds of noise, and the driving and control electronics in order to provide a user-friendly interface, a stand-alone and portable photonic sensing system will be developed and presented.

Three are the main optical interference schemes that are intensively investigated today: The Young's interferometer, the Mach-Zehnder interferometer (MZI) and the micro-ring resonator (MRR). The first one uses a laser source that is split into two beams. One of them serves as the reference, while the other senses the sample. The two beams are combined and create an interference pattern that is detected by a 2D detector array. The MZI relies on a similar principle. The input light is split into two parts that are recombined after the sensing area, and the final output is detected either by a photodetector or a spectrometer depending on whether the optical source is monochromatic or a broadband light source.

MRRs should be considered as the next reasonable step in the evolution of interferometric bio-photonic sensors. Compared to MZIs, the MRRs have the advantage of being extremely compact, thus allowing for a high level of miniaturization and sensor parallelization. Furthermore, as MZIs also do, MRRs represent periodic optical filters but with much higher filter finesse and sharpness of the peak resonance, which results in much higher system sensitivity compared to MZI-based systems. The theoretical limit in the detection of refractive index (RI) change by the MRRs goes down to 10^{-9} refractive index units (RIU) [Link Pythia], although in practice it is several orders away from this value. MRR-based biosensors have already been demonstrated on optical polymers with 60 μm diameter [Kitsara2010] and on the silicon-on-insulator (SOI) platform with diameters as short as 10 μm [Krioukov2003]. The detection limit of the SOI MRRs is in the order of 10^{-4}-10^{-5} RIU. To further reduce this limit, MRRs based on slot waveguides rather than conventional ridge waveguides have been developed allowing for stronger interaction between the sample and the propagating field and reducing the detection limit by a factor of 3.5 [Chao2006]. Moreover, MRRs were also shown on the TriPleX platform as test biosensor structures with diameters of 100 μm [De Vos2007], which are still short enough to comply with the minimum achievable size of functionalized areas on the sensor surface and to allow for ultra-compact sensor arrays. The detection limit that was achieved was lower than 10^{-6} RIU as a result of the overall potential of the TriPleX platform for high Q-factor MRRs and the transparency of the platform at 850 nm.

Silicon-nitride/silicon-oxide waveguiding (TriPleX [De Vos2007]) platform, will be used for the photonic engine of the bio-photonic sensor. In its typical geometry for sensing applications, TriPleX platform consists of a silicon-oxide (SiO_2) bottom cladding, a silicon-nitride (Si_3N_4) core layer, and a SiO_2 top cladding, which can be removed in the sensing area of the MRRs in order to allow for the interaction between the circulating lightwave inside the cavity with the targeted molecules of the sample, as shown in **Figure *1***. In this geometry, TriPleX features strong polarization birefringence that prevents signal fading in interferometric sensing applications. Moreover, the waveguide remains transparent and with ultra-low propagation loss (<0.01 dB/cm) at 850 nm, where the absorption by aqueous samples (or equivalently pre-treated samples in solvent phase) is low, and low-cost VCSELs are available. The minimization of the light absorption by the sample and of the propagation loss inside the waveguide is extremely favorable for two reasons: first it allows for the account of pure interference effects based only on the change of the (real part of the) effective RI inside the cavity, thus making the calibration and the final data processing straightforward and reliable. Second, it allows for the design of high Q-factor (>10.000) cavities that result in highly sensitive sensors with very low limits in the detection of RI changes [Link Pythia].

This thesis will further study the properties and the operation of the MRRs, resulting an optimum waveguide cross-section, shape and coupling coefficient with the two bus waveguides in order to achieve detection limits that are lower than 10^{-7} refractive index units (RIU). The free spectral range (FSR) of the MRRs, determined by the total length of their cavity, will be within the 0.5 - 1.0 nm range. In order to achieve this range, the radius of the curved section will be shorter than 75 µm and the length of the straight section of the cavity will be shorter than 150 µm. The use of the MRRs will be combined with a wavelength tunable VCSEL with tuning range in excess of 1 nm, linewidth lower than 0.05 nm and power consumption lower than 50 mW. This wide tuning range will be achieved through appropriate combination of operating temperature and driving current adjustment for the VCSEL [La Pera2002, De Vos2007]. Given that the detection accuracy of the system will be lower than 10^{-6} nm and the total scanning range higher than 1.5 nm, the targeted dynamic range of the measurement will be at least 5 orders of magnitude.

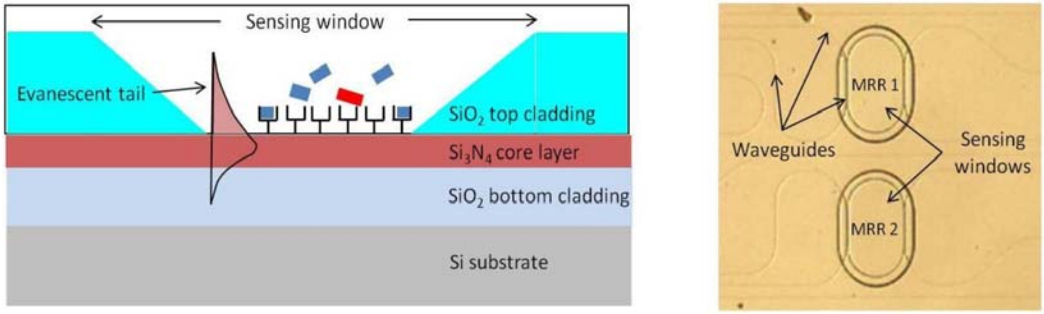

Figure 1: (a) Cross-section of the TriPleX platform showing the layered structure, the shape of the sensing window and the evanescent tail of the propagating mode, and (b) photograph of fabricated MRRs (shaped as racetracks) on TriPleX showing the waveguides and the shape of the sensing windows going around the MRRs.

The photonic sensor will monolithically integrate on TriPleX a circuit with main elements a multi-mode interference (MMI) coupler [Claes2009] and an 8-fold MRR array, which will allow the simultaneous detection of refractive index changes that happen in 6 different on-chip MRRs. The MMI coupler will split the VCSEL light into 8 equal parts that will be further guided to the inputs of the MRR array. The insertion loss for the MMI coupler will be lower than 1 dB and the imbalance between the optical powers at the 8 output ports will be lower than 0.5 dB. One MRR will remain non-functionalized serving as reference in order to account for VCSEL drifts. An asymmetric Mach Zehnder interferometer will be used for calibration purposes, while the remaining six MRRs will be used for the actual detection. The targeted insertion loss in the optical circuit described above will be <12 dB including the inelastic 9 dB loss of the MMI coupler due to the 1:8 power split.

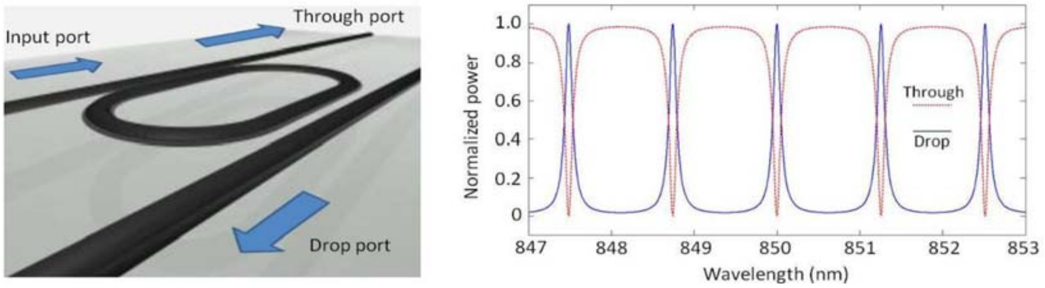

Figure 2: Artistic impression of a micro-ring resonators (MMR) structure (left). Normalized transmission of optical power at the “through” and the “drop” port of the structure as function of the input wavelength (right).

This thesis will also make a decisive step to adopt hybrid integration concepts that are widely used today for the fabrication of photonic integrated circuits in telecom sector and apply them for developing ultra-compact and highly functional optical circuits for sensing applications. More specifically, flip-chip bonding techniques will be used based on Indium or AuSn soldering systems [Iga2000] for the integration of the 850 nm emitting VCSEL on the TriPleX as well as for the integration of an 8-fold monolithic array of silicon photodiodes with the same chip. The size of the array will be as long as the size of the MRR array (8-fold) in order to monitor the “drop” port (**Figure *2***) of each MRR increasing in this way the system sensitivity and reliability. In the case of the VCSEL, a two-port grating coupler will be imprinted in the core layer of the waveguide to couple the light from the VCSEL inside the waveguide, while in the second case, single port grating couplers will be introduced in the TriPleX waveguides to improve the coupling to the photodiodes. The targeted coupling efficiencies will be 4-5 dB both for the VCSEL/TriPleX and the TriPleX/photodiode interface, resulting in a loss of <17 dB for the total of the optical circuit including the loss in the passive part. This value is expected to allow for sufficient system signal-to-noise ratio (SNR) and measurement resolution. The final optical chip will facilitate the operation of 8 sensing elements with two of them for reference/calibration purposes and will have a footprint of only 4x5 mm^2. **Figure *3*** presents an artistic view of the envisaged optical chip of the photonic sensing system.

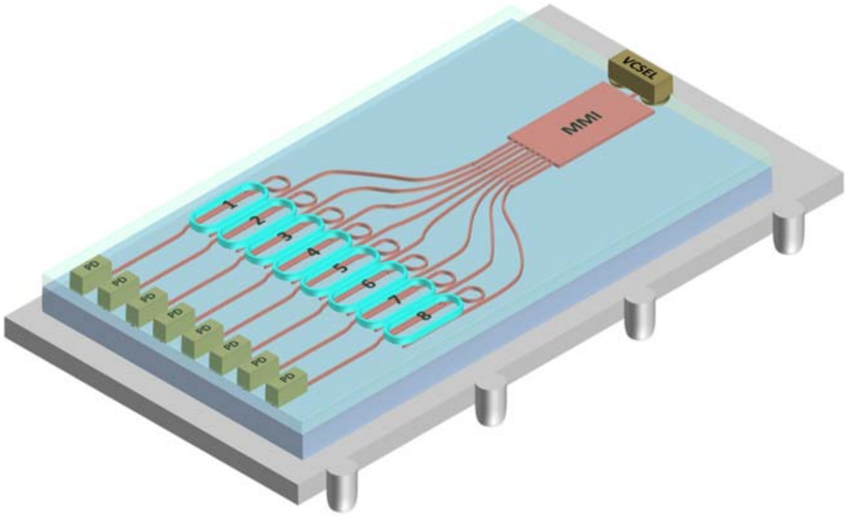

Figure 3: Artistic view of the optical chip of the photonic sensor fabricated on TriPleX photonic platform using monolithic and hybrid integration techniques.

References of Chapter 1

[Centi2009] Centi S, Laschi S, Mascini M., “Strategies for electrochemical detection in immunochemistry”, Bioanalysis. Oct;1(7):1271-91. 2009.

[Deisingh2004] Deisingh AK, Thompson M, “Biosensors for the detection of bacteria,” Can J Microbiol, 50(2):69-77. 2004.

[Iqbal2010] M. Iqbal, M. A. Gleeson, B. Spaugh, F. Tybor,W. G. Gunn, M. Hochberg,T. Baehr-Jones, R. C. Bailey, and L. C. Gunn, “Label-free biosensor arrays based on silicon ring resonators and high-speed optical scanning instrumentation,” IEEE J. Sel. Topics Quantum Electron., pp. 654–661, 2010.

[Di Stefano2012] Di Stefano V, Avellone G, Bongiorno D, Cunsolo V, Muccilli V, Sforza S, Dossena A, Drahos L, Vékey K. “Applications of liquid chromatography-mass spectrometry for food analysis,” J Chromatogr A. Oct 12;1259:74-85. 2012.

[Hua2012] Hua X, Yang J, Wang L, Fang Q, Zhang G, Liu F., “Development of an enzyme linked immunosorbent assay and an immunochromatographic assay for detection of organophosphorus pesticides in different agricultural products,” PLoS One. 2012;7(12), 2012.
[Zhang2012] Zhang R, Ying Y, Rao X, Li J, “Quality and safety assessment of food and agricultural products by hyperspectral fluorescence imaging,” J Sci Food Agric. Sep;92(12):2397-408, 2012.

[Guo2012] Guo X., “Surface plasmon resonance-based biosensor technique: a review.”, J Biophotonics, Jul;5(7):483-501. 2012.

[Yurii2012] Yurii A. Vlasov, “Silicon CMOS-Integrated Nano-Photonics for Computer and Data Communications Beyond 100G,” IEEE Communications Magazine, pp-567-572, February 2012.

[Herold2009] Herold, KE; Rasooly, A (editor), “Lab-on-a-Chip Technology: Fabrication and Microfluidics,” Caister Academic Press, ISBN 978-1-904455-46-2. 2009.

[Link Pythia] http://www.pythia-project.eu/index.php?id=11.

[Link BIOFOS] http://www.ict-biofos.eu/.

[Holford2012] Holford TR, Davis F, Higson SP., “Recent trends in antibody-based sensors,” Biosens Bioelectron. Apr 15;34(1):12-24. 2012.

[Boutopoulos,2008] Christos Boutopoulos, Vasiliki Tsouti, Dimitrios Goustouridis, Stavros Chatzandroulis and Ioanna Zergioti, “Liquid phase direct laser printing of polymers for chemical sensing applications,” APPLIED PHYSICS LETTERS 93, 191109, 2008.

[Ruigrok2011]Ruigrok VJ, Levisson M, Eppink MH, Smidt H, van der Oost J., “Alternative affinity tools: more attractive than antibodies?,” Biochem J., 436(1):1-13, 2011.

[Trilling2013] Anke K.Trilling, Michiel M. Harmsen, Vincent J.B.Ruigrok, Han Zuilhof, Jules Beekwilder, “The effect of uniform capture molecule orientation on biosensor sensitivity: Dependence on analyte properties,” Biosensors and Bioelectronics 40, 219–226, 2013.

[Kitsara2010] M. Kitsara, K. Misiakos, I. Raptis and E. Makarona, “Integrated optical frequency-resolved Mach- Zehnder interferometers for label-free affinity sensing,” Optics Express, 18 (8), pp. 8193 8206, Apr. 2010.

[Krioukov2003] E. Krioukov, J. Greve, C. Otto, “Performance of integrated optical microcavities for refractive index and fluorescence sensing,” Sens. Actuators B Chem. 90, pp. 58-67, 2003.

[Chao2006] Chung-Yen Chao, Wayne Fung, and L. Jay Guo, “Polymer Microring Resonators for Biochemical Sensing Applications,” IEEE JSTQE, 12 (1), pp. 134-142, Jan/Feb 2006.

[De Vos2007] K. De Vos, I. Bartolozzi, E. Schacht, P. Bienstman, and R. Baets, “Silicon-on-insulator microring resonator for sensitive and label-free biosensing,” Optics Express, 15 (12), pp. 7610-7615, Jun. 2007.

[La Pera2002] La Pera L, Lo Curto S, Visco A, La Torre L, Dugo G., “Derivative potentiometric stripping analysis (dPSA) used for the determination of cadmium, copper, lead, and zinc in Sicilian olive oils,” J Agric Food Chem., 50(11):3090-3., 2002

[Claes2009] T. Claes, J. G.Molera, K. De Vos, E. Schacht, R. Baets, and P. Bienstman, “Label-free biosensing with a slot-waveguide-based ring resonator in silicon on insulator,” IEEE Photon. J., vol. 1, no. 3, pp. 197–204, 2009.

[Iga2000] K. Iga, “Surface-emitting laser—Its birth and generation of new optoelectronics field,” IEEE J. Sel. Topics Quantum. Electron., vol. 6, no. 6, pp. 1201–1215, 2000.

Chapter 2. Design and characterization of photonic components

This chapter is dedicated to the design of the photonic components that were fabricated on the TriPleX platform. By using the proper simulation methods (FEM, BPM and FDTD) in Rsoft software, the basic waveguiding structure has been optimized in terms of very low propagation losses (0.01 dB/cm) and possibility for a more compact integration, while retaining single-mode operation at 850 nm. Three photonic structures have been designed within this thesis. Multimode Interference (MMI) couplers for the power splitting of the light, grating couplers for the vertical coupling of the light from and to the photonic integrated circuit (PIC) and a partial polarization rotator for having both TE and TM modes, propagated within the PIC. The MMI coupler, compared to a matrix of Y-junctions, offers significant advantages in terms of compactness and optical losses. The design of the MMI coupler has been made taking into account the refractive index contrast and the propagation loss on the TriPleX platform, as well as the technology limitations associated with the achievable refractive index and physical width homogeneity. The optimization of the MMI coupler design aimed at low insertion loss (1 dB) and low power imbalance (<0.5 dB) between the output ports. The grating coupler has been monolithically integrated in the core layer of the waveguide allowing for the vertical coupling of the emitted light inside the waveguide and outside from the waveguide to the photodiodes (PDs) of the final photonic sensor, respectively. As the vertical configuration may lead to back reflections, an asymmetric grating design has been adapted in order to properly adjust the angle of the reflected light. Main design parameter such as the perturbation depth, the length and the period of the grating has been optimized using different simulation methods and taking into account the mode field diameter of the VCSEL beam, the emission wavelength regime (around 850 nm), as well as the practical tolerances of the TriPleX fabrication process. The targeted coupling loss was lower than 1.5 dB. Finally, the results from simulation work that has been done regarding the properties and performance of a theoretical polarization partial rotator structure are presented. This polarization partial rotator enables the rotation of the perpendicular waveguide symmetry, which leads to indirect spatial rotation of the propagation axis causing the excitation of two hybrid modes, supporting both TE and TM polarization.

2.1 Simulation methods

2.1.1 Finite Element Method

The Finite Element Method (FEM) method is generally advantageous in complex geometries and/or high index contrast materials. Presented here is the basic theoretical background for the FEM for Electromagnetics as implemented in FemSIM [Link Rsoft-1], [Scarmozzino2000]. It is a full-vector implementation for both propagating and leaky waveguide modes, and cavity modes for 1D and 2D Cartesian cross-sections and 3D BORs (bodies of revolution) in cylindrical coordinates. The method uses state-of-the-art Hybrid Edge/Node Elements that allow for efficient separation of the spurious modes from the physical ones. First and second order interpolant basis are provided for both rectangles and triangles. PEC (perfect electrical conductor) or PML (perfectly matched layer) boundary conditions may be selected independently for each direction. It may be used to find all the modes or a small group of modes about a given wavelength.

As a start, the source-free time-harmonic form of the vector wave Equation in an arbitrary, anisotropic, lossy media [Jin2002], [Saitoh2002],

$$\nabla\times\left(\frac{1}{\bar{\bar{s}}}\cdot\left(\nabla\times E\right)\right)-k_0^2\bar{e}_r E=0 \tag{1}$$

subject to vanishing field boundary conditions at the domain edges.

$$\hat{n}\times E=0 \tag{2}$$

The complex diagonal tensors, s and ε, represent coordinate-stretching and the dielectric material, respectively. Throughout the domain s is the identity tensor, but in the boundary layer it has the following form

$$\begin{gathered}\bar{s}=\left(\frac{s_y s_z}{s_x}\right)\hat{x}\hat{x}+\left(\frac{s_x s_z}{s_y}\right)\hat{y}\hat{y}+\left(\frac{s_x s_x}{s_z}\right)\hat{z}\hat{z}\\ s_{a=x,y,z}=1-j\left(\frac{a-L}{L}\right)\delta_{\max}\end{gathered} \tag{3}$$

where δ_{max} is the loss tangent, α is the distance from the edge, and L is the thickness of this layer, known as the perfectly matched layer (PML). The tensor elements in the PML are matched to those in the rest of the domain according to the prescription

$$\overline{\varepsilon_2}=\varepsilon_1\bar{s} \tag{4}$$

to produce arbitrarily small reflections at the PML interface for all frequencies and angles of incidence. The PML is terminated at the domain edge with a perfect electrical conductor (PEC) boundary condition [Schulz1998].

The Finite Element Method (FEM) does not solve the boundary value problem (1-3) directly, but rather a related one based on a variational expression, or functional, constructed from the operator of the differential Equation (1). This functional in two dimensions, over domain A, is given by [Koshiba1994]

$$F\left(E\right)=\iint_A\left[\left(\nabla\times E\right)^*\cdot\frac{1}{\bar{\bar{s}}}\cdot\left(\nabla\times E\right)-k_0^2E^*\cdot\bar{\varepsilon}\cdot E\right]dA \tag{5}$$

For propagating and leaky modes [Tsuji2000], a separable field E(x,y,z) = E(x,y)exp(-jβz), where β is the modal propagation constant along z.

Instead of finding an expansion basis over the entire domain, which can be difficult in general, the Finite Element Method subdivides the domain into a collection of elements, for which a simple basis can be defined. This basis vanishes outside the element, so that the final solution is just a summation over the solutions of all the elements. For hybrid Node/Edge FEM, the transverse components are expanded in a vector (edge element) basis,

$$E_T\left(x,y\right)e^{-j\beta z}=\sum_{i=1}^{n}N_iE_{Ti}=\sum_{i=1}^{n}\left\{U_{\hat{x}}+U_{\hat{y}}\right\}E_{Ti} \tag{6}$$

where the E_{Ti} are the values of the field along each edge. The longitudinal component (perpendicular to the plane of the element) is represented by a scalar (node element) basis,

$$E_z\left(x,y\right)e^{-j\beta z}=\sum_{i=1}^{n}N_iE_{zi} \tag{7}$$

where the E_{zi} are the values of the field at each node. The basis dimension, n, depends on the geometry of the element and the order of the interpolation. Numerous interpolant basis has been described in the literature [Tsuji1997], [Koshiba2000], [Peterson1994], [Nédélec1980], and will not be repeated here, though most are based on the edge element proposed by Nedelec [Nédélec1980].

Lastly, the functional is minimized according to (8), yielding a matrix eigenvalue Equation with β^2 as the eigenvalue, and the field components at the nodes and edges as the eigenvector.

$$\left(\frac{\partial F}{\partial E_i}\right)=0 \tag{8}$$

A similar formulation can be made for cavity modes [Greenwood1999], [Lee1993].

2.1.2 Beam Propagation Method

The aim of Beam Propagation Method (BPM) [Link Rsoft-2] is to provide a general simulation package for computing the propagation of light waves in arbitrary waveguiding geometries. Given the fact that many assumptions are made at the outset and that some of them are later relaxed, BPM is still a difficult problem to solve. The computational core of the program, which is based on a finite difference beam propagation process, is defined in [Scarmozzino2000, Scarmozzino1991]. This technique employs finite difference methods to solve the well-known parabolic or paraxial approximation of the Helmholtz Equation. In addition, the software follows [Hadley1992] by using "transparent" boundary conditions.

The fundamental physical constraint of the BPM method is the paraxiality condition on the primary direction of propagation, which is derived from the parabolic approximation of the Helmholtz Equation. More precise approximations to the Helmholtz Equation, as defined in [Hadley1992-2], can be used to reduce these limitations. This technique can be implemented in BPM, which requires many Padé approximations.

BPM overcomes the second limitation of the above-described method, which stems from the presumption of scalar waves preventing polarization effects, by employing several vector beam propagation techniques described in [Huang1993, Xu1994] and related references.

The third drawback of the BPM method is its inability to account for back reflections, which is due to the one-way wave Equation's reluctance to accept positive and negative travelling waves. Reflection phenomena, such as resonant effects in grating structures, can be counted using the BPM algorithm, which considers coupled forward and backward moving waves and is defined in [Rao1999].

The physical propagation problem necessitates two main pieces of data:

1) the refractive index distribution, $n(x, y, z)$ and
2) the input wave field, $u(x, y, z=0)$.

Physics determines the wave field in the rest of the domain, $u(x, y, z>0)$, based on this knowledge. The solution algorithm involves additional data in the form of numerical simulation parameters, as shown below:

- A finite computational domain for x in range (x_{min}, x_{max}), y in range (y_{min}, y_{max}), and z in range (z_{min}, z_{max}).
- The transverse grid sizes, Δx and Δy.
- The longitudinal step size, Δz.

The program estimates these parameters correctly, but the user has the option to override them.

The BPM propagation technique is used to model integrated and fiber optic photonic systems. The most important explanation for the BPM approach's success is that it is conceptually simple, allowing for quick implementation of the basic technique. A user who is not an expert in numerical methods, as well as the implementer, can understand the findings, efficiently use the tool, and reap the benefits of a BPM-based modeling tool. Even though the BPM is simple, it is a very effective method since its computational complexity can be optimized in most cases, and the computational effort is proportional to the number of grid points used in the numerical simulation. Furthermore, the BPM approach can be used to build and simulate complex geometries without the need for specialized models. The BPM method automatically accounts for the effects of directed and radiating fields, as well as mode coupling and conversion. Furthermore, several extensions to the basic approach can be applied within the same overall structure, allowing for the inclusion of most interesting effects such as polarization, non-linearities, and so on, making the BPM technique very versatile and extensible.

Many prototypes of different photonic components and circuits can be found in the literature as models created with the BPM program. Examples include various passive waveguiding devices, [Eldada1992] channel-dropping filters, [Levy1992] electro-optic modulators, [Eldada1994] multimode waveguide devices, [Ilic1994, Ilic1997] ring lasers,[Shih1995] optical delay line circuits, [Eldada1995, Hu1998] novel y-branches, [Hu1997] optical interconnects, [Scarmozzino1997] polarization splitters, [Hu1997-2] multimode interference devices,[Levy1997, Levy1998, Levy1999, Huang1998-1, Huang1998-2] adiabatic couplers, [Ramadan1998] waveguide polarizers, [Fujita1998] and polarization rotators [Huang2000]. The majority of the citations above contain experimental demonstrations of novel system concepts created entirely or partially using BPM.

BPM is a method for approximating the exact wave Equation for single frequency waves and solving the resulting Equations numerically. The basic approach is demonstrated by expressing the problem as a scalar field (i.e., ignoring polarization effects) with paraxiality (i.e., propagation restricted to a narrow range of angles). A strategy for overcoming these constraints will also be discussed.

In the form of the Helmholtz Equation for single frequency waves, and assuming the scalar field, the wave Equation can be written as Equation 9:

$$\frac{\partial^2 \varphi}{\partial x^2}+\frac{\partial^2 \varphi}{\partial y^2}+\frac{\partial^2 \varphi}{\partial z^2} k\left(x,y,z\right)^2 \varphi = 0 \qquad (9)$$

$E(x, y, z, \mathrm{t}) = \varphi(x,y,z)e^{-i\omega t}$ is the scalar electric field and the notation $k(x,y,z) = k_0 n(x,y,z)$ has been introduced for the spatially dependent wavenumber, with $k_0 = 2\pi/\lambda$ being the wavenumber in free space. The refractive index distribution $n(x, y, z)$ defines the entire geometry of the problem.

Despite the scalar assumption, Equation (9) is exact. In traditional guided-wave problems, the most rapid variation in the field ϕ is the variation in phase along the propagation axis. If we assume that the axis is primarily in the z direction, it is advantageous to factor this rapid variation out of the problem by using the Equation (10) to introduce a slowly changing field u:

$$\varphi\left(x,y,z\right)=u\left(x,y,z\right)e^{i\bar{k}z} \qquad (10)$$

The reference wavenumber is k-bar, which is a constant number that represents the average phase variance of the field ϕ. With the addition of Equation 10, the Helmholtz Equation for a slowly varying field becomes:

$$\frac{\partial^2 u}{\partial^2 z}+2i\bar{k}\frac{\partial u}{\partial z}+\frac{\partial^2 u}{\partial x^2}+\frac{\partial^2 u}{\partial y^2}+\left(k^2-\bar{k}^2\right)u=0 \qquad (11)$$

Except for the fact that it is expressed in terms of u, Equation 11 is identical to the exact Helmholtz Equation. Assuming that the transition in u with z is slow enough that the first term above can be overlooked in comparison to the second. The famous slowly varying envelope, also known as the paraxial or parabolic approximation, is this approximation. With this assumption in mind, Equation 11 can be written as:

$$\frac{\partial u}{\partial z}=\frac{1}{2\bar{k}}\left(\frac{\partial^2 u}{\partial x^2}+\frac{\partial^2 u}{\partial y^2}+\left(k^2-\bar{k}^2\right)u\right) \qquad (12)$$

The simple BPM Equation is simplified by 3D to 2D dimensions if any dependency on y is skipped.

Equation 12 defines the evolution of a field in the space z>0 given an input field u(x,y,z=0).

We have advantages and drawbacks using the above-mentioned strategy. For many problems, factoring the rapid phase variance allows the slowly varying field to be numerically represented on a longitudinal grid (i.e., along z) that can be much coarser than the wavelength, adding to the technique's performance. Second, by removing the second derivative term in z, the problem is reduced from a second order boundary value problem that requires iteration or eigenvalue analysis to a first order initial value problem that can be solved by simply "integrating" the above Equation along the propagation direction z. This last point is also important in evaluating BPM's effectiveness, as it implies a time savings of at least Nz (the number of longitudinal grid points) as compared to a complete numerical solution of the Helmholtz Equation.

There is a cost associated with these advantages. The slowly varying envelope approximation restricts consideration to fields propagating mainly along the z axis (paraxiality), as well as the index contrast (more precisely, the rate of change of index with z, which is a combination of index contrast and propagation angle). Furthermore, if the phase variation is important to system action, fields with a complicated superposition of phase variation, such as those found in multimode devices like MMIs, might not be accurately modeled. A second important consideration, in addition to the constraints on u variation listed above, is that removing the second derivative also removes the possibility of backward traveling wave solutions. As a result, devices with substantial reflection cannot be correctly modeled. Fortunately, the aforementioned problems should be considered coalescent in the BPM approach and can be removed or greatly relaxed in certain cases by using so-called wide-angle and bi-directional extensions to BPM, as discussed next.

There are a few more drawbacks associated with the above-mentioned formula. This may involve polarization and simplification of material properties like isotropic or linear, which are not special to the BPM process. In the following paragraphs, the formulation's extensions are defined in order to resolve these issues. In the following paragraph, the numerical solution of the simple BPM process, as mentioned previously, is provided.

Equation 12 is a parabolic partial differential Equation that can be solved forward in the z axis using a variety of normal numerical techniques. For starters, in BPM [Feit1978], a technique known as the split-step Fourier method is used. Later, for several issues in integrated optics, an implicit finite-difference solution based on the well-known Crank-Nicholson scheme was demonstrated to be superior and thus became the standard procedure [Yevick1990, Chung1990, Scarmozzino1991]. This method is referred to in the literature as Finite Different – Beam Propagation Method (FD-BPM), but it will now be referred to simply as BPM.

The field in the transverse (xy) plane is only defined at discrete points on a grid and discrete planes along the longitudinal or propagation direction in the approach known as FD (z). By quarrying the numerical Equations and treating the field at one z plane as discretized, the aim is to evaluate the field at the next z plane. This step will be repeated as many times as required to establish the field's position in the structure. To keep the explanation short, only the approach for a scalar field in 2D is shown and only include a brief description in 3D.

We position the u_{in} the field at transverse grid point i and longitudinal plane n, assuming that the grid points and planes are evenly spaced by x and z. Equation 12 is defined as follows in the Crank-Nicholson method at the midplane between the known plane n and the unknown plane n+1.

$$\frac{u_i^{n+1}-u_i^{n}}{\Delta z}=\frac{1}{2\bar{k}}\left(\frac{\delta^2}{\Delta x^2}+\left(k\left(x_i, z_{n+\frac{1}{2}}\right)^2-\bar{k}^2\right)\right)\frac{u_i^{n+1}-u_i^{n}}{2} \tag{13}$$

Here, δ^{2ui} = (ui+1 + ui-1 -2ui), and $z_{n+1/2} \equiv z_{n+z/2}$ reflect the regular second order difference operator. In terms of known quantities, Equation (13) can be rearranged into a regular tridiagonal matrix Equation for the unknown field u^{in+1}, yielding:

$$a_i u_i^{n+1} + b_i u_i^{n+1} + c_i u_i^{n+1} = d_i \tag{14}$$

Equation (14) contains expressions for the coefficients that are easily derived and can be found in [Scarmozzino1991]. Equation (14)'s tridiagonal existence allows it to be solved quickly in order O(N) operations, where N is the number of grid points in x.

Only when the Equation is extended to a particular finite computational domain can the field be expressed as defined above. It refers to unknown quantities outside the domain when the boundary points are i = 1 and N. When applied to these points, the above-mentioned Equation should be replaced with suitable boundary conditions. The conditions that will be chosen are unnecessarily sensitive since a bad choice of these conditions could result in artificial reflection of light incident on the boundary (e.g., radiation) back into the computational domain. Simply requiring the field to vanish on the boundary, for example, is inadequate since it equates to putting perfectly reflecting walls at the domain's edge.

Several works have implemented artificial absorbing material near the domain's edge but changing the absorber's parameters to minimize reflection is time-consuming, and artificial reflections persist in certain cases because the problem space and the absorber's interface would be partly reflective as well. The so-called transparent boundary condition, or TBC [Hadley1992,] is a widely used boundary condition. The basic idea is that the field behaves like an outgoing plane wave near the boundary, with characteristics (amplitude, direction) that are dynamically determined by a heuristic algorithm. Because of the plane wave assumption, the field at the boundary point can be compared to the field at the adjacent interior point, completing the collection of Equations. [Hadley1992] explains the implementation in detail. The TBC is generally successful at allowing radiation to freely exit the computational domain, but there are some problems where it falls short. [Vassalo1996, Huang1996, Chiou1998] have discussed and studied these boundary conditions in depth.

The polarization effects can be included in BPM by realizing that the electric field E is a vector and beginning the derivation from the vector wave Equation rather than the scalar Helmholtz Equation, as shown in [Clauberg1991, Huang1993]. The Equations are formulated in terms of the field's transverse components (Ex and Ey) in one method [Huang1993], resulting in the following set of coupled Equations for the corresponding slowly changing fields (u_x and u_y):

$$\frac{\partial u_x}{\partial z} = A_{xx}u_x + A_{xy}u_y \tag{15}$$

$$\frac{\partial u_y}{\partial z} = A_{yx}u_x + A_{yy}u_y \tag{16}$$

The A_{ij} are complex differential operators given by:

$$A_{xx}u_x = \frac{i}{2\bar{k}}\left\{\frac{\partial}{\partial x}\left[\frac{1}{n^2}\frac{\partial}{\partial x}\left(n^2 u_x\right)\right] + \frac{\partial^2}{\partial y^2}u_x + \left(k^2 - \bar{k}^2\right)u_x\right\} \tag{17}$$

$$A_{yy}u_y = \frac{i}{2\bar{k}}\left\{ \frac{\partial^2}{\partial x^2}u_y + \frac{\partial}{\partial y}\left[\frac{1}{n^2}\frac{\partial}{\partial y}\left(n^2 u_y\right)\right] + \left(k^2 - \bar{k}^2\right)u_y \right\}$$

$$A_{yx}u_x = \frac{i}{2\bar{k}}\left\{ \frac{\partial}{\partial y}\left[\frac{1}{n^2}\frac{\partial}{\partial x}\left(n^2 u_x\right)\right] + \frac{\partial^2}{\partial y \partial x}u_x \right\}$$

$$A_{xy}u_y = \frac{i}{2\bar{k}}\left\{ \frac{\partial}{\partial x}\left[\frac{1}{n^2}\frac{\partial}{\partial y}\left(n^2 u_y\right)\right] + \frac{\partial^2}{\partial x \partial y}u_y \right\}$$

Equation (17) contains four distinct operators: A_{xx}, A_{yy}, A_{xy}, and A_{xy}. For TE and TM fields, the first two rely on polarization dependence due to different boundary conditions at interfaces, and explain effects such as different propagation constants, field shapes, bend loss, and so on. The latter two, as part of the off-diagonal terminology, depend on polarization coupling and hybrid modes due to geometric effects in the cross-sectional structure, such as the influence of corners or sloping walls.

All of the above-mentioned operators are taken into account in full vectorial BPM. Since the effect of the off-diagonal terms is extremely weak in semi-vectorial, which is an excellent approximation for the structures, unless they are explicitly constructed to induce coupling, we make the simplification $A_{xy} = A_{yx} = 0$. The transverse field components are decoupled in this scenario, greatly simplifying the problem while maintaining the most important polarization effects.

The wide-angle BPM and its extensions can be used to relax the restrictions of paraxiality, index contrast, and multimode propagation of the BPM, as defined in [Yevick1989, Hadley1992-2, Hoekstra1993]. The aim of both of these approaches is to reduce paraxial limitations by taking into account the impact of the $\partial^2 u/\partial z^2$ expression, which was overlooked in the simple BPM derivation. These methods differ only in the degree to which we calculate in order to achieve the goal. The most well-known is the multistep Padé-based wide-angle technique, which is defined below and presented in [Hadley1992-2]. We get the simplest approach for deriving a wide-angle BPM Equation by ignoring the $\partial^2 u/\partial z^2$ term while writing the Helmholtz wave Equation in terms of the slowly varying field as defined in Equation 11. Let us use D to denote $\partial/\partial z$, and D^2 to represent $\partial^2/\partial z^2$. If we neglect the fact that D is a differential operator, the Equation becomes a quadratic Equation that must be solved for D, yielding the following Equation (Equation18) for a first order Equation in z.

$$\frac{\partial u}{\partial z} = i\bar{k}\left(\sqrt{1+P} - 1\right)u \tag{18}$$

$$P \equiv \frac{1}{\bar{k}^2}\left(\frac{\partial^2}{\partial x^2} + \frac{\partial^2}{\partial y^2} + \left(k^2 - \bar{k}^2\right)\right) \tag{19}$$

Only forward traveling waves are allowed in Equation 18, the first order derivative, and thus Equation 18 is referred to as a one-way wave. Even though Equation 18 is limited to forward propagation, it is still exact in the sense that no paraxiality approximation is used. To test the differential operator P, the Taylor expansion is used. The Padé approximants are still more reliable for the same order of terms [Hadley1992-2], even though the first order of the Taylor expansion corresponds to the standard paraxial BPM and the higher order helps to become more accurate and obtain a wide-angle scheme. As a result, we can arrive at the following wide-angle Equation:

$$\frac{\partial u}{\partial z} = i\bar{k}\frac{N_m(P)}{D_n(P)}u \tag{20}$$

The N_m and D_n parameters, are polynomials in the operator P and (m, n) is the order of approximation. Several common approximants are presented in the next table:

Padé Order (m,n)	**Nm**	**Dn**
(1,0)	P/2	1
(1,1)	P/2	1+P/4
(2,2)	P/2+P2/4	1+3P/4+P2/16

Larger angles, higher index contrast, and more complex mode interference can be studied when the Padé order (m, n) is increased and the Equation 20 is used in both directed wave and free space problems [Hadley1992-2, Hoekstra1993, Ilic1996]. Different guidelines for using this technique are defined in [Ilic1996], as well as a discussion of the complex interrelationships between waveguide angle, index contrast, Padé order, reference wavenumber, and grid parameters.

By using the wide-angle BPM, the cone of angles in the propagation z axis gets wider and can only asymptotically reach ± 90 degrees, but it can never be expanded to accommodate wider angles, such as in the negative z axis. This is why the backward traveling waves should be viewed differently. This problem has been solved by a variety of bi-directional BPM techniques, as defined in [Kaczmarski1988, Chung1992, Chiou1997], which are primarily based on the coupling that occurs when a wave incident on an interface is reflected along z. [Rao1999] describes a subsequent attempt that considers various interfaces and reflections in a self-consistent and efficient manner.

As a result of the division of the propagated directed wave, this approach considered two distinct, but uniform regions. At any point along the structure, both the forward (represented by $u^{+}(x, y, z)$) and backward (represented by $u^{-}(x, y, z)$) will exist. The forward and backward waves are decoupled in uniform regions, but due to reflection, the forward and backward waves are coupled at the interfaces between these regions.

The use of a transfer matrix method, in which the individual matrices are differential operators, was suggested in [Rao1999]. The aim is to be able to evaluate both the back-reflected field at the start and the forward transmitted field at the end, thus solving the physical problem that the forward directed field has at the structure's input. To solve the transfer matrix problem, we assume that we know the forward and backward fields at the structure's input, as well as an overall transfer matrix M, and then define the system as follows:

$$\begin{pmatrix} u_{out}^{+} \\ u_{out}^{-} \end{pmatrix} = M \begin{pmatrix} u_{in}^{+} \\ u_{in}^{-} \end{pmatrix} \tag{21}$$

For Equation 21, we iteratively considered solutions for the reflected field (u_{in}^-), for a given incident field (u_{in}^+), with the backward field (u_{out}^-) at the output set to zero. The transfer matrix M, which defines the entire structure, is made up of several propagation and interface matrices. The propagation matrices define the uniform regions and use standard BPM to propagate u^+ and u^- separately (either paraxial or wide-angle depending on the situation). Generalized Fresnel formulas involving differential operators employing the Padé approximants used in wide-angle BPM [Rao1999] give the interface matrices, which relate u^+ and u^- through an interface.

Since several mode-solving techniques based on the BPM method have been developed, BPM could also be used as a mode-solver in a relatively straightforward manner. The first of these methods is defined in [Feit1980], and it is a correlation method that is used to measure multimode fiber modes and dispersion characteristics. After that, [Yevick1989, Jungling1994] identified a newly established technique that is both faster and more efficient in general. The use of BPM as a definition enables the reuse of existing code and concepts. Many other iterative mode solving techniques, such as those defined in [Yevick1992, Hadley1995], are similar to the previously stated imaginary distance BPM technique. The latter work [Hadley1995], in particular, contains findings that can be replicated using imaginary distance BPM and has shown excellent agreement with other published data.

In both BPM-based mode-solving techniques, an incident field is launched into a z-invariant geometry, and some form of BPM propagation is performed. A provided incident field is launched into a z-invariant geometry in both BPM-based mode-solving techniques, and some form of BPM propagation is performed. The propagation can be described in terms of the structure's modes and propagation constants since the structure is uniform along z. Consider 2D scalar field propagation for the sake of simplicity. In the structure's modes, the incident field, in(x), can be extended as follows:

$$\varphi_{in}(x) = \sum_m c_m \varphi_m(x) \tag{22}$$

Of course, the summation should include a true summation over guided modes and integration over radiation modes, but for the sake of brevity, the latter is not clearly evident. The propagation of the structure can then be expressed as:

$$\varphi(x,z) = \sum_m c_m \varphi_m(x) e^{i\beta_m z} \tag{23}$$

Each BPM-based mode-solving technique decides how to extract mode information from the BPM results by conceptually equating the propagating field obtained via BPM with the above expression.

In the imaginary distance BPM, the longitudinal coordinate z is replaced by z'=iz, as the name implies, so that propagation along this imaginary axis will obey:

$$\varphi(x,z^{'}) = \sum_m c_m \varphi_m(x) e^{\beta_m z^{'}} \tag{24}$$

The exponential term in Equation 23 has been replaced by exponential growth in Equation 24, with the growth rate of each mode equal to its actual propagation constant. The key idea behind the approach is to launch an arbitrary field, such as a Gaussian, and scatter it along the imaginary axis through the structure. Since the fundamental mode (m=0) has the highest propagation constant, its contribution to the field will grow at the fastest rate and progressively supplant all other modes, eventually leaving only the field pattern $\phi_0(x)$ after a certain distance. Using the variational-type expression below, the propagation constant can be determined:

$$\beta^2 = \frac{\int \varphi^* \left(\frac{\partial^2 \varphi}{\partial x^2} + k^2 \varphi \right) dx}{\int \varphi^* \varphi dx} \tag{25}$$

Higher order modes can be obtained by subtracting contributions from lower order modes during propagation using an orthogonalization method [Chen1994]. [Jungling1994, Hadley1995] address issues such as the best launch area, reference wavenumber, and phase scale.

It is important to note that the imaginary distance BPM is not the same as waiting for the solution to reach steady state in the traditional propagation technique. If the structure is single mode, the latter will only get the fundamental mode, and convergence will take longer. The imaginary distance BPM is closely related to the moved inverse power method for finding eigenvalues and eigenvectors of a matrix.

In the correlation process, an arbitrary field is launched into the structure and propagated through normal BPM. During propagation, the following correlation function between the input field and the propagating field is computed:

$$P(z) = \int \varphi_{in}^*(x) \varphi(x,z) dx \tag{26}$$

Equations 22 and 23 can also be used to express the correlation function.

$$P(z) = \sum_m |c_m|^2 e^{i\beta_m z} \tag{27}$$

According to this expression, a Fourier transform of the computed correlation function should have a continuum with peaks at the modal propagation constants. The corresponding modal fields can be obtained by beating the propagating field against the known propagation constants via a second propagation:

$$\varphi_m(x) = \frac{1}{L} \int_0^L \varphi(x,z) e^{-i\beta_m z} \tag{28}$$

There are several ways to correct the propagation constants:

- A correction is applied that takes into account the error introduced by solving the paraxial Equation rather than the exact Helmholtz Equation.
- Second, by substituting the mode profile in the wave Equation and solving for the propagation constant, the imaginary component of the propagation constant can be found. This yields not only an imaginary value, but also a corrected real value.

While the correlation method is slower in general than the imaginary distance BPM, it has the advantage of being able to solve problems that the imaginary distance BPM is unable to solve, such as leaky or radiating modes.

2.1.3 Finite Difference Time Domain Method

Consider an area of space that is devoid of all moving currents and isolated charges. In Cartesian coordinates, Maxwell's curl Equations can be written as six simple scalar Equations. Here are two examples:

$$\frac{\partial H_x}{\partial t} = \frac{1}{\mu}\left(\frac{\partial E_y}{\partial z} - \frac{\partial E_z}{\partial y}\right)$$
$$\frac{\partial E_y}{\partial t} = \frac{1}{\varepsilon}\left(\frac{\partial H_x}{\partial z} - \frac{\partial H_z}{\partial x}\right) \quad (29)$$

The other four are symmetric equivalents of the above, obtained by swapping the x, y, and z subscripts and derivatives in a cyclic manner. Maxwell's Equations describe a situation in which the E field's temporal variation is based on the H field's spatial variation, and vice versa [Link Rsoft-3]. The FDTD approach solves Maxwell's Equations by first discretizing them using time and space core differences, and then numerically solving them in software.

The most popular approach for solving these Equations is to use Yee's mesh [Yee1966], which calculates the E and H field components at grid points spaced x, y, and z apart. Along each axis, the grid sizes can be non-uniform. As shown in **Figure 4**, the E and H field components are then interlaced in all three spatial dimensions. In addition, time is divided into discrete t-steps. The E and H field components are then computed at times t = nΔt and t = (n+1/2)Δt, respectively, where n is an integer representing the compute phase. The E field at t = nt, for example, is equivalent to the E field at t = (n-1)Δt plus a term computed from the spatial difference, or curl, of the H field at time t.

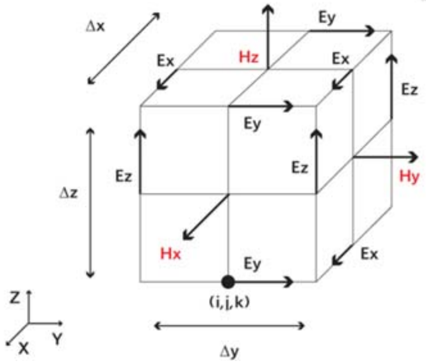

Figure 4: In a Yee cell of dimension Ax, Ay, Az, note how the H field is computed at points shifted one-half grid spacing from the E field grid points [Yee1966].

The field at a given mesh point, denoted by the integers i, j and k, can be computed using this method, which yields six Equations. Two of the six, for example, are:

$$
\begin{aligned}
H^{n+1/2}_{x(i,j,k)} &= H^{n-1/2}_{x(i,j,k)} + \frac{\Delta t}{\mu \Delta z}\left(E^{n}_{y(i,j,k)} - E^{n}_{y(i,j,k-1)}\right) - \frac{\Delta t}{\mu \Delta y}\left(E^{n}_{z(i,j,k)} - E^{n}_{z(i,j-1,k)}\right) \\
E^{n+1/2}_{x(i,j,k)} &= E^{n-1/2}_{x(i,j,k)} + \frac{\Delta t}{\varepsilon \Delta z}\left(H^{n+1/2}_{z(i,j,k+1)} - H^{n+1/2}_{z(i,j,k-1)}\right) - \frac{\Delta t}{\varepsilon \Delta z}\left(H^{n+1/2}_{y(i,j,k+1)} - H^{n+1/2}_{y(i,j,k)}\right)
\end{aligned}
\tag{30}
$$

These Equations are solved iteratively in a leapfrog fashion, with the E and H fields computed at successive Δt/2 intervals.

To run a FDTD simulation, two physical parameters are needed: material parameters, such as relative permittivity ε(r, ω) and relative permeability μ(r, ω) as functions of space and/or frequency, and electromagnetic field excitation. Physics dictates the electromagnetic field as a function of space and time centered on these parameters (r, t) FDTD utilizes the following formulas to specify the material properties of a waveguide:

$$
\begin{aligned}
D &= \varepsilon_o E + P \\
B &= \mu_o\left(H + M\right)
\end{aligned}
\tag{31}
$$

P which M denote polarization and magnetization, respectively, and may be dispersive, non-linear, or anisotropic.

A simulation requires a driving feature in time as well as an initial launch condition ϕ_L at time t=0. This includes both spatial and temporal excitation, for example:

$$\varphi_L\left(r,t\right) = f\left(r_o\right) g\left(t\right) \tag{32}$$

The spatial excitation at the launch plane is $f(r_o)$, and the temporal excitation is g(t).

Additional numerical simulation parameters required by the FDTD algorithm include a finite simulation domain, boundary condition(s), spatial grid sizes, and a temporal grid (time step and the simulation time length).

The boundary conditions at the computational domain's spatial edges must be carefully considered. An absorbing boundary condition is used in many simulations to remove any outward propagating energy that crosses the domain boundaries. The perfectly matched layer (PML) [Berenger1994], which introduces both electric and magnetic conductivities in such a way that the wave impedance remains constant, absorbing energy without causing reflections, is one of the most efficient. Because of their applicability to periodic structures like PBGs, periodic boundary conditions (PBC) are also relevant. There are many variants on the PBC, but they all have the same general idea: the boundary condition is chosen in such a way that the simulation is analogous to an infinite structure made up of the basic computational domain replicated in all dimensions indefinitely.

A combination of spatial grid sizes (in μm) or 'points-per-wavelength' may be used to specify the spatial grid (PPW). The grid is graded or varied between regions in a smooth manner. The spatial grid must be small enough to overcome the smallest aspect of the field to be simulated in order to create an accurate simulation. The wavelength in the material to be simulated usually determines this, but the geometry of the photonic system can also determine it in some cases. The grid spacing must usually be able to resolve the wavelength in time, and therefore be less than λ/10, where is the content wavelength.

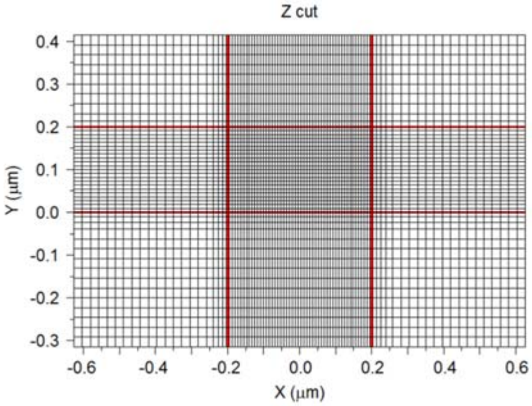

Figure 5: A sample FDTD non-uniform grid.

The time step and the stop criteria are the two most important temporal domain settings.

- Time step: The Courant condition, which relates the spatial and temporal step sizes, must be followed to obtain a stable simulation:

$$c\Delta t < \frac{1}{\sqrt{\left(1/\Delta x^2 + 1/\Delta y^2 + 1/\Delta z^2 \right)}} \tag{33}$$

where c is the speed of light and the grid sizes reflect the smallest grid size in the simulation in the case of a non-uniform grid.

- Stop Criteria: A simulation runs from the start time (t=0) to a specific stop time. It is vital to determine when to end the simulation: Stopping a simulation too soon yields inaccurate results, while stopping it too late yields inefficient results.

Since it is essentially full-vectorial, the FDTD algorithm is extremely flexible when it comes to optical effects like propagation direction, index contrast, and backward reflections. It is tried and true, and it can handle material dispersion and nonlinearities with ease. It can also cover a wide frequency spectrum with a single simulation run since it is centered in the time domain. The FDTD approach is computationally intensive since it necessitates a dense grid of points where all three vector components of the E and H fields must be preserved. A complete three-dimensional simulation of some relatively simple problems, such as a simple, planar, evanescent splitter, can be difficult to achieve.

2.2 TriPleX platform

TriPleX is made up of silicon nitride and silicon dioxide films that alternate [Worhoff2015]. Fabrication using CMOS-compatible equipment and low-pressure chemical vapor deposition allows for the development of stable material compositions, which is essential for controlling waveguide properties and modal form. Both materials have a transparency window that enables low-loss waveguides to be realized over a broad wavelength range (0.4 µm – 2.35 µm). There have been reports of propagation losses as low as $5\cdot10^{-4}$ dB/cm. There are three simple geometries (box shell, double stripe, and filled box). For on-chip, low-loss (<0.1 dB) spot size convertors, a specific tapering technology is developed, allowing for efficient fiber to chip coupling with high-contrast waveguides required for increased functional complexity, as well as hybrid integration with other photonic platforms such as InP and SOI. Checked basic building blocks capture the functionality of the TriPleX platform.

[Heideman2006, Morichetti2007] TriPleX waveguide technology is based on alternating well-defined and highly stable silicon oxide (SiO_2) and silicon nitride (Si_3N_4) layers. [Heideman2009, Heideman2007] CMOS-compatible fabrication equipment based on batch processing by low-pressure chemical vapor deposition (LPCVD) enables volume output and good reproducibility. Waveguides made of TriPleX are transparent for wavelengths ranging from 0.4 to 2.35 µm and have very low optical transmission losses. This technology blends high design versatility with strong integration potential, enabling waveguide properties to be customized. [2008Hoving]. Three commercially available basic waveguide geometries [Heideman2012] have been defined, each of which can be obtained by changing individual steps in the generic fabrication flow. Type I subdivided into the symmetric double stripe (IIa), the asymmetric double stripe (IIc), and the single stripe (IIb), which is a special case of IIc. Type II is subdivided into the symmetric double stripe (IIa), the asymmetric double stripe (IIc), and the filled box (III). **Figure *6*** shows schematic layouts of geometries as well as SEM micrographs of realized structures. **Figure *7*** depicts a standardized process flow that covers the fabrication steps for all TriPleX forms.

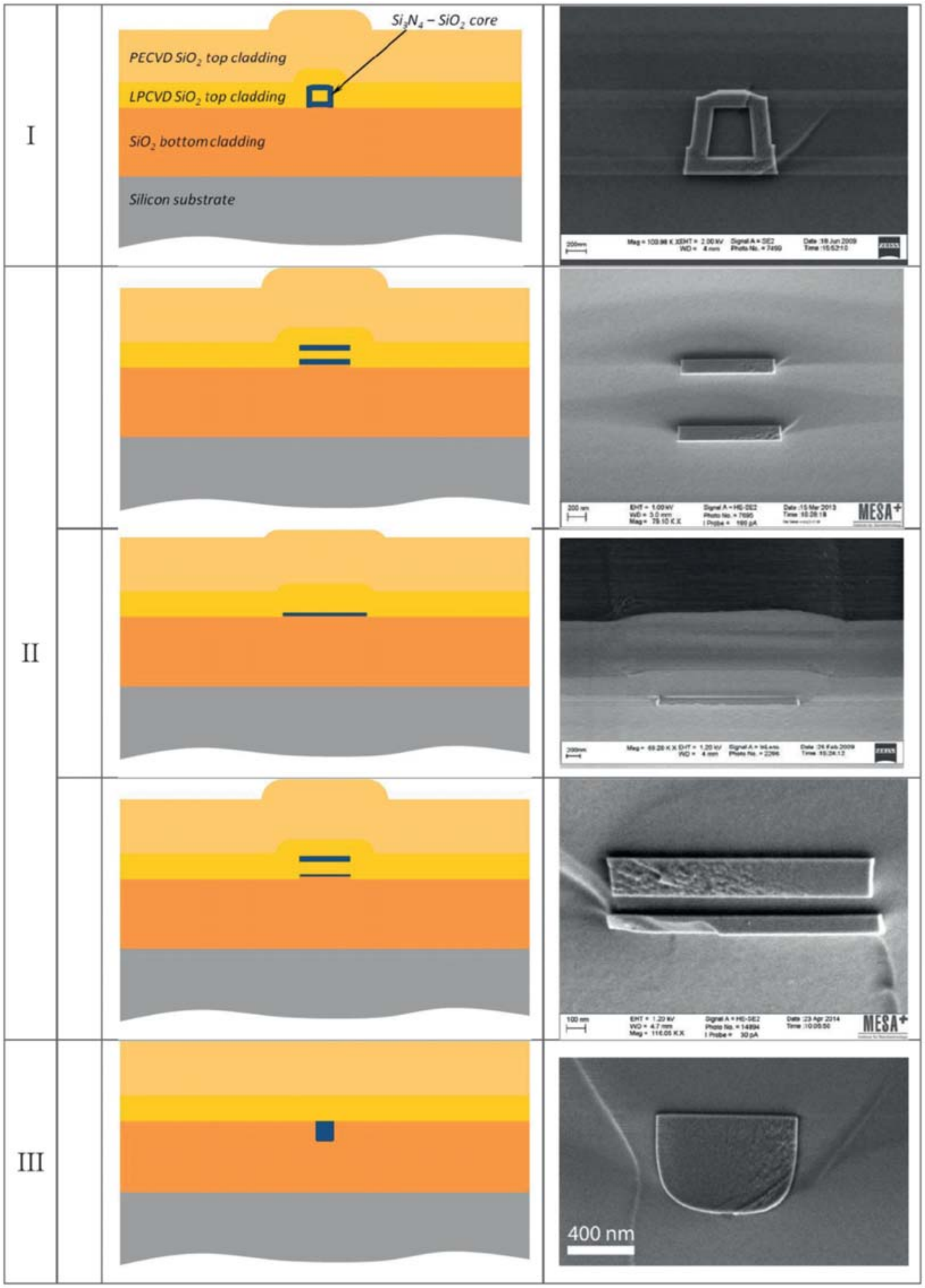

Figure 6: SEM photos of understanding structures and schematic layout of the TriPleX geometries: Box shell (I), Symmetric double stripe (IIa), Single stripe (IIb), asymmetric Double stripe (IIc), and filled Box shell (III).

Although the waveguide cores of these shapes have overall geometrical dimensions in the order of 1 µm^2, their waveguide characteristics and possible application areas are vastly different. The effective index of the waveguide mode Neff and the group index Ng (for TE-polarized light), channel propagation loss α_{ch} (dB/cm]), polarization-dependent loss PDL (dB), minimum bending radius R_b (µm), mode field diameter MFD (µm) (TE_{00} mode), fiber-chip coupling loss $\alpha_{f\text{-}c}$ (dB/facet]), and waveguide birefringence ΔNeff are some of the most important characteristics. The box shell structure is ideal for telecom applications because of its symmetrical form, which reduces polarization dependency [Heideman2005].

Based on different ratios of Si_3N_4 and SiO_2 thicknesses in the core area, the box shell is available in a low [Morichetti2007] and a high [Marpaung2010] index contrast version. A 1 x 1 μm^2 SiO_2 core is surrounded by 50 nm thick Si_3N_4 in the low contrast version, while the high contrast version has SiO_2 and Si_3N_4 core dimensions of 0.5 x 0.5 μm^2 and 170 nm, respectively. The high-contrast box shell geometry has a waveguide propagation loss of less than 0.2 dB/cm, which drops to 0.06 dB/cm for the low-contrast version [Yurtsever2014]. The key difference between the two models is the bending radius, which is designed to meet the 0.01 dB/cm bend loss criterion, and the mode field diameter of the circular mode shape: R_b = 500 µm, MFD = 3.6 µm (low contrast) and R_b = 150 µm, MFD = 1.4 µm (high contrast) (high contrast).

The symmetric double stripe layout is commonly used in components that require high polarization birefringence and close bending radii. Two 170 nm thick and 1.2 µm deep Si_3N_4 layers are separated by a 500 nm thick SiO_2 interlayer in the optimized geometry. The waveguide mode's effective index and group index at 1.55 m wavelength are 1.535 and 1.72, respectively, and the waveguide birefringence is 5.3×10^{-2}. In [Zhuang2011] the waveguide attenuation is ≤ 0.1 dB/cm. At the VLSI stage, the close bending radius allows for practical complexity. In optical ring resonator (ORR) structures with bending radius as small as 70 µm **Figure *8***, waveguide propagation loss as low as 0.095 dB/cm was measured [Zhuang2011]. The mode field diameter of this waveguide geometry's circular mode is ~1.5 µm. Both Si_3N_4 stripes are adiabatically tapered in the vertical direction to allow low loss coupling to standard single-mode fibers (SMF28). If the angle of the MFD transition is less than 1° (i.e., geometrical taper angle ≤ 0.01°), the adiabaticity criterion is met. This results in standard taper lengths of 600 µm in this TriPleX geometry. Fiber-chip coupling losses of <0.5 dB was demonstrated at an optimized thickness of 35 nm for both-tapered Si_3N_4 layers.

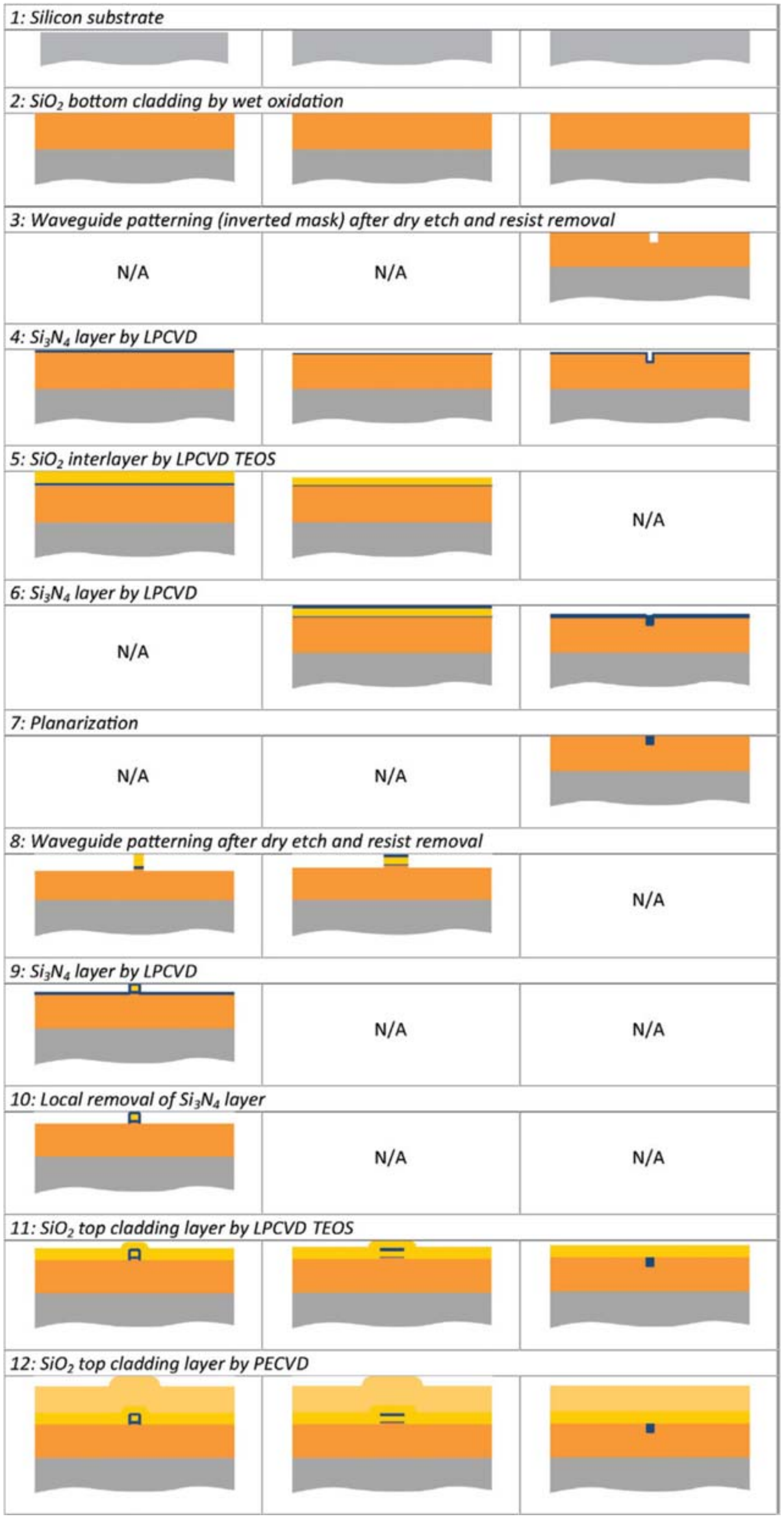

Figure 7: Generic process flow for the fabrication of the three basic TriPleX geometries.

On a single chip, the asymmetric double stripe geometry is ideal for combining regions with low and high effective indices of the mode. A 40 nm thick low-contrast Si_3N_4 stripe is separated from a 175 nm thick high-contrast Si_3N_4 channel in the vertical direction by a 100 nm SiO_2 interlayer in a realized example of this geometry form [Spencer2014]. The thicker layer is tapered to zero, creating an adiabatic transition between the two contrast regions. The channel width in the high-contrast area is 1.5 µm, while the width in the low-contrast area is variable. In the in-plane and out-of-plane directions, the high contrast waveguide has an MFD of 1.7 µm and 1.3 µm, respectively. The birefringence of the waveguide is on the order of 5 x 10^{-2}. On the same chip, demonstrated loss values for low and high modal confinement areas were 0.015 dB/cm and 0.15 dB/cm, respectively.

When extremely low optical losses are needed, the single stripe geometry is used: as previously mentioned, the single stripe can be converted from the asymmetric double stripe by removing the high-contrast waveguide locally. Over a broad range of layer thicknesses (20 – 100 nm) and channel widths (0.3 – 14 µm), a thorough analysis of propagation loss and bending radii as a function of core aspect ratio (width/thickness) of this low-contrast stripe was carried out [Bauters2011-1]. Although high aspect ratios (channel width over thickness) favor low propagation losses, lower aspect ratios minimize the bending radius. On light propagation at 1.5 µm wavelength, propagation losses as low as 0.03 dB/cm were demonstrated in a stripe geometry allowing for 2 mm bending radii. Stripe propagation losses could be due to residual roughness and layer imperfections resulting from the fabrication processes after analyzing calculated loss values with models considering various loss mechanisms. [Dai2010] investigated the waveguide birefringence of 100 nm thick Si_3N_4 waveguides with channel widths ranging from 1.4 to 3.5 µm. For core widths above 2 µm, the birefringence exceeds 10^{-2} and good polarization-maintaining performance can, therefore, be expected. TE-pass polarizers with cross-polarization as low as -75 dB (measurement limited) have been reported [Bauters2013].

The loss figure was improved significantly by improving the channel fabrication process and replacing the upper PECVD SiO_2 cladding layer with a bonded thermal SiO_2 film [Bauters2011-2]. The propagation loss through a 50 nm x 5.3 µm geometrical cross section single mode waveguide channel was reduced to 0.007 dB/cm [Bauters2011-3]. At 1.58 µm wavelength, record-low loss of less than 0.0005 dB/cm was measured on 40 nm x 13 µm and 50 nm x 6.5 µm multimode stripe waveguides [Bauters2011-2].

Various methods were used to resolve the challenge of minimizing the bend radius while preserving low propagation losses. Light propagation through a stripe geometry centered on a 40 nm thick and 14 µm wide Si_3N_4 core with a bending radius of 165 µm can be achieved in a spiral-shaped waveguide. However, the channel is multimode in that geometrical range, necessitating an additional tapering segment for adiabatic widening of the channel width [Bauters2011-2].

Finally, the filled-box geometry was created for applications that require extremely tight modal field confinement in the core layer. Core widths of 0.8 – 1.0 µm and thicknesses ranging from 0.8 to 1.2 µm were achieved in this geometry [Epping2015]. There are up to three modes in the waveguide. The corresponding effective index of the mode and MFD of the fundamental mode (TE_{00}) for the 1.55 µm wavelength and TE-polarized light are about 1.79 and 1 µm, respectively. Using the 0.01 dB/cm loss criterion, a minimum bending radius of 12.5 µm was determined for the TE_{00} mode. The layer thickness growth is limited to <500 nm in stoichiometric LPCVD Si_3N_4 films due to high tensile stress. For the fabrication of label-free waveguides, trench etching (into the thermal oxide layer) and trench filling (by LPCVD Si_3N_4 deposition) were used in conjunction with chemical mechanical polishing (CMP) (see also **Figure *7***). These waveguides had a 0.4 dB/cm optical propagation loss at 1.55 µm wavelength [Epping2015].

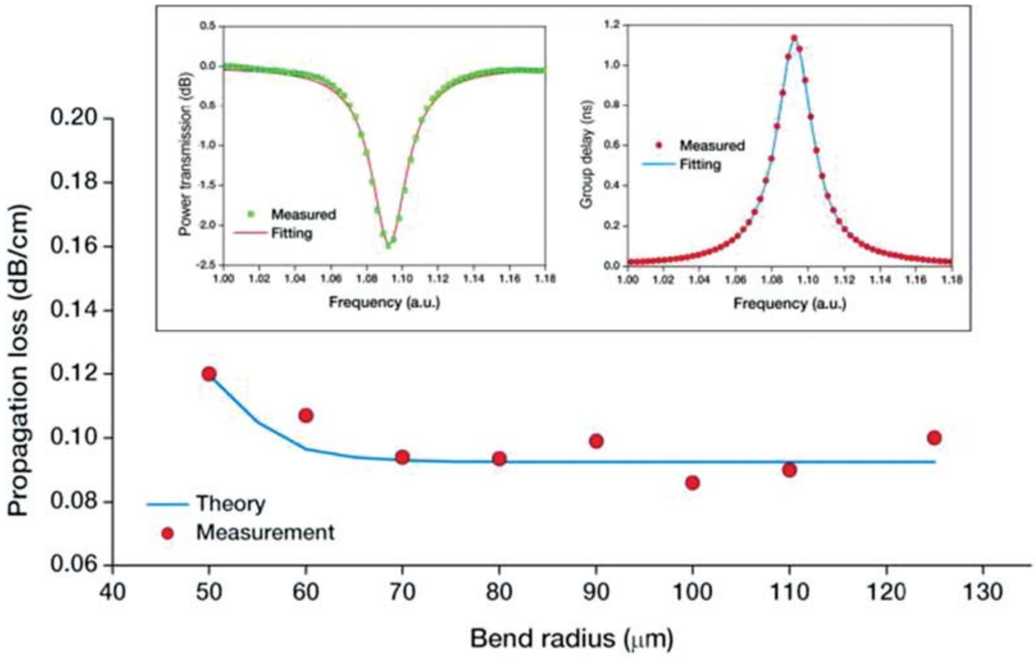

Figure 8: Waveguide propagation loss as function of ORR bending radius (inset: measurement and fit of ORR frequency responses) [Zhuang2011].

The design of the waveguide used for the sensor design is based on an asymmetric double stripe Triplex geometry which is specifically optimized for a wavelength of 850 nm. As mentioned before, the waveguide structure is built with two Si_3N_4 layers and an intermediate SiO_2 layer. It is containing a thin 35 nm stoichiometric Si_3N_4 bottom stripe, a 100 nm intermediate layer of LPCVD SiO_2 (TEOS) and a top stripe of 78 nm stoichiometric Si_3N_4. These three layers form together the core of the waveguide and are built upon a Si wafer with 6-micron thermal oxide. On top the waveguide structure a top cladding of LPCVD SiO_2 (TEOS) layer is deposited to completely encapsulate the waveguide with SiO_2. (see **Figure *9***)

For this waveguide design, we have determined a waveguide stack of 35 nm Si_3N_4 has been determined, 100 nm SiO_2, 78 nm Si3N4 and a width of 1000 nm which result in single mode behavior and high sensitivity with minimal bend and transmission loss (<0.1 dB/cm). The double stripe nature of this design enables reliable production of low and high contrast waveguides on the chip design.

For the structures with, as e.g., MRR design it is particularly desired to use a high contrast waveguide (bottom and top stripe) and for the fiber/VCSEL coupling at the butt end of the chip it is desired to have a low contrast waveguide (only bottom stripe) for optimal coupling. Therefore, at the butt end of the chip the thickness of the top stripe waveguide is tapered down to zero and the remaining strip waveguide of 35 nm is optimized to have an optimal mode match/overlap between fiber/VCSEL to minimize coupling losses.

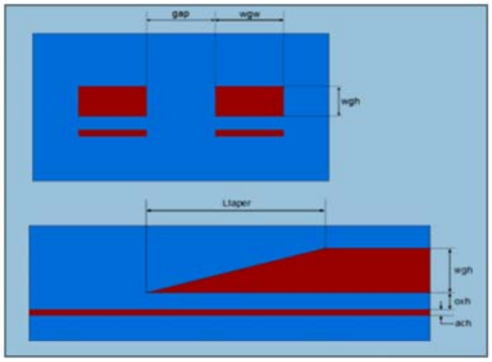

View of the device transverse cross section near the coupling region of the bus and ring resonator waveguides. (Not to scale)

View of the device longitudinal cross section at the butt end of the chip showing the doubles tripe geometry and the vertical taper design. (Not to scale)

Figure 9: Cross sections of the high and low area of the double stripe waveguide design.

As shown in simulation results below (**Figure *10***) the TE mode coupling from HP-780PM fiber of a 1-micron width optical waveguide channel an optimum coupling efficiency is obtain at 25 nm which will rapidly decrease when the layer is thinner. To be on the safe side regarding production tolerances the target thickness of the bottom strip waveguide is set to 35 nm resulting in a coupling loss around - 1.5dB.

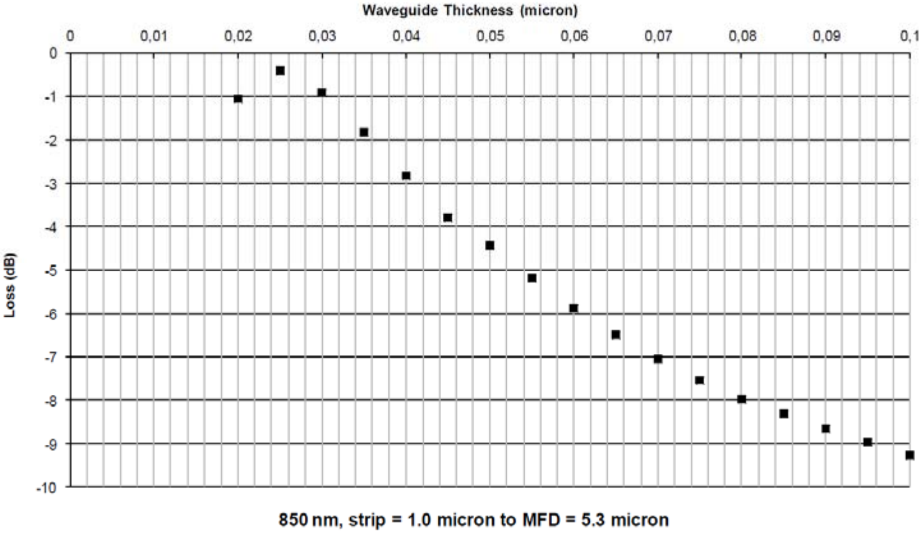

Figure 10: Coupling efficiency for a 1-micron width waveguide and h HP-780PM fiber with a MFD of 5.3 microns.

Simulations on bend losses at 850 nm for the double stripe waveguides are performed for the low contrast area (bottom stripe, 35 nm, 1000 nm width) and the high contrast area (double stripe 35/100/78 nm, 1000nm width). The results for both TE and TM mode are shown respectively in **Figure *11*** and **Figure *12***.

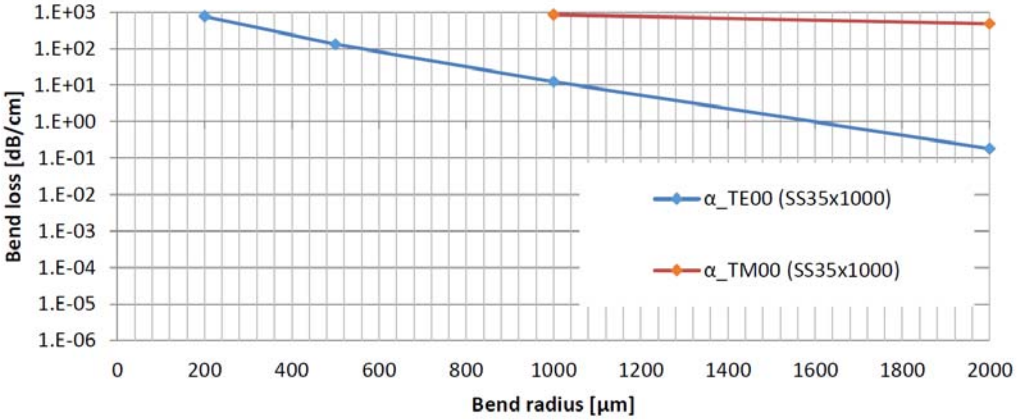

Figure 11: Bend loss for a bottom stripe, 35 nm, 1000 nm width waveguide for TE and TM mode.

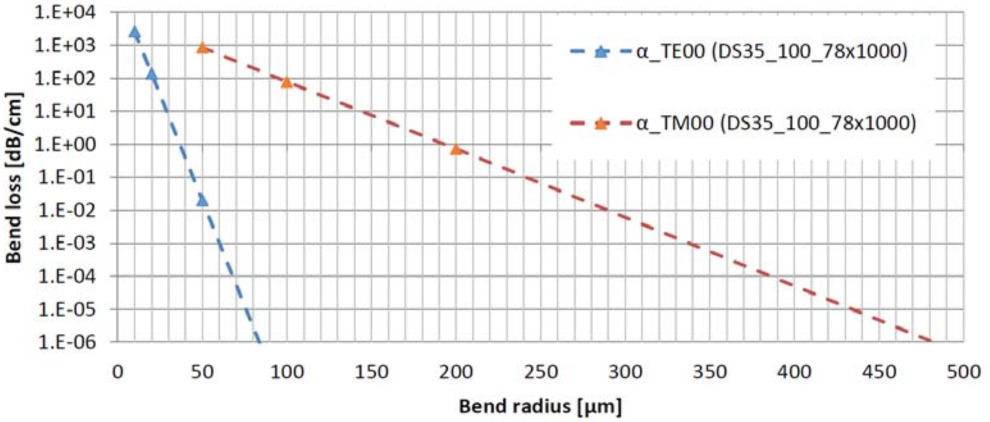

Figure 12: Bend loss for a double stripe, 35-100-78 nm, 1000nm width waveguide for TE and TM mode.

The bend loss calculations show that in the low contrast regime the bend losses are several orders higher compared to the high contrast area. Therefore, bending structures are practically not feasible in the low contrast area and would require a large chip size. Bending structures and the splitter are therefore positioned in the high contrast area of the chip with a minimum bend radius of 100 micron. This result in bending losses << 10^{-3} dB/cm for the TE mode. The bend losses for the TM mode are significantly higher, which is favorable since the MRR design is optimized for a single TE mode. Due to the high loss of the TM modes the laser input will be effectively filtered on chip and not deteriorate the MRR response.

2.3 Multimode Interference Couplers (MMI)

2.3.1 Theory

The self-imaging of periodic objects illuminated by coherent light was first identified 170 years ago [Talbot1836]. Self-focusing (grading index) waveguides could also generate periodic real images of an object [Marcuse1972]. Ulrich [Ulrich1975-1], [Ulrich1975-2] made a detailed suggestion and description of the possibility of achieving self-imaging in uniform index slab waveguides. Self-imaging is a property of multimode waveguides in which an input field profile is replicated in single or multiple images at periodic intervals along the propagation path of the guide, according to the statement of the working theory.

Soldano established a full-modal propagation analysis as the most detailed method to explain the self-imaging phenomena that occur in multimode waveguides [Soldano1994]. This work offers a thorough understanding of the mechanism of multimode interference, in addition to providing a foundation for numerical modeling and design. The guided-mode propagation analysis (MPA) was first suggested in [Ulrich1975-2] for the formulation of periodic imaging. This method decomposes an input field into all directed mode fields, propagates these modes independently, and calculates the output field after re-combination of the propagated fields. Multimode interference (MMI) is the process that represents this form of study.

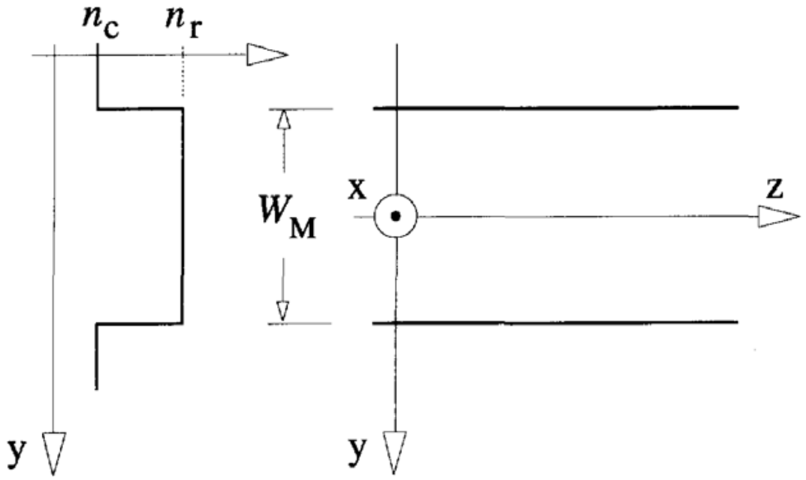

Figure 13: Two-dimensional representation of a step-index multimode waveguide: Effective index lateral profile (left), and top-view of ridge boundaries and coordinate system (right).

The waveguide portion of the MMI is its core, and it is built to support more than three modes. A number of input waveguides (usually single mode) are positioned and used to launch light into this MMI segment at the start. In order to recover the light, the same applies to the end of the multimode field. This type of system is known as a NxM MMI coupler, with N denoting the number of input waveguides and M denoting the number of output waveguides.

Self-imaging is also possible in 3D multimode structures [Simon1977]. The combination of MPA and 2D cross-section calculations (either finite-element or finite-difference methods) aims to be a useful simulation tool [Weinert1994]. In most cases, etch-patterning generates single-mode step-index waveguides in the transverse direction. Since the lateral dimensions are much larger than the transverse ones, we can conclude that the modes have the same transverse behavior in the waveguide. As shown in **Figure *13***, the problem can be analyzed using a two-dimensional structure (lateral and longitudinal). The study that follows is based on a two-dimensional representation of the multimode waveguide. The above can be derived from the real 3D physical multimode waveguide using a variety of techniques.

The distance W_M, ridge (effective) refractive index n_r, and cladding (effective) refractive index n_c of a step-index multimode waveguide are shown in **Figure *13***. At a free space wavelength λ, the waveguide supports m lateral modes with mode numbers v= 0, 1, ... (m-1) as shown in

Figure *14*. The lateral wavenumber k_{yv}, the propagation constant β_v, and the ridge index n_r are all related by the dispersion Equation 34.

$$k_{yv}^2 + \beta_v^2 = k_0^2 n_r^2 \tag{34}$$

With

$$k_0 = \frac{2\pi}{\lambda} \tag{35}$$

$$k_{yv} = \frac{(v+1)\pi}{W_{ev}} \tag{36}$$

The effective width W_{ev}, correlated with the Goos-Hahnchen shifts at the ridge boundaries, has taken into account the polarization dependent lateral penetration depth of each mode filed. Because the penetration depth of high-contrast waveguides is so limited, $W_{ev} \sim W_M$. The effective widths W_{e0}, which correspond to the fundamental mode, can be approximated by the effective widths W_{ey} [Kapany1972]. [Ulrich1975-3] provides the W_e for convenience:

$$W_{ev} \approx W_e \approx W_M + \left(\frac{\lambda}{\pi}\right)\left(\frac{n_c}{n_r}\right)^{2\sigma} \frac{1}{NA} \tag{37}$$

Where σ= 1 for TM, σ= 0 for TE, and the lateral numerical aperture, NA, is defined as:

$$NA = \sqrt{n_r^2 - n_c^2} \tag{38}$$

Using the binomial expansion $k_{yv}^2 \ll k_0^2 n_r^2$, the propagation constants β_v can be deduced from Equations 34, 35, and 36:

$$\beta_v \approx k_0 n_r - \frac{(v+1)^2 \pi\lambda}{4 n_r W_e^2} \tag{39}$$

As a consequence, the propagation constants in a step-index multimode waveguide have a nearly quadratic dependence on the mode number v.

The beat length of the two lowest-order modes is described as L_π:

$$L_\pi = \frac{\pi}{\beta_0 - \beta_1} \approx \frac{4 n_r W_e^2}{3\lambda} \tag{40}$$

As a consequence, the propagation constants spacing can be written as follows:

$$(\beta_0 - \beta_v) \approx \frac{v(v+2)\pi}{3L_\pi} \tag{41}$$

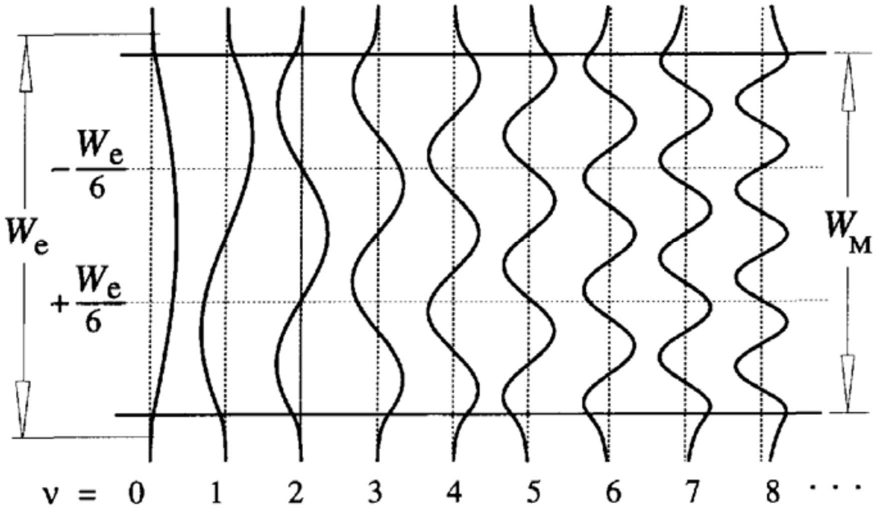

Figure 14: Example of amplitude-normalized lateral field profiles ψ$_v$(y), corresponding to the first nine guided modes in a step-index multimode waveguide.

An input field profile Ψ(y,0) imposed at z=0 and totally contained within W_e, will be decomposed into the modal field distributions ψ$_v$(y) of all modes:

$$\Psi(y,0)=\sum_{v} c_v \psi_v(y) \tag{42}$$

Using overlap integrals, the field excitation coefficients c_v can be estimated by the Equation:

$$c_v=\frac{\int \Psi(y,0)\psi_v(y)\,dy}{\sqrt{\int \psi_v^2(y)\,dy}} \tag{43}$$

based on the field-orthogonality relations.

It could be decomposed into the directed modes alone if unguided modes are not excited due to the narrow spatial range of the input field Ψ(y,0), which is a requirement that is fulfilled for all practical applications:

$$\Psi(y,0)=\sum_{v=0}^{m-1} c_v \psi_v(y) \tag{44}$$

As a superposition of all the directed mode field distributions at a distance Z, the field profile Ψ(y,z) can be written as:

$$\Psi(y,z)=\sum_{v=0}^{m-1} c_v \psi_v(y)\exp\left[j\left(\omega t-\beta_v z\right)\right] \tag{45}$$

The fundamental mode's phase can be dropped as a common factor of the number, and the time dependence exp(jωt) can be assumed implicitly hereafter, resulting in the filed profile Ψ(y,z):

$$\Psi(y,z)=\sum_{v=0}^{m-1}c_v\psi_v(y)\exp\left[j(\beta_0-\beta_v)z\right] \tag{46}$$

By substituting Equation 41 into Equation 46 at a particular distance z= L, a useful expression for the field can be written as:

$$\Psi(y,L)=\sum_{v=0}^{m-1}c_v\psi_v(y)\exp\left[j\frac{v(v+2)\pi}{3L_\pi}L\right] \tag{47}$$

The modal excitation c_v, as well as the properties of the mode phase factor, will specify the types of images that have been produced as a result of the shape of Ψ(y,L):

$$\exp\left[j\frac{v(v+2)\pi}{3L_\pi}L\right] \tag{48}$$

In such conditions, the input field Ψ(y,0) will be replicated in a field Ψ(y,L), which is the actual self-imaging. We refer to self-imaging mechanisms that are obtained solely by exciting such modes as restricted interference, and self-imaging mechanisms that are independent of modal excitation as general interference.

Two Equations are followed:

$$v(v+2)=\begin{pmatrix} even\rightarrow v:even \\ odd\rightarrow v:odd \end{pmatrix} \tag{49}$$

and,

$$\psi_v(-y)=\begin{pmatrix} \psi_v(y)\rightarrow v:even \\ -\psi_v(y)\rightarrow v:odd \end{pmatrix} \tag{50}$$

The latter being a consequence of the structural symmetry with respect to the plane y=0.

2.3.2 Simulation results

MMI couplers support the same functionality as conventional Y power splitters but in a more compact way especially for a large number of output ports. Within this thesis, they consist of a multimode region with one input and different number of output single mode waveguides (4 and 8) to feed the MRR array of the photonic sensor which is described in the next chapters [Gounaridis2015]. For a given multimode region width, its length must be chosen appropriately to yield the desired performance. In our case a clear 8-fold self-images (in the case of 8 output waveguides) of the input mode must be formed at the length where the output waveguides are placed. Their design is based on both single strip and asymmetric double stripe TriPleX waveguide geometry but designs with the lower (35 nm) strip geometry were also studied to take into consideration the scenario where the tapered transition from the lower strip to double strip geometry is placed after the MMI coupler. Appropriate 3D Beam Propagation Software (BPM) was used for designing the structures and simulations have shown that output port power imbalance and insertion loss below 0.5 dB can be achieved for various combinations of widths and lengths for 1x8 MMIs and in addition, they operate almost wavelength independent.

Simple designs, as well as more complex ones involving the use of tapered sections at the input and output waveguides (taper length 3 µm), prismatic and curved multimode regions were studied. **Figure *15*** presents the layout of the designs that were studied.

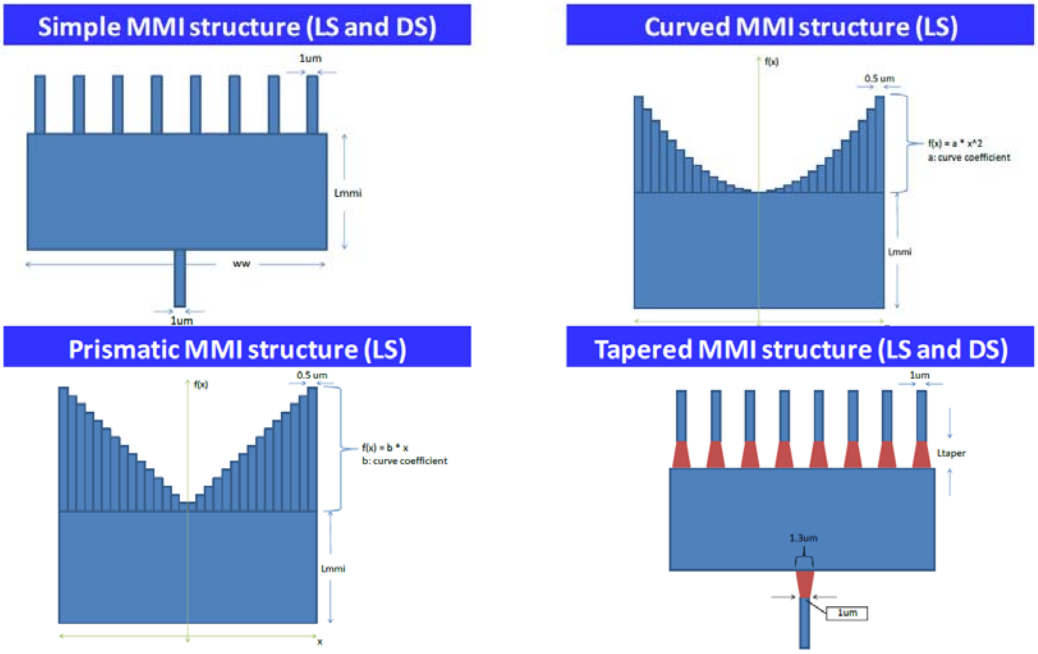

Figure 15: Layout of the simulated MMI coupler designs.

The simulation results are presented in **Figure *118*** - **Figure *127***, in Appendix I, where the red circles indicate designs that were chosen to be included in a first fabrication run. In total 51 designs were chosen and are summarized in the **Table *6*** in Appendix I as well.

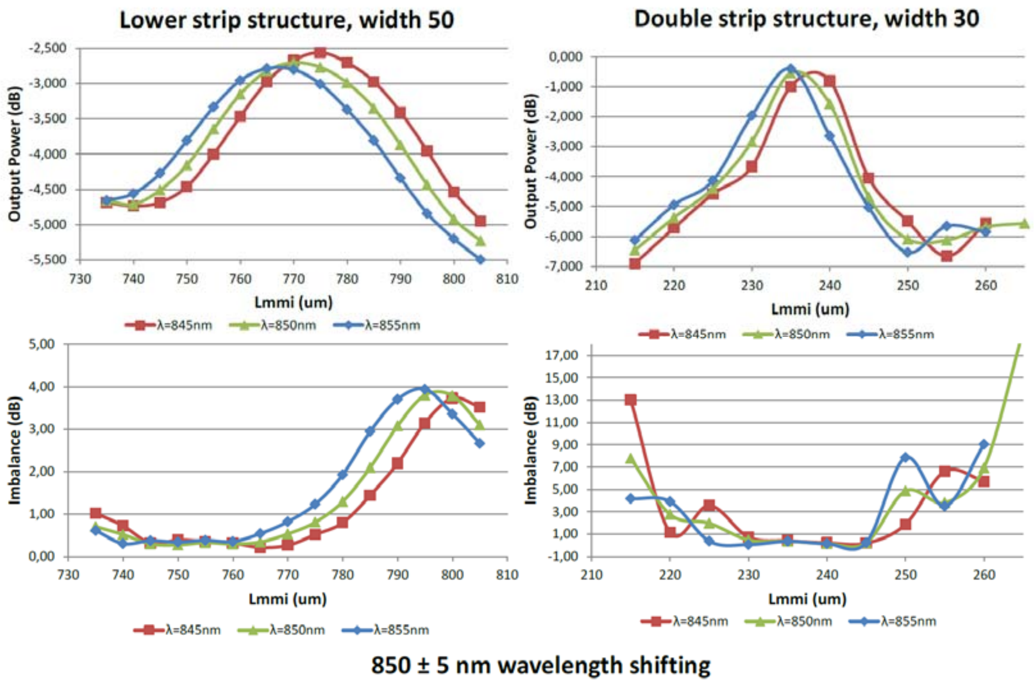

Figure 16: Dependence of port imbalance and insertion loss on shifting of the operation wavelength by 5 nm.

The simulations show that the double stripe structured is the most promising one since it has less losses and less imbalance with respect to wavelength variations. The best designs to be monolithically integrated with the MRR array will be chosen after experimental characterization. The mask file with the MMI designs to be fabricated on TriPleX platform can be seen on **Figure *17*** and **Figure *18***.

A second round of simulations have been also made [Gounaridis2019] for 1x8 MMI based again on both TriPleX geometries, the SS and the DS. 14 designs have been delivered to LioniX for fabrication which are presented in **Table *8*** in Appendix I. Different parameters have been taken into account in order to increase the efficiency of these structures. Compared to the first round, where a Gaussian mode field was used as the excitation mode, the fundamental TE mode was the excitation source in the second round of simulations. Moreover, the variations in the cross section of the fabricated waveguides were also investigated. As a result, deviations of 10% compared to the ideal values on the width and the length of MMI region that had appeared in the first run, are not anymore present.

Moreover, a complete simulation study has been made also for 1x4 MMI couplers. These photonic structures will be used together with the 2-port grating coupler as it is described in the corresponding chapter. The simulation results are presented in **Table *9*** in Appendix I. In total, more than 200 MMI photonic structures have been designed, including the two generations of 1x8 and the one generation of 1x4 MMI couplers.

2.3.3 Characterization results

The masks of the fabricated structures (1x8 and 1x4) are presented in the next figures. These structures had been used to optimize the performance of the photonic chip design.

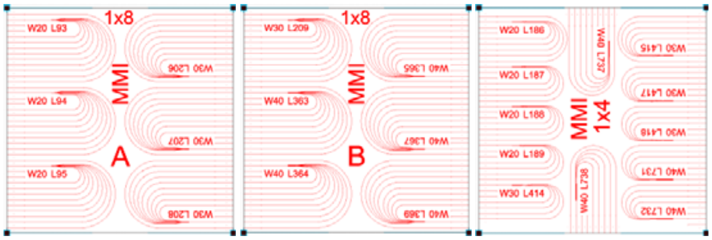

Figure 17: Mask design of the MMI test structures (part A).

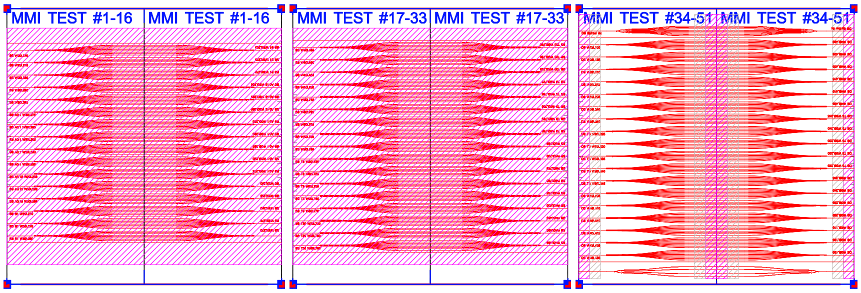

Figure 18: Mask design of the MMI test structures (part B).

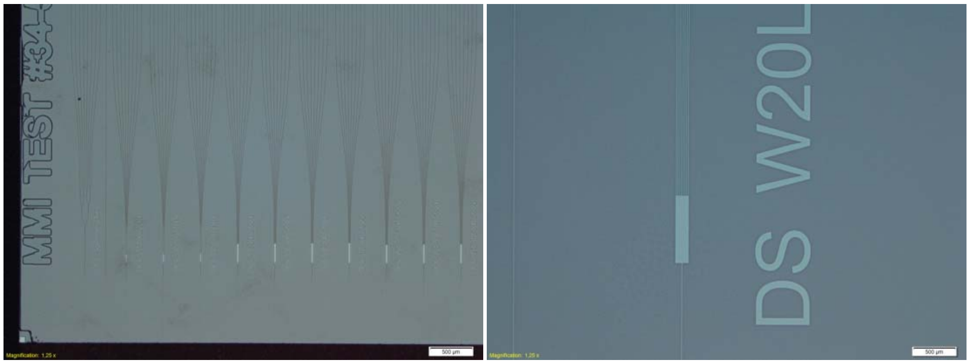

Figure 19: Microscope pictures of the MMI test structures.

For the experimental characterization of these photonics structures, a testbed has been built up. In the next two figures, this testing setup is presented, consisting of a VCSEL light source at 855 nm center operation wavelength, an isolator in order to avoid any harmful reflections back to the VCSEL, a polarization controller for propagating only the TE mode in the TriPleX chip, a 12-fold fiber array unit (FAU) placed on a 6-axis probe station for coupling the light into the PIC and a power meter in the receiver side for validating in terms of output power the photonic structures.

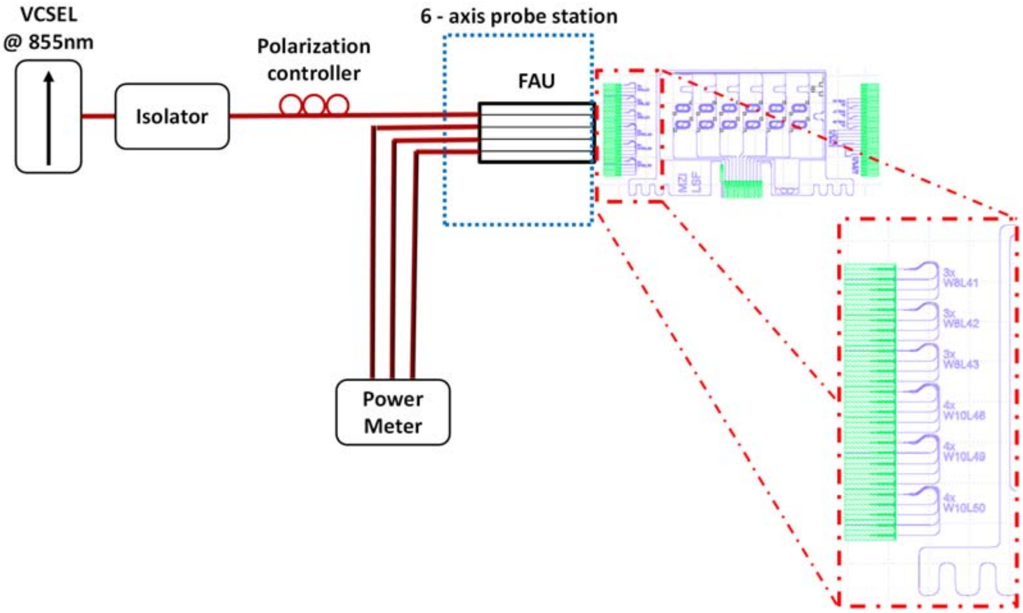

Figure 20: Schematic of the experimental setup which is used for the characterization of the passive components.

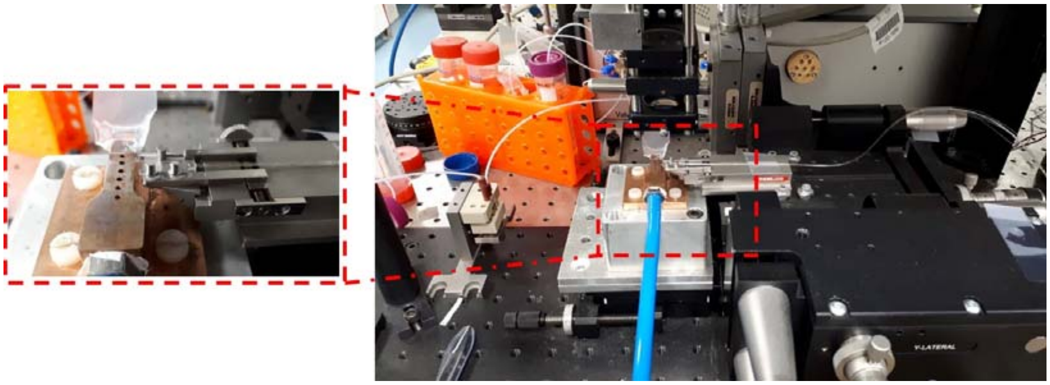

Figure 21: Part of the experimental setup which is used for the characterization of the MMI structures. Right: 6-axis probe station for the optical alignment of the FAU with the photonic chip. Left: Vacuum chuck as chip holder and FAU.

In the **Table *7*:** Measurement results of the 1G 1x8 MMIs. in Appendix I, the measurement results of the MMI structures of the 1G 1x8 MMI, are presented. The MMIs were characterized in terms of output power in each port and for each design the imbalance and insertion loss were calculated. Two sets of chips from wafers 102 and 201 were characterized for two different wavelengths (853.96 nm and 855.77 nm). Apart from a specific design, the values measured were above the targeted values showing that the design and fabrication of a high output number (>4) MMI is challenging. The MMI imbalance seems to be dependent in a greater extend from the operating wavelength and the temperature of the chip. Taking into consideration these results the designs of the second-generation structures were further optimized.

In the **Figure *128*-Figure *151*** in Appendix I, the detailed measurements of the 1G 1x8 MMIs are presented.

Below, in the bar figures, the characterization results of the 1G 1x8 MMI couplers from two wafers (wafer 102 and 201) for two wavelengths (853.96 and 855.77 nm) are summarized.

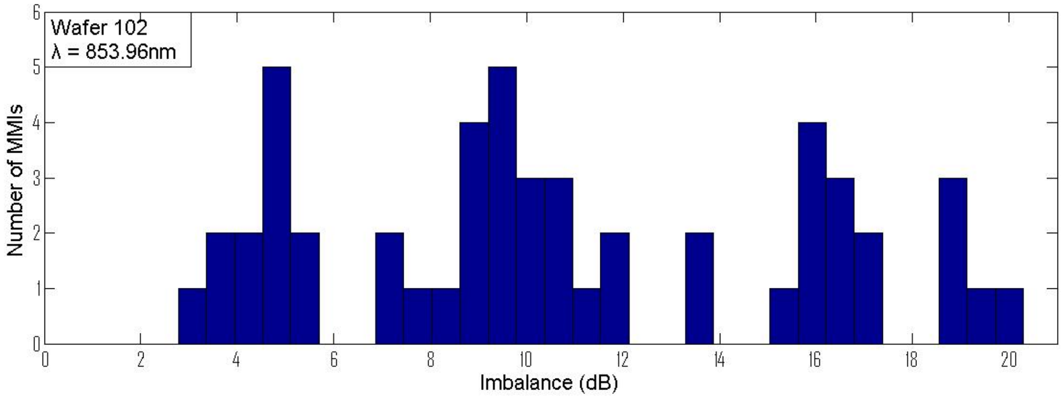

Figure 22: MMI with best performance is the DS T3 W30 L225um with Imbalance 2.78 dB.

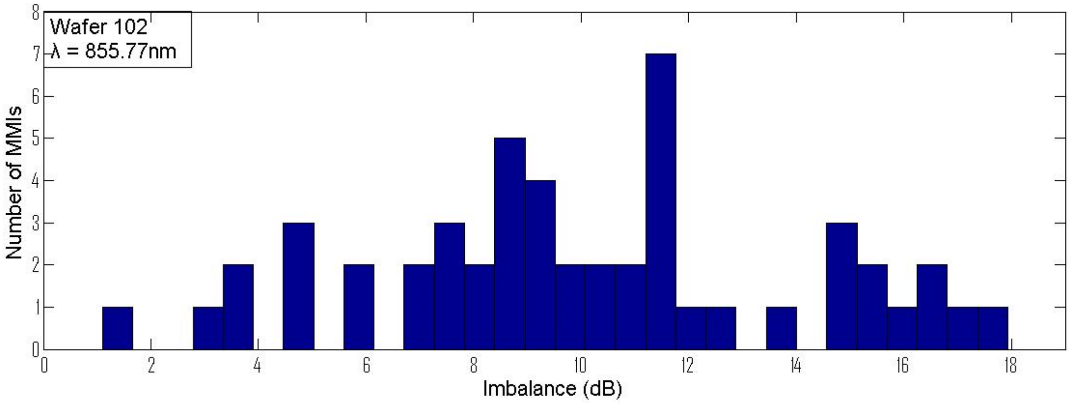

Figure 23: MMI with best performance is the DS T3 W30 L225um with Imbalance 1.10dB.

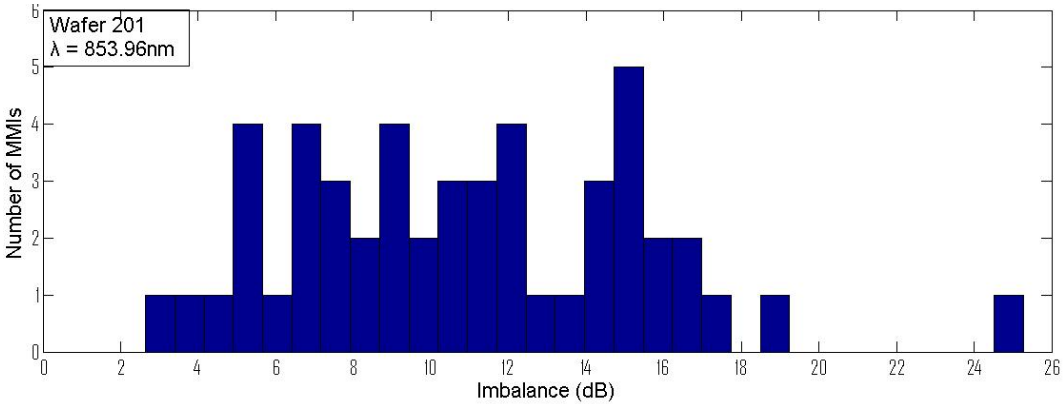

Figure 24: MMI with best performance is the SS A0.1 W30 L280um with Imbalance 2.64dB.

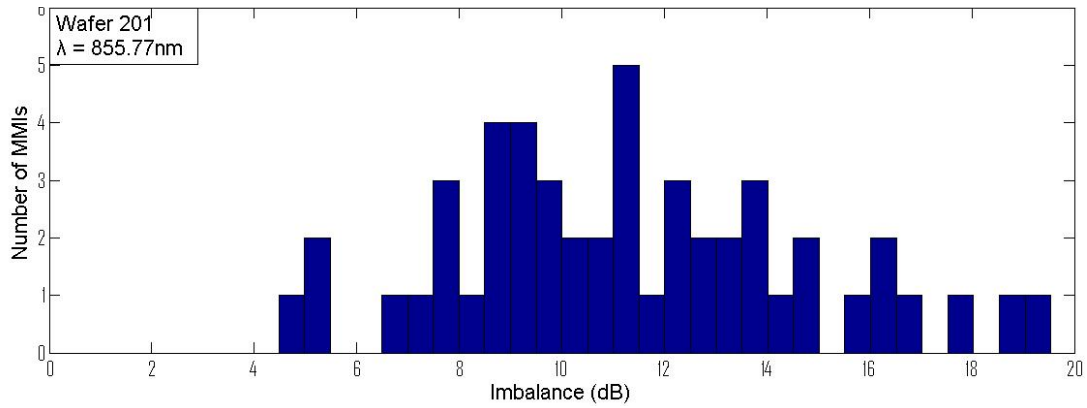

Figure 25: MMI with best performance is the SS A0.15 W30 L285um with Imbalance 4.48dB.

As it was expected from the simulation results, due to the non-optimum length of the multimode region and the Gauss excitation mode compared to the supported from the waveguide fundamental one, the goals and targets in terms of insertion losses and the imbalance at the output waveguides, are not reached in the 1G 1x8 MMIs.

The experimental results of the second simulation run passive components' characterization are being shown in the next figures. These passive structures are the 2nd generation (2G) 1x8 MMI couplers and the 1st generation (1G) 1x4 MMI couplers. There is also characterized, a different type of photonic power spitter, the Y-junction, and the corresponding results are presented in **Figure *152*** and **Figure *153***, in Appendix I.

The next 3 figures present the testing results of the 2G 1x8 MMI couplers.

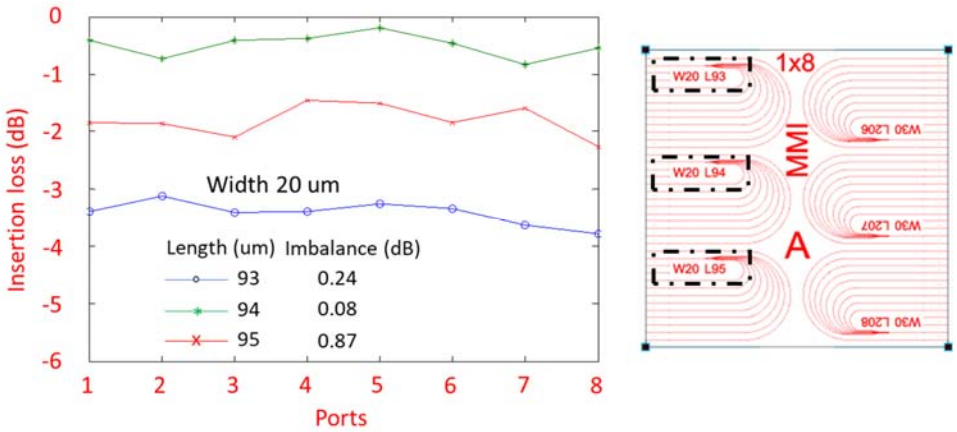

Figure 26: Characterization results of the 2G 1x8 MMI with width 20.

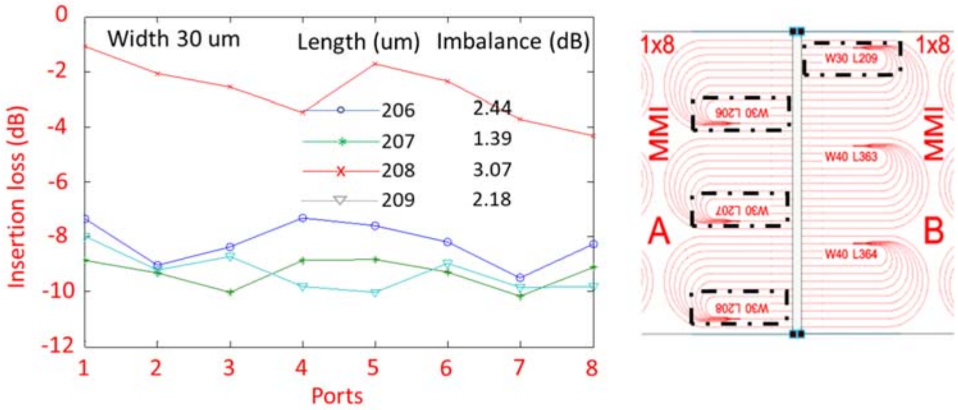

Figure 27: Characterization results of the 2G 1x8 MMI with width 30.

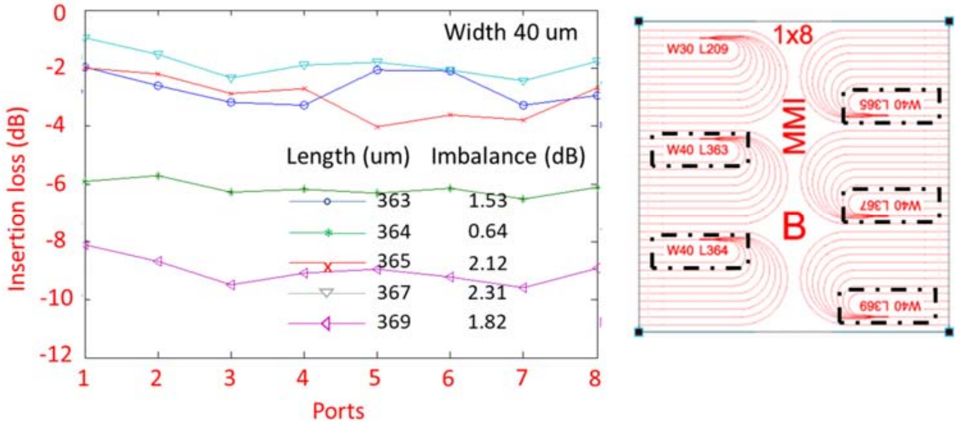

Figure 28: Characterization results of the 2G 1x8 MMI with width 40.

The following 3 graphs are shown the testing results of the 2G 1x4 MMI couplers.

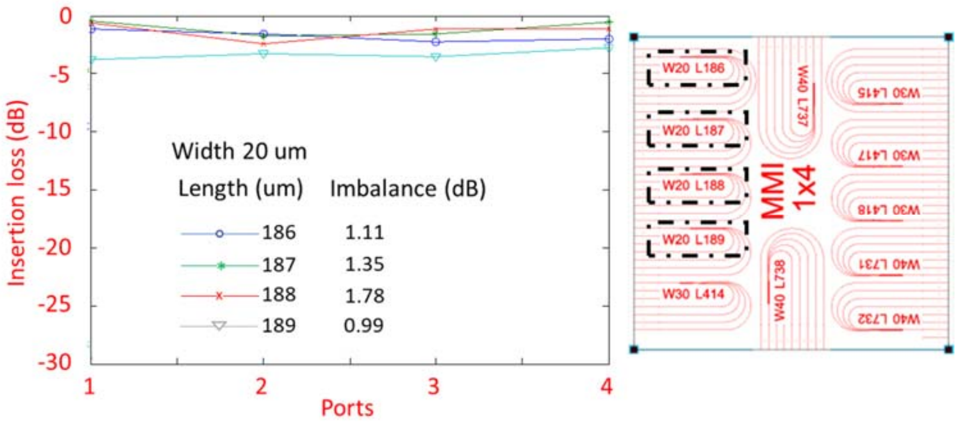

Figure 29: Characterization results of the 1G 1x4 MMI with width 20.

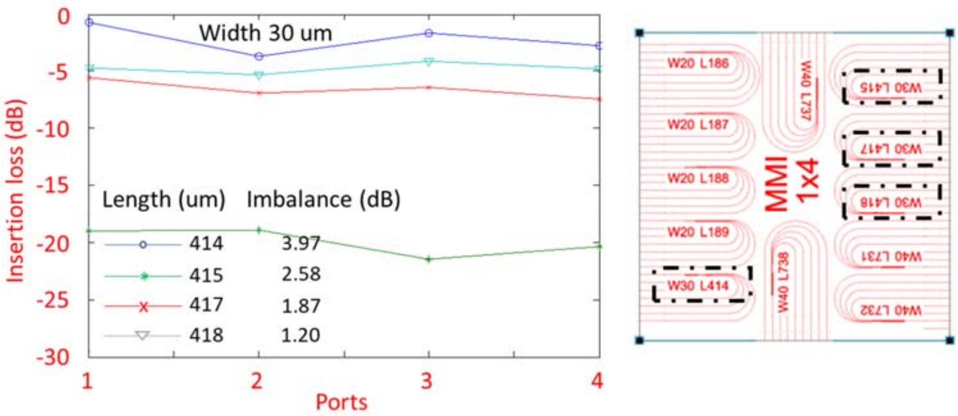

Figure 30: Characterization results of the 1G 1x4 MMI with width 30.

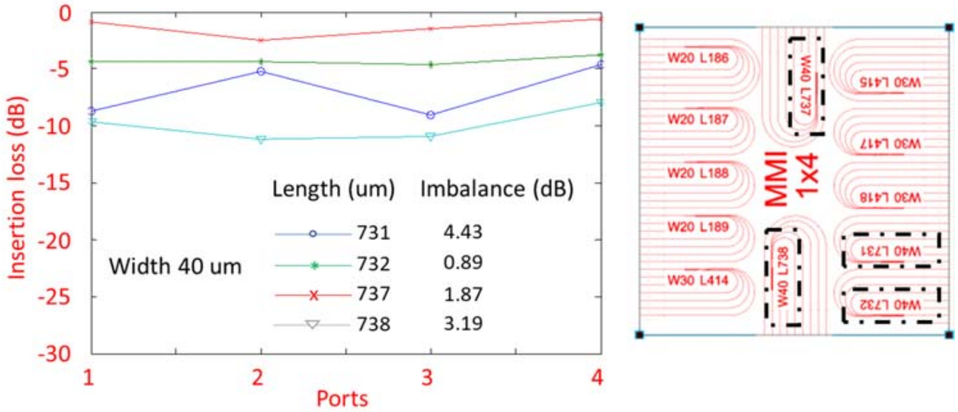

Figure 31: Characterization results of the 1G 1x4 MMI with width 40.

These characterization results show that within the 2G set of the 1x8 MMI, there are structures that address the targets that had been set in terms of insertion losses and imbalance. More specifically, the 1x8 MMI photonic structure with width of 20 um and length 94 um is the best performing one with insertion losses and imbalance 0.6 and 0.08 dB, respectively. The characterization results that correspond to the 1x4 MMI structures, show that none of them managed to reach the targets of insertion losses and imbalance. The best performing structure is the one with width 20 um and length of 186 um with measured insertion losses and imbalance of 2.1 and 1.11 dB, respectively. Nevertheless, there is a moderate agreement between the theoretical and the experimental values, at least for the structures that correspond to the second simulation run out of the 100 in total MMIs that have been fabricated. Regarding the deviations of the insertion losses that are present, there are many reasons that could be responsible, starting from the characterization setup (dusty fibers, temperature instability of the VCSEL) up to the level of the test chips (scratched chip facets). However, the differences between the simulation and the characterization results of the insertion losses do not impose significant constraint since the power budget of the photonic chip is more than enough for this kind of values.

2.4 Grating Couplers

2.4.1 Theory

A grating coupler is a periodic corrugated waveguide structure that couples light from an out of plane location into a photonic chip waveguide and vice versa. To pair the light coming from a fiber, these devices use the diffraction phenomenon. To reduce the losses, several variants of this initial principle have been proposed. **Figure *32*** illustrates the fiber coupling scheme. These structures are less sturdy, but they have the advantage of coupling light from non-lensed single mode fibers.

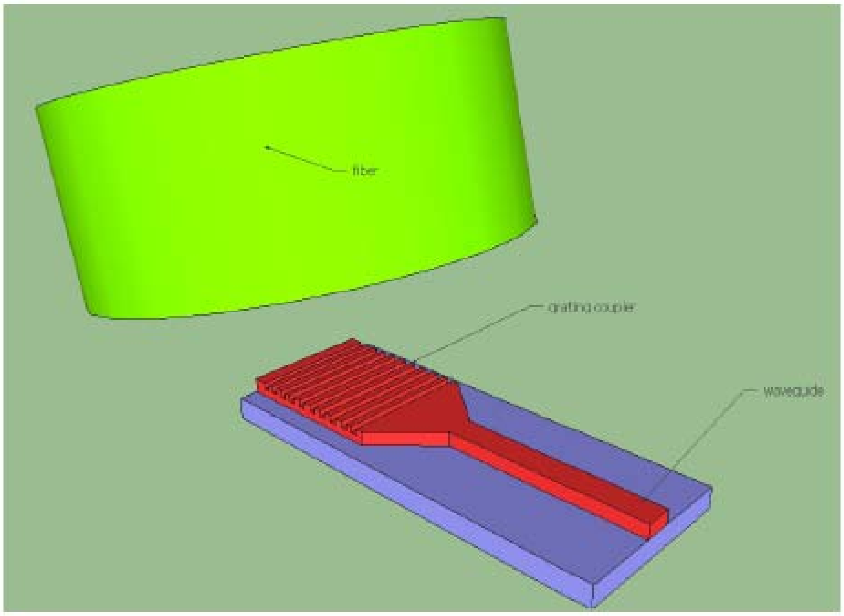

Figure 32: Using a grating coupler, coupling to/from fiber from/to a waveguide.

The theoretical issues that are important to understand the grating coupler, as well as the parameters that play a role in the design process, are discussed in this section.

The incident light is diffracted as it hits the surface of a periodic structure. The Bragg condition [Villasante2010] describes the relationship between the wave-vectors of incident and diffracted waves. The Bragg condition is the same as Snell's Law, which defines refraction at the interface between two materials, when there is no grating at the interface between the two materials. The Bragg condition for grating couplers can be written as follows for first order diffraction:

$$k_{in} \sin\theta + \frac{2\pi}{\lambda} = \beta \tag{66}$$

With $\beta = \frac{2\pi}{\lambda_0} n_{eff}$ the propagation constant of the guided mode, λ_0 the desired wavelength and neff the effective index of the fundamental mode, $k_{in} = \frac{2\pi}{\lambda_0} n_{top}$ is the wave vector of the incident wave, n_{top} the refractive index of the background, θ is the incidence angle, and Λ is the grating period. [Galan2008]

Only infinite structures satisfy the Bragg condition. Diffraction occurs in a finite range of k vectors around the projected one in finite structures. The wave diffraction on the grating surface is depicted in simplified form in **Figure *33***.

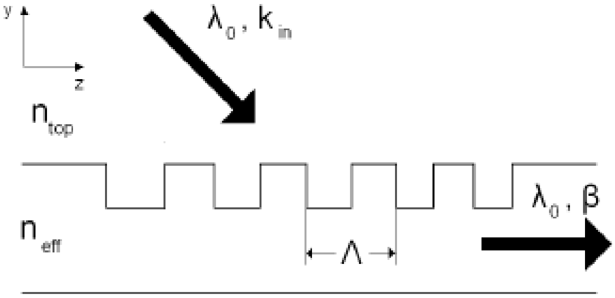

Figure 33: Bragg diffraction on the grating surface.

When the materials in a device are reciprocal, the scattering matrix, which defines the relationships between the inputs and outputs, is symmetrical, according to electromagnetic theory. The reciprocity or symmetry theorem is the name for this. The elements of this matrix are then connected in the following way [Taillaert2004]:

$$S_{ij} = S_{ji} \tag{67}$$

This can also be extended to systems that leak energy. This is especially useful in our case because it allows us to simulate coupling from fiber to waveguide or from waveguide to fiber. The coupling efficiency would be the same in both cases since single-mode waveguides and fibers are used.

When an optical fiber is vertically coupled to a grating, as shown in **Figure *34***, half of the power couples in one direction and the other in the other, resulting in a coupling efficiency of less than 50% [Taillaert2004].

In order to prevent this problem, symmetry must be broken in some way. This was done by using an asymmetrical grating or coupling the fiber at an angle rather than vertically (8 to 10 degrees). In this work, the completely vertical position is used.

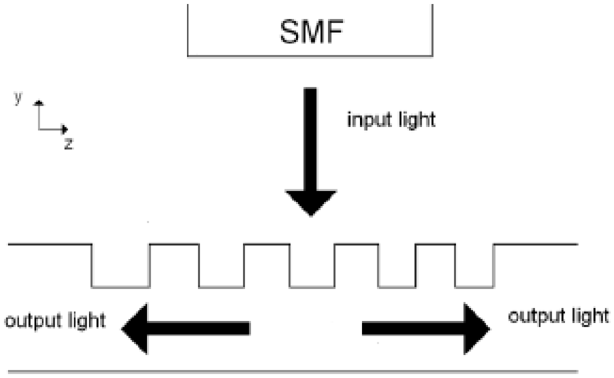

Figure 34: Perfectly vertical coupling.

The grating coupler structure is three-dimensional, but since its width is much greater than the wavelength and core height, it can be approximated by a two-dimensional structure. As a consequence, the structure can only be simulated in a plane, making measurements possible and much simpler.

Figure *35* depicts the basic design parameters.

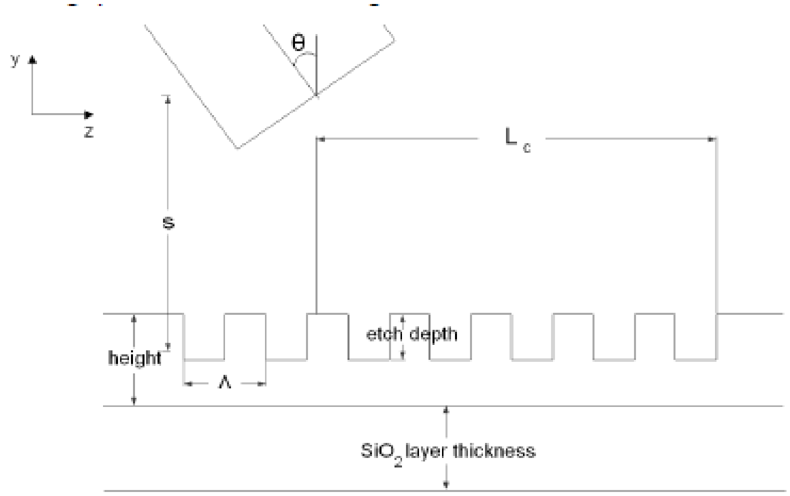

Figure 35: Lateral view of the grating coupler and parameters of design.

Etching depth (ed): depth with which the guiding silicon layer is etched, i.e., the depth of the grating grooves.

Height: the height of the silicon guiding core.

SiO_2 layer thickness: the thickness of the buried oxide cladding layer.

θ: incidence angle of the launched field (0°).

Coupling length in the y direction (s): vertical distance between the fiber core center and the waveguide center.

Coupling length in the z direction (Lc): the length in the z direction between the fiber core center and the beginning of the grating that provides maximum power at the output (expressed as $L_{c,\,opt}$) can be demonstrated to be equal to [Laurent2006]:

$$L_{c,opt} = \frac{w_0}{1.37\cos\theta} \tag{68}$$

With w_0 half the width (MFD) of the Gaussian incident beam, and θ the incidence angle.

Grating period (Λ): its theoretical value is obtained from (Equation 66) [Taillaert2004, Tsuchizawa2005, Laurent2006]:

$$\Lambda_{theor} = \frac{\lambda_0}{n_{eff} - n_{top}\sin\theta} \tag{69}$$

With neff the effective index of the guided mode, and n_{top} the refractive index of the background (normally air or silicon dioxide).

Filling factor (ff) or Duty Cycle (DC): relation between the widths of the etched sections and the sections without etching.

Number of periods (N): enough to make sure the surface of the grating is properly illuminated by the fiber.

Effective index (n_{eff}): The effective index of the structure must be determined using Equations 68 and 69 in order to determine the optimal coupling length and theoretical optimal grating time. The structure must be divided into two parts, one for the etched grooves and the other for the sections without etching, before the average effective index can be calculated. **Figure *36*** depicts the procedure.

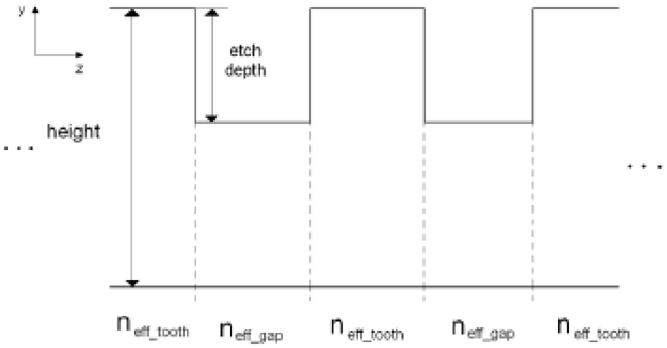

Figure 36: Effective index calculation.

The conventional Effective Index Method is used to find the effective index of the etched parts, n_{eff_gap}, and the sections without etching, n_{eff_tooth}. The global effective index can be found as the ratio of these two effective indexes related to the fill factor since there are the same number of parts with and without etching:

$$n_{eff} = (1 - ff)\, n_{eff\_gap} + ff n_{eff\_tooth} \tag{70}$$

2.4.2 Simulation results

Grating coupler is a waveguide structure that has periodic corrugations, used to couple light from an out of plane position into a photonic chip waveguide and vice versa. In our case, the grating coupler will be used to couple the output mode from a flip-chip bonded VCSEL into a 1 μm wide waveguide as it shown in **Figure 37**(a). **Figure 37**(b) presents a layout of the designed grating coupler. It has a curved shape (in the form of a taper) which additionally focuses the light down the 1 μm single mode waveguide avoiding in that way a long-tapered section, leading to a more compact structure [Gounaridis2015].

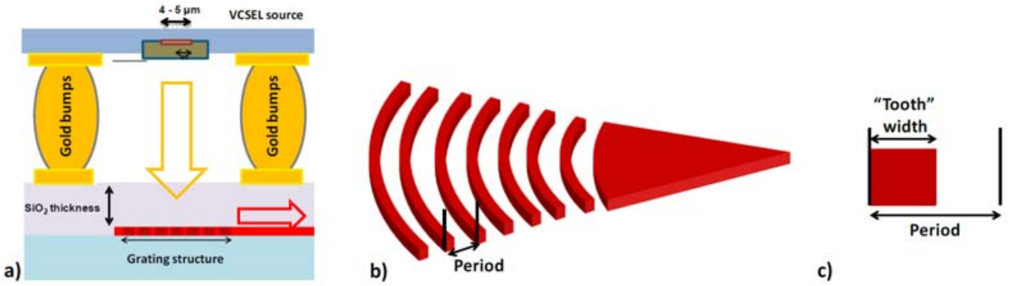

Figure 37: Vertical coupling scheme from flip-chip bonded VCSEL (a), curved grating coupler structure (b) and definition of the period and the fill-factor parameters (c).

The curved grating coupler has an angle of 18°, 60 µm length and consists of 26 periods with the first period placed 30 µm from the grating coupler's narrowest (1 µm) edge. The corrugations are formed by completely etching the waveguide in a way that eases fabrication since no extra etching step is required. In order to efficiently couple light from the VCSEL into the waveguide, the period and fill factor of the grating coupler have to be appropriately chosen, depending on the operating wavelength and the effective refractive index (N_{eff}) of the waveguide. The period is defined as the distance of two consecutive corrugations and the fill factor (or duty cycle, DC) as the length of the waveguide over the length of the period as seen in **Figure *37***(c). The structure was designed in a CAD environment and simulated using appropriate 3D Finite Difference Time Domain (FDTD) software. Initial simulation runs using the 35 nm lower strip waveguide geometry (**Figure 38**(a)) showed that coupling efficiency was limited to 4%. The weak perturbation caused by the thin geometry cannot couple the light efficiently into the waveguide leading to poor performance of the coupler. The double strip geometry (**Figure 38**(b)) achieved better coupling efficiency close to 20% assuming an infinite bottom SiO_2 thickness (so the light that was transmitted through the grating was absorbed at the computational boundary) and 30% if we also take advantage of the light reflected back at the interface between the SiO_2 and the Si substrate as seen in **Figure *38***(c).

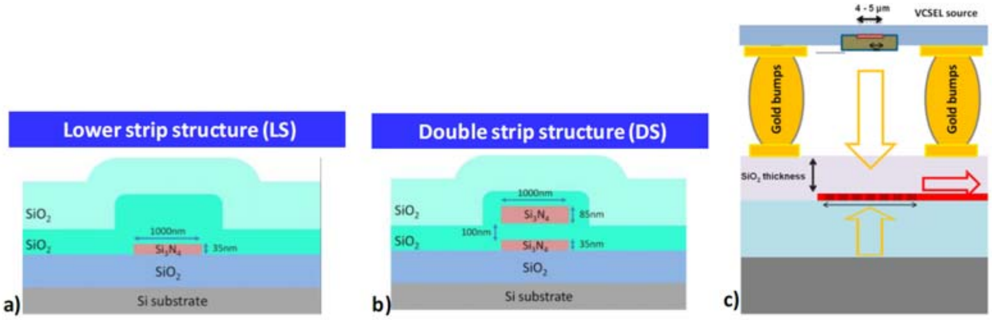

Figure 38: Lower stripe geometry (a), double stripe geometry (b) and schematic depicting light reflected-back at the SiO_2 - Si interface.

A Gaussian incident field with 10 µm size is assumed for the simulations. The simulations were carried out for a period range from 0.53 to 0.59 µm with 0.01 µm step and for each period different fill-factors (0.44 – 0.62 with 0.02 step) were studied. The results are presented in **Figure 39**(a). The best coupling efficiency close to 20% was achieved for 0.565 µm period and

0.52 fill-factor. **Figure 39**(b) presents the wavelength dependence of the grating for the best performing period for different fill factors. The coupling efficiency drops from 20% to 18% and 17% for 845 nm and 855 nm operating wavelengths, respectively.

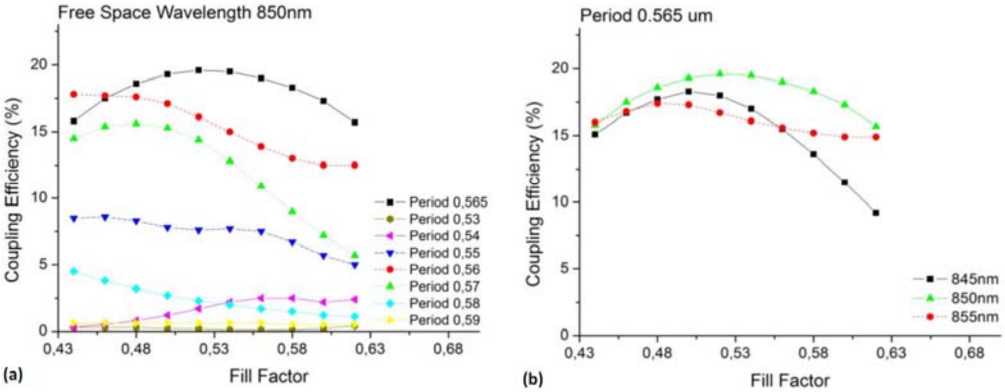

Figure 39: Coupling efficiency dependence on fill-factor for different periods (a) and on different wavelength values (b) for the DS structure.

The effect of the lower SiO_2 cladding thickness on the coupling efficiency was also studied. The thickness of the lower SiO_2 cladding varied from 3 to 4 µm with 0.05 µm step. **Figure 40**(a) shows that coupling efficiency can be improved to 30% and at the same time the power reflected backwards to the source to be at its minimum value. Changing the thickness of the lower layer essentially changes the distance the light has to travel before again reaching the grating structure and therefore reaches with a different phase each time, exhibiting a periodic pattern. When the two signals interfere constructively coupling efficiency is improved. The same study was carried out for 845 nm and 855 nm and minimum coupling efficiency of 25 % was achieved as presented in **Figure 40**(b). Adjusting the lower cladding height can be within fabrication tolerances.

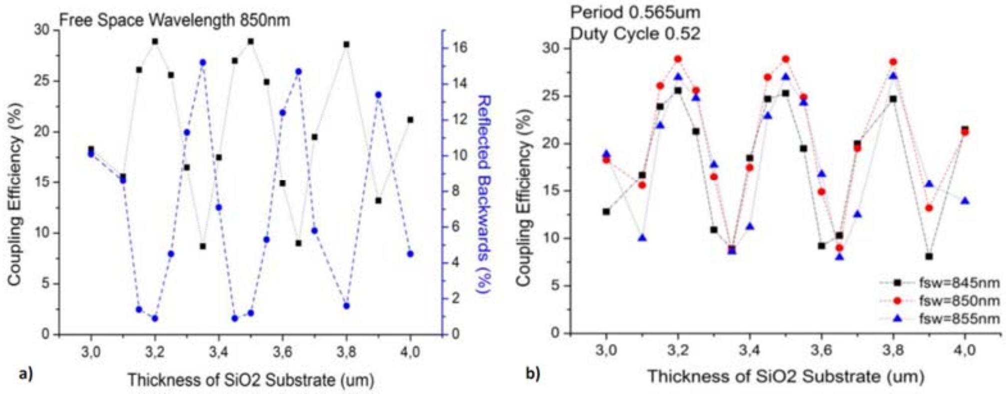

Figure 40: Coupling efficiency and power reflected backwards dependence on SiO2 cladding thickness at 850 nm (a) and comparative graph showing coupling efficiency dependence on SiO2 cladding for 845 - 855 nm wavelengths (b) for DS structures.

The same simulation study has been made for different values of the lower SiO_2 thickness. This time, the thickness was varied around 6 and 8 um. The reason of this additional set of values was that the wafer which was used for the fabrication of such structures has had a lower SiO₂ layer of 8 um thickness. Moreover, having a thicker lower cladding, the waveguiding leaks to the silicon substrate, are avoided. The results are presented in the next figure.

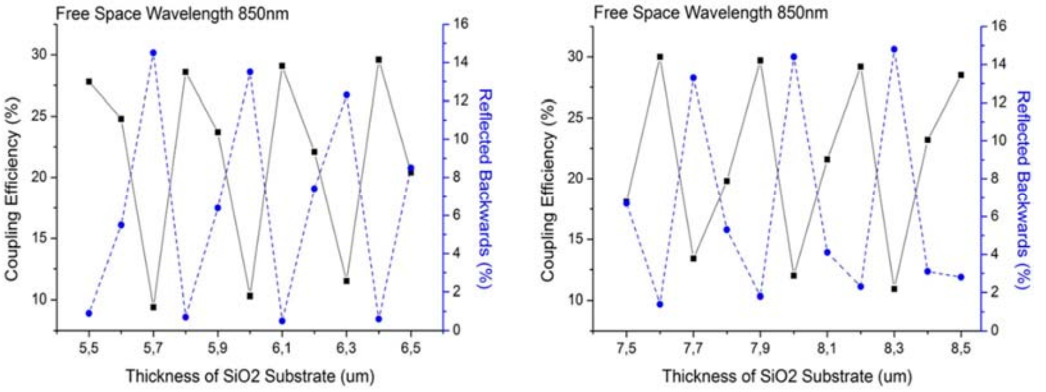

Figure 41: Coupling efficiency and power reflected backwards dependence on SiO₂ cladding thickness around (left) 6 um and (right) 8 um.

The effect of the VCSEL source's height from the TriPleX platform was also studied since it will be placed on gold bumps which can vary in height. The VCSEL beam diverges as it exits the source and travels in free space, so the size of the beam that reaches the grating depends on the height of the placement. To study how this affects coupling efficiency, the diameter of the excitation field varied from 4 to 15 μm by 1 μm step. The coupling efficiencies achieved for each diameter along with the calculated distance from the grating can be seen in **Figure *42***. The coupling efficiency remains almost constant for a diameter within the 8 - 15 μm range and drops rapidly for low values (4 - 8 μm).

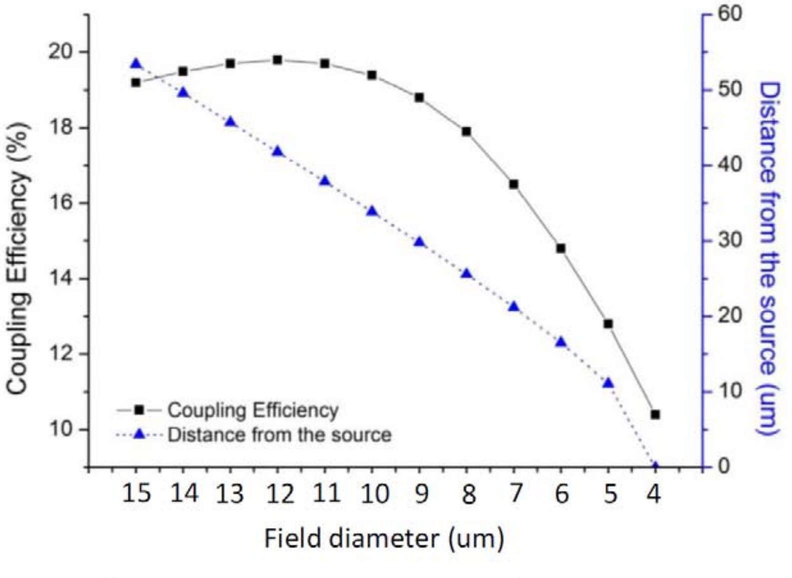

Figure 42: Coupling efficiency dependence on VCSEL distance from the source.

The same set of simulations have been repeated for the single stripe waveguide geometry. Starting from the case of considering as semi-infinite the lower SiO₂ layer, whose results are presented in **Figure *43***.

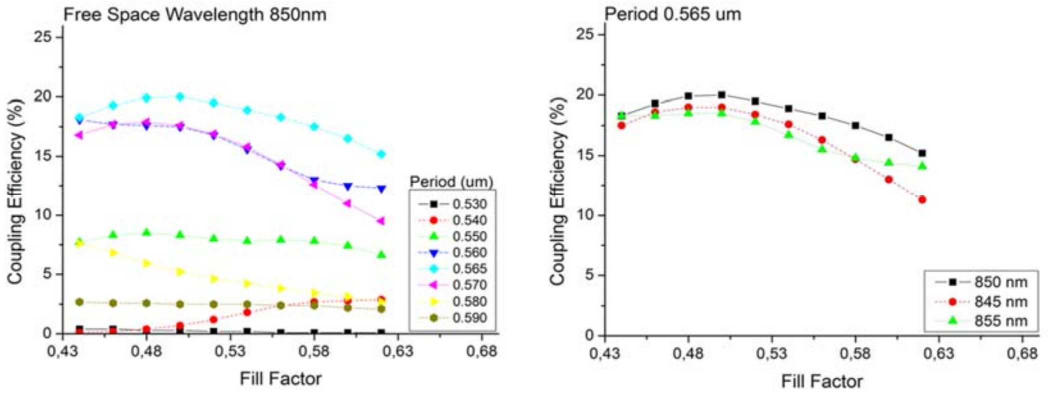

Figure 43: Coupling efficiency dependence on fill-factor for different periods (a) and on different wavelength values (b) for the SS structure.

As a next step, we have again taken into account a specific range of lower SiO_2 layer's height of 3-4 um (**Figure *44***). As it can be observed, the maximum coupling efficiency in both waveguide geometries is similar at 30%.

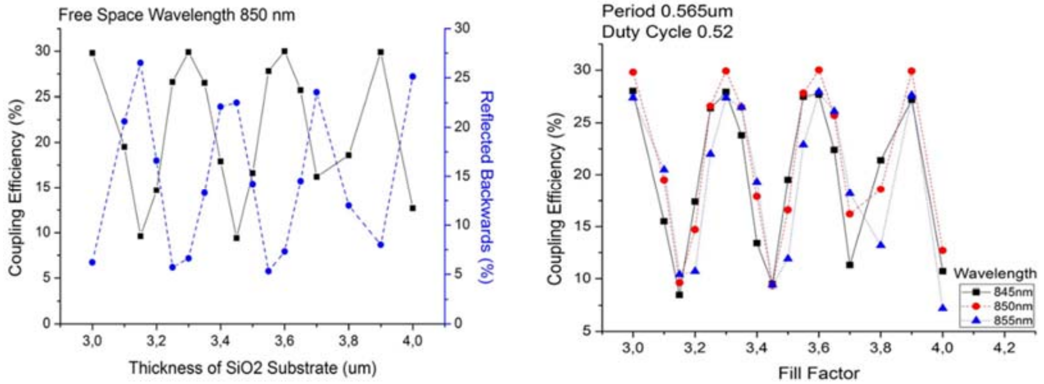

Figure 44: Coupling efficiency and power reflected backwards dependence on SiO_2 cladding thickness at 850 nm (a) and comparative graph showing coupling efficiency dependence on SiO_2 cladding for 845 - 855 nm wavelengths (b) for SS structures.

During the simulations of the single port grating coupler, it was observed that the same portion of light that had been waveguided to the one direction, had been guided also to the other one. It was an expected phenomenon since the incidence angle was in all cases 0 degrees. Based on this, a new structure called 'two-port' grating coupler has been designed (**Figure *45***) [Gounaridis2019], to reclaim the whole performance of the grating coupler by collecting the coupled light from both sides. Since the single grating couplers have achieved a coupling efficiency above 25%, this new design looked ambitious with coupling efficiency of 50-55%.

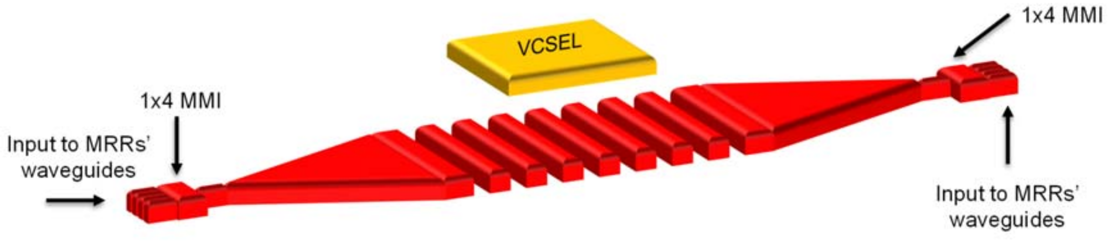

Figure 45: The design of the 'two port' grating coupler.

Simulation results were very promising and are presented in the next figure. The thickness of the SiO_2 substrate was studied to take account the interference between the two last platform layers.

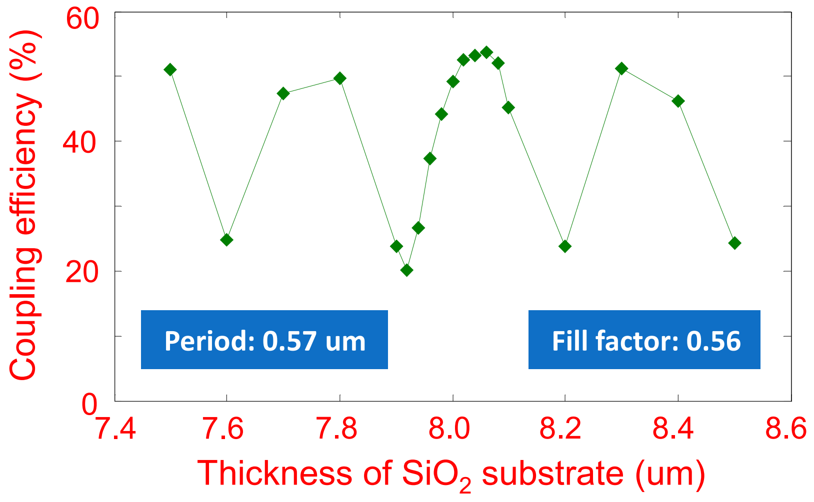

Figure 46: Simulation results for the 2-port grating coupler efficiency.

The backwards waveguided light is planned to be gathered and be used as an input to the MRRs so this structure can achieve a coupling efficiency of 54%.

2.4.3 Characterization results

The testing of these photonic structures was performed at PCRL with the MRR chips including the grating components. Below in **Figure 47** and **Figure 48** you can see how the light is coupled out for red and green at different angles. The target wavelength 850 nm (not visible) is coupled 90 degrees from the surface as shown in **Figure *48***.

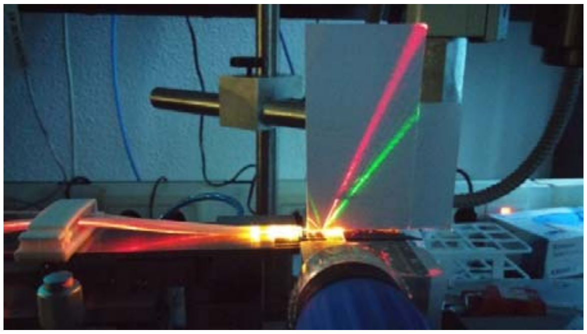

Figure 47: Setup for measuring grating output coupling.

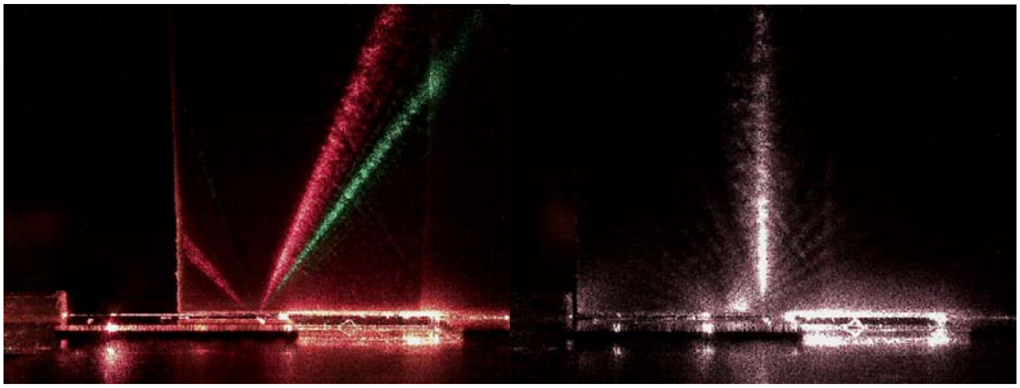

Figure 48: Left side, grating output coupling for red and green right side, grating output coupling for 850nm (VCSEL).

In figure 48 the grating output coupling is shown for red (632nm) and Green (532nm). The right picture shows the grating output for the used 850 nm VCSEL. It shows nicely that the light is transmitted perpendicular from the chip surface which results in optimal coupling when a VCSEL is mounted flat on the chip surface.

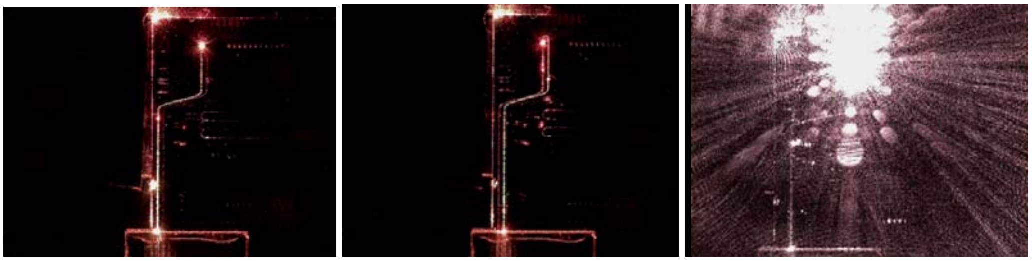

Figure 49: Top view of the grating output for both sides of the grating (left). The right picture shows it for 850 which is saturated due to the 90 degrees output of the chip directly into the camera.

Regarding the characterization of the grating coupler structures, 6 chips with grating coupler test structures have been tested. These chips contained 18 different grating designs (3 different period values, 6 different duty cycles each) and were characterized using the experimental setup seen in the figure below.

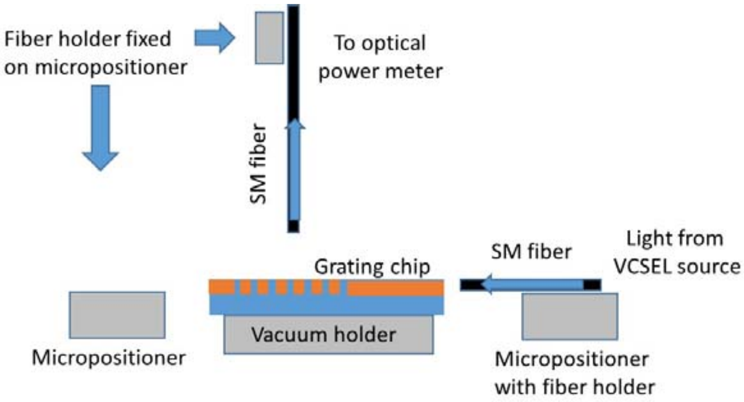

Figure 50: Experimental setup at PCRL/NTUA to characterize the grating coupler structures.

The grating chip under test was placed on a vacuum holder, ensuring that it would be fixed in position. Light from an 850 nm VCSEL source was coupled in a single mode optical fiber placed on a fiber holder on a micro-positioning stage and launched into the grating chip input waveguide using butt coupling. A second fiber holder placed also on a micro-positioning stage was configured so that another optical fiber came to the grating chip from above in a 90^o angle. A polarization controller was also used in the input fiber. The grating chips were characterized in terms of coupling efficiency and polarization dependence in three different wavelengths (854.4 nm, 854.9 nm, 855.4 nm) and two polarization states (optimal state or "good", and sub-optimal state or "bad"). The characterization results can be seen in the figures below.

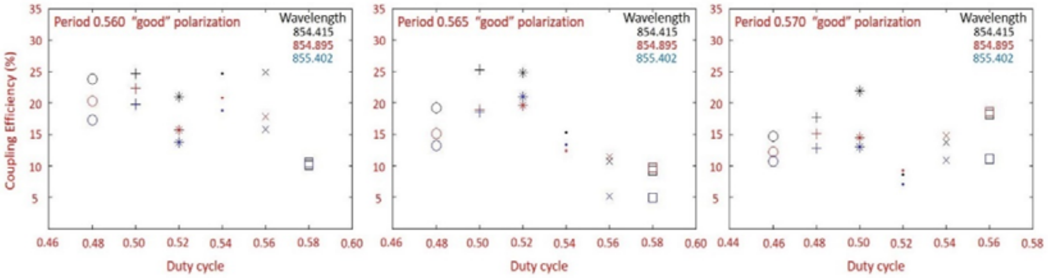

Figure 51: Grating coupler coupling efficiency for the optimum polarization for periods 0.560 (left), 0.565 (middle) and 0.570 um (right).

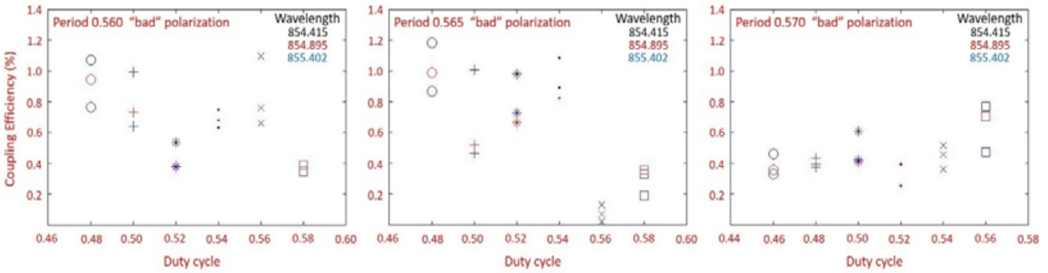

Figure 52: Grating coupler coupling efficiency for the sub-optimal polarization for periods 0.560 (left), 0.565 (middle) and 0.570 um (right).

The grating couplers achieved satisfactory coupling, which in some cases exceeded 25% when light enters with the optimal polarization state. In the sub-optimal case, the coupling efficiency is reduced significantly.

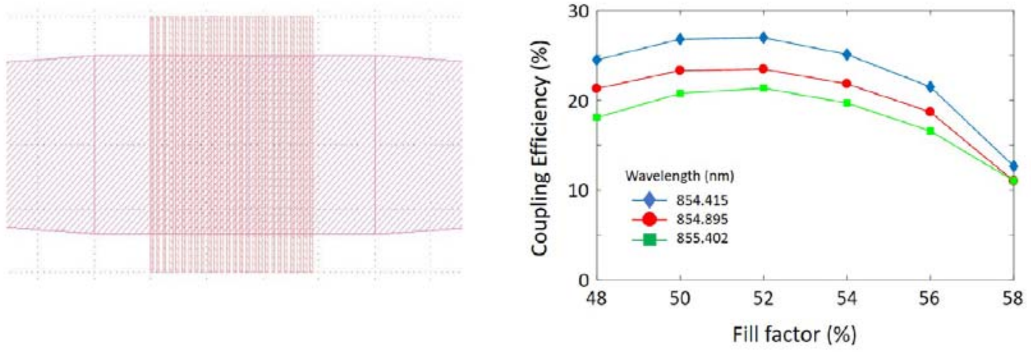

(a)

(b)

Figure 53: Mask layout of the two-port grating coupler (a), and experimental results of the grating structures' coupling efficiency with period 0.57 um and SiO$_2$ substrate with height 8.1 um, on the fill factor for three different wavelengths (b).

The upgraded “two-port” grating coupler has been also characterized. Each time, one output port was plugged in the power meter. Both output ports provided the same results which are presented in **Figure *53***. On the photonic chip, both outputs have been taken advantages, so the total usable coupling efficiency is two times the maximum value, which is presented before, achieving in that way a 54% of total coupling efficiency.

2.5 Polarization partial rotator

2.5.1 Theory

The excitation of the flip chip bonded VCSEL is a TE mode. For this reason, a TE grating coupler will be used in order to change the TE mode from vertical to horizontal and be waveguided into the photonic circuit. The characteristic that we are taking advantage of the TE mode is the evanescent tail which is able to detect any refractive index changes which take place on the top of the waveguide of the sensing MRR into the sensing window. Since it is known that the evanescence tail of TM mode is longer than the TE’s and it can lead to deeper sample probing, both modes should be present on the sensing chip. The availability of these two modes could be done with the rotation of the VCSEL by 45 degrees on the top of the waveguide. But then, it is needed a complicated structure, a dual grating coupler which couples both modes at the same time. Nevertheless, initial simulation studies show that the high performance and the coupling efficiency of this passive structure is not straightforward to achieve and not guaranteed. For that reason, a simulation study of a component which also extracts the TM from the TE mode was made. Thus, a polarization partial rotator has been studied as the theoretical component that will partially turn the TE propagation mode into a TM mode. The specific passive component had been chosen as a solution in terms of simplicity and straight forward function. By using the word ‘partial’ for its description, we want to mention that we have to take into account both TE and TM modes and extract the sensing information from both of them at the same time. In other words, both modes have to be propagated into the photonic circuit and pass through the sensing elements. This partial rotator does not have to have the best conversion efficiency, otherwise we will have only TM mode, and there is no need to have exactly 50% ratio between the two modes. Just to be present both modes. For the out-coupling of the light from the photonic circuit to the photodiodes, there will be used two different grating couplers, one for each mode as it is shown in **Figure *54***.

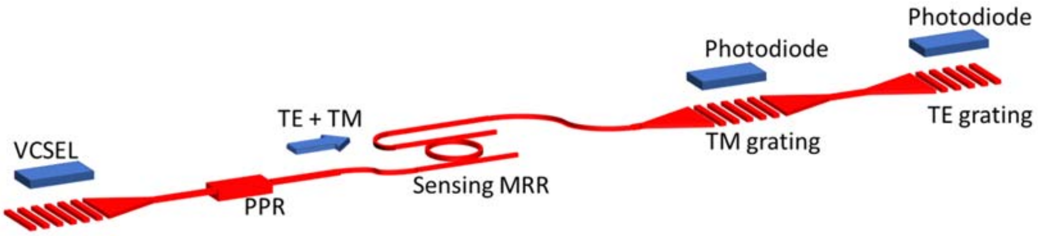

Figure 54: Schematic representation of the photonic circuit.

2.5.2 Simulation results

In ***Figure 55***, a schematic of the polarization partial rotator is presented with the parameters which are necessary for its functional operation and which have been theoretically studied during the simulations.

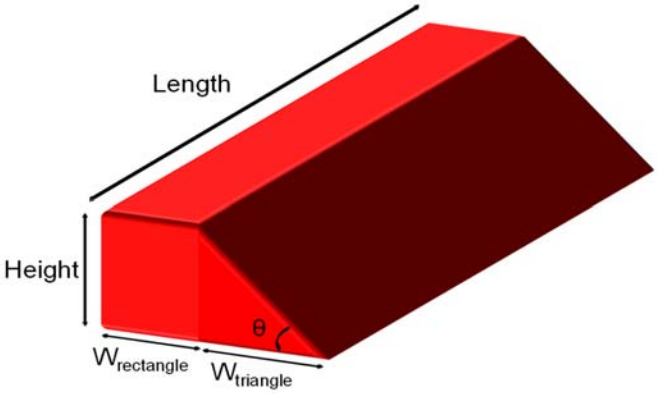

Figure 55: Schematic of the polarization partial rotator.

This polarization partial rotator employing a trapezoidal waveguide. This waveguide's topology enables the rotation of the perpendicular waveguide symmetry, which leads to indirect spatial rotation of the propagation axis causing the excitation of two hybrid modes, supporting both TE and TM polarization. The two hybrid modes beat each other along the propagation axis resulting a periodic power transfer between the TE and TM polarization. So, if the beating length is chosen properly, the state of the polarization of the input signal can be rotated from TE to TM in a preferable percentage. For the simulation study, the Rsoft and the Lumerical software have been used and specifically the Eigen Mode Expansion (EME) and the Beam Propagation Method (BPM).

The trapezoidal shape consists of a rectangle with width $W_{rectangle}$ and a triangle with base $W_{triangle}$. The sum of these two parameters remains the same in whole simulation study and equal to 1 um, as the width of the single stripe waveguide on TriPleX platform. Regarding the waveguide height, it takes values from 0.1 to 1 um. For each height value (0.1, 0.2, 0.4, 0.6, 0.8 and 1.0 um), the $W_{triangle}$ increasing from 0.2 to 1 um as well. The two hybrid modes which are supported in each waveguide structure, are characterized by different values of effective indices and thus different propagation constants and different phases between them. So, if the phase difference reaches π rad, polarization conversion is achieved when the conversion length of the rotator is given by:

$$L_{\pi} = \frac{\pi}{\beta_1 - \beta_2} \qquad (71)$$

In our case, in which we need both TE and TM modes, the proper length has to be Lπ/2. The choice of the polarization partial rotator length is being made by the Equation 71 which gives the Lπ. **Figure *56*** shows the switching between the TE and the TM mode versus the length of the rotator. It corresponds to the case of $W_{triangle}$ and height at 1 um and presents the function of the single rotator without the previous and the next part of the single stripe waveguide. If these two parts have been taken into account, due to the reflections and the non-optimal overlap between them and the rotator, the rotation efficiency will be slightly lower.

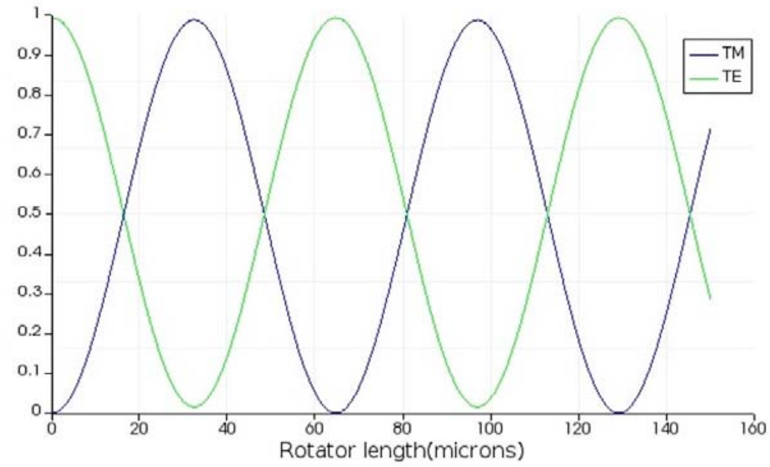

Figure 56: Rotator efficiency versus segment length.

For the perfect polarization rotation, the first hybrid mode has to be characterized by 45 degrees optical axis angle and the hybrid modes have to be equally excited by one of the polarization states, TE or TM, propagating in the input waveguide. The formula which has been used to calculate each hybrid mode optical axis is:

$$\tan\theta = R = \frac{\iint n^2(x,y)\cdot H^2x(x,y)dxdy}{\iint n^2(x,y)\cdot H^2y(x,y)dxdy} \tag{72}$$

where R is the polarization rotation parameter, n is the refractive index distribution profile and Hx and Hy are the transverse and horizontal components of the hybrid modes. In our case, the polarization rotation parameter has not had to be equal to 1, since there is no need of equal presence of the two modes, but just their presence in a sufficient way for the sensing purposes.

Figure 57 and Figure 58 show representative results of the hybrid modes called 'TE' and 'TM' for horizontal and vertical component respectively (if they supported by the structures) and the corresponding R parameter for each pair of waveguide dimensions. The complete number of graphs which corresponds to the full simulation study, are presented in the Appendix II.

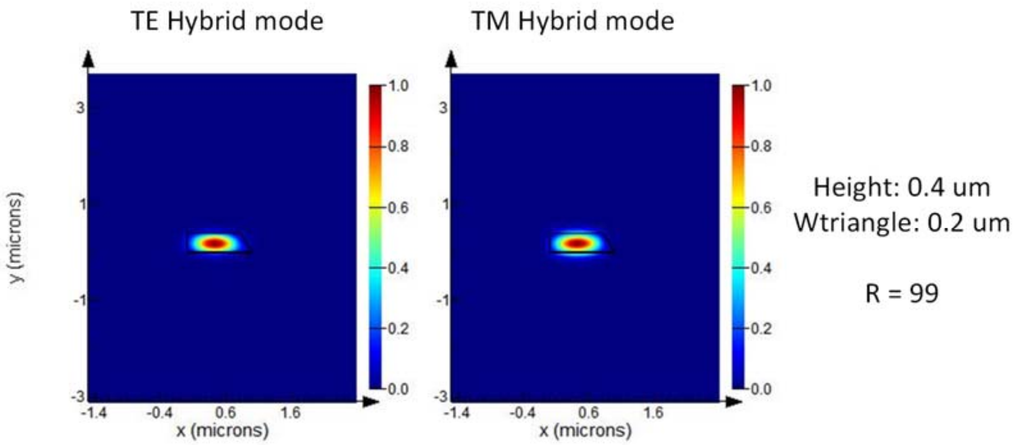

Figure 57: *Polarization partial rotator with Height= 0.4 um and W$_{triangle}$= 0.2 um.*

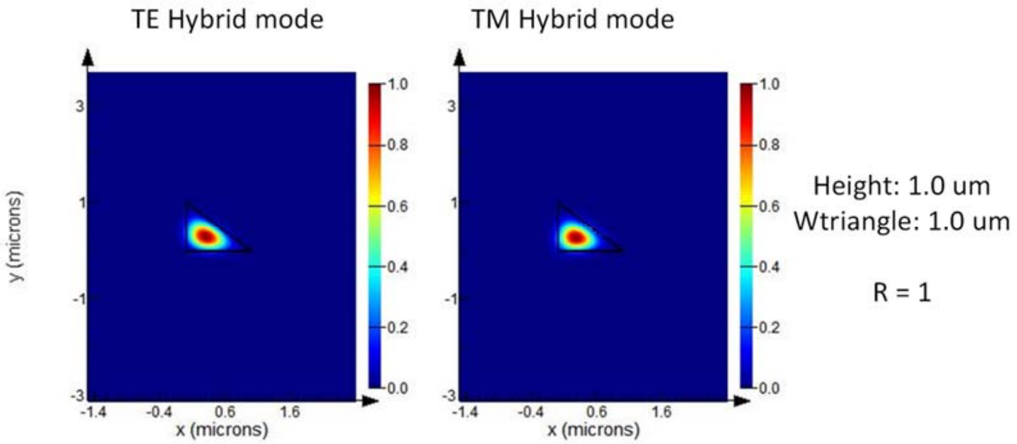

Figure 58: Polarization partial rotator with Height= 1.0 um and W$_{triangle}$= 1.0 um.

In **Figure *59***, the summarized results of the simulation study are presented. It shows the R parameter versus the width of the tringle part of the rotator for different heights.

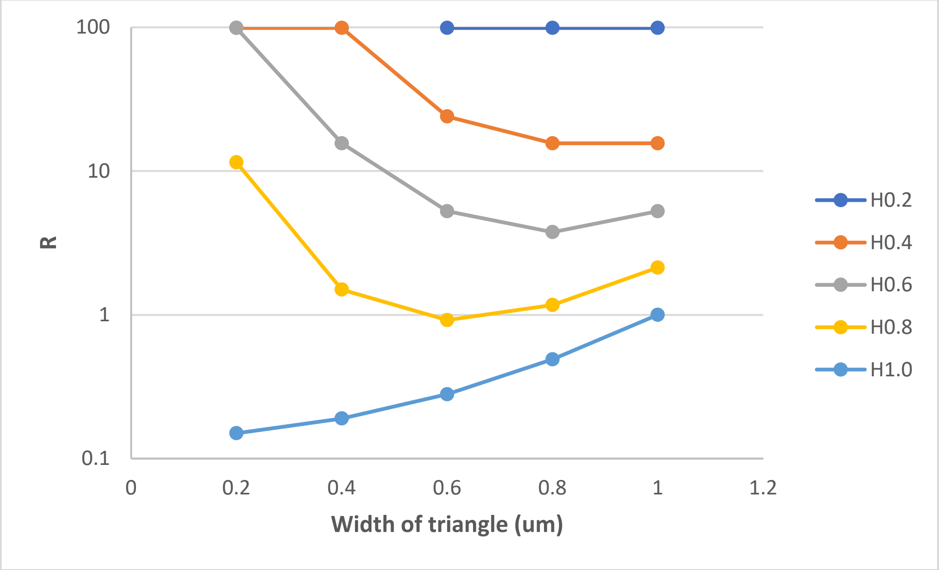

Figure 59: Polarization rotator parameter (R) values for each width and height of the triangle part of the rotator.

The polarization conversion efficiency is given by the Equation:

$$PCE = 4\sin^2\theta\cos^2\theta\sin^2\left(\frac{\pi L}{2L\pi}\right)x\ 100\% \tag{73}$$

where θ is the optical axis rotation angle (tanθ = R) and L is the actual length of the structure. As the simulation study shows, for low values of waveguide height (<0.4 um), it is not possible to rotate even partially the TE mode. The best case where we have equal rotation state for both modes, is in triangle waveguide with width and height at 1 um. As it mentioned before, for the sensing proposes of our sensor, it is acceptable to have both modes in different power values. So, for heights between 0.6 and 1 um, for any kind of widths, TE and TM mode will be present and waveguided into the circuit and able to extract the sensing information of any change which happens on the sensing MRR. Unfortunately, it is exceedingly difficult to produce the proposed Si_3N_4 layer structures by means of cleanroom processing. Especially, introduction of the steps in layer thickness, necessitates the use of a series of masks that have to be applied in successive order with very low, impracticable tolerances.

An additional simulation study for the polarization partial rotator with the height value remaining constant at 103 nm in terms of simplicity during the fabrication process has been completed without any compensatory results. The total width of the rotator in this study counted from 0.1 to 0.9 um with different ratios of the $W_{triangle}$ over the $W_{rectangle}$ for each value.

2.6 References of Chapter 2

[Jin2002] J. Jin, The Finite Element Method In Electromagnetics, 2nd Ed., John Wiley & Sons, New York, 2002.

[Link Rsoft-1] https://www.nusod.org/nusod05/MS3.pdf.

[Saitoh2002] K. Saitoh and M. Koshiba, “Full-Vectorial Imaginary-Distance Beam Propagation Method Based on a Finite Element Scheme: Application to Photonic Crystal Fibers,” *IEEE JQE,* **38-7**, p.927 (2002).

[Scarmozzino2000] R. Scarmozzino, A. Gopinath, R. Pregla and S. Helfert, "Numerical techniques for modeling guided-wave photonic devices," in IEEE Journal of Selected Topics in Quantum Electronics, vol. 6, no. 1, pp. 150-162, (2000).

[Schulz1998] D. Schulz, C. Glingener, M. Bludszuweit, and E. Voges, “Mixed Finite Element Beam Propagation Method,” *IEEE JLT*, **16-7**, p.1336 (1998).

[Koshiba1994] M. Koshiba, S. Maruyama, and K. Hirayama, “A Vector Finite Element Method with the High-Order Mixed-Interpolation-Type Triangular Elements for Optical Waveguiding Problems,” *IEEE JLT*, **12-3**, p.495 (1994).

[Tsuji2000] Y. Tsuji and M. Koshiba, “Guided-Mode and Leaky-Mode Analysis by Imaginary Distance Beam Propagation Method Based on Finite Element Scheme,” *IEEE JLT,* **18-4**, p.618 (2000).

[Tsuji1997] Y. Tsuji, M. Koshiba, and T. Shiraishi, “Finite Element Beam Propagation Method for Three-Dimensional Optical Waveguide Structures,” *IEEE JLT*, **15-9**, p. 1728 (1997).

[Koshiba2000] M. Koshiba and Y. Tsuji, “Curvilinear Hybrid Edge/Nodal Elements with Triangular Shape for Guided-Wave Problems,” *IEEE JLT,* **18-5**, p.737 (2000).

[Peterson1994] A.F. Peterson, “Vector Finite Element Formulation for Scattering from Two-Dimensional Heterogeneous Bodies,” *IEEE Trans. On Antennas and Propagation*, **43-3**, p. 357 (1994).

[Nédélec1980] J. C. Nédélec, “Mixed finite elements in R3,” *Numerische Mathematik*, **35**, p. 315 (1980).

[Greenwood1999] Greenwood and J. Jin, “A Novel Efficient Algorithm for Scattering from a Complex BOR Using Mixed Finite Elements and Cylindrical PML,” *IEEE Trans. on Antennas and Propagation,* **47-4**, p.620 (1999).

[Lee1993] J-F. Lee, M. Wilkins, and R. Mittra, “Finite-Element Analysis of Axisymmetric Cavity Resonator Using a Hybrid Edge Element Technique,” *IEEE Trans. on Microwave Theory and Techniques*, **41-11**, p. 1981 (1993).

[Feit1978] M.D. Feit and J.A. Fleck, “Light propagation in graded-index optical fibers,” *Appl. Opt*. **17**, 3990 (1978).

[Eldada1992] L. Eldada, M.N. Ruberto, R. Scarmozzino, M. Levy, and R.M. Osgood, Jr., “Laser-Fabricated Low-Loss Single-Mode Waveguiding Devices in GaAs,” *J. Lightwave Tech.* **10**, 1610 (1992).

[Levy1992] M. Levy, L. Eldada, R. Scarmozzino, R.M. Osgood, Jr., P.S.D. Lin, and F. Tong, “Fabrication of Narrow-Band Channel-Dropping Filters,” *Photon. Tech. Lett.* **4**, 1378 (1992).

[Eldada1994] L. Eldada, M.N. Ruberto, M. Levy, R. Scarmozzino, and R.M. Osgood, Jr., “Rapid Direct Fabrication of Active Electro-Optic Modulators in GaAs,” *J. Lightwave Tech.* **12**, 1588 (1994).

[Ilic1994] I. Ilic, R. Scarmozzino, R.M. Osgood, Jr., J.T. Yardley, K.W. Beeson, and M.J. McFarland, “Modeling Multimode-Input Star Couplers in Polymers,” *J. Lightwave Tech.* **12**, 996 (1994).

[Ilic1997] I. Ilic, R. Scarmozzino, R.M. Osgood, Jr., J.T. Yardley, K.W. Beeson, and M.J. McFarland, and J. Schweyen, “Photopattermed Polymer Multimode 8x8 Star Couplers: Comparative Design Methodologies and Device Measurements,” *IEICE Trans. Commun.* **E80-B** (1997).

[Link Rsoft-2] http://www.ipsi.smr.ru/Lab/CKPO/Nanofot/doc/beamprop.pdf.

[Shih1995] M.C. Shih, M. Hu, M.B. Freiler, M. Levy, R. Scarmozzino, R.M. Osgood, Jr., I.W. Tao, and W.I. Wang, “Fabrication of an InGaAs SQW Circular Ring Laser By Direct Laser Patterning,” *Appl. Phys. Lett.* **66**, 2608 (1995).

[Eldada1995] L. Eldada, R. Scarmozzino, R.M. Osgood, Jr., D.C. Scott, Y. Chang, and H.R. Fetterman, “Laser-Fabricated Delay Lines in GaAs for Optically-Steered Phased-Array Radar,” *J. Lightwave Tech.* **13**, 2034 (1995).

[Hu1998] M.H. Hu, Z. Huang, K.L. Hall, R. Scarmozzino, and R.M. Osgood, Jr., “An Integrated Two-Stage Cascaded Mach–Zehnder Device in GaAs,” *J. Lightwave Tech.* **16**, 1447 (1998).

[Hu1997] M. Hu, R. Scarmozzino, M. Levy, and R.M. Osgood, Jr., “A low-loss and compact waveguide y-branch using refractive index tapering,” *Photon. Tech. Lett.*, **9**, 203 (1997).

[Scarmozzino1997] R. Scarmozzino, R.M. Osgood, Jr., L. Eldada, J.T. Yardley, Y. Liu, J. Bristow, J. Stack, J. Rowlette, and Y.S. Liu, “Design and Fabrication of Passive Optical Components for

Multimode Parallel Optical Links," *SPIE Photonic West Meeting, San Jose, CA*, **3005**, 257 (1997).

[Hu1997-2] M. Hu, J.Z. Huang, R. Scarmozzino, M. Levy, and R.M. Osgood, Jr., "Tunable Mach-Zehnder polarization splitter using height-tapered y-branches," *Photon. Tech. Lett.* **9**, 773 (1997).

[Levy1997] D.S. Levy, Y.M. Li, R. Scarmozzino, and R.M. Osgood, Jr., "A Multimode Interference-Based Variable Power Splitter in GaAs–AlGaAs," *Photon. Tech. Lett.* **9**, 1373 (1997).

[Levy1998] D.S. Levy, R. Scarmozzino, Y.M. Li, and R.M. Osgood, Jr., "A New Design for Ultracompact Multimode Interference-Based 2x2 Couplers," *Photon. Tech. Lett.* **10**, 96 (1998).

[Huang1998-1] J. Z. Huang, M. H. Hu, J. Fujita, R. Scarmozzino, and R. M. Osgood, Jr., "High-Performance Metal-Clad Multimode Interference Devices for Low-Index-Contrast Material Systems," *Photon. Tech. Lett.* **10**, 561 (1998).

[Huang1998-2] J. Z. Huang, R. Scarmozzino, and R. M. Osgood, Jr., "A New Design Approach to Large Input/Output-Number Multimode Interference Couplers and Its Application to Low-Crosstalk WDM Routers," *Photon. Tech. Lett.* **10**, 1292 (1998).

[Levy1999] D.S. Levy, K.H. Park, R. Scarmozzino, R.M. Osgood, Jr., C. Dries, P. Studenkov, and S. Forrest, "Fabrication of ultracompact 3-dB 2x2 MMI power splitters," *Photon. Tech. Lett.* **11**, 1009 (1999).

[Ramadan1998] T.A. Ramadan, R. Scarmozzino, and R.M. Osgood, Jr., "Adiabatic Couplers: Design Rules and Optimization," *J. Lightwave Tech.* **16**, 277 (1998).

[Fujita1998] J. Fujita, M. Levy, R. Scarmozzino, R.M. Osgood, Jr., L. Eldada, and J.T. Yardley, "Integrated Multistack Waveguide Polarizer," *Photon. Tech. Lett.* **10**, 93 (1998).

[Huang2000] J. Z. Huang, R. Scarmozzino, G. Nagy, M. J. Steel and R. M. Osgood, Jr., "Realization of a compact and single-mode optical passive polarization converter," *Photon. Tech. Lett.* **12**, 317 (2000).

[Yevick1990] D. Yevick and B. Hermansson, "Efficient beam propagation techniques," *J. Quantum Electron.* **26**, 109 (1990).

[Chung1990] Y. Chung and N. Dagli, "An assessment of finite difference beam propagation method," *J. Quantum Electron* **26**, 1335 (1990).

[Scarmozzino1991] R. Scarmozzino and R.M. Osgood, Jr., "Comparison of finite-difference and Fourier-transform solutions of the parabolic wave Equation with emphasis on integrated-optics applications," *J. Opt. Soc. Amer. A* **8**, 724 (1991).

[Hadley1992] G.R. Hadley, "Transparent boundary condition for the beam propagation method", *Opt. Lett*. **16**, 624, (1991); G.R. Hadley, "Transparent boundary condition for the beam propagation method," *J. Quantum Electron* **28**, 363 (1992).

[Vassalo1996] C. Vassalo and F. Collino, "Highly efficient absorbing boundary condition for the beam propagation method," *J. Lightwave Technol.***14**, 1570 (1996).

[Huang1996] W.P. Huang, C.L. Xu, W. Lui, and K. Yokoyama, "The perfectly matched layer (PML) boundary condition for the beam propagation method," *Photon. Technol. Lett.* **8**, 649 (1996).

[Chiou1998] Y.P. Chiou and H.C. Chang, "Complementary operators' method as the absorbing boundary condition for the beam propagation method," *Photon. Technol. Lett.* **8**, 976 (1998).

[Clauberg1991] R. Clauberg and P. Von Allmen, "Vectorial beam propagation method for integrated optics," *Electron. Lett.* **27**, 654 (1991).

[Huang1993] W.P. Huang and C.L. Xu, "Simulation of three-dimensional optical waveguides by a full-vector beam propagation method," *J. Quantum Electron.* **29**, 2639 (1993).

[Yevick1989] D. Yevick and M. Glasner, "Analysis of forward wide-angle light propagation in semiconductor rib waveguides and integrated-optic structures," *Electron. Lett.* **25**, 1611 (1989).

[Hadley1992-2] G.R. Hadley, "Wide-angle beam propagation using Pade approximant operators", *Optics Letters* **17**, 1426, (1992); G.R. Hadley, "Multistep method for wide-angle beam propagation," *Optics Letters* **17**, 1743 (1992).

[Hoekstra1993] H.J.W.M. Hoekstra, G.J.M. Krijnen, and P.V. Lambeck, "New formulations of the beam propagation method based on the slowly varying envelope approximation," *Optics Communications*, **97**, 301 (1993).

[Kaczmarski1988] P. Kaczmarski and P.E. Lagasse, "Bidirectional beam propagation method," *Electron. Lett.* **24**, 675 (1988).

[Chung1992] Y. Chung and N. Dagli, "Modeling of guided-wave optical components with efficient finite-difference beam propagation methods," *Tech. Dig. IEEE AP-S Int. Symp., 1992* **1**, 248 (1992).

[Chiou1997] Y. Chiou and H. Chang, "Analysis of optical waveguide discontinuities using the Pade approximants," *Photon. Technol. Lett.* **9**, 964 (1997).

[Rao1999] H. Rao, R. Scarmozzino, and R.M. Osgood, Jr., "A bidirectional beam propagation method for multiple dielectric interfaces," *Photon. Technol. Lett.* **11**,830 (1999).

[Xu1994] C.L. Xu, W.P. Huang, J. Chrostowski, and S.K. Chaudhuri, “A full-vectorial beam propagation method for anisotropic waveguides,” *J. Lightwave Tech.* **12**, 1926 (1994).

[Feit1980] M.D. Feit and J.A. Fleck, “Computation of mode properties in optical fiber waveguides by a propagating beam method,” *Applied Optics*, **19**, 1154 (1980).

[Jungling1994] S. Jungling and J.C. Chen, “A study and optimization of eigenmode calculations using the imaginary-distance beam-propagation method,” *J. Quantum Electron.* **30**, 2098 (1994).

[Yevick1992] D. Yevick and Witold Bardyszewski, “Correspondence of variational finite-difference (relaxation) and imaginary-distance propagation methods for modal analysis,” *Opt. Lett.* **17**, 329 (1992).

[Hadley1995] G.R. Hadley and R.E. Smith, “Full-vector waveguide modeling using an iterative finite-difference method with transparent boundary conditions,” *J. Quantum Electron.* (1995).

[Chen1994] J.C. Chen and S. Jungling, “Computation of higher-order waveguide modes by the imaginary-distance beam propagation method,” *Optical and Quantum Electron.* **26**, S199 (1994).

[Berenger1994] J.P. Berenger, “A Perfectly Matched Layer for the Absorption of Electromagnetic waves,” J. *Comput. Phys.*, **114**, 185 (1994)

[Yee1996] K.S. Yee, “Numerical solution of initial boundary value problems involving Maxwell’s Equations in isotropic media,” IEEE Trans. Antennas Propagat., **AP-14**, 302 (1966).

[Worhoff2015] K. Wörhoff, R. G. Heideman, A. Leinse and M. Hoekman, “TriPleX: a versatile dielectric photonic platform,” Review article, Adv. Opt. Techn. 2015; 4(2): 189–207.

[Link Rsoft-3] http://www.ipsi.smr.ru/Lab/CKPO/Nanofot/doc/fullwave.pdf.

[Heideman2006] R. G. Heideman and J. A. Walker, in ‘Proc. SPIE Vol. 6125’, (SPIE, Photonics West, San Jose, 2006) paper 021.

[Morichetti2007] F. Morichetti, A. Melloni, M. Martinelli, R. G. Heideman, A. Leinse, et al., J. Lightwave Technol. 25, 2579 (2007).

[Heideman2009] R. G. Heideman, A. Leinse, W. Hoving, R. Dekker, D. H. Geuzebroek, et al., in ‘Proc. SPIE Vol. 7221’, (2009) pp. 72210R1.

[Heideman2007] R. G. Heideman, D. Geuzebroek, A. Leinse, A. Melloni, F. Morichetti, et al., in ‘Proc. ECIO’, Copenhagen, April 25–27, 2007) invited paper WB0.

[Hoving2008] W. Hoving, D. Geuzebroek and R. Heideman, SPIE Newsroom 2008. http://www.spie.org/x25303.xml?pf=true&highlight=x2414.

[Heideman2012] R. G. Heideman, M. Hoekman and E. Schreuder, IEEE J. Sel. Top. Quant. 18, 1583 (2012).

[Heideman2005] R. G. Heideman, A. Melloni, M. Hoekman, A. Borreman, A. Leinse, et al., in ‘Proc. IEEE/LEOS Benelux Ann. Symp.’, (IEEE, Mons, December 1–2, 2005), pp. 71–74.

[Marpaung2010] D. A. I. Marpaung, C. G. H. Roeloffzen, A. Leinse and M. Hoekman, Opt. Express 18, 27359 (2010).

[Yurtseve2014] G. Yurtsever, B. Považay, A. Alex, B. Zabihian, W. Drexler, et al., Biomedical Opt. Express 5, 1050 (2014).

[Zhuang,2011] L. Zhuang, D. Marpaung, M. Burla, W. Beeker, A. Leinse, et al., Opt. Express 19, 23162 (2011).

[Spencer2014] D. T. Spencer, M. J. R. Heck, R. Moreira, J. Bovington, J. E. Bowers, et al., in ‘Proc. OFC’, (OSA, San Francisco, March 9–14, 2014) paper Th1A.

[Bauters2011-1] J. F. Bauters, M. J. R. Heck, D. John, D. Dai, M. C. Tien, et al., Opt. Express 19, 3163 (2011).

[Dai2010] D. Dai, Z. Wang, J. F. Bauters, M. C. Tien, M. Heck, et al. Bowers, in ‘Proc. GFP’, (IEEE, Bejing, September 1–3, 2010) , P2.13.

[Bauters2013] J. F. Bauters, M. J. R. Heck, D. Dai, J. S. Barton, D. J. Blumenthal, et al., IEEE Photonics J. 5, 6600207 (2013).

[Bauters2011-2] J. F. Bauters, M. J. R. Heck, D. D. John, J. S. Barton, C. M. Bruinink, et al., Opt. Express 19, 24090 (2011).

[Bauters2011-3] J. F. Bauters, M. J. R. Heck, D. D. John, M.-C. Tien, W. Li, et al., in ‘Proc. ECOC’, (OSA, Geneva, September 18–22, 2011) paper Th12.3.

[Epping2015] J. P. Epping, M. Hoekman, R. Mateman, A. Leinse, R. G. Heideman, et al., Opt. Express 23, 643 (2015).

[Soldano1994] L. B. Soldano, “Multimode interference couplers design and applications,” Delft, 1994.

[Gounaridis2015] L. Gounaridis, P. Groumas, E. Schreuder, R. Heideman, V. Katopodis, C. Kouloumentas, H. Avramopoulos, “Design of grating couplers and MMI couplers on the TriPleX platform enabling ultra-compact photonic-based biosensors,” Sensors and Actuators B: Chemical, Volume 209, 2015.

[Gounaridis2019] L. Gounaridis, P. Groumas, E. Schreuder, C. Tsokos, E. Mylonas, A. Raptakis, R. Heideman, H. Avramopoulos, C. Kouloumentas, “Design of ultra-compact multimode interference (MMI) couplers and high efficiency grating couplers in TriPleX platform as part of a photonic-based sensor,” Proc. SPIE 10921, Integrated Optics: Devices, Materials, and Technologies XXIII, 1092127 (4 March 2019).

[Talbot1836] H. F. Talbot et al., “Facts relating to optical science No IV,” The London and Edinburgh Philosophical Magazine and Journal of Science, vol 9, pp. 401-407, December 1836, Third series.

[Marcuse1972] D. Marcuse, “Light Transmission Optics,” New York, Van Nostrand Reinhold, 1972.

[Ulrich1975-1] R. Ulrich, “Image formation by phase coincidences in optical waveguides,” Optics Communications, vol 13, no. 5, pp. 259-264, 1975.

[Ulrich1975-2] R. Ulrich, “Light propagation and imaging in planar optical waveguides,” Nouv. Rev. Optique, vol 6, no. 5, pp. 253-262, 1975.

[Ulrich1975-3] R. Ulrich and G. Ankele, “Self-imaging in homogeneous planar optical waveguides,” Appl. Phys. Letter., vol 27, no. 6, pp. 337-339, 1975.

[Simon1977] A. Simon and R. Ulrich, “Fiber optical interferometer,” Appl. Phys. Lett., vol 31, no. 2, pp. 77-79, 1977.

[Weinert1994] C. M. Weinert and N. Agrawal, “Three-dimensional simulation of multimode interference devices,” in Proc. Integrated Photonics Research Topical Meeting (IPRC), San Francisco, 1994.

[Kapany1972] N. S. Kapany and J. J. Burke, “Optical waveguides,” New York, Academic Press, 1972.

[Villasante2010] O. G. de Villasante, “Design and simulation of vertical grating coupler for photonic integrated system in package,” Master thesis, Berlin, 2010.

[Taillaert2004] D. Taillaert, “Grating couplers as Interface between Optical Fibres and Nanophotonic Waveguides,” Ghent University, PhD Thesis, June 2004.

[Galan2008] J. V. Galan, P. Sanchis, J. Blasco, and J. Marti, “Study of High Efficiency Grating Couplers for Silicon-Based Horizontal Slot Waveguides,” IEEE Photonics Technology Letters, Vol. 20, no. 12, pp.985-987, June 2008.

[Laurent2006] Laurent Vivien, Daniel Pascal, Sebastien Lardenois, Delphine Marris-Morini, Eric Cassan, Frédéric Grillot, Suzanne Laval, Jean-Marc Fédéli, and Loubna El Melhaoui, “Light Injection in SOI Microwaveguides Using High-Efficiency Grating Couplers,” Journal Of Lightwave Technology, Vol. 24, no. 10, pp.3810-3815, October 2006

[Tsuchizawa2005] T. Tsuchizawa, K. Yamada, H. Fukuda, T. Watanabe, J. Takahashi, M. Takahashi, T. Shoji, E. Tamechika, S. Itabashi and H. Morita, “Microphotonics Devices Based on Silicon Microfabrication Technology,” IEEE Journal Of Selected Topics In Quantum Electronics, Vol. 11, no. 1, pp.232-240, January/February 2005.

Chapter 3. Algorithm: The Fast Fourier Transform method

In this chapter, the method that was developed for the accurate estimation of the wavelength shift due to the refractive index change on the sensing surface of the MRR-based chips, is in detail exhibited. More specifically, in the first part, the theory of the MMR photonic structures is presented. In the second part, the modelling and the performance quantification of MRR-based sensors is described. The simulation studies compared the FFT method over the peak search method and have proved that the ultra-high Q-factor resonators are not necessary to achieve low detection limits. The FFT method performs better for moderate Q-factor resonators which require relaxed fabrication tolerances. In part three, the core of the Fast Fourier Transform (FFT) algorithm is presented. Moreover, simulation studies were carried out to cover the effect of the amplitude and the spectral noise, the number of resonance peaks inside the wavelength scanning window, the effect of the power dependence of the tunable laser source on the wavelength, the effect of the position of the transfer functions inside the scanning window. The main conclusions are that the presence of additional peaks in the processed window can average out the noise and improve accuracy in a noisy environment, the FFT method is very tolerant even when there is power dependence of the wavelength, the position of the transfer function inside the scanning window should be position in such a way that the signal power at the edge of the window is minimal to avoid asymmetries in the periodic signal assumption of the method.

3.1 Microring Resonators Theory – Basic MRR structures

In general, a ring resonator consists of a looped optical waveguide and a coupling mechanism to access the loop. When the waves in the loop build up a round trip phase shift that equals an integer times 2π, the waves interfere constructively, and the cavity is in resonance. Two main forms are presented in the following paragraphs, the all-pass and the add-drop concept.

3.1.1 All-pass MRR

A simple ring resonator is created by taking one output of a generic directional coupler and feeding it back into the input. Such a device exhibits a periodic cavity resonance when light traversing the ring acquires a phase shift corresponding to an integer multiple of 2π radians. The resonator is mathematically formulated from two components: a coupling strength and a feedback path.

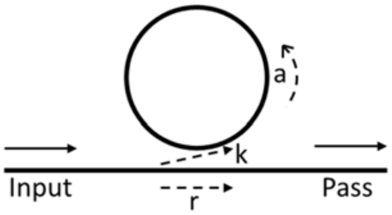

Figure 60: All-pass filter (APF).

The basic spectral properties of an all-pass ring resonator can easily be derived by assuming continuous wave (CW) operation and matching fields. Under the assumption that reflections back into the bus waveguide are negligible, the ratio of the transmitted and incident field in the bus waveguide as can be written as:

$$\frac{E_{pass}}{E_{input}} = e^{i(\pi+\varphi)} \frac{a - re^{-i\varphi}}{1 - rae^{i\varphi}} \tag{74}$$

$\Phi=\beta L$ is the single-pass phase shift, with L the round-trip length and β the propagation constant of the circulating mode. a is the single-pass amplitude transmission, including both propagation loss in the ring and loss in the couplers. It relates to the power attenuation coefficient α [1/cm] as a^2 =exp(-αL). By squaring Equation 74, we obtain the intensity transmission T_n:

$$T_n = \frac{I_{pass}}{I_{input}} = \frac{a^2 - 2ra\cos(\varphi) + r^2}{1 - 2ar\cos(\varphi) + (ra)^2} \tag{75}$$

r is the self-coupling coefficient. Similarly, k can be defined as the cross-coupling coefficient, and so r^2 and k^2 are the power splitting ratios of the coupler, and they are assumed to satisfy $r^2 + k^2 = 1$, which means there are no losses in the coupling section. This assumption can introduce a small error on the transmission power levels. The width of the resonance remains correct, if the losses that are introduced by the couplers are included in the resonator round trip loss coefficient a.

We find the ring to be on resonance when the phase ϕ is a multiple of 2π, or when the wavelength of the light fits a whole number of times inside the optical length of the ring.

For ideal cavities with zero attenuation, a = 1, the transmission is unity for all values of detuning ϕ. Under critical coupling, when the coupled power is equal to the power loss in the ring $1-a^2 = k^2$ or r = a, the transmission at resonance drops to zero. The phase argument of the field transmission varies periodically with frequency. All-pass resonators delay incoming signals via the temporary storage of optical energy within the resonator.

From Equation 74 we can also calculate the effective phase shift φ induced by the ring resonator.

$$\varphi = \pi + \varphi + \arctan\frac{r\sin(\varphi)}{a - r\cos(\varphi)} + \arctan\frac{ra\sin(\varphi)}{1 - ra\cos(\varphi)} \tag{76}$$

3.1.2 Add-drop MRR

The direct waveguide analogy of a free space Fabry-Perot is obtained by adding a second guide that side couples to the resonator as in the next figure. Because this configuration behaves as a narrow-band amplitude filter that can add or drop a frequency band from an incoming signal, it is commonly termed an add-drop filter. Because this configuration is mathematically equivalent to the extensively studied classic Fabry-Perot interferometer, the Equations from transmission coefficients are simply stated: the intensity throughput coefficient corresponding to light bypassing the lower excitation waveguide is presented in the Equation 77. This corresponds to a transmitted signal modified such that a narrow frequency band has been extracted. The extracted band exists at the drop port with transmission coefficient is presented again in Equation 78.

Although there are similar enhancements as in the all-pass resonator in the effective phase shifts at the two ports, they are intermingled with the dominant amplitude effects. Hence, although the phase response should not be ignored, it is rarely implemented for its phase properties.

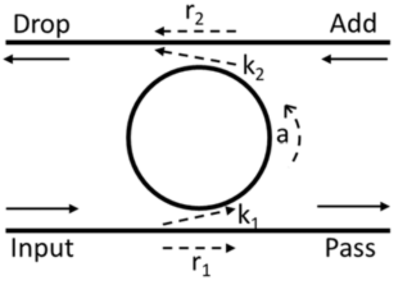

Figure 61: Add-drop filter.

$$T_p = \frac{I_{pass}}{I_{input}} = \frac{r_2^2 a^2 - 2 r_1 r_2 a \cos(\varphi) + r_1^2}{1 - 2 r_1 r_2 a \cos(\varphi) + (r_1 r_2 a)^2} \tag{77}$$

$$T_d = \frac{I_{drop}}{I_{input}} = \frac{(1 - r_1^2)(1 - r_2^2) a}{1 - 2 r_1 r_2 a \cos(\varphi) + (r_1 r_2 a)^2} \tag{78}$$

3.2 Model and performance quantification of Micro-Ring Resonator (MRR) sensors

3.2.1 Operating principle of micro-ring resonators and model structure for sensing applications

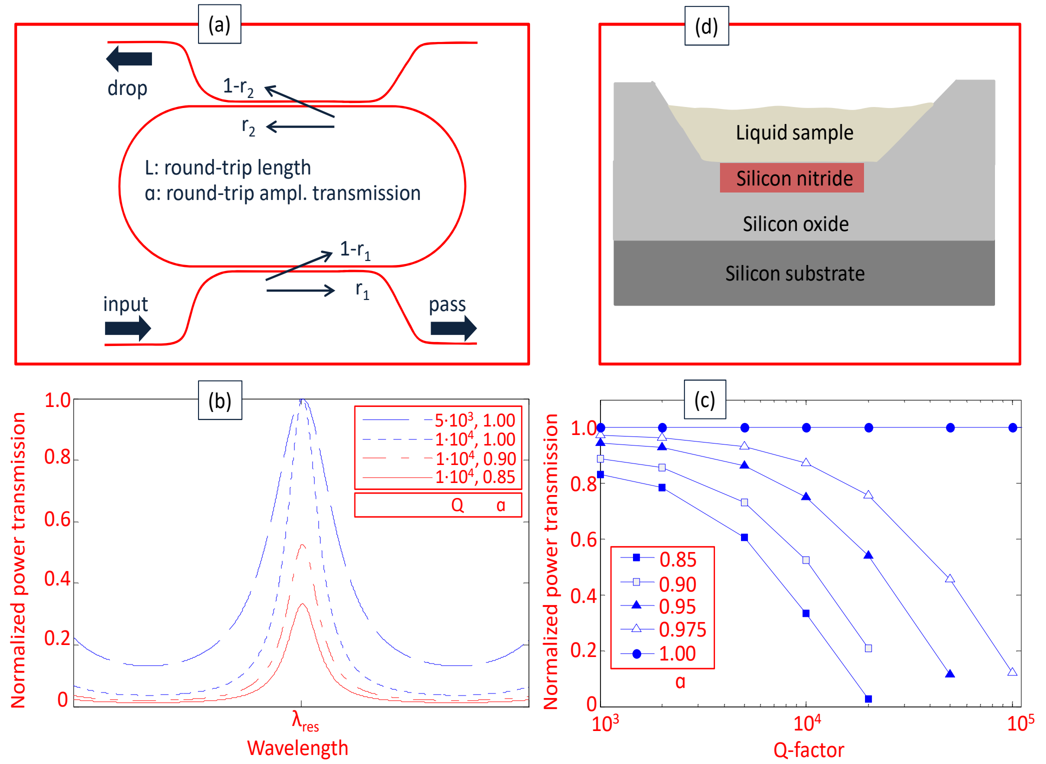

Figure 62: Layout of a typical MRR (a), indicative transfer functions at drop port for different Q-factors and round-trip amplitude transmission coefficients α (b), optical power transmission at resonance as a function of Q-factor and α (c) and structure of the reference MRR in this work based on the TriPleX platform (d).

Figure *62*(a) presents the layout of an add-drop MRR that serves as the reference cavity in our study. Its operating principle and its main design parameters have been previously described in [Bogaerts2012]. When light comes from the input port, it is coupled to the looped waveguide of the MRR and finds its way out of it through the pass and the drop ports of the element. The transmission of optical power at the two ports is a function of the self-coupling coefficients $r_1$and r_2 at the two couplers, the round-trip amplitude transmission α that depends on the propagation loss inside the MRR and the loss at the two couplers, and the round-trip phase ϕ that is accumulated inside the MRR. At the drop port, this transfer function is given by [Bogaerts2012]:

$$T_d(\varphi) = \frac{(1-r_1^2)\cdot(1-r_2^2)\cdot a}{1-2r_1\cdot r_2\cdot a\cdot\cos(\varphi)+(r_1\cdot r_2\cdot a)^2} \tag{79}$$

The same Equation can be also expressed as a function of the operating wavelength λ:

$$T_d(\lambda) = \frac{(1-r_1^2)\cdot(1-r_2^2)\cdot a}{1-2r_1\cdot r_2\cdot a\cdot\cos(\dfrac{2\pi\cdot n_{eff}\cdot L}{\lambda})+(r_1\cdot r_2\cdot a)^2} \tag{80}$$

where n_{eff} is the effective index of the propagating mode and L the physical length of the MRR. When ϕ is a multiple of 2π, the cavity is at resonance and the waves inside the MRR interfere constructively at the drop port. The wavelengths in this case fit to the optical length of the MRR by an integer number of times and can be calculated as follows:

$$\lambda_{res} = \frac{n_{eff} \cdot L}{m},\ m = 1,2,3,\ldots \tag{81}$$

Using a first order approximation of the dispersion, the free spectral range (FSR) of the MRR that describes the spectral distance between successive resonances in the vicinity of a wavelength λ_0 is given by:

$$FSR = \frac{\lambda_0^2}{n_g \cdot L} \tag{82}$$

In this relation, n_g is the group index of the propagating mode that is associated in turn with the effective index and the derivative of the effective index at λ_0 as follows:

$$n_g = n_{eff} - \lambda_0 \frac{dn_{eff}}{d\lambda} \tag{83}$$

Finally, the sharpness of the resonance is described by the full width at half maximum (FWHM) of the resonance spectrum and to our specific interest in this work by the Q-factor of the MRR. The two quantities are related to each other and can be derived by the following relations:

$$FWHM = \frac{(1 - r_1 \cdot r_2 \cdot a) \cdot \lambda_{res}^2}{\pi \cdot n_g \cdot L \cdot \sqrt{r_1 \cdot r_2 \cdot a}} \tag{84}$$

$$\mathrm{Q-factor} = \frac{\lambda_{res}}{FWHM} = \frac{\pi \cdot n_g \cdot L \cdot \sqrt{r_1 \cdot r_2 \cdot a}}{\lambda_{res} \cdot (1 - r_1 \cdot r_2 \cdot a)} \tag{85}$$

Figure *62*(b) presents an indicative set of transfer functions at the drop port for MRR designs with different Q-factors and amplitude transmission coefficients. **Figure *62***(c) encodes the information from a larger set of curves and reveals that the normalized transmission at the resonance is unity for ideal MRRs (α=1), but it drops for real life elements (α<1). This drop is relatively slow for low Q-factor MRRs, but much quicker for higher Q-factor designs.

Finally, **Figure 62**(d) presents the cross-section of the waveguiding structure for the modeling of the sensing MRRs in this work. It is based on the TriPleX platform [Heideman2012, Leinse2013], which combines a thin silicon nitride strip as the waveguide core and surrounding silicon oxide layers as the cladding. In the location of the MRRs on the optical chip, the upper silicon oxide layer is removed making the surface of the strip accessible to the liquid biochemical samples. Depending on the application and the employed biochemical technique, the target molecules can get close to this surface or be truly captured on this surface resulting in either case in a local change of the refractive index in the upper cladding of the MRR. This change is sensed by the evanescent field of the propagating mode and modifies its effective index. This modification can then be quantified through the measurement of the MRR resonance shift.

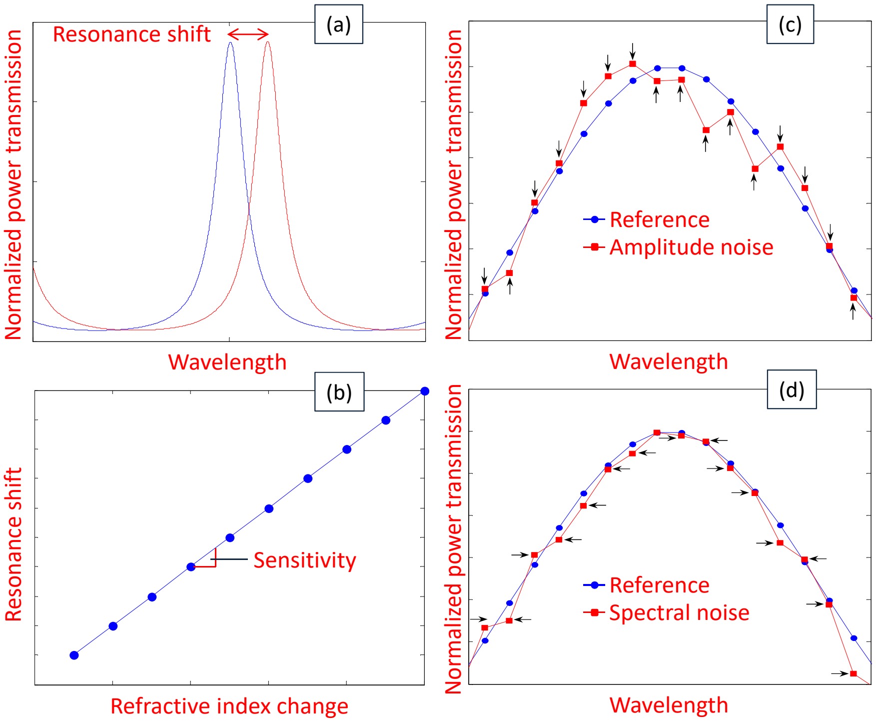

Figure 63: Qualitative representation of the resonance shift at drop port (a), method for estimating the system sensitivity based on resonance shift measurements (b). Zoom inside the resonance spectrum of the transfer function and representation of the effect of the amplitude noise (c), and the spectral noise (d).

3.2.2 Performance evaluation of MRR sensors and model of measurement noise factors

The methodology described in [White2008] for the performance quantification of the MRR sensors is followed in this work. The main criterion is the detection limit DL, which is defined as the minimum refractive index change that can be reliably detected by the system in the upper cladding of the MRR. Depending on the size of the target molecules and the way, in which they are captured near the surface of the MRR, the DL can be translated into the minimum quantity of the molecules that can be detected and quantified. As mentioned, the DL is associated with the resolution R and the sensitivity S of the system through the relation:

$$\mathrm{DL} = \frac{R}{S} \tag{86}$$

The sensitivity describes the level of the resonance shift per RIU change. As shown in **Figure *63***(a) and **Figure *63***(b), it can be measured as the slope of the general trend in a diagram with multiple resonance shift measurements that have been made for known levels of refractive index change [White2008, Barrios2007]. For all types of cavities, the sensitivity depends on the level of interaction between the optical wave and the sample. For MRRs in general and TriPleX MRRs in specific, this interaction is moderate and results in moderate sensitivity levels (100 nm/RIU). The resolution on the other hand describes the minimum resonance shift that is detectable by the system using the wavelength scanning process. Ideally, it is an infinitely small number, but in reality, it has specific limitations originating from the amplitude, spectral and temperature noise of the measurement system, as well as from the intrinsic limitations of the method that is used for the processing of the measurement data. Without considering the processing method at this point, the resolution can be established as the 3σ standard deviation of the measured resonance position $3\sigma_{meas-n}$, which represents the total measurement noise:

$$3\sigma_{meas-n} = 3 \cdot \sqrt{\sigma_{ampl-n}^2 + \sigma_{spect-n}^2 + \sigma_{temp-n}^2} \tag{87}$$

In this Equation σ_{ampl-n}, $\sigma_{spect-n}$ and σ_{temp-n} represent the individual contributions to the measurement noise due to the amplitude, spectral and temperature noise, respectively. **Figure *63***(c) and **Figure *63***(d) zooms inside the resonance spectrum of a typical transfer function and show the way, in which the amplitude and the spectral noise contribute to errors in determining the spectral position of the resonance. The amplitude noise is added to the signal affecting only the vertical position of each sample. It relates to the relative intensity noise of the scanning laser, the photodetector noise and the quantization error in the read-out unit of the system [White2008]. For typical systems with relatively low levels of optical power incident at the photodetector, the shot noise appears to dominate [Misiakos2014, Agrawal2002]. The amplitude noise of each sample can be produced in this case by a Poisson process, which is very well approximated by the normal distribution [Agrawal2002]. The Equations that determine the standard deviation (σ_{shot-n}) of this distribution and describe the relation between this standard deviation and the SNR are as follows:

$$\sigma_{shot-n} = \sqrt{2 \cdot q \cdot (R \cdot P) \cdot \Delta f} \tag{88}$$

$$SNR = \frac{(R \cdot P)^2}{\sigma_{shot-n}^2} \tag{89}$$

where q is the elementary charge, R the responsivity of the photodetector, P the incident optical power on the photodetector, and Δf the electrical bandwidth of the photodetector.

The look of the spectral noise on the transfer function is remarkably similar to the look of the amplitude noise as evident in **Figure *63***(d), but the perturbation in this case relates to the horizontal position of each sample along the wavelength axis. The statistical properties of the spectral noise vary among the different systems and depend on the type, accuracy and stability of the wavelength tuning mechanism of the laser. However, for moderate scanning steps Δλ that are much larger than the laser linewidth, it is reasonable to expect that the wavelength allocation of each sample follows again a normal distribution around its nominal value. Finally, the temperature noise relates to fluctuations of the ambient temperature that change the refractive index of the core and cladding material of the MRR via the thermo-optic effect. These changes affect the effective index of the propagating mode and result in random resonance shifts that are added to the actual signal of the sensor. Provided that the scan duration is reasonably low (on the order of a second or lower), the temperature noise affects the total of the transfer function samples in a homogeneous way and corresponds to a measurement offset, which should be either prevented or taken into account during the measurement. Efforts to this direction include the development of athermal MRRs [Han2007, Djordjevic2013], the incorporation of active temperature control, and the use of reference MRRs on the chip for the identification of the temperature-induced offset by means of differential measurements [Heideman2012, Zhu2007].

Within this context, the peak-search is the simplest and fastest method for the localization of the resonance peak and the estimation of the resonance shift, but it is not the most effective one. Even in the absence of any type of noise in the measurement system, the method has a fundamental resolution limit related to the wavelength scanning step as follows:

$$R_{\text{limit}} = \frac{\Delta\lambda}{2} \tag{90}$$

In the presence of spectral or amplitude noise, the resolution is further degraded with fast increasing number of peak localization errors for increasing level of noise. The resolution can improve with very high Q-factor cavities and small scanning steps [White2008], but only at the expense of exceptionally expensive and impractical systems. The use of Lorentzian fitting can improve the performance of the peak-search method and provide good tolerance to measurement noise. The price that someone has to pay is the increase in the computation time, which can be significant and can challenge a real-time implementation of the method with high scanning frequency [Lamberti2014]. On the other hand, the requirement for ultra-short scanning steps remains very strong, as the estimation of the resonance shift can be very far from the true value, when the scanning step Δλ is not sufficiently short. This effect is well known for all peak-search method variants as peak locking effect [Lamberti2014, Gui2002].

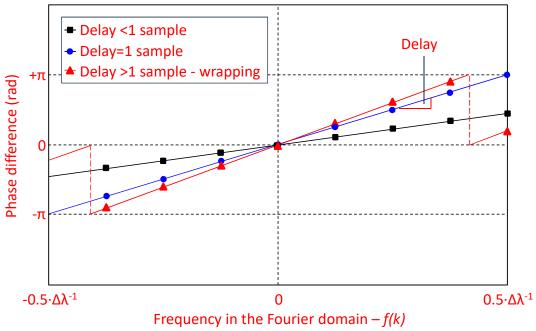

Figure 64: Phase difference between the Fourier transforms of two transfer functions T_{d1} and T_{d2} in the case of delay between these functions that is shorter than one sample, exactly equal to one sample and longer than one sample. In the last case the curve wraps around the [-π+π] range. The delay can be calculated in principle from the slope of each curve.

3.3 The Fast Fourier Transform method for the estimation of the resonant shift

The method that has been investigated in this thesis uses the FFT for the estimation of the relative delay between two identical waveforms. It is based on the well-known property of the Fourier transform that translates any delay between two functions in the time domain into a phase difference between the Fourier transforms in the frequency domain. Hence, if it is possible to precisely estimate this phase difference, it is also possible to go back and estimate the delay. This property is not limited only to functions of time, but concerns any physical function including to our interest in this work the optical transmission at the drop port $T_d(\lambda)$ against the wavelength. In this case, the delay in the "time domain" between two functions $T_{d1}(\lambda)$ and $T_{d2}(\lambda)$ directly translates to the wanted resonance shift.

In more detail, the method takes two sampled functions $T_{d1}(\lambda_j)$ and $T_{d2}(\lambda_j)$ from two independent scans of the spectral window assuming that the scans have been performed with the same number of samples N and the same wavelength vector λ_j, and that the signals are cyclic and already in steady state. The FFTs of the two transfer functions are computed as:

$$\mathbb{F}_1(f_k) = \sum_{j=1}^{N} T_{d1}(\lambda_j) \cdot e^{-\frac{2\pi i}{N}(j-1)\cdot(k-1)} \tag{91}$$

$$\mathbb{F}_2(f_k) = \sum_{j=1}^{N} T_{d2}(\lambda_j) \cdot e^{-\frac{2\pi i}{N}(j-1)\cdot(k-1)} \tag{92}$$

where k=1…N. The phase difference $\phi\{F_1(f_k)\}-\phi\{F_2(f_k)\}$ between the two FFTs depends on f_k and evolves linearly along the frequency axis in the Fourier domain, as shown in **Figure *64***. The delay in the "time domain" can then be calculated as the rate of this evolution or equivalently as the slope of the linear curve. When the delay is shorter than one sample (i.e., the resonance shift is shorter than the scanning step Δλ), the phase difference remains confined within the [–π +π] range. When it is equal to one sample the phase difference becomes π at the highest frequency in the Fourier domain, which is in our case equal to 0.5·Δλ-1. Finally, when the delay is longer than one sample, the phase difference wraps around the [–π +π] range creating ambiguity. In all cases, a good estimation of the delay can be made by calculating the local slope at each point of the phase difference curve, and by taking the median value of these local slopes [Lamberti2014]. An alternative method that we follow in this work and can safely remove the ambiguity of the wrapping comprises two discrete steps [Nentwig2011]. In the first step, we calculate the coarse part of the delay, which equals to the integer number of samples n that resides closer to it. For example, for delay of 5.3 samples, the coarse part is 5 samples. The calculation is based on the maximization of the cross-correlation of the two transfer functions, which is defined as:

$$T_{d1}(\lambda_j) * T_{d2}(\lambda_j) = \mathbb{F}^{-1}\{\mathbb{F}_1(\mathrm{f}_k)\cdot\mathbb{F}_2{}^{*}(\mathrm{f}_k)\} = \mathbb{F}^{-1}\{U(f_k)\} \tag{93}$$

where F^{-1} is the inverse Fourier transform, and the asterisks in the left and the middle part of the Equation indicate the cross-correlation and the complex conjugate, respectively. It is also noted that the phase of $U(f_k)$ is by definition the same as the difference $\phi\{F_1(f_k)\}-\phi\{F_2(f_k)\}$ between the FFTs of the two transfer functions, and thus it can be used for the calculation of the delay. In order to cancel out the effect of the coarse part and get rid of the ambiguity of the phase wrapping, we rotate the phase of $U(f_k)$ by the opposite of the phase that corresponds to this coarse part using the following relation:

$$U_{rotated}(f_k) = U(f_k)\cdot e^{-j\cdot 2\pi\cdot n\cdot \widehat{f_k}} \tag{94}$$

where f_k is the normalized frequency of each frequency bin within the [-0.5 +0.5] range. After this rotation, the phase of $U_{rotated}(f_k)$ remains confined within the [–π +π] range along the frequency axis and can be used in the second step of the method for the calculation of the remaining delay (0.3 samples in our example) using a simple linear regression method. It is also noted that in order to take into account the power level in the different frequency bins, and thus the different importance of the phase along the frequency axis, the phase in each bin is scaled with the corresponding signal power using the following relation:

$$phase\{U_{rotated}(\mathrm{f}_k)\} = phase\{U_{rotated}\left(f_k\right)\} \cdot |U_{rotated}(\mathrm{f}_k)|^x \tag{95}$$

where x is an exponent equal or larger than 1. The same scaling is also carried out for the quantity 2π·f(k), which describes the linear phase increase for one sample delay and is used for the normalization and the final estimation of the fractional delay. After this second step, the total delay between the two functions $T_{d1}(\lambda_j)$ and $T_{d2}(\lambda_j)$ is finally calculated as the sum of the coarse and the fractional part, as follows:

$$\mathrm{Total\,Delay} = \mathrm{n} \cdot \Delta\lambda + \mathrm{Fractional\,Delay} \tag{96}$$

It is thus clear that the FFT method achieves to remove the fundamental limitation of the peak-search method allowing for resolution that is in theory an infinitely small fraction of the scanning step. Of course, the presence of noise places limits in the resolution of a real system, but the noise tolerance of the method is very high, as it will be shown in the next section.

It is also noted that unlike the peak-search method, which is based on the interrogation of a very narrow spectrum around the resonance peak, the FFT method usually interrogates samples within a wider spectral window. The use of a wider window could be viewed as a disadvantage regarding the necessary scanning time and the entailed difficulties in averaging a large number of measurements in order to effectively reduce the system noise [Hu2009]. However, taking into account the lower requirements of the FFT method for the size of the scanning step and the intrinsic processing time advantage of the FFT compared in particular to the fitting algorithms [Lamberti2014], it is expected that the FFT method will have an overall time advantage and will allow for real-time implementations with scanning frequencies in the range of tens of Hz, hundreds of Hz or even kHz, leveraging the processing power of conventional computer or embedded hardware systems. Given the usual biochemical dynamics in lab-on-a-chip applications, this range is considered to be sufficient for these applications. Moreover, the use of a wider spectral window makes the measurement process perfectly straightforward, since it eliminates the need for carefully locating the resonance peak before the start of the measurement, and for continuously and precisely adjusting the scanning window thereafter.

3.4 Simulation study and results

In the present section, the comparison between the FFT method and the simple peak-search method goes beyond the fundamental resolution limit and involves the study of the system resolution taking into account the measurement noise as per the description in paragraph 3.2.2 Performance evaluation of MRR sensors and model of measurement noise factors. The study is based on Monte-Carlo simulations and follows the methodology described in [White2008]. Without loss of generality, it is also based on the MRR design and the waveguide structure of **Figure *62***(a) and **Figure *62***(d), respectively. The dimensions of the silicon-nitride strip and the refractive indices of the materials inside the waveguide have been adequately selected to model existing MRR designs with single-mode operation at 850 nm [Heideman2012]. The effective index of the transverse electric (TE) mode is 1.52064. The MRR has a physical length of 696 μm that corresponds to an FSR of 682.66 pm without taking into account the dispersion. The study assumes a wavelength scanning over a spectral range of 1.02 nm around the resonance peak (854.88 nm) of the first transfer function T_{d1}, which serves as the reference curve. The second transfer function T_{d2} corresponds to the same design and scanning parameters, but it is subject to the measurement noise according to the description in paragraph 3.2.2 Performance evaluation of MRR sensors and model of measurement noise factors. For each set of design and scanning parameters, the resonance shift of the second curve with respect to the reference curve is calculated for 10000 times using both the FFT and the peak-search method. The theoretical resonance shift for each one of these calculations is zero, but due to the measurement noise the simulation results are characterized by the parameter $3\sigma_{meas\text{-}n}$, which finally determines the resolution of the system for each set of parameters. More specifically, the study compares the two processing methods taking into account the design parameters of the MRR (i.e., the Q-factor and the round-trip amplitude transmission), the type and the level of the measurement noise and the wavelength scanning step. It is noted that the noise types considered in this study include only the amplitude and the spectral noise. The temperature noise is not included, as neither method can provide any tolerance to this type of noise leaving the use of reference MRRs or the use of an active temperature control mechanism as the only practical means to minimize its effect.

3.4.1 System resolution in the case of amplitude noise – Study and results

The spectral and the temperature noise are not taken into account in this case, leaving the amplitude noise as the only contributor to the measurement noise. Equation 87 is thus simplified as follows:

$$3\sigma_{meas-n} = 3\sigma_{ampl-n} \tag{97}$$

As already explained, the parameter $\sigma_{ampl\text{-}n}$ does not directly refer to the amplitude noise that is added to the transfer function, but it rather represents the contribution of the amplitude noise to the final measurement noise, thus being dependent on the data processing method. The amplitude noise itself is modeled as the shot-noise of the photodetector described by Equation 88. In order to take into account, the difference in the incident optical power between the different transfer functions as well as between the different samples in the same transfer function, the noise level is first determined by the highest possible SNR (SNR_{max}), which corresponds to a normalized incident power level equal to 1. This level corresponds to the power at the resonance peak of an MRR with α=1. The standard deviation of the shot noise for the particular SNR is denoted as $\sigma_{shot\text{-}n\text{-}max}$ and is given by the following relation:

$$\sigma_{shot-n-\max} = \sqrt{\frac{1}{SNR_{\max}}} \tag{98}$$

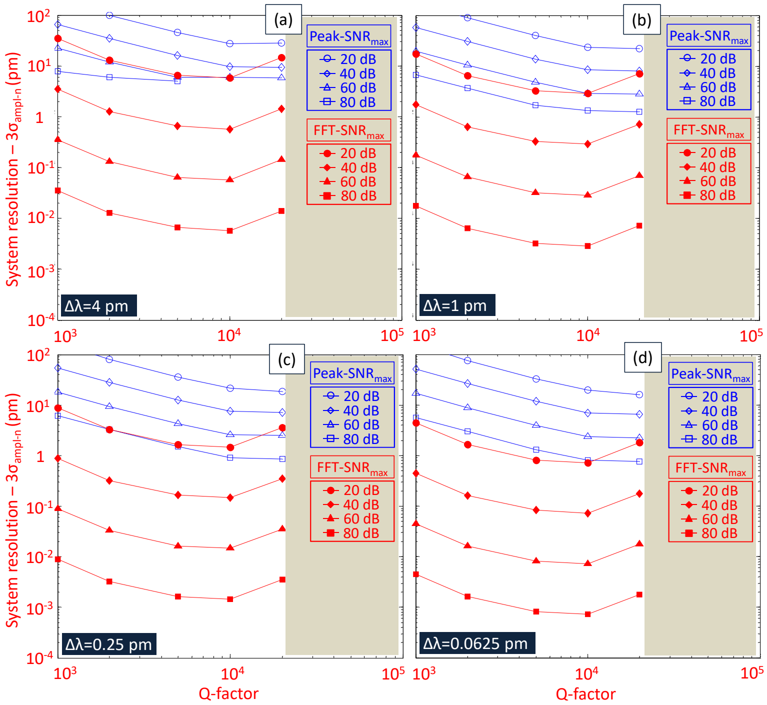

Figure 65: System resolution of FFT and peak-search method in the case of amplitude noise as a function of the Q-factor and $\Delta\lambda$. In all cases, the amplitude transmission is 0.85.

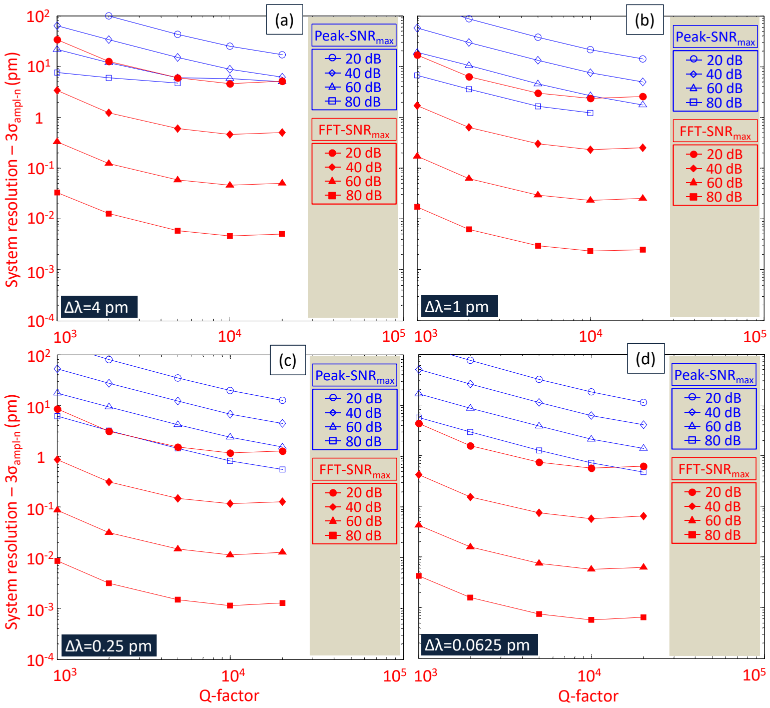

Figure 66: System resolution of FFT and peak-search method in the case of amplitude noise as a function of the Q-factor and Δλ. In all cases, the amplitude transmission is 0.90.

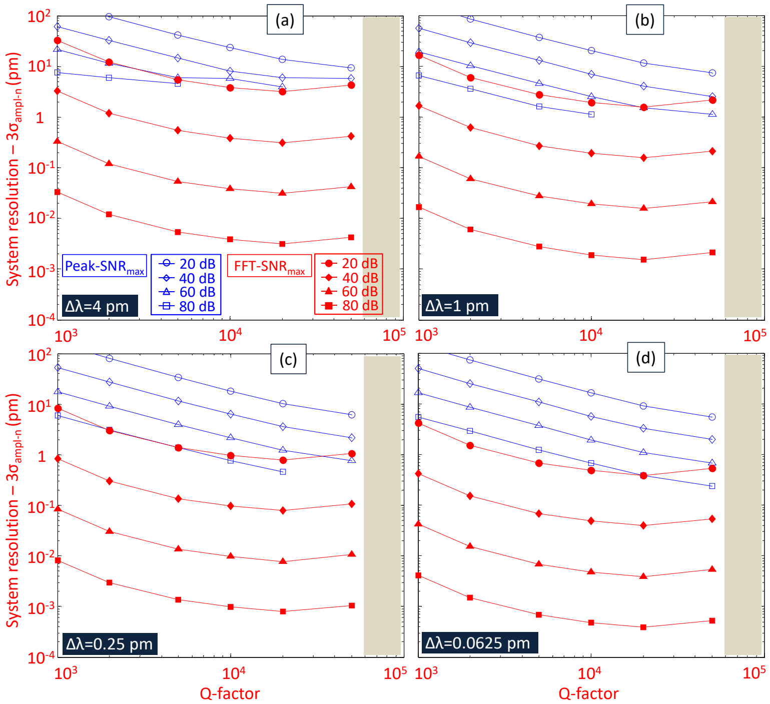

Figure 67: System resolution of FFT and peak-search method in the case of amplitude noise as a function of the Q-factor and Δλ. In all cases, the amplitude transmission is 0.95. The legend in all diagrams is as in **Figure 67**(a).

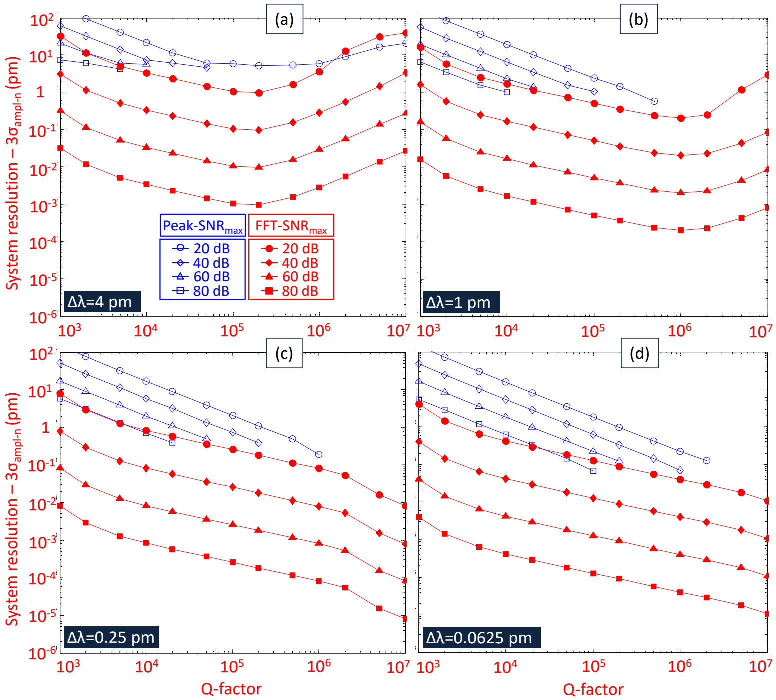

Figure 68: System resolution of FFT and peak-search method in the case of amplitude noise as a function of the Q-factor and Δλ. In all cases, the amplitude transmission is 1. The legend in all diagrams is as in **Figure 68**(a).

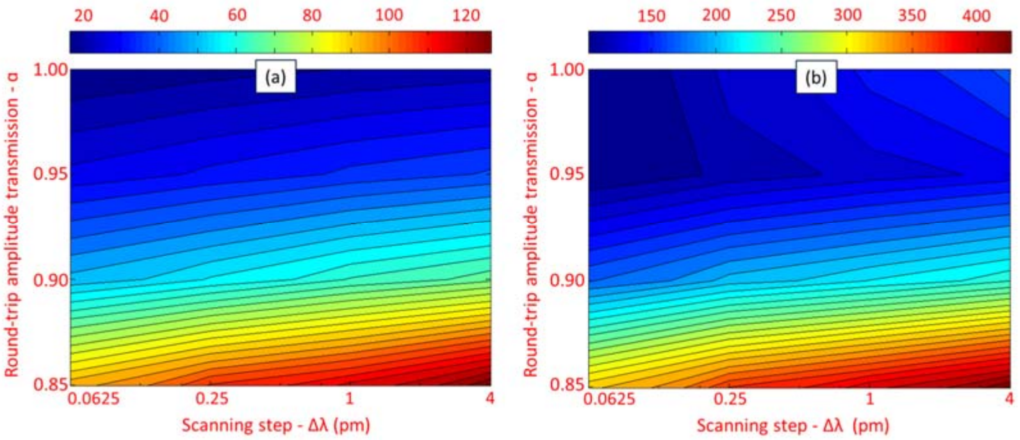

Figure 69: Gain in system resolution of the FFT over the peak-search method in the case of amplitude noise for Q-factor equal to 10^4 and SNR_{max} equal to: 40 (a) and 60 dB (b). The gain is calculated against the amplitude transmission α and the scanning step Δλ.

The standard deviation of the shot noise for any sample in the same curve or in any other curve of a different MRR design can be calculated in turn with $P_{sample} \leq 1$ as follows:

$$\sigma_{shot-n-sample} = \sqrt{\frac{P_{sample}}{P_{\max}}} \cdot \sigma_{shot-n-\max} = \sqrt{\frac{P_{sample}}{1}} \cdot \sigma_{shot-n-\max} \tag{99}$$

With this definition of the amplitude noise, the study compares the system resolution ($3\sigma_{ampl-n}$) provided by the FFT and the peak-search method taking into account the SNR_{max}, the Q-factor, the amplitude transmission coefficient and the scanning step. **Figure 65** - **Figure 68** present the results for a equal to 0.85, 0.90, 0.95 and 1, and show that for realistic MRR designs with α<1 the Q-factor is limited below a certain value, which is in fact the value in **Figure *62***(c), where each curve tends to meet the Q-factor axis. On the contrary, for α=1 the Q-factor can be in theory infinitely high through the proper adjustment of the self-coupling coefficients. It is also noted that in all diagrams in **Figure 65** - **Figure 68**, the points of the peak-search method, which are clearly out of the trend and give a $3\sigma_{ampl-n}$ below the fundamental resolution limit, are not adequate to characterize the resolution and have been removed from the corresponding curves.

To my interest in this work, the resolution of the FFT method in all diagrams of **Figure 65** - **Figure 68** is orders of magnitude better than the resolution of the peak-search method. The improvement is particularly important for practical designs with α<1, where the resolution of the peak-search method is 1-10 pm. The FFT method on the other hand enables resolution in the order of 1 pm for extremely low SNR_{max} and resolution between 0.001 and 0.01 pm for SNR_{max} higher than 60 dB. The picture remains the same also for ideal MRRs (α=1) as shown in **Figure *68***. The resolution of the peak-search method in this case is limited by the size of the scanning step, which remains equal or larger than 0.0625 pm in our study. However, even if this limitation was not present, the trend of the peak-search curves indicates that the improvement with the FFT method would be still two orders of magnitude.

Referring back to the realistic MRR designs (α<1), a local minimum is observed in all FFT curves in **Figure *65*** - **Figure *67***. For α=0.85 this minimum is close to 10^4, whereas for higher α it shifts towards 2·10^4. The existence of this minimum confirms that unlike the peak-search method, which has a strong preference for high Q-factors and short scanning steps, the FFT method can perform well also in the case of lower Q-factors. In combination with the higher optical power that is incident on the photodetector in the latter case, the system turns out to perform better having a minimum in the standard deviation of the measured resonance shift.

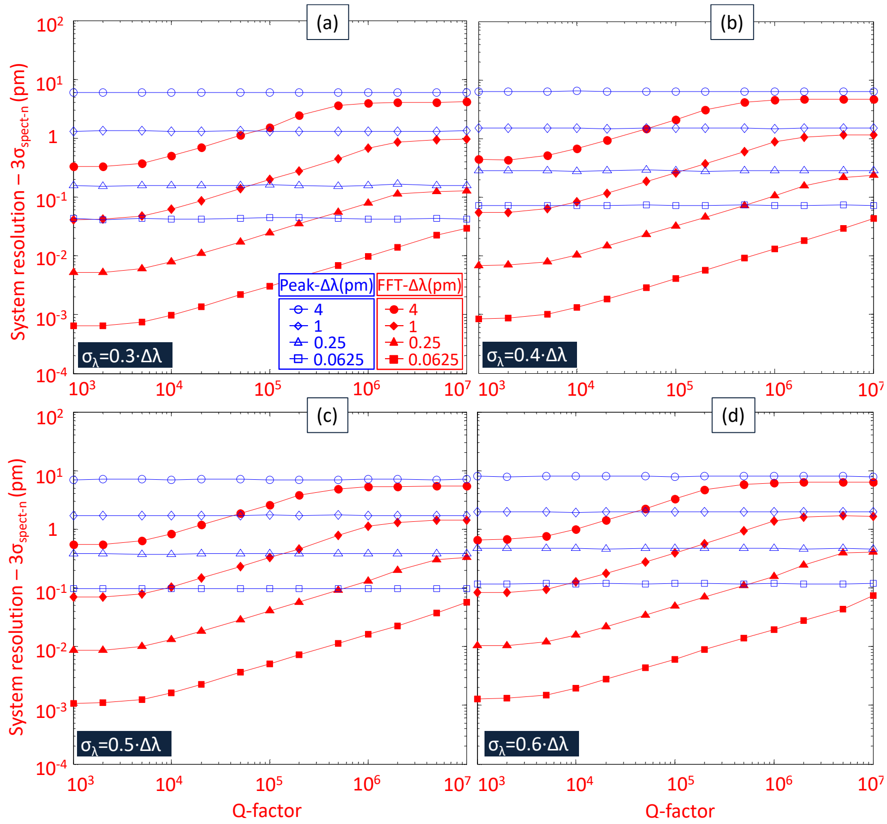

Figure 70: System resolution of FFT and peak-search method in the case of spectral noise with σ_λ equal to: a) 0.3·Δλ, b) 0.4·Δλ, c) 0.5·Δλ, and d) 0.6·Δλ. System resolution is shown for amplitude transmission equal to 1, but it is in fact independent from this parameter. The legend in all diagrams is as in **Figure 70**(a).

For α=1, the dependence of the optical power on the Q-factor is not present anymore, and the standard deviation of the FFT method can be a strictly decreasing function, as in **Figure *68***(c) and **Figure *68***(d). However, for larger Δλ as it is the case in **Figure *68***(a) and **Figure *68***(b), the minimum can be present again due to the fact that for high Q-factors the number of samples inside the resonance spectrum may not be large enough to give a good estimation of the resonance shift. The problem can be partially resolved by using in Equation 95 an exponent x larger than 1.

With these interdependencies between the system parameters, **Figure *69*** summarizes a set of indicative results for Q-factor equal to 10^4 and SNR_{max} equal to 40 and 60 dB. The two contour plots illustrate the gain of the FFT method in the case of amplitude noise defined as:

$$\mathrm{Gain}_{ampl-FFT} = \frac{3\sigma_{ampl-n-ps}}{3\sigma_{ampl-n-FFT}} \qquad (100)$$

where $3\sigma_{amp-n-ps}$ and $3\sigma_{ampl-n-FFT}$ are the standard deviations of the peak-search and the FFT method, respectively. As observed, the FFT gain ranges from 20 to 125 in the low SNR case and from 100 to 420 in the high SNR case for the whole 2D space of the amplitude transmission α and the scanning step Δλ considered in this study.

3.4.2 System resolution in the case of spectral noise – Study and results

In this case the amplitude and the temperature noise are not taken into account, leaving the spectral noise as the only contributor to the noise of the measurement system. Equation 87 is thus simplified as follows:

$$3\sigma_{mean-n} = 3\sigma_{spect-n} \tag{101}$$

Also, in this case, the parameter $\sigma_{spect-n}$ does not directly refer to the spectral noise, but rather to the contribution of the spectral noise to the total measurement noise, which depends on the data processing method. The actual spectral noise, which describes the wavelength allocation of the samples around their nominal value, is assumed to follow a normal distribution with standard deviation (σ_λ) equal to a fraction of the scanning step Δλ. The diagrams in **Figure *70*** compare the way, in which the FFT method and the peak-search method translate the spectral noise into measurement noise affecting the system resolution. The comparison is made for σ_λ equal to 0.3·Δλ, 0.4·Δλ, 0.5·Δλ and 0.6·Δλ and involves four scanning steps and various Q-factors. Since this part of the study does not involve the amplitude noise, the difference in the incident power that relates to the different amplitude transmission coefficients α has not any effect, thus making the system resolution independent from α. In order, however, to include the broadest possible range of Q-factors in our study, the simulations presented in **Figure *70*** were made for α=1.

As observed in all diagrams, the use of the FFT method brings significant improvement and allows for system resolution $3\sigma_{spect-n}$ below the standard deviation $3\sigma_\lambda$. On the other hand, while the Q-factor appears in all diagrams to have no practical effect in the case of the peak-search method, it is obvious that it has a significant effect in the case of the FFT method. More specifically, the system resolution is moderate for high Q-factors but improves remarkably for lower Q-factors, where a large number of samples can reside inside the resonance spectrum and participate in the FFT calculation. For Q-factor equal to 10^4, the gain of the FFT method is between 10 and 100 for all scanning steps and all spectral noise levels. This gain is defined now as follows:

$$\mathrm{Gain}_{spect-FFT} = \frac{3\sigma_{spect-n-ps}}{3\sigma_{spect-n-FFT}} \tag{102}$$

3.4.3 Effect of number of resonance peaks inside the wavelength scanning window

Without loss of generality, we focus now on a realistic set of parameters and study the effect of the presence of additional resonance peaks on our method [Gounaridis2017]. We use a model measurement system with 50 dB maximum signal-to-noise ratio (SNR_{max}) [Gounaridis2016] and a model MRR design with a Q-factor of $1.5\cdot10^4$, a round-trip amplitude transmission of 0.9 [Bogaerts2012, Gounaridis2016], a round-trip length of 872 μm, and an effective refractive index of 1.65. These parameters result in a free spectral range (FSR) of 505 pm at 855 nm. We assume that this effective refractive index is constant across our scanning window. Although this assumption is not completely true due to the dispersion effects, which are always present in waveguiding systems, it is a safe and meaningful simplification in the case of the FFT method due to the tolerance of the method to these effects. This tolerance originates from the handling of the total waveform inside the scanning window as a single block and the calculation of a unique wavelength shift. This calculation is a result of a sample averaging and weighting process, which is inherent to the method and can eliminate the wavelength shift variations across the scanning window due to the dispersion effects. For our first study, we take as an example the case of a moderate effective RI change of the propagating mode inside the MRR equal to 10^{-6} RIU, and we perform a series of Monte-Carlo simulations with 10000 runs for each combination of scanning step and number of resonance peaks. The system resolution for each combination is extracted through the mean error and the standard deviation in the estimation of the actual resonance

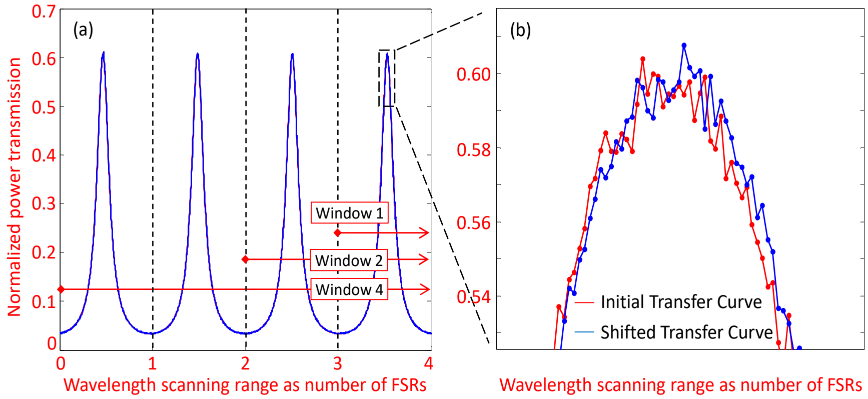

Figure 71: Typical pair of initial and wavelength shifted TF of an MRR with Q-factor equal to 10^4 and α equal to 0.9 for an effective RI change of 10^{-6}: Options for a symmetric scanning window with one, two or four resonance peaks (a), and Zoom-in on the rightmost resonance peaks of the two TFs (b).

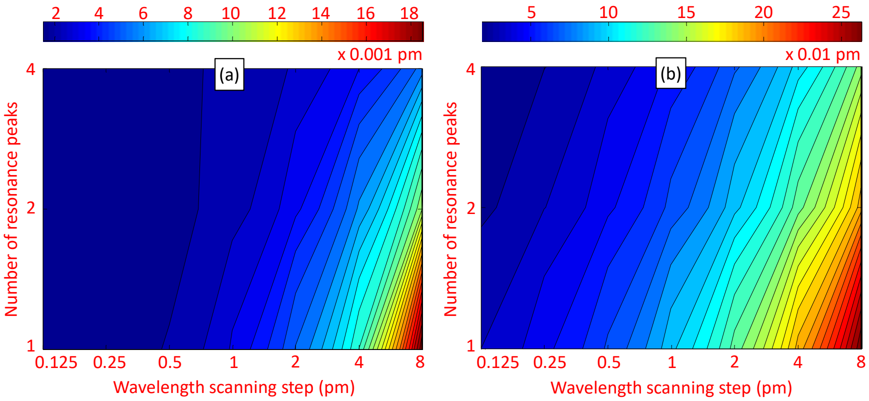

Figure 72: System performance using the FFT method as a function of the number of resonance peaks and the scanning step: Mean error (a), and 3σ standard deviation in the calculation of the resonance shift (b). The results refer to Monte Carlo simulations with 10.000 runs for each point in the two contour plots. The simulations were made for an effective RI change equal to 10^{-6}, using an MRR with Q-factor=10^4 and α=0.9. The model measurement system has both amplitude (SNRmax=50 dB) and spectral noise (σ_λ=0.4·Δλ).

shift between the initial and the shifted TF, as per the analysis in [Gounaridis2016]. For the calculation of these statistical parameters, we have pre-calculated the theoretical resonance shift for the specific effective RI change with ultra-high precision (0.56030487 pm). In order to make this pre-calculation, we temporarily removed any source of measurement noise, and used the peak search method with an unrealistically short scanning step (0.00390625 pm).

As illustrated in **Figure *71***, the study involves the use of three different scanning windows that contain exactly one, two or four complete periods of the initial and the shifted TF. The resonance peaks reside symmetrically inside these windows and are sampled with seven different scanning steps (0.125, 0.25, 0.5, 1, 2, 4 and 8 pm). **Figure 72**(a)-**Figure 72**(b) presents the results of the study in terms of mean error and 3σ standard deviation, respectively, revealing that the presence of additional peaks in the processed parts of the TFs can average out the noise and improve the accuracy of the FFT method in a noisy environment. As the mean error remains negligible in all cases, the improvement is more evident in the 3σ standard deviation, which drops by almost a factor of 2 for all scanning steps, when we switch from single-peak to four-peak operation. It is noted, however, that this improvement is achieved at the expense of a broader scanning range, which entails higher complexity for the TL and the driving electronics and longer duration for the scanning process.

3.4.4 Effect of power dependence of the tunable laser source on the wavelength

Using the same MRR design and the same effective RI change, we study next the effect of the wavelength dependence of the laser output power on the performance of the FFT method and the final system resolution. Since the TL in this type of sensors is usually a vertical cavity surface emitting laser (VCSEL) at 850 nm, the wavelength scanning is based on the strong adiabatic chirp of the VCSEL and can be realized through a corresponding scanning of the injection current. **Figure 73**(a) presents a realistic model of the optical power as a function of the emission wavelength, assuming that the wavelength dependence is linear within the 4-peak scanning window with total range of 2.02 nm, and that the output optical power at the lower end of this window is only 35% of the optical power at the upper end. In order to assess the effect of the power dependence, we compare the system accuracy in the case of one, two or four resonance peaks under the presence or absence of this dependence. In all cases, we define the individual scanning windows taking from the total range of 2.02 nm, the corresponding number of rightmost resonance peaks, as shown in **Figure 73**(a), in order to retain the optical power levels as high as possible. Since the mean error in the estimation of the actual resonance shift remains negligible in all cases, we base our comparison again on the study of the corresponding 3σ standard deviations. **Figure 73**(b) presents the simulation results and reveals the high tolerance of the FFT method. More specifically, the diagram shows that the power dependence has practically no effect in the case of a single peak, has a very weak effect in the case of two peaks, and a larger but still weak effect in the case of four peaks. The mechanism of this effect does not relate to the fundamental properties of the FFT method, but rather to the lower optical power levels at the leftmost part of the scanning window. Since the method uses the samples from all parts of the TFs in order to extract the resonance shift, these lower power parts make the measurement noisier, increasing in this way the 3σ standard deviation.

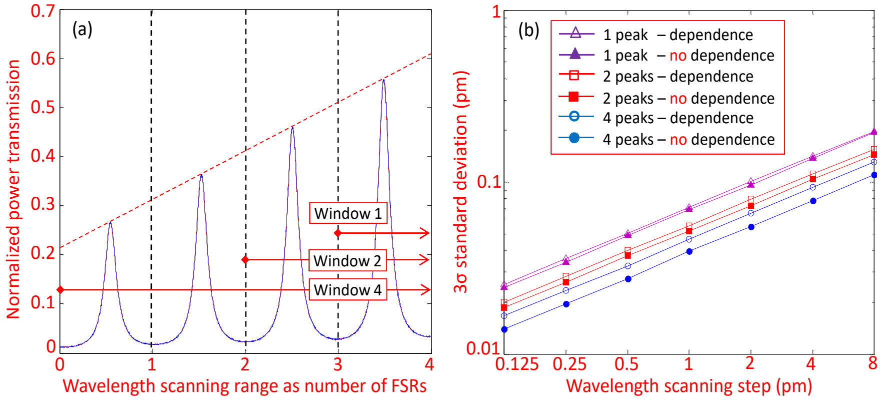

Figure 73: Initial and wavelength shifted TF of our model MRR in the presence of wavelength dependence of the laser output power, and options for a symmetric scanning window with one, two or four resonance peaks (a). 3σ standard deviation in the calculation of the resonance shift using the FFT method as a function of the scanning step in the case of presence or absence of wavelength dependence of the laser output power (b).

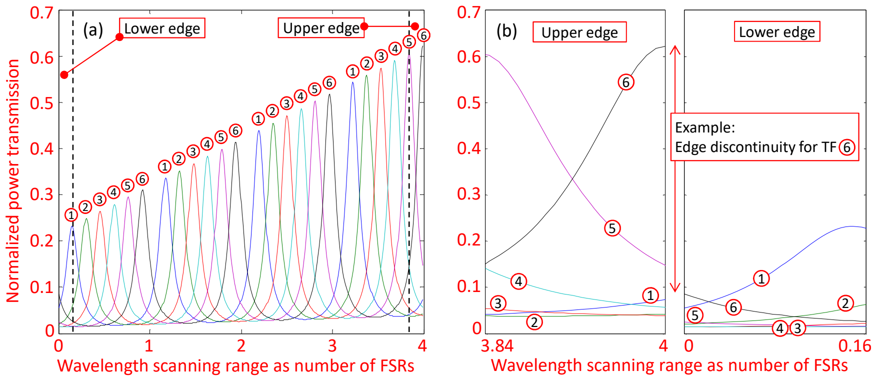

Figure 74: Five different TFs of our model MRR corresponding to five different relative positions inside a scanning window with range equal to four times the FSR (a). Zoom-in on the lower and the upper edge of the scanning window revealing the edge discontinuity for each one of the five cases (b).

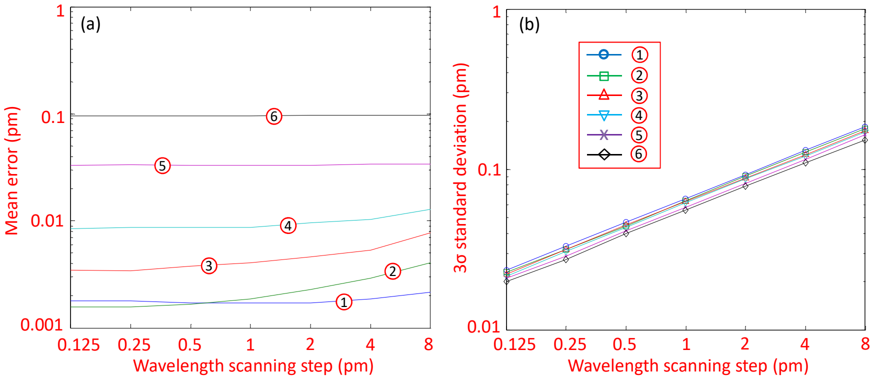

Figure 75: System performance using the FFT method in the five cases of the relative position of the TF of our model MRR inside the scanning window: Mean error (a), and 3σ standard deviation (b) in the calculation of the resonance shift as a function of the scanning step for an effective RI change of 10^{-6}.

3.4.5 Effect of relative position of transfer functions inside the scanning window

So far, we have assumed that the range of the scanning window is a multiple of the FSR. In the absence of any laser power dependence, this assumption is sufficient to ensure that the TFs, which are mathematically treated by the FFT as cyclic functions, do not present any discontinuity at the edges of the scanning window. Moreover, we have also assumed that the scanning window is always symmetrical with respect to the resonance peaks of each TF, which ensures in turn that the values of the TF at the edges of the scanning window are the minimum ones, and that the possible discontinuity of the TF remains negligible even in the presence of laser power dependence. This fact is very important, since the presence of any large discontinuity can lead to a false mathematical calculation of a strong high-frequency component in the spectrum of the TF and can result in significant error in the phase calculation of the Fourier transform. We now go further and investigate the actual impact of this type of discontinuity on a real measurement, working with a system that features both laser power dependence and asymmetry between the scanning window and the resonance peaks. We take as an example the 2.02 nm scanning window, which is four times as wide as the FSR of our model MRR and assume that the same noise level and the same laser power dependence as before are present. **Figure 74**(a) presents five cases with different relative positions of the TF inside the scanning window, and **Figure 74**(b) provides a zoom-in on the lower and the upper edge of the scanning window, revealing the level of discontinuity in each case. As observed, the third case corresponds to the perfect symmetry, whereas the other cases correspond to various degrees of asymmetry between the scanning window and the resonance peaks, resulting in different degrees of edge discontinuity.

Figure 75(a)-**Figure 75**(b) present the impact of these variations on the final performance of the system in terms of mean error and standard deviation in the estimation of the resonance shift for an effective RI change of 10^{-6}. As observed, the asymmetry does not affect the standard deviation of the simulation runs but can affect the mean error of the measurement in a critical way, degrading the actual resolution and reliability of the system. More specifically, as shown in **Figure 75**(a), the mean error increases together with the edge discontinuity, and almost irrespectively of the scanning step. Since the use of windowing techniques based on Gaussian, tapered cosine or Chebyshev windows [Harris1978] cannot sufficiently resolve this problem, it is evident that the elimination of the edge discontinuity is necessary for reliable measurements. In practice, this can be easily achieved by using a larger scanning window and selecting for further processing out of this window a smaller one that is a multiple of the FSR and symmetric with respect to the resonance peaks. This approach has been successfully used in the experimental part of our work and is presented in the next section.

3.4.6 Benchmarking of the FFT method against the peak search method with Lorentzian fitting

In order to extend the benchmarking, we present in this paragraph a set of further simulation results that compare the FFT method against a more complex variant of the peak-search method, which involves Lorentzian fitting. The function that the measured data are intended to fit to is defined as follows:

$$f(x) = \frac{1}{2\pi}\cdot\frac{a}{(x-b)^2+\left(\frac{c}{2}\right)^2} \tag{103}$$

where a, b and c are the parameters that are iteratively optimized for optimum fitting. Although time- and computational resource-consuming, this type of fitting is considered as a standard approach in order to increase the noise tolerance when relying on a peak-search method [Iqbal2010]. For our comparison in this paragraph, we use again an MRR with 10^4 Q-factor, and we apply a change in the refractive index of the top-cladding of the MRR that results in 0.5603 pm resonance shift. This result has been carefully pre-calculated using an ultra-short step in the peak search method (0.00390625 pm) without any source of noise present in the measurement system. We then switch on only the amplitude noise in order to keep things simple, and we compare the performance of the FFT method against the Lorentzian fitting for SNR_{max} equal to 40 and 60 dB and for different values of the amplitude transmission α and the scanning step Δλ. The comparison is based on 10000 calculation runs for each set of parameters, and in this case, it does not involve only the standard deviation $3\sigma_{meas-n}$ as per the definition in paragraph 3.2.2 Performance evaluation of MRR sensors and model of measurement noise factors but also the mean error in the estimation of the actual resonance shift. This is particularly important, as the fitting-based variants of the peak-search method are known to be vulnerable to the peak locking effect [Lamberti2014, Gui2002].

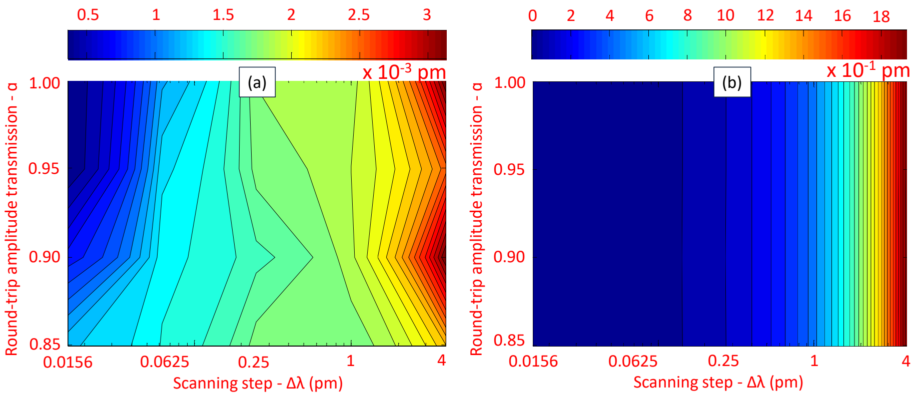

Figure 76: Mean error in the estimation of the real resonance shift using: the FFT method (a), and the peak-search method with Lorentzian fitting (b). In both cases the Q-factor is 10^4 and the SNR_{max} 40 dB.

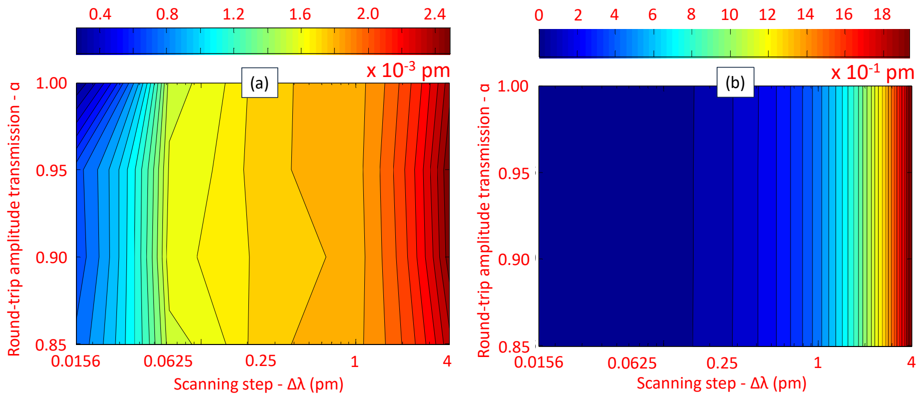

Figure 77: Mean error in the estimation of the real resonance shift using: the FFT method (a), and the peak-search method with Lorentzian fitting (b). In both cases the Q-factor is 10^4 and the SNR_{max} 60 dB.

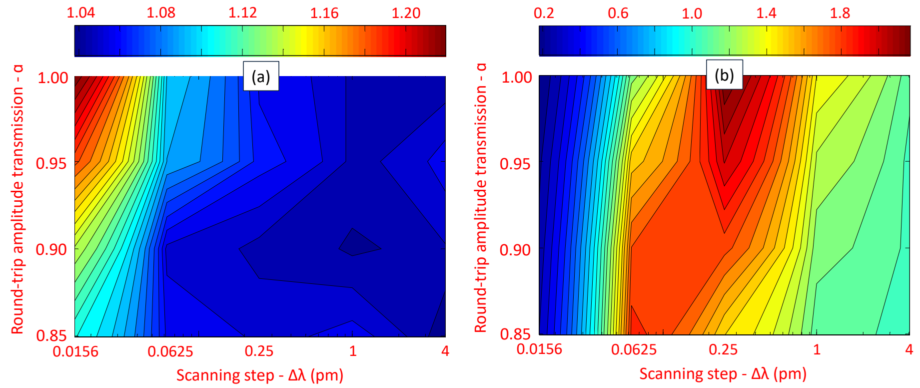

Figure 78: Gain in the standard deviation of the measurement for the FFT method over the peak-search method with Lorentzian fitting. The results correspond to Q-factor 10^4 and SNR_{max} equal to: 40 (a), and 60 dB (b).

The main results of the study are summarized in **Figure 76**, **Figure 77** and **Figure 78**. **Figure 76** presents the absolute value of the mean error in the resonance shift estimation by the two methods for 40 dB SNR_{max}. As shown on the left diagram, the FFT method achieves an error that remains lower than 0.003 pm in an almost homogeneous way for the total of the 2D space of parameters, including extremely long scanning steps (i.e., 4 pm). On the other hand, the right diagram reveals that the mean error of the fitting method is remarkably larger and has a very strong dependence on the scanning step. In more detail, the error remains larger than 0.19 pm even for a scanning step of 0.0625 pm and becomes comparable with the error of the FFT method (i.e., 0.003 pm), only when the scanning step has become as short as 0.015 pm. Comparing this value with the scanning step in the FFT method that ensures the same mean error, it is concluded that the relevant scanning step requirements are almost 300 times lower in the FFT method. **Figure *77*** presents the same type of diagrams for 60 dB SNR_{max}, revealing the same picture and a similar level of improvement by the FFT method. Finally, **Figure *78*** presents the comparison of the two methods with respect to the standard deviation of the estimated resonance shift in the case of 40 and 60 dB SNR_{max}. The comparison is visualized in a way similar to Fig. 8, using the definition of the gain factor $Gain_{ampl\text{-}FFT\text{-}LorFit}$ as:

$$\mathrm{Gain}_{ampl-FFT-LorFitting} = \frac{3\sigma_{ampl-n-LorFitting}}{3\sigma_{ampl-n-FFT}} \qquad (104)$$

As observed in both diagrams, the gain factor remains close to 1, meaning that the standard deviations of the two methods are comparable, and thus both very good. It is noted, however, that the combination of a small standard deviation with a large mean error in the estimation of the resonance shift, which is the case for the Lorentzian fitting in the largest part of the investigated scanning steps, means that the system fails to get close to the actual shift in almost all calculation runs. On the other hand, the efficiency of the Lorentzian fitting can be indeed very high but only when the scanning step becomes ultra-short (e.g., almost 0.015 pm), which is of course not practical for lab-on-a-chip systems, and thus not to our interest in this work.

Finally, it is noted again that also timewise the FFT method has a significant advantage compared to the fitting method and can conveniently enable real-time implementations and high scanning rates. Although the MATLAB scripts used in this study were not optimized in terms of computation time neither for the FFT nor for the fitting method, the difference in their execution time was more than 60 times giving a picture of this advantage.

3.4.7 Effect on the detection limit of the system

In this part of the work, we go back to the comparison with the simplest form of the peak-search method, and we try to translate the resolution improvement of the FFT method into actual improvement in the detection limit DL and the complexity of real sensor systems. Table 2 outlines the methodology for this translation starting from a practical design that has been used in part as an example also in the previous paragraphs. The design involves an MRR with low Q-factor (10^4), low amplitude transmission α (0.85) and moderate wavelength scanning step Δλ (0.25 pm). The SNR_{max} is high (60 dB), but still achievable in practical systems, while the standard deviation in the wavelength allocation of the samples is 0.3·Δλ. In the third and the fourth column of Table 2, the resultant amplitude noise, spectral noise and system resolution are presented for the FFT and the peak-search method, respectively, based on **Figure 65**(c), **Figure 70**(a) and Equation 87. As observed, the improvement of the FFT method in the system resolution is more than two orders of magnitude. This gain can directly translate into an equivalent improvement in the detection limit taking into account that the calculation of the sensitivity is independent from the processing method. Using a sensor sensitivity equal to 100 nm/RIU, which is reasonable for conventional MRR designs [Yalçin2006, Barrios2007], the detection limit of the FFT method becomes approximately $1.7\cdot10^{-7}$ RIU, whereas the detection limit of the peak-search method remains approximately $2.6\cdot10^{-5}$ RIU.

The last column relies on the design rules highlighted in the previous paragraphs and presents an MRR design that can provide in combination with the peak-search method resolution on the same order as the FFT method in the third column. In this case, the MRR design has to rely on extremely high Q-factors (around $2\cdot10^6$), which are only compatible with extremely high amplitude transmission coefficients (around 0.999) and extremely short and precise steps (e.g., 0.015625 pm). The resolution improves indeed by more than two orders of magnitude, but this improvement comes with dramatic increase in the fabrication and operation complexity and dramatic reduction in the sensor sensitivity. The trade-off is better explained through the following relation, which relates the Q-factor to the ratio η of the evanescent intensity inside the sample over the total intensity of the propagating mode [White2008]:

$$\eta \cdot A = \frac{2\pi n_{eff}}{\lambda_{res} \cdot Q_A} \tag{105}$$

In this relation, A is the optical absorption of the sample in m-1 and Q_A is the part of the Q-factor owing to this absorption. Although there is a second part denoted as Q_0, which relates to other types of losses inside the MRR and is combined with Q_A to provide the total Q-factor as $1/Q=1/Q_A+1/Q_0$, it is evident that the increase in the total Q-factor from 10^4 to $2\cdot10^6$ requires a similar level of increase in Q_A. Equation 102 implies in turn that the reduction in η and consequently in the sensor sensitivity is also close to 200 times, leading to values around 0.5 nm/RIU. The DL in this case is close to $2.6\cdot10^{-5}$, thus remaining more than two orders of magnitude higher than the DL of the system based on the lower Q-factor and the FFT method. From the analysis in the previous paragraph 3.4.6 Benchmarking of the FFT method against the peak search method with Lorentzian fitting, it is clear of course that a similar improvement in the system resolution can be also achieved using the initial MRR design (Q-factor equal to 10^4) in combination with Lorentzian fitting. However, for reliable estimation of the resonance shift, the scanning step has to become also in this case ultra-short (in the order of 0.015625 pm), and the computation time has to increase by almost 2 orders of magnitude. Finally, it is noted that the conclusions for the detection limit of the two methods in terms of bulk refractive index changes can be converted into conclusions for the detection limits in terms of targeted analyte molecules per area or mass of targeted analyte per area on the MRR surface. The methodology for this conversion has been described in detail in [Zhu2007].

Table 2 Comparison of the detection limit using the FFT and the peak-search method.

Data processing method	-	FFT	Peak-search	Peak-search
Q-factor	-	10^4	10^4	$2\cdot10^6$
Amplitude coefficient α	-	0.85	0.85	0.999
Scanning step	pm	0.25	0.25	0.015625
SNR_{max}	dB	60	60	60
$3\sigma_{ampl-n}$	pm	0.015	2.603	0.010
$3\sigma_{spect-n}$	pm	0.008	0.147	0.008
Resolution: $3\sigma_{meas-n}$	pm	0.017	2.607	0.013
Refractive index sensitivity	nm/RIU	100	100	0.5
Detection limit (DL)	RIU	$1.7\cdot10^{-7}$	$2.6\cdot10^{-5}$	$2.6\cdot10^{-5}$

3.5 References of Chapter 3

[Yalçin2006] A. Yalçin, K.C. Popat, J.C. Aldridge, T.A Desai, J. Hryniewicz, N. Chbouki, B.E. Little, O. King, V. Van, S. Chu, D. Gill, M. Anthes-Washburn, M.S. Ünlü, and B.B. Goldberg, "Optical sensing of biomolecules using microring resonators," IEEE J. Sel. Top. Quant. 12, 148–155 (2006).

[Zhu2007] H. Zhu, I. M. White, J. D. Suter, P. S. Dale and X. Fan, "Analysis of biomolecule detection with optofluidic ring resonator sensors," Opt. Express 15, 9139-9146 (2007).

[Vos2007] K. De Vos, I. Bartolozzi, E. Schacht, P. Bienstman, and R. Baets, "Silicon-on-Insulator microring resonator for sensitive and label-free biosensing," Opt. Express 15, 7610-7615 (2007).

[Iqbal2010] M. Iqbal, M. A. Gleeson, B. Spaugh, F. Tybor,W. G. Gunn, M. Hochberg,T. Baehr-Jones, R. C. Bailey, and L. C. Gunn, "Label-free biosensor arrays based on silicon ring resonators and high-speed optical scanning instrumentation," IEEE J. Sel. Top. Quant. 16, 654-661 (2010).

[Heideman2012] R. Heideman, M. Hoekman, E. Schreuder, "TriPleX-based integrated optical ring resonators for lab-on-a-chip and environmental detection," IEEE J. Sel. Top. Quant. 18, 1583-1596 (2012).

[White2008] I.M. White and X. Fan, "On the performance quantification of resonant refractive index sensors," Opt. Express 16, 1020-1028 (2008).

[Misiakos2014] K. Misiakos et al., "Broad-band mach-zehnder interferometers as high performance refractive index sensors: theory and monolithic implementation," Opt. Express 22, 8856-8870 (2014).

[Lamberti2014] A. Lamberti, S. Vanlanduit, B. De Pauw, and F. Berghmans, "A novel fast phase correlation algorithm for peak wavelength detection of fiber Bragg grating sensors," Opt. Express 22, 7099-7112 (2014).

[Leinse2013] A. Leinse, R.G. Heideman, M. Hoekman, F. Schreuder, F. Falke, C.G.H. Roeloffzen, L. Zhuang, M. Burla, D. Marpaung, D.H. Geuzebroek, R. Dekker, E.J. Klein, P.W.L. Van Dijk, R.M. Oldenbeuving, "TriPleX™ waveguide platform: Low-loss technology over a wide wavelength range," Proc. SPIE, 8767, art. no. 87670E (2013).

[Bogaerts2012] W. Bogaerts, et al., "Silicon microring resonators," Laser Photonics Rev. 6, 47-73 (2012).

[Barrios 2007] C. A. Barrios, K. B. Gylfason, B. Sánchez, A. Griol, H. Sohlström, M. Holgado, and R. Casquel, "Slot-waveguide biochemical sensor," Opt. Lett. 32, 3080-3082 (2007).

[Agrawal2002] G. P. Agrawal, Fiber-Optic Communication Systems, Third edition, (Wiley Interscience, 2002), New York.

[Han2007] M. Han and A. Wang, “Temperature compensation of optical microresonators using a surface layer with negative thermo-optic coefficient,” Opt. Lett. 32, 1800-1802 (2007).

[Djordjevic2013] S. S. Djordjevic, K. Shang, B. Guan, S. T. S. Cheung, L. Liao, J. Basak, H.-F. Liu, and S. J. B. Yoo, “CMOS-compatible, athermal silicon ring modulators clad with titanium dioxide,” Opt. Express 21, 13958-13968 (2013).

[Gui2002]. Gui and S. T. Wereley, “A correlation-based continuous window-shift technique to reduce the peak-locking in digital PIV evaluation,” Experiments Fluids 32, 506–517 (2002).

[Nentwig2011] M. Nentwig, “Signal fitting with subsample resolution,” (2011) Available from: http://www.dsprelated.com/showcode/207.php.

[Hu2009] J. Hu, X. Sun, A. Agarwal, and L. C. Kimerling, “Design guidelines for optical resonator biochemical sensors,” J. Opt. Soc. Am. B 26, 1032-1041 (2009).

[Gounaridis2016] L. Gounaridis, P. Groumas, E. Schreuder, R. Heideman, H. Avramopoulos, and Ch. Kouloumentas, “New set of design rules for resonant refractive index sensors enabled by FFT based processing of the measurement data,” Opt. Express 24(7), 7611-7632 (2016).

[Gounaridis2017] L. Gounaridis, P. Groumas, E. Schreuder, G. Tsekenis, A. Marousis, R. Heideman, H. Avramopoulos, and C. Kouloumentas, “High performance refractive index sensor based on low Q-factor ring resonators and FFT processing of wavelength scanning data,” Opt. Express 25, 7483-7495 (2017).

[Harris1978] F. J. Harris, “On the use of windows for harmonic analysis with the discrete Fourier transform,” in Proceedings of the IEEE 66(1), 51-83 (1978).

Chapter 4. Development of the electronics and experimental results

In this chapter, a detailed description of the electronic platform is being provided as well as the software platform and the user interface of the photonic biosensor and the detailed description of a representative experiment with specific proteins.

In the first part of this chapter the architecture of the electronics platform is given and the different components comprising the platform are described in detail. Specifically, the components comprising the platform are the master control unit, the pretreatment unit, the detection unit (in turn comprising of the optoelectronics and microfluidics control units) and the power distribution network. The specifications of the components are given. At the physical layer, the master control unit will be connected via Ethernet with the optoelectronics and the pretreatment units (direct links). The microfluidics and master control units will be connected through USB-to-serial communication (simple UART).

In the second part of this chapter the focus is on the software platform and user interfaces of the biosensor, describing in detail the programming of the electronics. The main programming language used is National Instruments LabVIEW. LabVIEW is a graphical language, that eases programming, allowing the developer to focus more on the application, and also offers the developer a straightforward graphical user interface design tool. LabVIEW programs consist of two parts that communicate bilaterally, namely the block diagrams, where the code lies and all processing takes place, and the front panels where the user interacts with the program, changing the values of variables and visualizing the results. A host program running on the master control unit will control the optoelectronics, microfluidics and pretreatment units. At the application layer the pretreatment and master control will communicate and parse xml files containing the commands and messages, through FTP server/client pairs, the microfluidics and master control will communicate exchanging UTF-8 characters, the optoelectronics and master control unit will communicate using network shared variables, a LabVIEW proprietary technology which is seen as a black box to the developer, but offers seamless communication between the two devices by establishing again shared variable server/client pairs.

In the last part of the chapter, an evaluation experiment for the specific binding of the mycotoxin OTA and copper target molecules to the aptamers targeting OTA and copper, respectively is presented. Moreover, the effect of the $MgCl_2$ presence on the binding has been investigated. Different kind of buffers have been used during these experiments.

The biosensing system that has been developed aims to be a sophisticated, standalone, portable biophotonic sensor system, capable of detecting in short time and accurately different analytes in olive oil, nuts and milk. Having these prerequisites in mind, the biosensor was conceived from the beginning of its development as an embedded system that would perform all necessary actions i.e., sample pretreatment, sample dispensing and flow control, data acquisition and detection in a single package.

The plan to use a laptop as an accompanying unit for control of the sensor and presentation of the results was dropped during this work, and a single board computer with a LCD screen were chosen to be embedded, adding more to the autonomy and compactness of the system.

This biosensing system was designed to work in the ELV (Extra-low voltage) range requiring only 12V DC, so as to be absolutely safe for the user and for being compatible with the 12V outlet of a car (cigarette lighter receptacle) for maximum portability.

The hardware architecture of the biosensing system follows a hierarchical scheme as it will be described in detail later on in this chapter. The hardware components were carefully chosen for high performance, compatibility, low power consumption and ease of programming.

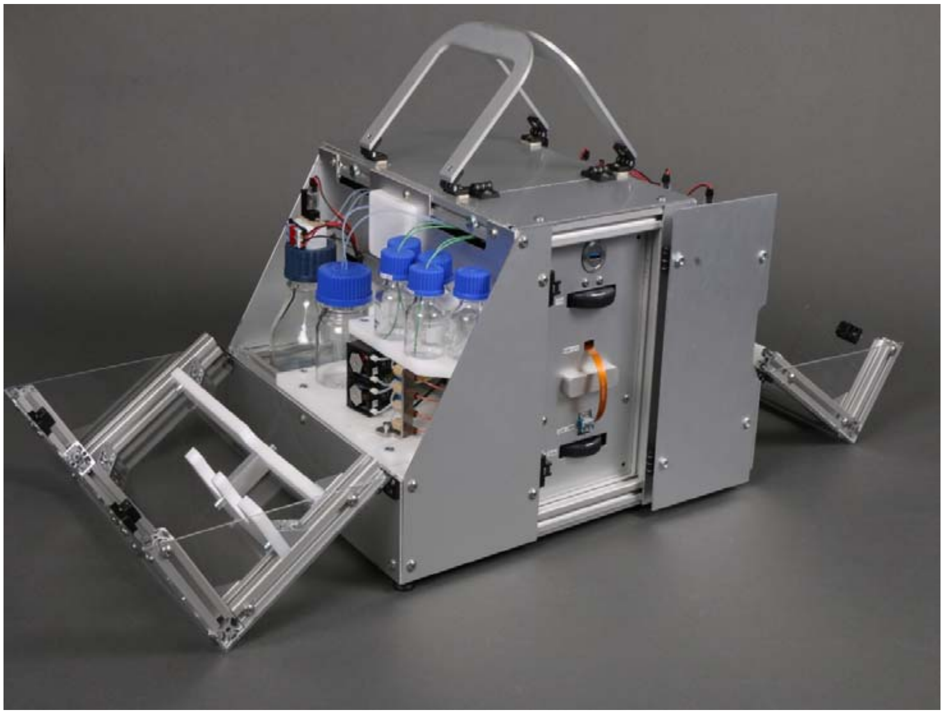

Figure 79: Biophotonic system – Packaged.

4.1 Electronic platform of the system

The following subsections will describe in more detail the architecture of the system and the different components comprising the electronic platform of the biophotonic system. The power distribution network and its associated electronics will be described in a separate section.

4.1.1 Architecture of electronic platform

The biophotonic system follows a hierarchical architecture for the control and communication of the different components as it can be seen in **Figure *80***. This paragraph will mainly focus on all the units.

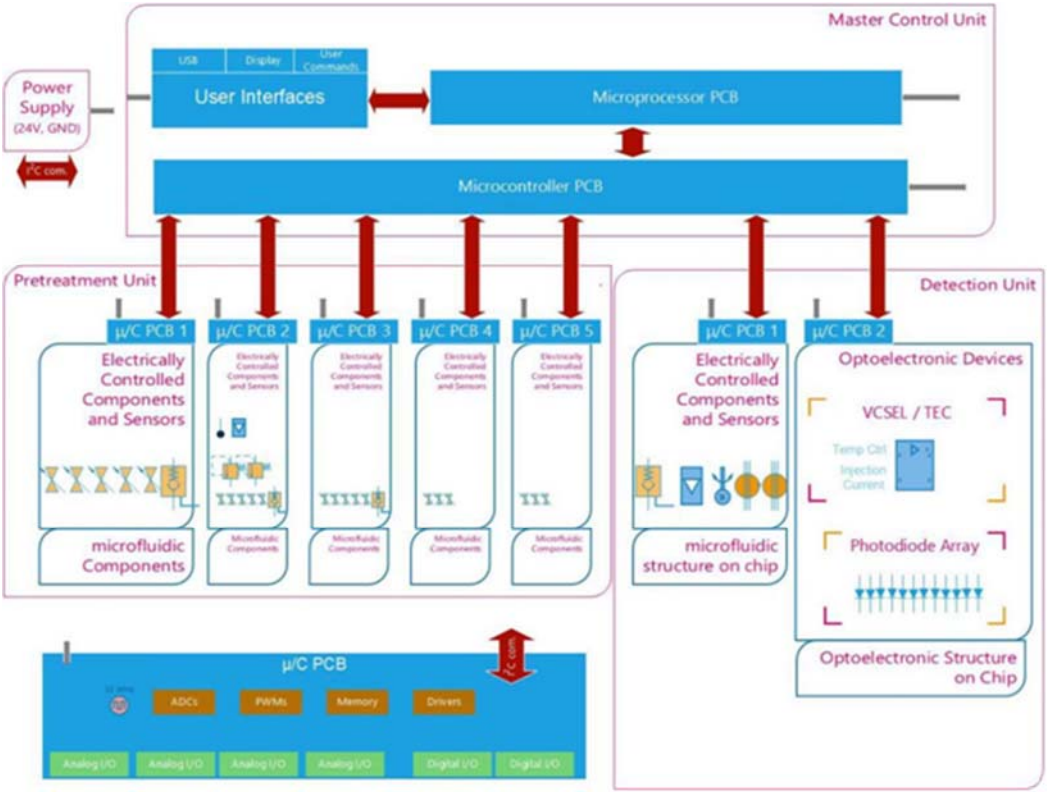

Figure 80: Architecture of RI photonic sensing system's electronic platform.

The electronic platform consists of the pretreatment and detection units, both of which are located on "level zero" of the hierarchy. On top of them, the master control unit is placed which is responsible for the control of the different processes and handling of events. The detection unit itself consists of the microfluidics control unit (uC PCB 1) and the optoelectronics control unit (uC PCB 2) both of which will be described. Specifically, the following units will be described in detail in the following subsections:

1. Master control unit
2. Pretreatment unit
3. Microfluidics control unit
4. Optoelectronics control unit

4.1.2 Master control unit

The master control unit responsible for the control of the biophotonic system, consists of a Minnowboard Turbot [Link Minnowboard] single board computer (**Figure *81***). Minnowboard is a small footprint, yet powerful computer with intel-based processor (x64 architecture) capable of running a full Windows version, which is necessary for proper installation of the LabVIEW runtime engine as it will be explained later on.

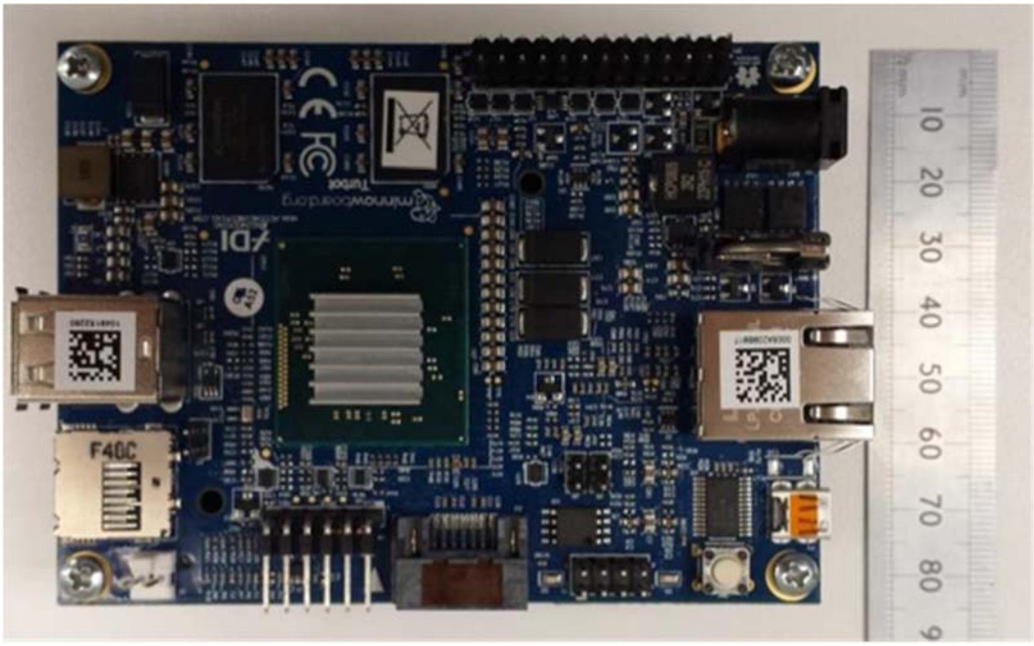

Figure 81: Top view of Minnowboard Turbot with ruler for scale.

The following table provides the Minnowboard specifications:

Table 3: Minnowboard Turbot technical specifications.

Form Factor	MinnowBoard compatible 99 x 74mm
CPU	Intel® Atom™ E3826 (Dual Core) (2 x 1.46 GHz, 1MB cache, 7W, AES-NI)
DRAM	2GB DDR3L 1067MT/s, Memory down (non expandable)
Ethernet	1x 1Gb Ethernet RJ45
Video	Intel HD Graphics, 1x micro HDMI out
Storage	1x SATA2, 1x MicroSD
I/O Connectors	1x USB 2.0 host, 1x USB 3.0 host, 8x buffered GPIO
Expansion Interface	MinnowBoard Max compatible Lure interface
	High-speed expansion connector
	Low-speed expansion connector
Operating voltage	5V DC

The available options for installing windows OS in the Minnowboard were:

1. a high-capacity SD card
2. a USB 3.0 stick
3. a SATA hard disk drive (HDD)
4. mSATA expansion board (Flotsam Lure)

All the above options were investigated in order to find the best performing one for our application. A high speed (Class UHS), high capacity (>16 GB) SD card was tested first, giving low read/write speeds in the order of 20 MB/s and 13 MB/s respectively. These speeds might be sufficient for lighter versions of Windows (e.g. Windows IoT) or Linux but not for a full version which is required for LabVIEW runtime engine.

Regarding installation of Windows on a USB stick, Microsoft supports only Windows 8.1 On the Go version. In order to install the specific version, a Microsoft Windows on the go certified USB stick would be required for full compatibility. Microsoft supports only a small list of certified USB sticks, which apart from being expensive, would impose a hardware limitation in case the USB stick needs to be replaced (e.g., upgrading to a larger capacity stick).

The SATA port on Minnowboard allows the installation of a SATA 2 hard disk drive (max theoretical speed 300MB/s) and allows for installation of operating systems without any restrictions, as it is like installing windows on a desktop/laptop computer. We have successfully installed a full Windows 8.1 version on a SATA HDD and the LabVIEW runtime engine as it can be seen in **Figure *82***

Although the HDD would provide the required performance, it required additional cabling for connection (SATA cable), an extra bulk hardware component (HDD) to integrate during packaging and would draw up to 1 A of current at 5V when fully operational (access operations).

For the reasons above, we have opted on choosing the expansion board (Flotsam Lure) [Link Flotsam Lure], which connects to the high-speed expansion board located on the back of the MinnowBoard (not seen in the figure) and provides a mSATA 3 port for installing an SSD disk (**Figure *83***). The mSATA 3 protocol provides 600 MB/s speed which currently is the fastest. The Minnowboard with the expansion board attached can be seen in **Figure *84***. It is seen that with this board, the footprint of the master control unit changes only slightly in the Z direction which is tolerable (total height with expansion board 3 cm max, as be seen in **Figure *86***). Using

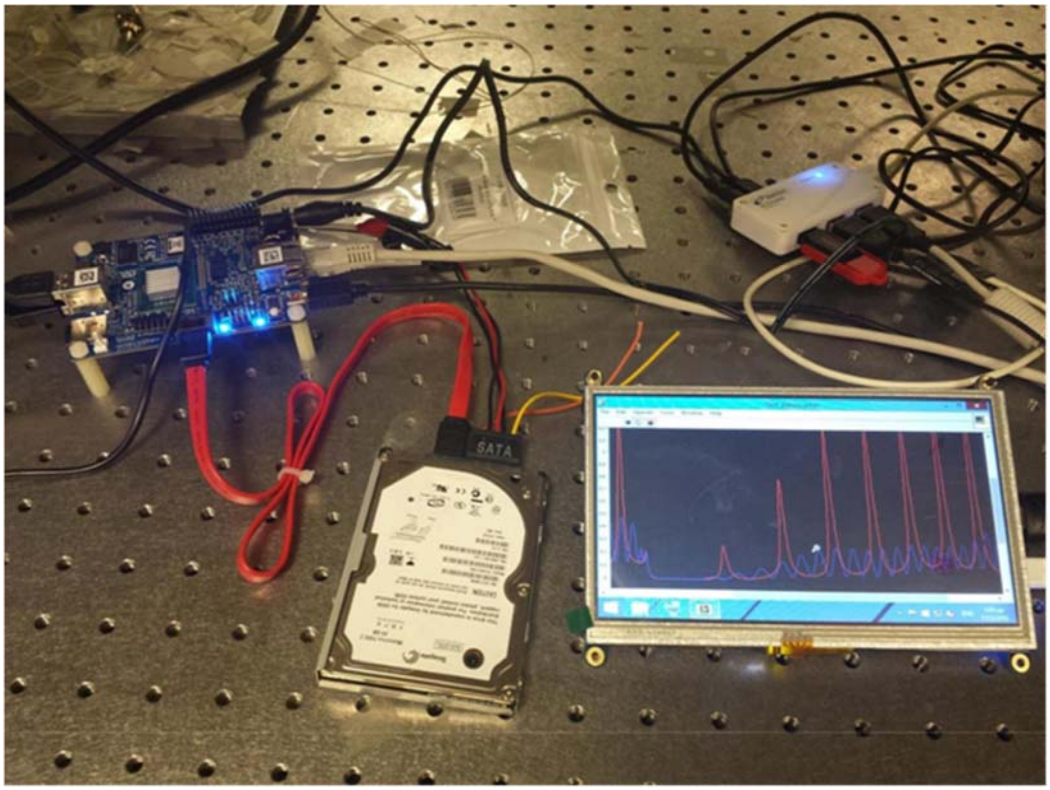

Figure 82: Windows 8.1 and LabVIEW runtime engine running on the Minnowboard from SATA HDD.

this configuration, we have installed a full Windows 8.1 version and the LabVIEW runtime engine on a 120GB mSATA SSD and have tested it with a LabVIEW executable, as it is seen in **Figure *85***.

As it can be seen in **Figure *85***, in order to interface with the master control unit, a 7-inch LCD touchscreen display with resolution of 800x480 from Adafruit is used. This screen connects to the Minnowboard via HDMI (black cable on the figure, HDMI port on the LCD screen, micro HDMI on the Minnowboard). The LCD screen is powered on by the USB port (white cable on figure), which additionally communicates the touchscreen controls to the Minnowboard. In case additional USB ports are required, a USB hub can be used (e.g. the white one in the above figure).

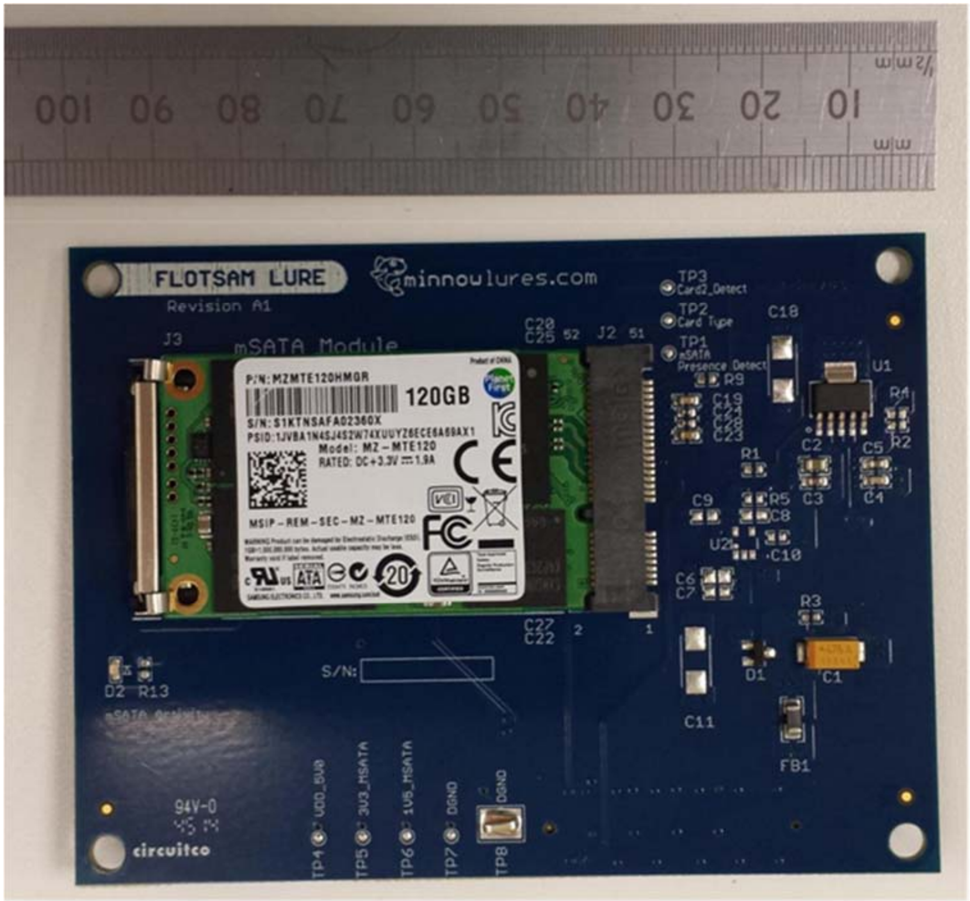

Figure 83: Minnowboard mSATA expansion board (Flotsam Lure).

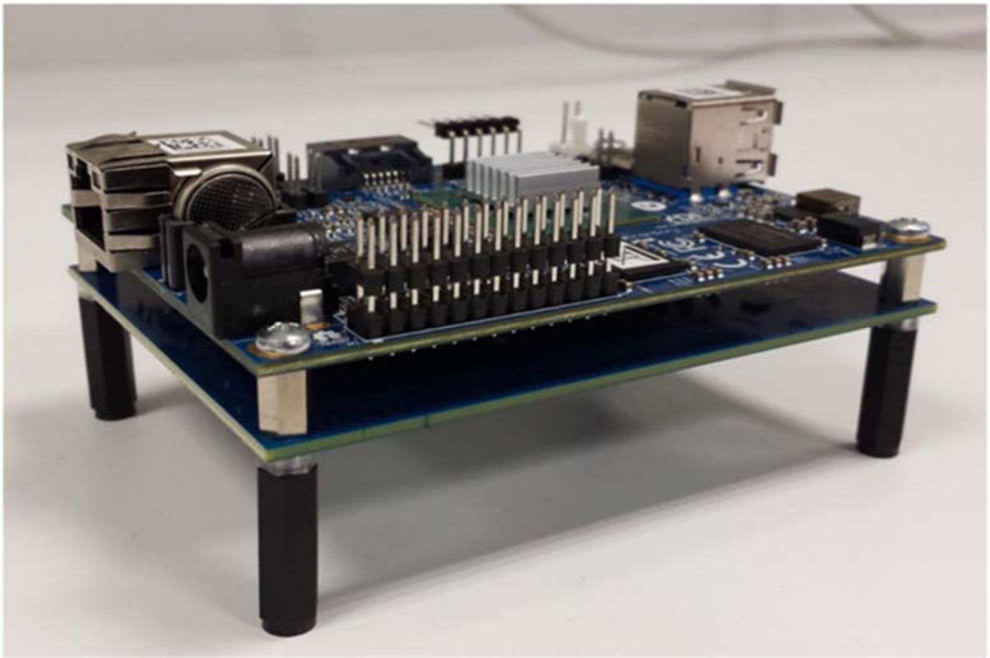

Figure 84: Minnowboard with expansion board installed.

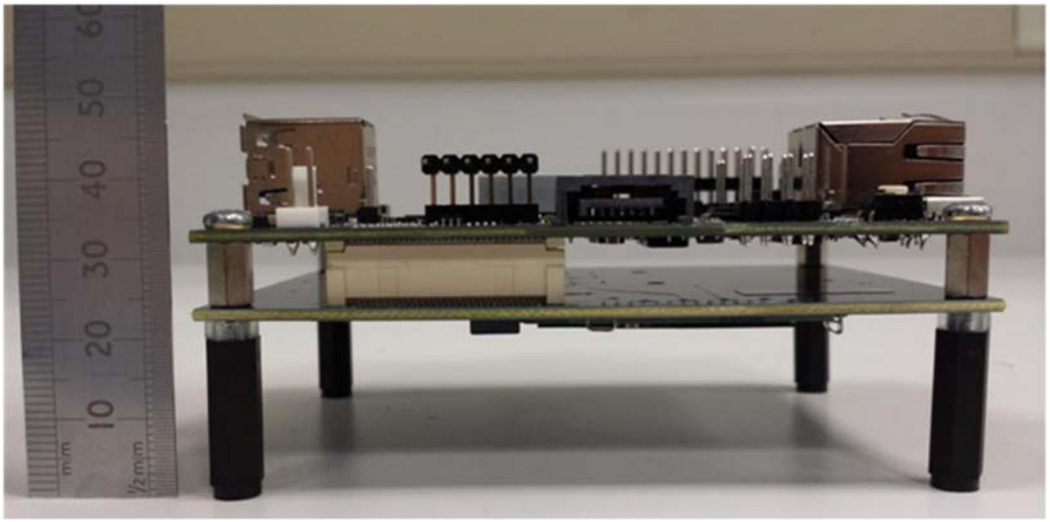

Figure 86: Minnowboard with expansion board from the side with ruler for scale.

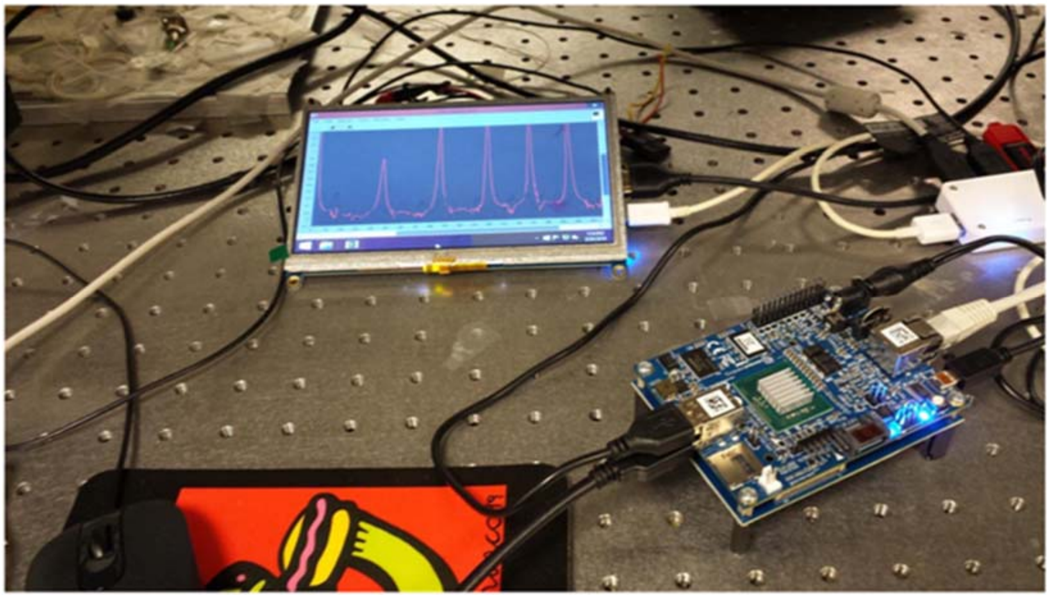

Figure 85: Minnowboard with SSD disk running LabVIEW runtime engine on Windows 8.1.

4.1.3 Pretreatment unit

The pretreatment unit has been designed as a standalone unit, having its own electronic PCB for controlling all different modules of the photonic system - Pretreatment unit (valves, pump, sensors etc.). Additionally, the unit has its own firmware developed, and it only requires basic communication with the master control unit such as “start”, “stop”, “ready” commands. The master control unit essentially sees the pretreatment unit as a “black box”, having only inputs and outputs for synchronization signals mainly.

More specifically, the electronic board contains:

- 12VDC input plug
- 5 digital outputs for 12VDC
- 1 conductivity sensor
- I2C communication port

- USB port
- Stroke counter
- 2 pressure sensors (including temperature sensor)

Apart from the aforementioned electronic board, the pretreatment unit has a BBB (Beaglebone Bone Black) [Link BBB] single board computer embedded as a controller that will also be responsible for the communication with the master control unit. Their communication will rely on exchanging xml files over Ethernet by establishing an FTP server/client pair between the two boards. The packets will mainly be xml files for configuring the pretreatment unit and commands for operating the pretreatment unit.

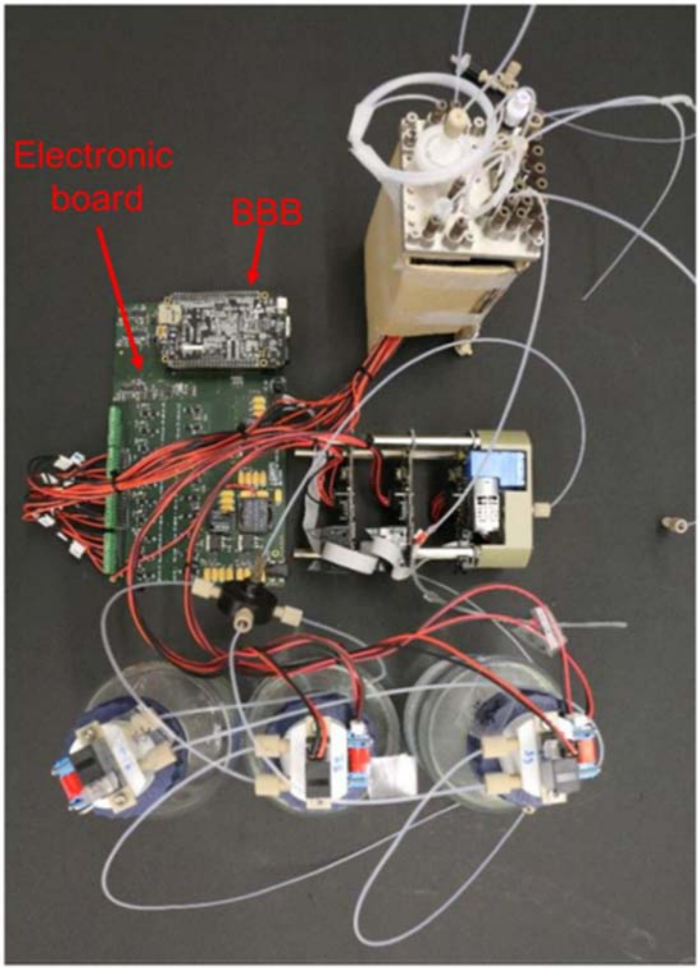

Figure 87: Pretreatment unit with the electronic board, various components and BBB laid out.

4.1.4 Detection unit

As already described the detection unit consists of the microfluidics control unit and the optoelectronics control unit. The first will be responsible for taking the sample from the pretreatment unit, dispense it over the optochip and control the flow rate of the sample (or buffer solutions) in the microfluidic system. Additionally, it will control the different protocol stages (washing, regeneration, sample deposition etc.).

The optoelectronics control unit is responsible for generating the signal function that will drive the VCSEL source, the data acquisition, by digitizing the analog signals coming from the photodiodes, the processing of the results and further streaming them to the master control unit for presentation and/or further processing.

4.1.4.1 Microfluidics control unit

The microfluidics control unit is based on an Arduino Mega 2560 Rev.3 microprocessor [Link Arduino Mega], which can be seen in **Figure *88***.

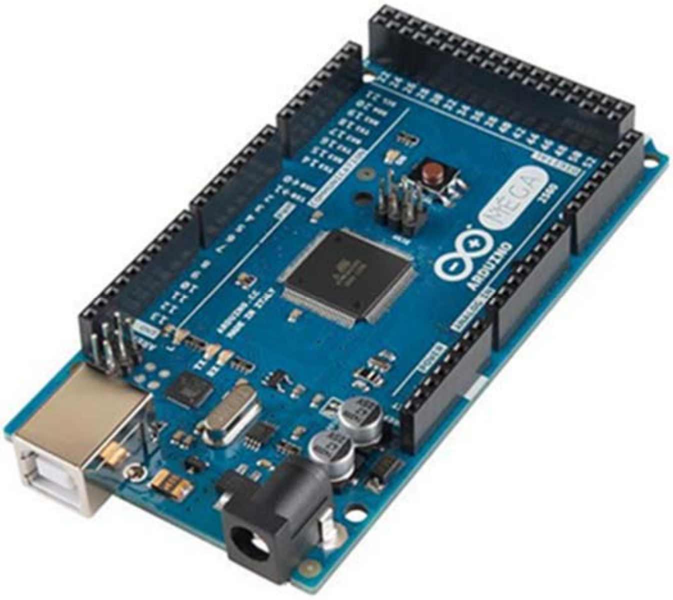

Figure 88: Arduino MEGA 2560 Rev.3.

The Mega 2560 is a microcontroller board based on the ATmega2560. It has 54 digital input/output pins (of which 15 can be used as PWM outputs), 16 analog inputs, 4 UARTs (hardware serial ports), a 16 MHz crystal oscillator, a USB connection, a power jack, an ICSP header, and a reset button. The specifications can be seen in the table below.

Table 4: Arduino MEGA 2560 technical specifications.

Form factor	101 x 53 mm^2
Input Voltage	7-12V DC
Microcontroller	ATmega2560
Flash Memory	256 KB of which 8 KB used by bootloader

SRAM	8 KB
EEPROM	4 KB
Clock Speed	16 MHz
Digital I/O Pins	54 (of which 15 provide PWM output)
Analog Input Pins	16
DC Current per I/O Pin	20 mA
DC Current for 3.3V Pin	50 mA

Using the specific microcontroller as the basis, the Adafruit Motor/Stepper/Servo Shield V2 expansion board for Arduino was added that provided up to 4 DC motor driving capabilities through two independent H-bridges (the H-bridges can handle up to 2 Amps current each). The shield also has overvoltage protective circuitry, as well as thermal shutdown protection circuitry. The motor shield will be programmed to drive the two 12V DC peristaltic pumps responsible for sample dispensation over the optochip.

In addition, the control unit has a Pololu A4988 stepper motor driver for driving the stepper motor that controls the rotary valve. The particular driver is rated up to 2 A per coil with sufficient additional cooling (heatsink). Both drivers can be seen in **Figure *90*** and **Figure *91***.

The microfluidics control unit also has circuitry for biasing an optical switch that will serve as the position sensor of the rotary valve. The optical switch is the Optek/TT Electronics Photologic® Slotted Optical Switch, model OPB940.

The peristaltic pumps, the stepper driver and the optoswitch biasing circuit require either 5V or 12V to operate which are already available. The Arduino MEGA requires 7 V when powered externally to operate without overheating. For that reason, a LM317 [Link LM317] voltage regulator was used with the appropriate filtering circuitry for stable 7V output. The complete microfluidics control unit can be seen in **Figure *89***.

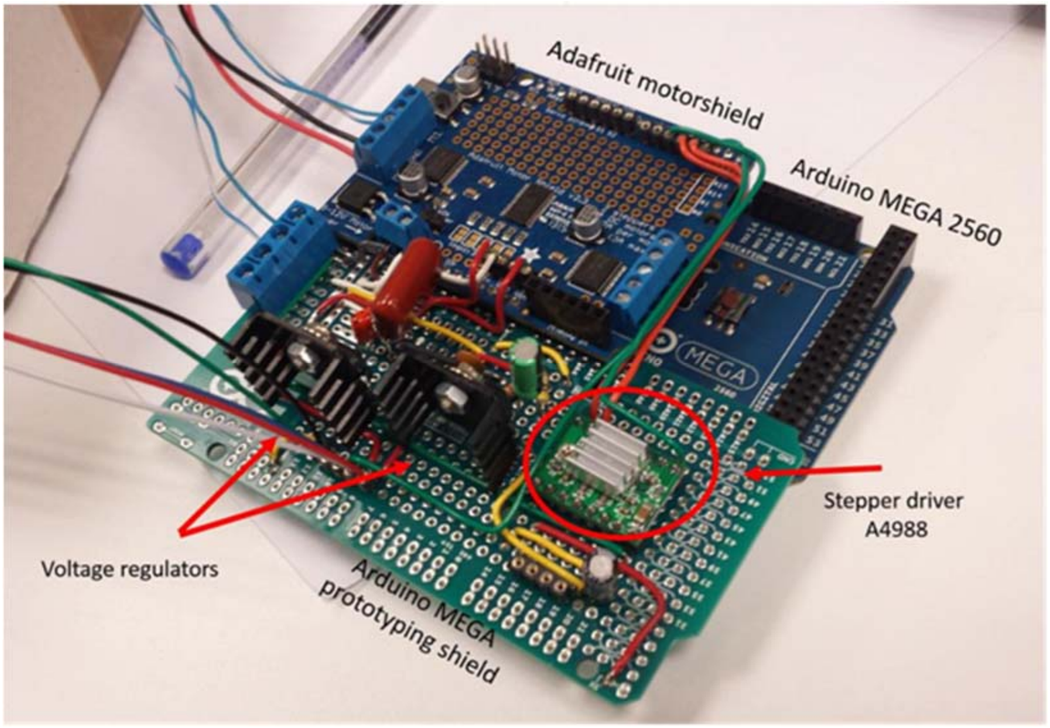

Figure 89: Microfluidic control unit assembled.

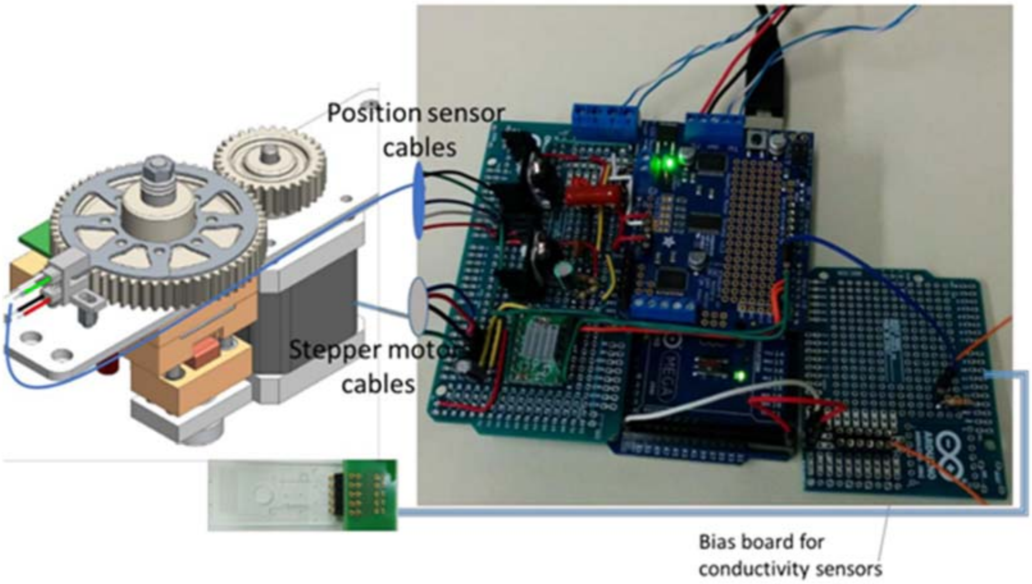

Figure 90: Microfluidic control unit assembly with interfaces to stepper motor and position sensor visible.

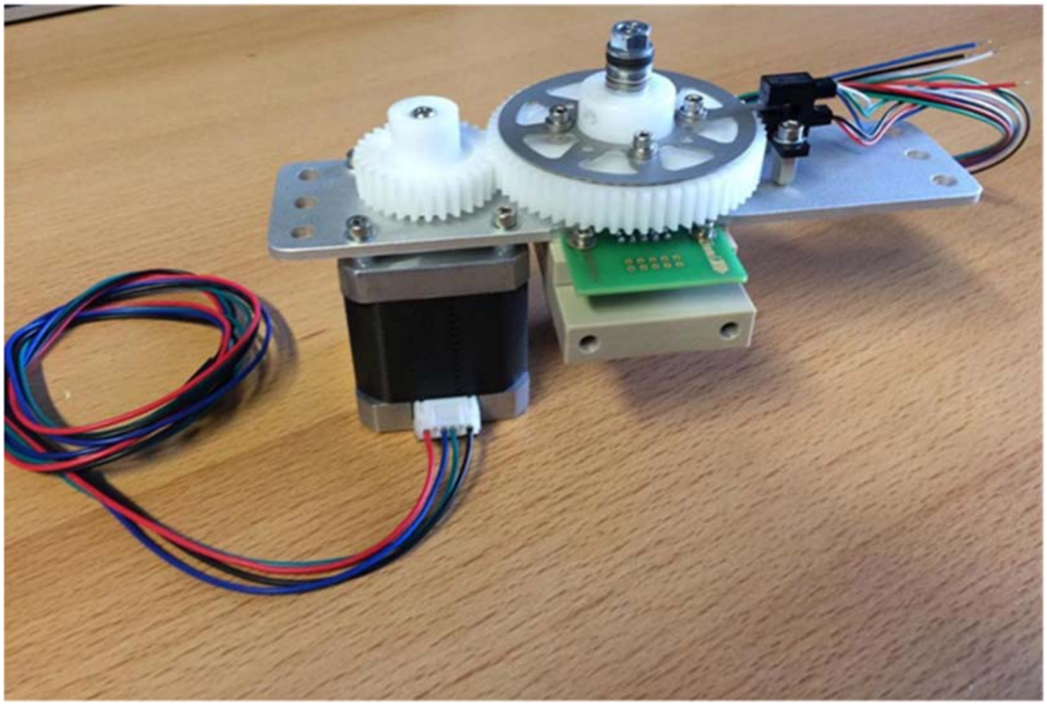

Figure 91: Photograph of the stepper motor on the rotary valve and the optoswitch.

4.1.4.2 Optoelectronics control unit

The optoelectronics control unit is responsible for the generation of the modulation function that will drive the VCSEL source (sawtooth or approximately sawtooth function after

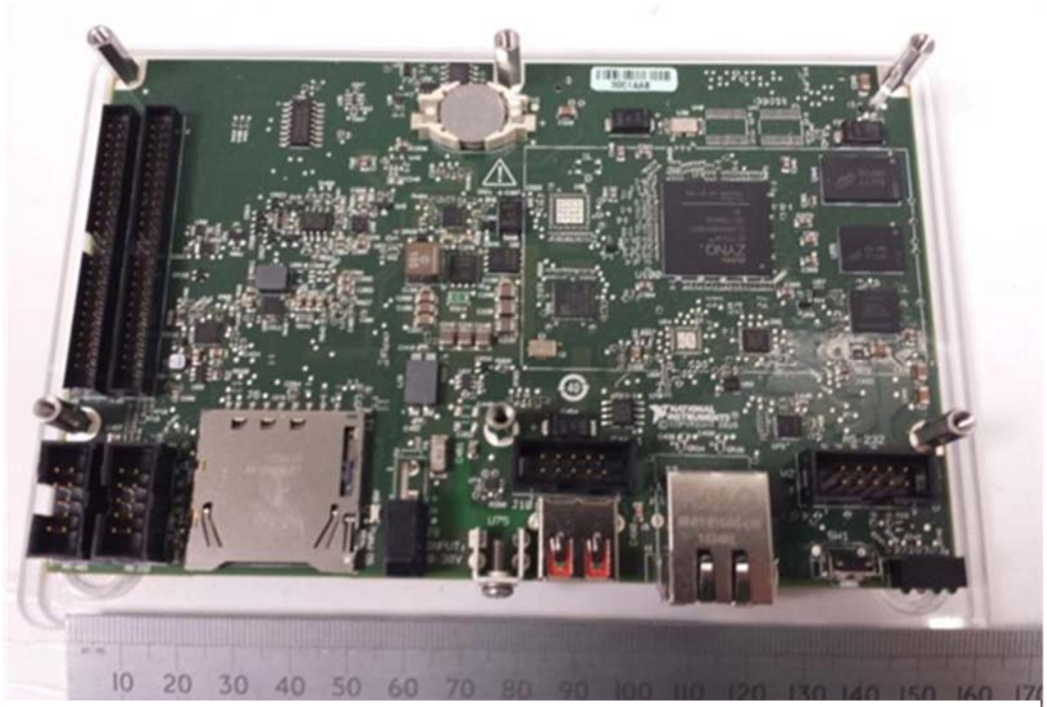

Figure 92: Optoelectronics control unit - single board RIO 9637.

calibration is performed), and for digitizing the signals coming from the photodiodes on the optochip.

On the base of the optoelectronics control unit lies another single board computer from National Instruments, the sbRIO 9637 (**Figure *92***) [Link sbRIO-9637]. The specific board is fully programmable through LabVIEW and integrates on the same board Analog-to-Digital (ADC) converters, Digital-to-Analog converters (DAC), FPGA chip, ARM microprocessor together with memory (RAM).

In more detail the technical specifications of the sbRIO 9637 can be seen on the table below.

Table 5: National Instruments sbRIO-9637 technical specifications.

Processor	
Type	Xilinx Zynq-7000, XC7Z020 All Programmable SoC
Architecture	ARM Cortex-A9
Speed	667 MHz
Cores	2
Operating system	NI Linux Real-Time (32 bit)
Nonvolatile memory	512 MB
Volatile memory (DRAM)	512 MB
Reconfigurable FPGA	
Type	Xilinx Zynq-7000, XC7Z020 All Programmable SoC
Number of logic cells	85000
Number of flip-flops	106400
Number of 6-input LUTs	53200
Number of DSP slices (18x25 multipliers)	220
Network/Ethernet port	
Number of interfaces	1
Network interface	10Base-T, 100Base-TX, and 1000Base-T Ethernet
Communication rates	10 Mbps, 100 Mbps, 1000 Mbps auto-negotiated, half-/full-duplex
Serial ports	
RS-232 (DTE) serial port	2 interfaces (Serial 1, Serial 2)
RS-485 serial port	1 interface (Serial 3)
Embedded CAN	
Onboard CAN	1 (CAN0)
Maximum baud rate	1 Mbps
Minimum baud rate	10 kbps
USB port	

Front Panel USB Host	1 (USB0)
Compatibility	USB 2.0, Hi-Speed
Maximum data rate	480 Mb/s
Maximum front panel USB current	900 mA
SD Card slot	
Front Panel SD	1 (SDIO0)
Supported standards	SD, SDHC
Read	12.0 MB/s maximum
Write	9.0 MB/s maximum
3.3 V Digital I/O on 50- PIN IDC Connector	
Number of DIO channels	28
Maximum tested current per channel	±3 mA
Input low voltage, VIL	-0.3 V minimum; 0.8 V maximum
Input high voltage, VIH	2.0 V minimum; 5.25 V maximum
Output high voltage, VOH when sourcing 3 mA	2.4 V minimum; 3.45 V maximum
Output low voltage, VOL when sinking 3 mA	0.0 V minimum; 0.4 V maximum
Analog Input Characteristics	
Number of channels	16 single-ended or 8 differentials
ADC resolution	16 bits
Maximum aggregate sampling rate	200 kS/s
Input range	±10 V, ±5 V, ±2 V, ±1 V
INL	±64 ppm of range, maximum
DNL	No missing codes guaranteed
Input bandwidth (-3 dB)	540 kHz, typical
Settling error (multichannel scanning)	±60 ppm step size, typical
Crosstalk (10 kHz)	-70 dB
Analog Output Characteristics	
Number of channels	4
DAC resolution	16 bits
Maximum update rate	336 kS/s
Range	±10 V
Current drive	±3 mA/channel maximum
Power-on state	0 V
INL	±194 ppm of range, maximum
DNL	±16 ppm of range, maximum
CMOS Battery	
Type	BR1225 coin cell
Manufacturer	RAYOVAC

The reconfigurable architecture of the sbRIO from National Instruments offers significant benefits when it comes to analog waveform generation and data acquisition. The processes of generating the modulation signal for the VCSEL source and the data acquisition from the 8 photodiodes are controlled by the FPGA processor, since it can guarantee true parallel execution with high fidelity, as jitter is eliminated. Then the data are forwarded to the ARM processor for processing. Some data are sent back to the FPGA for calibration of the VCSEL output (linearize the injection current-output wavelength relation). The following figure presents the architecture with a schematic.

We use 8 analog input ports on the board for digitizing the signals coming from the photodiodes and 1 analog output port for generating a function that will drive the VCSEL laser source. Since the analog inputs and outputs on the board read and write voltage signals respectively, additional circuitry is needed to convert the photocurrent coming from the photodiodes into voltage signal and the voltage function from the analog output into current that will drive the VCSEL source.

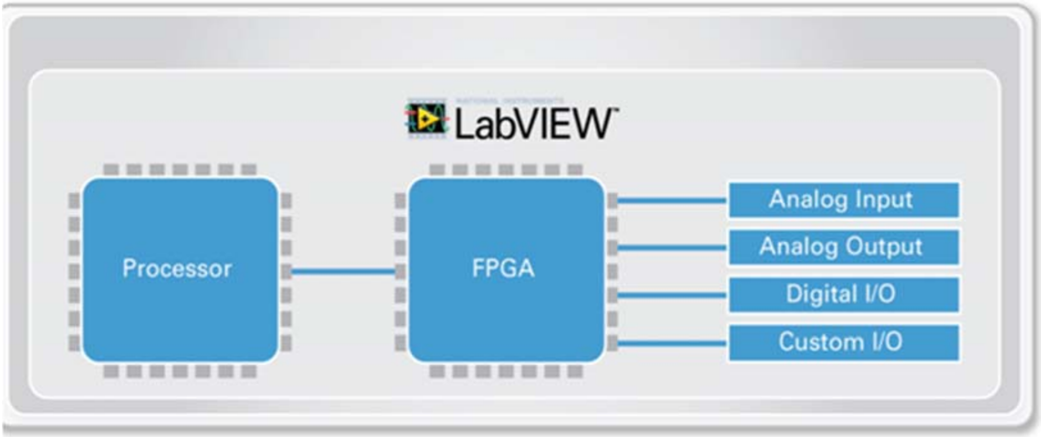

Figure 93: Reconfigurable architecture used in the optoelectronics control unit.

The additional circuitry used consist of a) a voltage to current converter board from Texas Instruments, the XTR111-2EVM, which is a high precision, highly linear voltage to current converter board that takes as input a voltage signal in the range of 0V-10V and outputs 0mA-20mA [Link XTR111-2EVM] and b) a custom, in-house designed, transimpedance amplifier (TIA) board that converts the photocurrent signal coming from the photodiodes into voltage and amplifies it so that it can be accurately resolved from the analog inputs of the sbRIO. The boards can be seen in **Figure 94** and **Figure 95**. **Figure 96** shows how the sbRIO and the boards are connected. **Figure *97*** gives the pinout on the different boards for application reference.

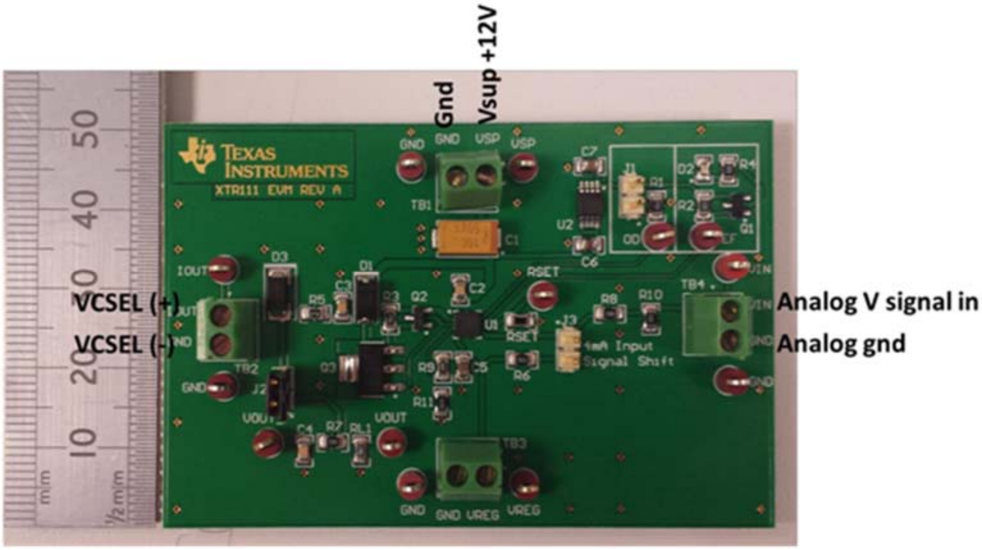

Figure 94: Texas Instruments voltage to current converter board.

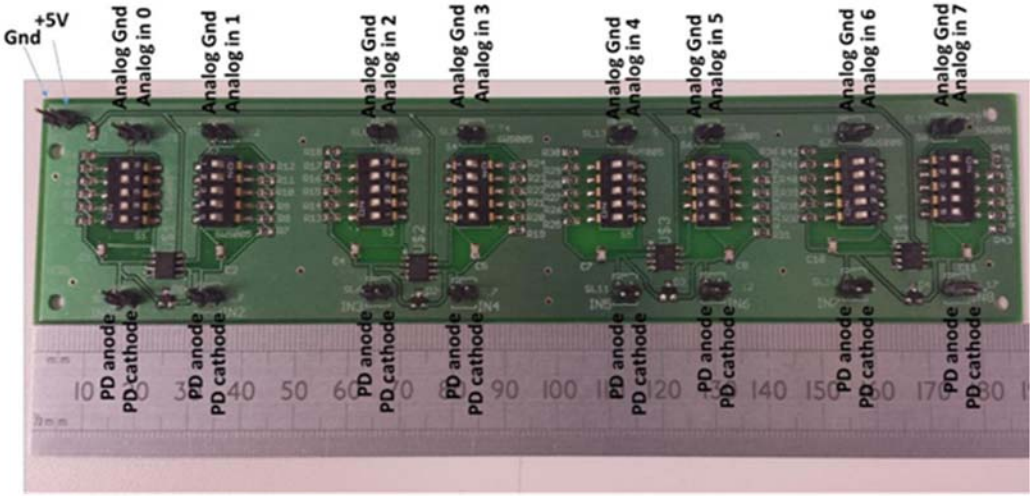

Figure 95: Transimpedance amplifier board.

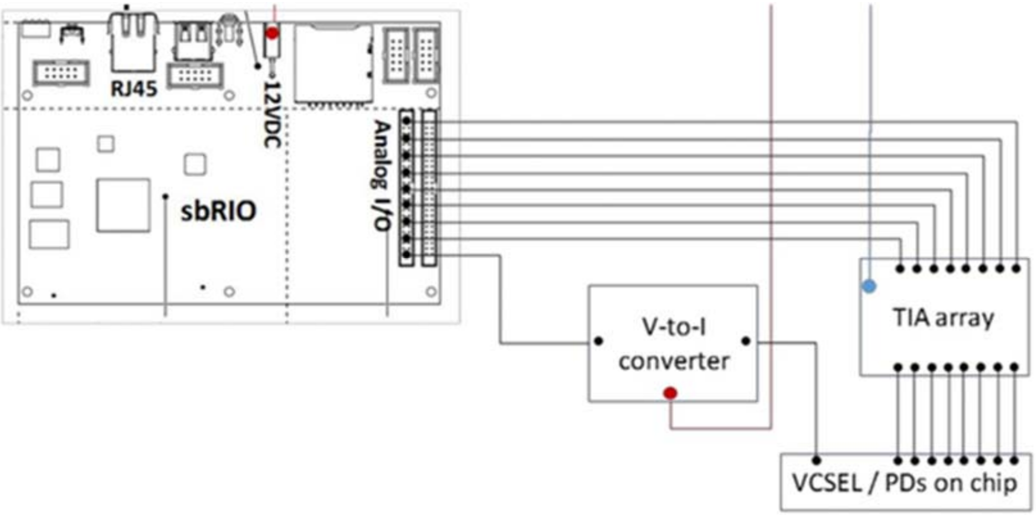

Figure 96: sbRIO and accompanying circuitry connection schematic.

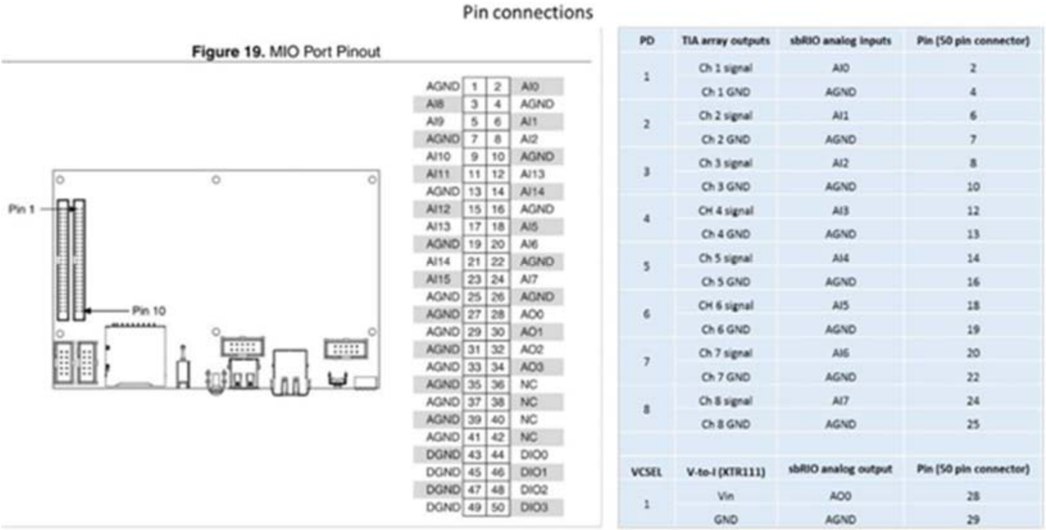

Pin connections

Figure 19. MIO Port Pinout

AGND	1	2	AI0
AI8	3	4	AGND
AI9	5	6	AI1
AGND	7	8	AI2
AI10	9	10	AGND
AI11	11	12	AI13
AGND	13	14	AI14
AI12	15	16	AGND
AI13	17	18	AI5
AGND	19	20	AI6
AI14	21	22	AGND
AI15	23	24	AI7
AGND	25	26	AGND
AGND	27	28	AO0
AGND	29	30	AO1
AGND	31	32	AO2
AGND	33	34	AO3
AGND	35	36	NC
AGND	37	38	NC
AGND	39	40	NC
AGND	41	42	NC
DGND	43	44	DIO0
DGND	45	46	DIO1
DGND	47	48	DIO2
DGND	49	50	DIO3

PD	TIA array outputs	sbRIO analog inputs	Pin (50 pin connector)
1	Ch 1 signal	AI0	2
	Ch 1 GND	AGND	4
2	Ch 2 signal	AI1	6
	Ch 2 GND	AGND	7
3	Ch 3 signal	AI2	8
	Ch 3 GND	AGND	10
4	CH 4 signal	AI3	12
	Ch 4 GND	AGND	13
5	Ch 5 signal	AI4	14
	Ch 5 GND	AGND	16
6	CH 6 signal	AI5	18
	Ch 6 GND	AGND	19
7	Ch 7 signal	AI6	20
	Ch 7 GND	AGND	22
8	Ch 8 signal	AI7	24
	Ch 8 GND	AGND	25
VCSEL	**V-to-I (XTR111)**	**sbRIO analog output**	**Pin (50 pin connector)**
1	Vin	AO0	28
	GND	AGND	29

Figure 97: Connection pinout between the sbRIO and the XTR111-2EVM / TIA boards.

4.1.5 Power distribution network and temperature control

As already described, the biophotonic system operates on 12V DC for safety and car adapter compatibility. An AC power adapter will be used for converting the 230 V AC to 12V DC in order to supply the biophotonic system and an internal DC/DC converter will down convert the 12V to 5V and supply it where necessary. A picture of the power distribution network and how everything is connected, can be seen in **Figure *98***.

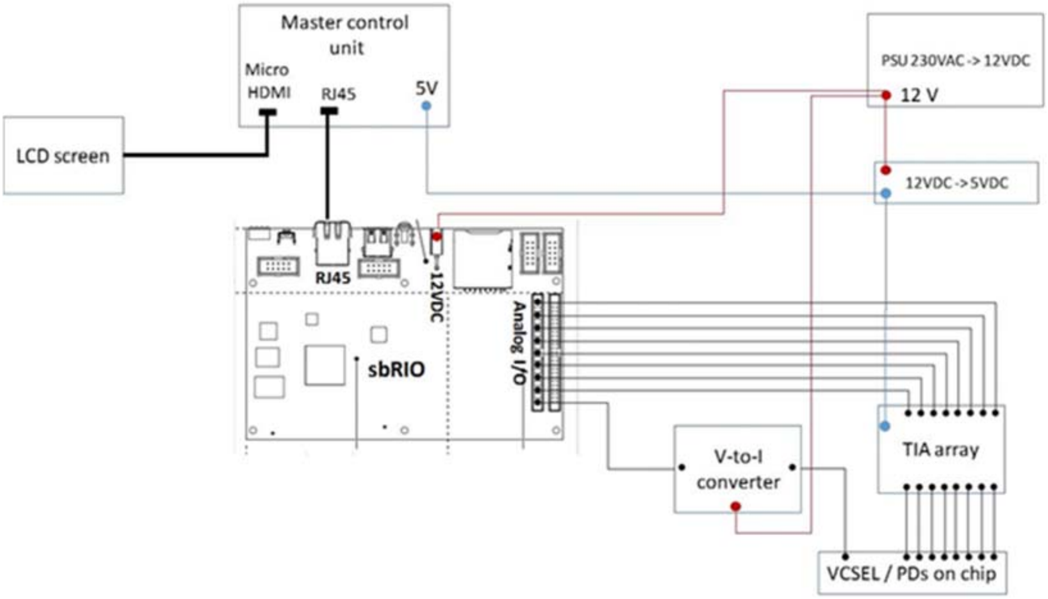

Figure 98: Power distribution network schematic.

The following figure presents the power supply distribution hardware that is used. The AC adapter provides 200W of power at 12V. The power rating was chosen having in mind the worst-case scenario, when all subsystems of the biophotonic unit operate at the same time.

In that case the power consumption can go up to 180W, that's why an AC adapter that can handle power higher than that was chosen. Additionally, the power rating of the DC/DC converter was chosen following this rule of thumb. RHM5K-CH is a TEC controller specifically designed for laser diodes [Link RHM5K-CH], with high accuracy and stability (see below for more details) capable of handling 20 W of power.

Figure 99: Power supply hardware used in the biophotonic system.

In more detail:

- Desktop AC power adapter (ETA-USA, DTE200-12SX-F-W-C2)
    - Power: 200 W
    - Vin: 230 V AC
    - Vout: 12 V DC / 16.66 A
    - 4 pin DIN connector
- Chassis mount DC/DC converter (CUI Inc, PYB30-Q24-S5-H-U)
    - Power: 30 W
    - Vin: 9 - 36 V DC
    - Vout: 5 V DC / 6 A
    - Isolated

  - Dimensions: 67.5 x 55 x 19 mm
  - Heatsink integrated
- Chassis mount TEC controller (Wavelength Electronics, RHM5K-CH)
  - Supply: 12V DC
  - TEC output current: 5A unipolar max (20W max dissipation)
  - Temperature stability: 0.001o C, over 1 h
  - Adjustable Current Limit
  - PID controller
  - Dimensions: 55 x 55 x 20 mm

All connections between components are with screw terminals that makes connections ease and reliable.

4.2 Software platform and user interface of the system

All the key hardware components of biophotonic system (sbRIO, Minnowboard Turbot) were chosen specifically so that they are fully compatible for programming with LabVIEW software [Link LabVIEW2015]. LabVIEW is a graphical software language from National Instruments that provides short time to application development when used with compatible hardware and easiness in creating a user interface, since it provides front panel functions by default. The biophotonic firmware is entirely developed in LabVIEW for complete integration, using LabVIEW version 2015.

The master control unit will run the software for controlling the pretreatment unit, the sbRIO and the microfluidic control unit. The pretreatment unit will have its own firmware and will be seen as a “black box” from the master control unit.

4.2.1 Master control unit (Minnowboard)

The master control unit runs a fully operational version of Windows 8.1. This is needed for being able to install LabVIEW runtime engine and run the LabVIEW executables. The master control unit will run the host executable programs (Vis and TCP/IP server) that will communicate with and control the detection unit (sbRIO, microfluidic unit) and the pretreatment unit. The host vis is designed as finite state machines (FSMs) that will change their state according to the desired operation that the user inputs (start program, calibrate, confirm calibration, acquire data, save data, stop acquisition, exit program). The states on the host VI running in the master control unit correspond to similar states in the sbRIO device, so the state transition diagram will be given in the sbRIO subsection. **Figure *100*** presents how a first version of the user interface looks like. It is noted that the user interface will be under continuous optimization and therefore the final version might look different than the one presented in **Figure *100***.

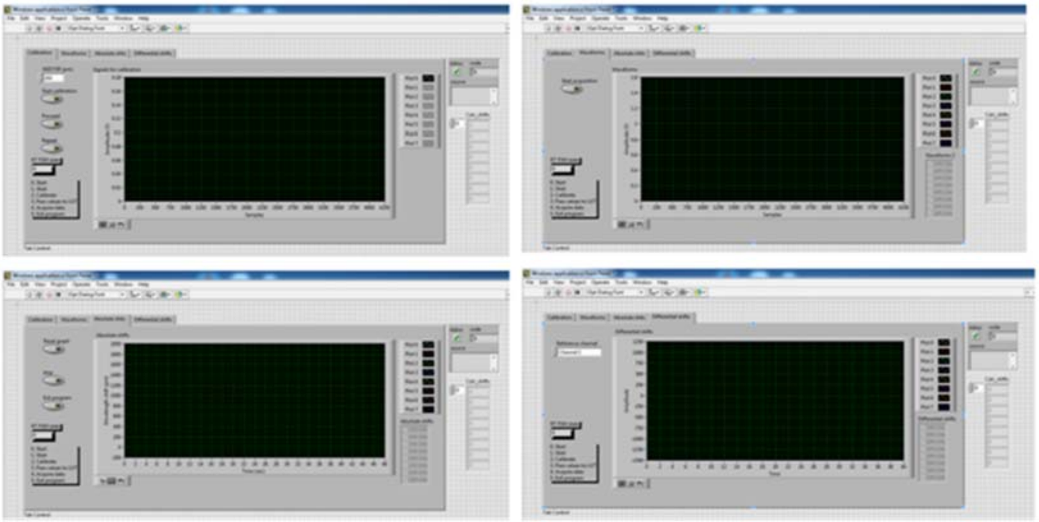

Figure 100: First version of the host vi's user interface in the master control unit (4 different windows for each tab).

4.2.2 Detection unit

4.2.2.1 Optoelectronic control unit (sbRIO)

The optoelectronics control unit runs a Linux real time operating system with an ARM processor, and it has also a FPGA integrated. The software that runs on the sbRIO consists of a program in the FPGA, which is responsible for data acquisition and signal generation with high accuracy in time, and an FSM programmed in the real time (RT) operating system that controls the data acquisition in the FPGA, runs the calculation algorithms for the calibration, delay estimation and streams the processed results to the master control unit for visualization and storing. The state transitions of the FSM can be seen in **Figure *101***. The local program that runs on the sbRIO has its own interface for debugging and testing purposes, similar to the user interface of the host program. This interface, although not visible to the user of the master control unit, can be seen in **Figure *102***.

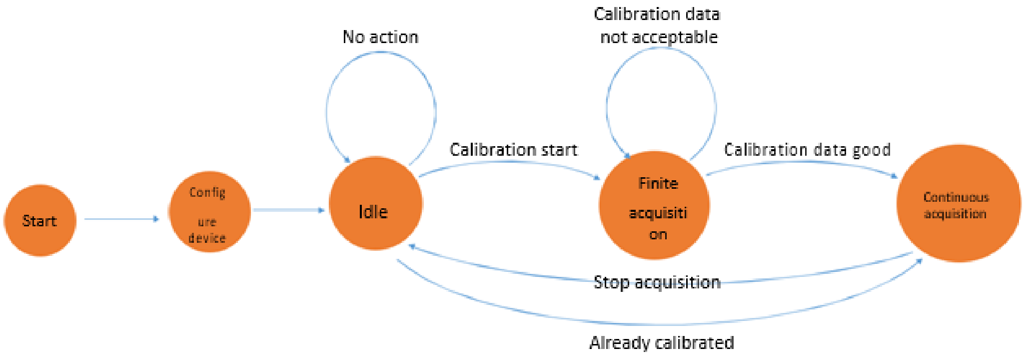

Figure 101: State transition diagram for the FSM running on the real-time target (sbRIO).

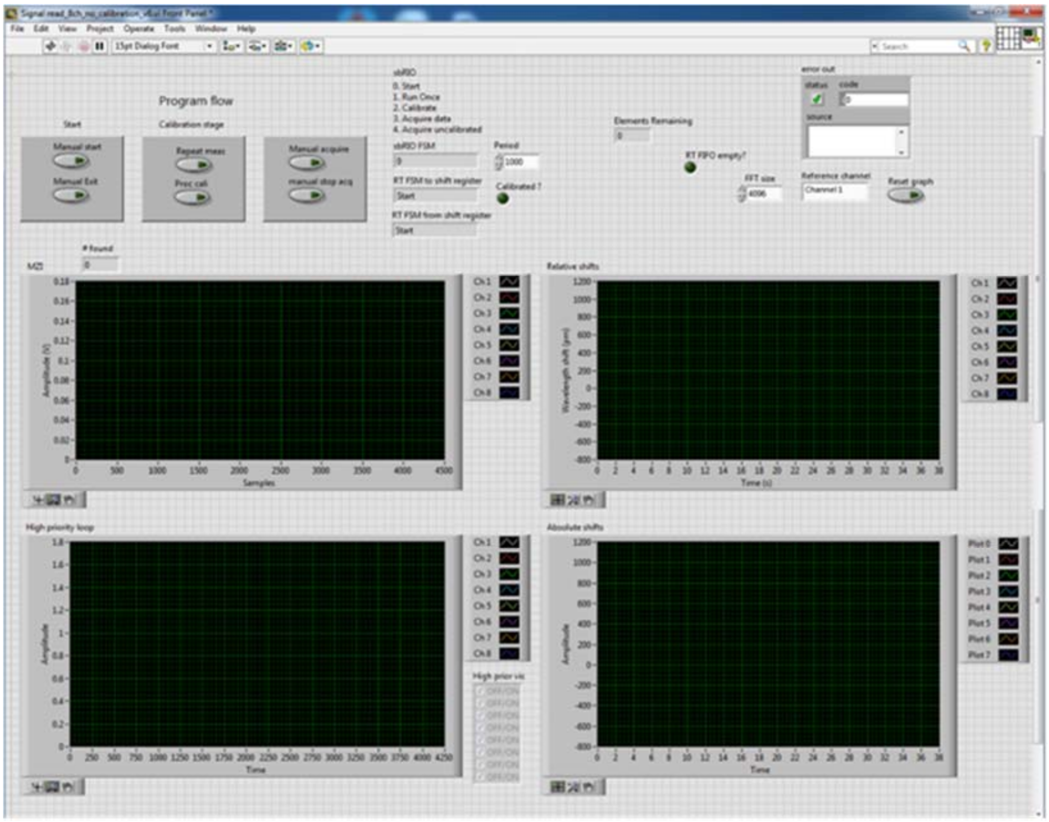

Figure 102: User interface (for debugging purposes) of the program running on the sbRIO.

4.2.2.2 Microfluidics control unit

The program that controls the microfluidic control unit consists of the Arduino firmware that is loaded in the processor, and a host VI program that will run on the master control unit and controls it. At the first version, this program will be standalone and not integrated with the sbRIO program, so that testing, and debugging is straightforward and more efficient. At a later

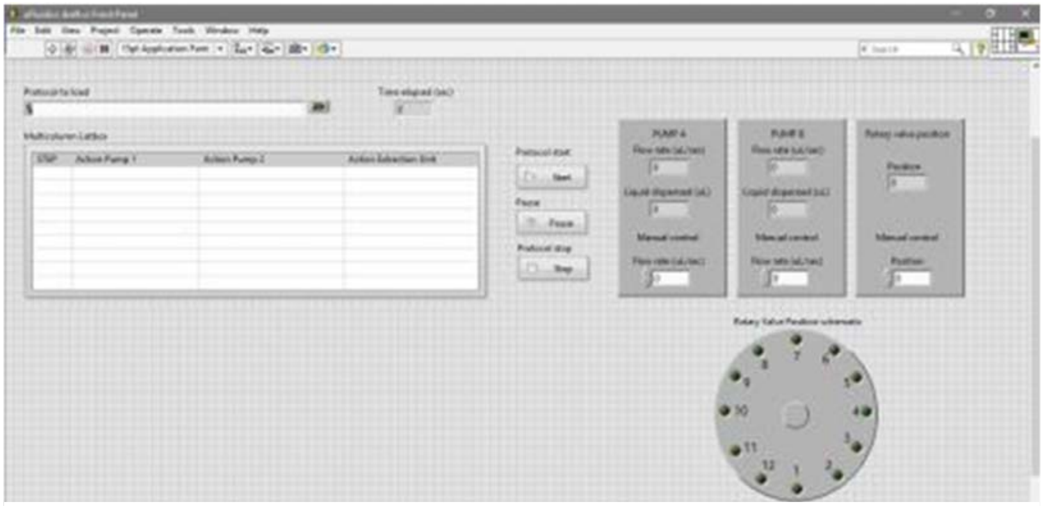

Figure 103: User interface of the microfluidics control unit.

version, the two softwares will be integrated into one host VI executable. A first version of the user interface, again mainly for debugging purposes, can be seen in **Figure *103***.

4.2.2.3 Pretreatment unit

The communication of the pretreatment unit with the master control unit is realized using an ftp server/client pair. This pair establishes communication through parsing xml files containing commands or messages via ftp. As already discussed, the pretreatment unit has its own firmware and will be seen by the master control unit as a black box communicating commands and messages for the type of pretreatment protocol and state of the pretreatment unit. The protocol can be seen in the following figure.

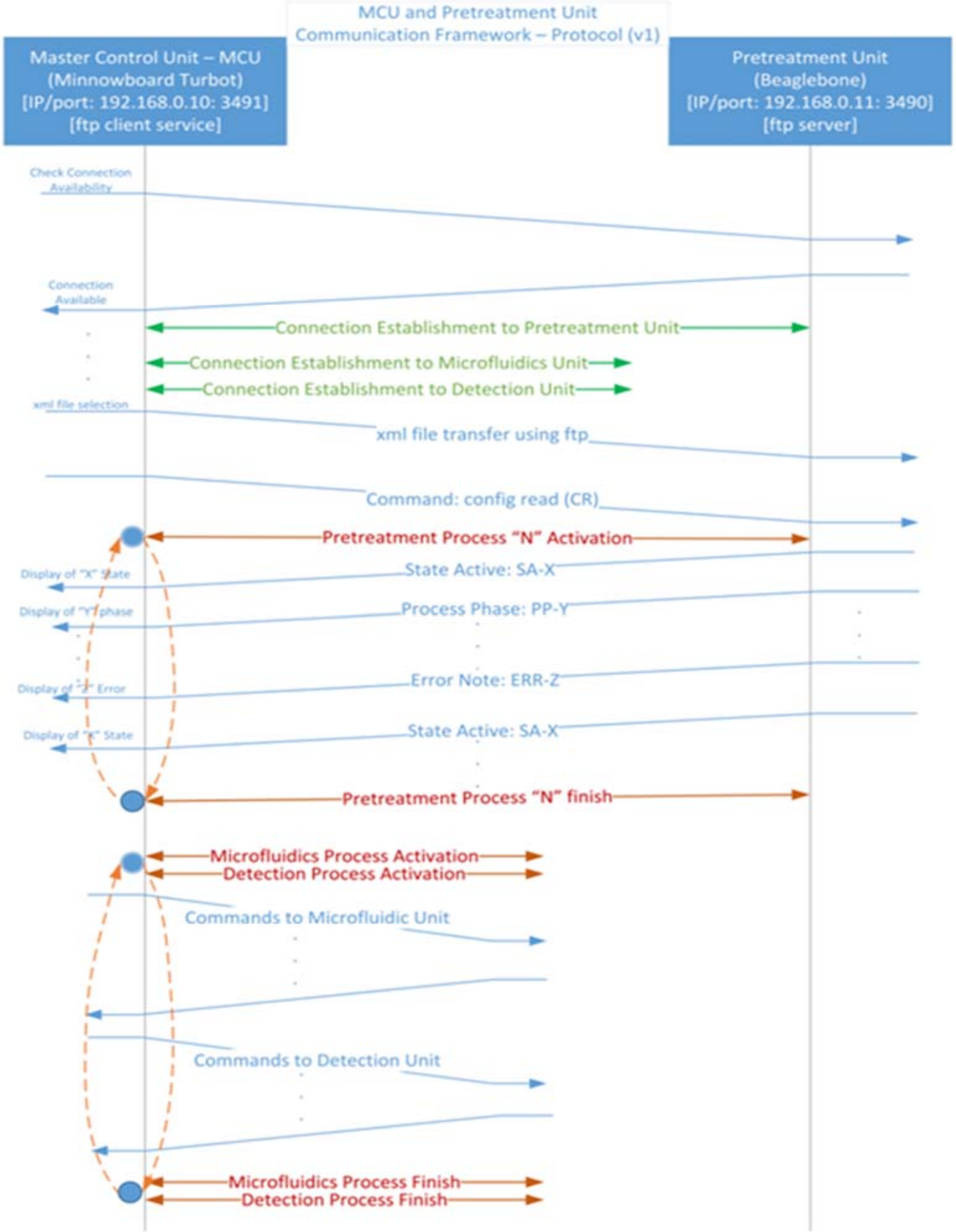

Figure 104: Communication protocol between Pretreatment unit and master control unit based on ftp server/client pair for parsing xml files.

4.3 Experimental results

Within this paragraph, the optimization of the integration process of the MRR chips with the biochemical process so as to achieve the optimum outcome in terms of sensitivity and selectivity, is presented.

All the validation experiments performed using the reference measuring sensing system at PCRL. The figure below presents the experimental setup for the use of the TriPleX chip and the implementation of the reference measuring sensing system. For the coupling of light in and out of the integrated circuit, we use a fiber array unit with one polarization maintaining (PM) fiber and 8 single-mode fibers at 850 nm. Light from a single-mode VCSEL with transverse electric (TE) polarization is transported through the PM fiber and is coupled into the chip. The VCSEL is biased above its lasing threshold and is driven by a sawtooth injection current waveform with 4 mA amplitude. This driving signal enables the repetitive wavelength scanning of a spectral range of 1.86 nm around 855.105 nm. During operation, the temperature of the VCSEL is kept at 30°C using active cooling. The optical signals at the output port of the MZI and the drop ports of the MRRs are coupled out of the chip using the single-mode fibers of the fiber array unit. Eight specific fibers that carry the signal from the MZI, the signal from the reference MRR, and the signals from three sensing MRRs are further connected to an 8-fold array of silicon photodiodes for detection. A low noise transimpedance amplifier (TIA) array with adjustable gains is also used at the back end of the photodiodes in order to amplify the generated photocurrents and adjust their levels within the operating range of the data acquisition system. The latter is based on a board with digital-to-analog converters (DACs) and analog-to-digital converters (ADCs) that are responsible for the generation of the driving waveform and the synchronous sampling of the detected signals.

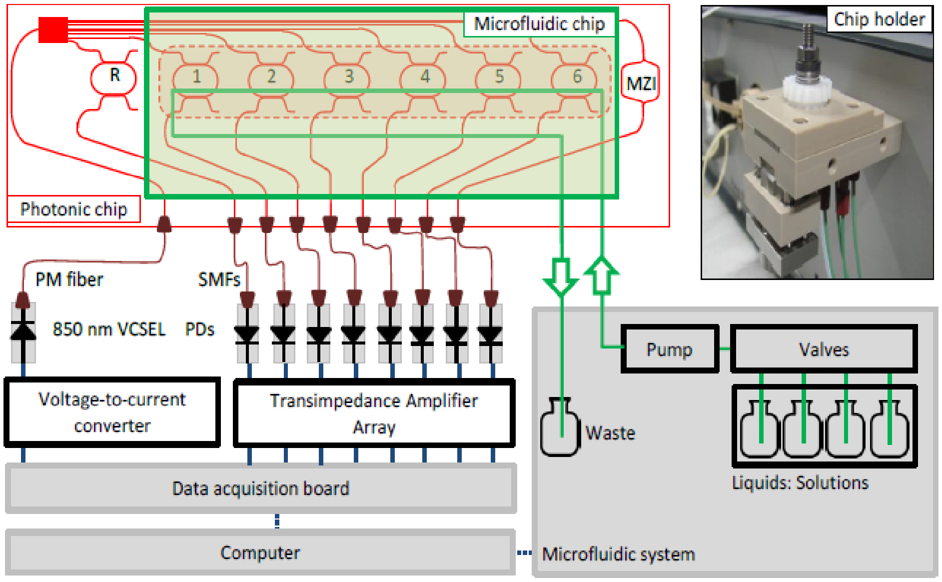

Figure 105: Schematic of the experimental setup for the validation of the FFT method. It is based on the use of the TriPleX chip and a microfluidic system that delivers the solutions inside the sensing window of the MRRs. The RI change is estimated through the resonance shift of the MRRs, which is calculated using the FFT method. The photograph in the upper right part shows the holder the holds together the TriPleX and the microfluidic chip.

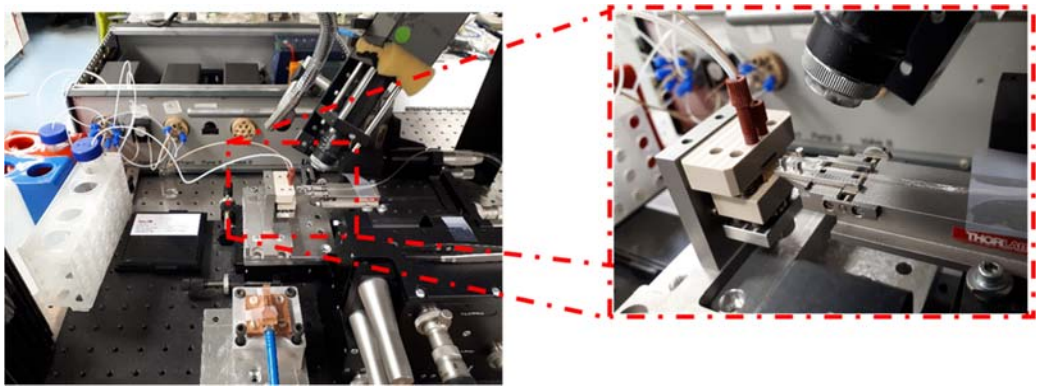

Figure 106: Part of the experimental setup, including the 6-axis probe station with the FAU for the optical alignment and the chip holder through which the liquids are passing over the sensing MRRs.

The maximum sampling rate of the board and the resolution of the converters are 1MS/s and 16 bits, respectively. Using a DAC with this resolution and an additional voltage-to-current conversion circuit, it is possible to generate the sawtooth waveform with high precision and adjust the scanning step to sizes down to 0.5 pm. Using the ADCs on the other hand, it is possible to sample the five detected signals and reconstruct with high fidelity the TFs of the corresponding optical structures that fall within the 1.86 nm scanning range. Although the maximum sampling rate of the board can support scanning frequencies up to several hundreds of Hz, the scanning frequency in our experiments is set to 1 Hz irrespectively of the scanning step. Given the dynamics of the biochemical reactions (binding of the target analytes from the specific aptamers), this frequency is considered sufficient for detecting and tracking all transient effects.

In our proof of principle measurements, we used double-distilled (dd) water with 1.3290 refractive index (RI), and four aqueous solutions of sucrose with mass-to-mass concentrations of 1% w/w, 2% w/w, 4% w/w and 8% w/w. The estimated RI of the first solution is 1.3372, whereas the RI change of the second, third, and fourth solution compared to the first one is $1.6{\cdot}10^{-3}$, $4.8{\cdot}10^{-3}$ and $1.12{\cdot}10^{-2}$, respectively. The liquids are hold in glass containers and are transferred to the sensing window of the chip via a microfluidic system. This system comprises a number of port valves, a peristaltic pump and proper tubing that interconnects the individual elements and ends at the input port of a chip holder [Besselink2016]. The latter provides a means for the physical interfacing between the photonic and the microfluidic part and facilitates the actual access of the liquids to the sensing window of the sensing MRRs. During the measurements, the flow rate of the peristaltic pump is kept constant at 2 micro-liters per second (μl/s). The data acquisition system and the microfluidic system are controlled via a proper software platform (LabVIEW) running on a personal computer. The FFT processing algorithm and the method for the selection of a proper scanning window out of a broader one has been incorporated into this platform in order to perform the signal processing in real-time using the same software environment. The time evolution of the calculated resonance shift of each sensing MRR is visualized also in real time, using either the absolute value of the shift or the relative value of the shift compared to the reference MRR or compared to a different sensing MRR (differential measurement).

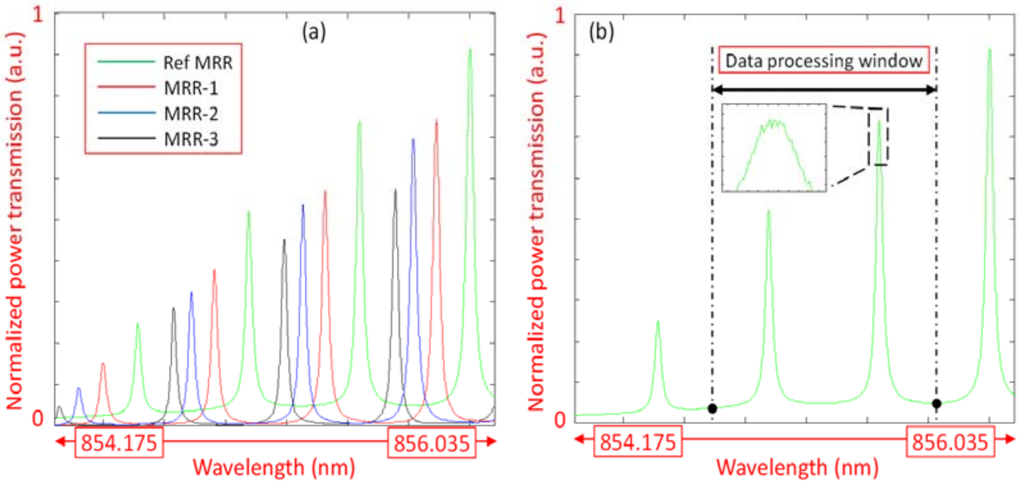

Figure 107: Indicative snapshot of the measurement process, showing the TFs of the reference and the sensing MRRs inside the scanning window from 854.175 to 856.035 nm (a). Algorithm for the selection of a smaller window for data processing out of the initial scanning window in the case of the reference MRR (b). The data processing window is symmetrical and has a width twice as large as the FSR of the MRR. The inset in Figure 130(b) presents a zoom-in on the TF peak.

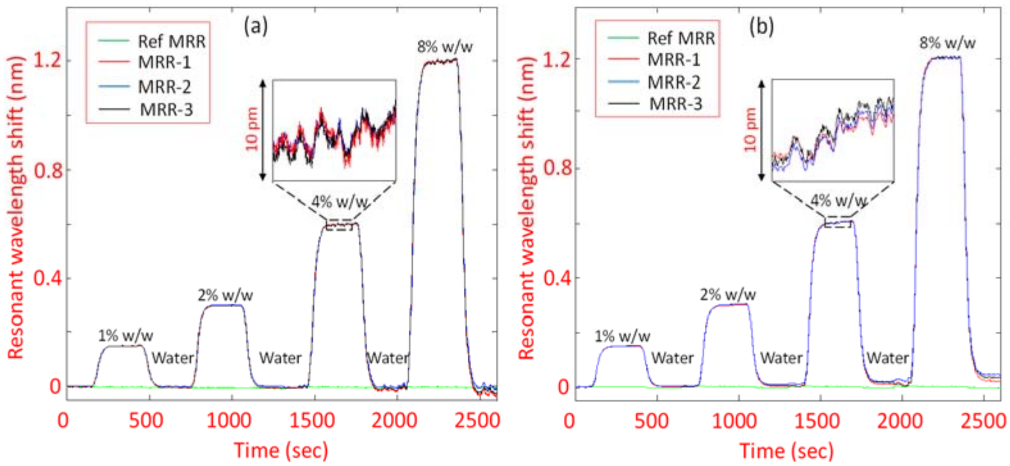

Figure 108: Time evolution of the cumulative resonance shifts corresponding to the reference and the three sensing MRRs during the execution of the main microfluidic protocol with a total duration of 2600 sec (a). The measurements have been performed using the FFT method with 1 Hz scanning frecuency and 0.5 pm scanning step. Results from the execution of the same protocol with a scanning step of 8 pm (b).

Figure 107(a) presents an indicative snapshot of the measurement process showing the TFs of the reference and the sensing MRRs in the spectral window from 854.175 to 856.035 nm. In this exemplary case, the liquid brought inside the sensing window of the MRRs is water and the wavelength step of the VCSEL is 0.5 pm. The time for the scanning of the spectral window and the extraction of the TFs is only one second. In the next snapshot, the TFs are re-extracted, and their possible wavelength shift compared to the previous snapshot is calculated using the FFT method. Since the peaks of each TF are not symmetrical within the scanning window, the calculation of the corresponding wavelength shift is based on a part of the window as per the description in our simulation study. **Figure 107**(b) presents as an example the case of the reference MRR. The part of the window we use for further processing is twice as large as the

FSR of the reference MRR and starts from a point that corresponds to a minimum of the TF. Among the possible intervals that satisfy these conditions for each TF, we always take the right-most one in order to maximize the signal-to-noise ratio. The inset in **Figure 107**(b) presents a zoom-in on the right-most peak of the TF within the selected interval and reveals the amplitude perturbation that is present in our measurement. Using fitting algorithms, it is possible to estimate the standard deviation of this perturbation and conclude that the maximum signal-to-noise ratio (SNR_{max}) of our system is close to 50 dB, remaining in good agreement with the value we used in our simulation study.

Figure 108 presents indicative results from the operation with the four sucrose solutions. The measurement protocol includes four steps, each one with flow of the corresponding solution over the sensing MRRs. Each step lasts 300 sec and is followed by a washing step of the same duration with flow of double distilled water over the MRRs. The measurement of the resonance shifts is made with 1 Hz repetition rate. **Figure 108**(a) illustrates the time evolution of the cumulative resonance shifts that correspond to the reference and the three sensing MRRs over a total period of 2600 sec. All measurements composing the four curves in the particular diagram have been carried out using a scanning step of 0.5 pm. However, the same measurements have been also repeated with scanning steps of 1, 2, 4 and 8 pm. **Figure 108**(b) depicts in fact the execution of the same protocol with a scanning step of 8 pm. As observed in the two diagrams, the evolution of the cumulative resonance shift is very similar for the three sensing MRRs and the two scanning steps, revealing the homogeneity of the sensing MRRs on the TriPleX chip, and the potential of the FFT method to provide reliable results even in the case of coarse scanning steps. On the other hand, the resonance shift of the reference MRR remains in both cases below the noise level, as the liquids have not access to the cladding area of the particular MRR and do not affect the resonance conditions.

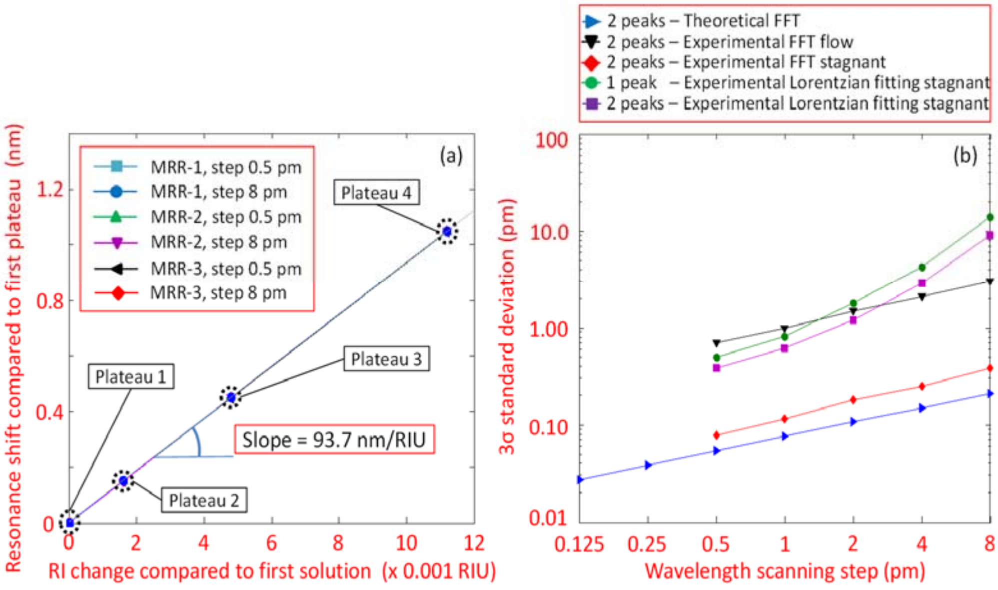

Figure 109: Extraction of the sensitivity of each MRR based on the resonance shift difference of the second, third and fourth plateau from the first one, and the difference in the RI of the corresponding sucrose solutions (a). The sensitivity is extracted from the slope of the fitted curves for the different MRRs and scanning steps. Dependence of the wavelength resolution (given as the 3σ standard

deviation of the measurements) on the scanning step in the case of operation with constant microfluidic flow (2ul/sec) and the case of stagnant sucrose solutions on the MRRs (b). In the case of stagnant solutions., the processing of the measurements has been made both with the FFT method and with two variations of the Lorentzian method. The theoretical curve according to the simulation in **Figure 73** is also presented as a reference.

Figure 109(a) presents the analysis of the measurements concerning the sensitivity of the three sensing MRRs. The diagram presents six sets of points, which correspond to the three MRRs and the two extreme scanning steps (0.5 and 8 pm) in our system. Nine more sets of points that correspond to the intermediate scanning steps (1, 2 and 4 pm) have been also extracted, but are not shown in the diagram in order to keep it clear, since they have practically a perfect overlap with the illustrated data. Each point associates the difference of the second, third and fourth plateau from the level of the first plateau (in pm) with the RI change of the second, third and fourth sucrose solution compared to the first one (in RIU). For each set of points, the estimation for the sensitivity can be made through the calculation of the slope of the fitted linear curve, as shown in **Figure 109**(a). It is noting that the estimated value in all cases presented in the diagram is around 93.7 nm/RIU with standard deviation smaller than 0.1 nm/RIU.

Figure 109(b) presents in turn an analysis of the standard deviation of the measurements, providing an estimation of the wavelength resolution of the system. As a reference for the evaluation of our results we use the blue curve, which corresponds to the simulation results of **Figure 73**(b) for TFs with two resonance peaks and power dependence. The black curve in **Figure 109**(b) refers to experimental data from the run of our microfluidic protocol with different scanning step and shows the dependence of the 3σ standard deviation of the resonance shifts on this step. The measurements that are taken into account for this calculation include all measurements at the four plateaus of each protocol run. In order to ensure that the transients at the rising and the falling edge of each plateau will not disturb the calculation, we use only the measurements that fall within the time interval between 100 and 250 seconds after the start of each protocol step with flow of a sucrose solution. Moreover, for the same calculation we do not employ the absolute resonance shifts, but rather the relative ones by subtracting the absolute values of the first sensing MRR from the absolute values of the second one. This differential scheme is necessary in order to eliminate the measurement noise from the perturbations of the VCSEL source and the fluctuations of the ambient temperature, which are always present in the measurement system [Heideman2012]. Compared to the use of the reference MRR as the reference in this scheme, the use of a second sensing MRR is highly preferable since it can eliminate the temperature noise much more efficiently. The reason for this is that the two sensing MRRs have the same structure and are affected in the same way by the changes in the ambient temperature. On the contrary, the silicon-oxide layer that serves as top cladding in the reference MRR has a thermo-optic coefficient with opposite sign compared to the aqueous solutions that have the same role in a sensing MRR, leading inevitably to different behaviors.

As shown in the black curve of **Figure 109**(b), the standard deviation using the conventions and the techniques described above, remains relatively large (0.6 pm) even in the case of a short scanning step (0.5 pm). This deviation from the theoretical values is associated with the presence of pressure fluctuations on the surface of the sensing MRRs. These pressure fluctuations originate from the microfluidic components in our system and can lead to perturbations of the TFs. These perturbations can be detrimental, since they do not shift together with the TFs, when there is a change in the effective refractive index of the sensing MRRs. Hence, they can affect the center of gravity of the Lorentzian resonances, deforming the shape of the TFs and reducing the accuracy in the calculation of the actual resonance shifts. A possible solution can be the use of digital band-stop filters in order to filter out the spectral components of the perturbations without affecting the useful part of the signals. This type of digital filtering can be applied prior to the FFT in order to improve the tolerance of our method to this type of non-random noise. Work to this direction is ongoing and involves the spectral analysis of the pressure-induced perturbations, the interrelation of this spectral profile with the flow rate and the micro-mechanical properties of the microfluidic chip, and the cancellation of the noise using proper filter designs. It is noted that the same approach can be also used for the cancellation of other non-random patterns in the TFs, like for example the periodic patterns from Fabry-Perot cavities that can be formed in the optical path of the system. Although such patterns are not evident in our experimental results, in principle they can be present in similar experimental setups deteriorating the system accuracy.

In order to experimentally validate our explanation for the deviation between the measurements and the theoretical values of the standard deviation, we have repeated the measurements with a modified protocol, pausing temporarily the flow of the liquids at each plateau, and taking into account for the calculation of the standard deviation only the points that correspond to the time intervals with stagnant sucrose solutions on the sensing MRRs. The red curve in **Figure 109**(b) presents the corresponding results and shows that without the impact of the microfluidic noise, they are remarkably close to the theoretical ones. More specifically, the 3σ standard deviation for 8 pm step is 0.38 pm, whereas for 0.5 pm step is only 0.08 pm, validating the efficiency of the FFT method and indicating that the achievable LOD of our system can be only $8.5\cdot10^{-7}$ RIU. Since our differential scheme is based on the use of two sensing MRRs, the actual demonstration of this ambitious LOD can be realized using either a different photonic chip with separate sensing windows and different solutions flowing over the different groups of MRRs or using the same chip with a single sensing window and surface functionalization of selected MRRs in order to selectively capture the target analytes. The implementation of either approach was not within the scope of the present work. The second approach, however, is the main one for the detection of small biomolecules in various biochemical applications.

Finally, in order to experimentally validate the advantage of the FFT method over the Lorentzian fitting in terms of accuracy, we have re-processed off-line the data from the wavelength scans that correspond to the time intervals with stagnant solutions, using Lorentzian fitting (Equation 103 – paragraph 3.4.6 Benchmarking of the FFT method against the peak search method with Lorentzian fitting).

The parameters a, b and c are iteratively optimized. We have used the same data processing window as before [see **Figure 107**(b)] and have employed two different ways for the optimization of the fitting process. The first one takes into account only the right-most resonance peak inside the data processing window and uses a single Lorentzian function for the fitting of the TF in the area around this peak. The second way takes into account both peaks inside the data processing window and uses the superposition of two Lorentzian functions for the fitting process. The green and purple curves in **Figure 109**(b) present the standard deviation of the differential resonance shift that is obtained with either way, and can be directly compared to the red curve, which presents the corresponding results with the FFT method. As observed in **Figure 109**(b), the superposition of two functions appears to improve the accuracy of the Lorentzian fitting in a way similar to the way that a larger number of peaks improve the accuracy of the FFT method (see **Figure *72***). Nevertheless, even with this improvement, it is clear that the FFT method has a big advantage compared to the Lorentzian fitting, especially for operation with coarse scanning steps.

Interestingly, this higher accuracy of the FFT method comes with a huge advantage also in terms of computation resources and script running speed. More specifically, the execution of our FFT script takes in our LabVIEW platform less than 1 ms. On the other hand, our single-peak Lorentzian fitting script based on the Levenberg-Marquardt method takes almost 1365 ms, prohibiting the data processing in real-time for a scanning rate of 1 Hz. Although certain that our Lorentzian fitting script is not optimum in terms of speed and that the actual running time difference between the two methods can be closer to 100 rather than to 1000, the difference in the running time of the two scripts observed in our platform is indicative for the time and resource efficiency of our FFT method.

The biosensor has also validated by performing proof-of-principle experiments on optical chips which are chemically modified with aptamers for OTA. The different activation steps were monitored using the MRR measurement. One example of the successful preparation of the aptamer layer against OTA is shown in the following **Figure 111**.

In order to be able to check the specificity of the biomodified MRRs with aptamers against OTA (MRR1 and MRR2), two of the six (6) MRRs of the photonic chips were modified with aptamers against Copper ions (MRR5 and MRR6).

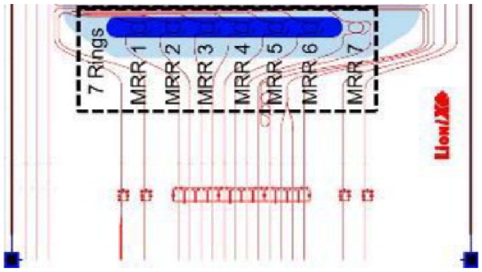

Figure 110: Chip layout used for the biochemical experiments.

Mg^{2+} is crucial for the proper functioning of the OTA aptamer. As illustrated in **Figure 111**, in the absence of the divalent cation, the analyte cannot bind onto the immobilized aptamer. The situation is reversed in the presence of magnesium. The shift observed is due to presence of magnesium in the binding buffer. Upon addition of OTA, the MRRs that had been functionalized with the aptamers against OTA gave a response which was significant, compared to the MRRs that had been functionalized with aptamers against copper which were also thiol modified and did not respond as shown in **Figure 112**. This confirms the specific binding of the mycotoxin OTA target molecules to the aptamers targeting OTA.

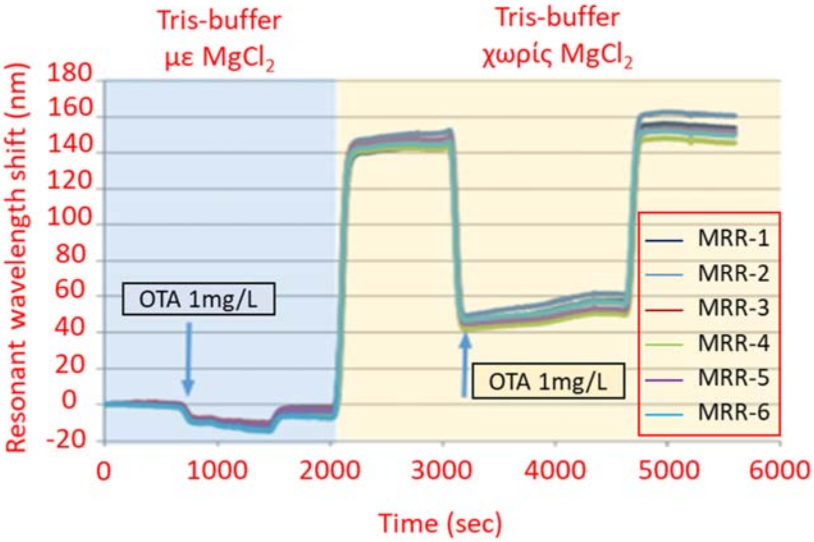

Figure 111: Sensorgram obtained on a multi (6) MRR chip sowing the sequence of OTA target binding onto the aptamer modified sensor, for the two different binding buffers with and without Mg^{+2} ions.

As shown after differentiating the signal of MRR1 (modified with aptamers against OTA) with the negative control of MRR5 (modified with aptamers against copper), there is a significant shift of 6 pm.

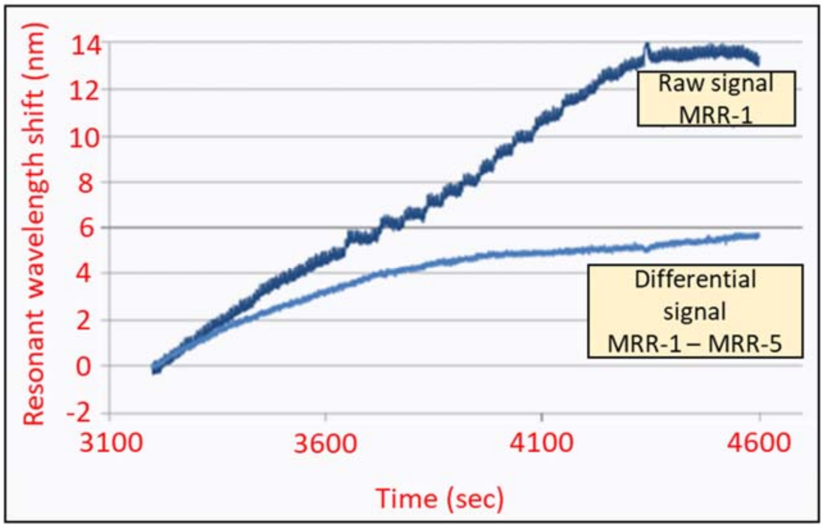

Figure 112: The raw and processed data as received from the **Figure 111** for the MRR1.

Furthermore, another technique of transferring and immobilizing the bio-recognition elements (aptamers against OTA) on the MRRs of the photonic chips, employing by our colleagues from MLMP group of NTUA, the Laser Induced Forward Transfer technique (LIFT). In this frame, several assays performed on optimizing the LIFT technique parameters (such as laser fluence, laser beam profile, position of the optical chip from the donor substrate) for immobilizing the aptamers on specific MRRs of the photonic chips with complete spatial control and ultimate immobilization efficiency. The laser-based technique has been employed for bio-modifying either functionalized or non-functionalized photonic chips. **Figure *113*** shows, the modification of specific MRRs applying the laser induced forward transfer-LIFT technique compared to the deposition with a pipette on silane-modified MRRs. In comparison to pipette deposition (one droplet of minimum volume), the LIFT technique can successfully transfer and immobilize aptamers at each individual MRR of the chip making thus feasible the bio-modification of the chip with different aptameric sequences.

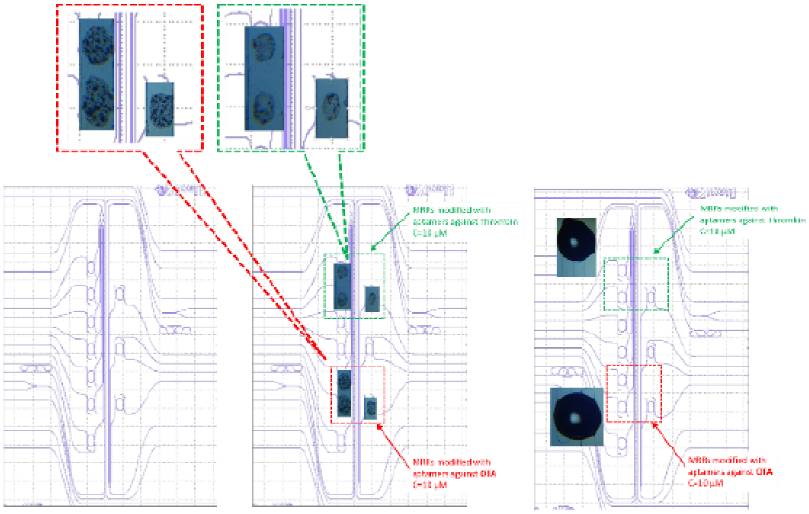

(a) Non-modified (b) LIFT (c) pipette

Figure 113: Optical chip containing six (6) MRRs and an additional reference from the left side and from three (3) MRRs from the right side (a), modified with aptamers against Thrombin (2 MRRs top-left side and 1 top-right side) and against OTA (down-side) using the LIFT technique (b). Aptamers were also deposited on the respective MRRs using pipette at the smallest possible volume.

Moreover, a lot of assays performed on validating bio-modified chips, using different aptamers and functionalization protocols. As a second round of the validation experiments on biomodified optical chips with aptamers targeting the target analyte Ochratoxin A, we observed that using as binding buffer the phosphate buffer (Phosphate Buffer 10 mM, 10mM KCl, pH 7.5) containing 5 mM $MgCl_2$, which was considered as the optimum one from the assays. Through several assays, it was concluded that the recorded signal which were initially defined as ‘false’ where the extremely sensitive response of the MRRs to the refractive index changes induced by the precipitation of magnesium phosphate, as the latter is known to be insoluble on aqueous solutions.

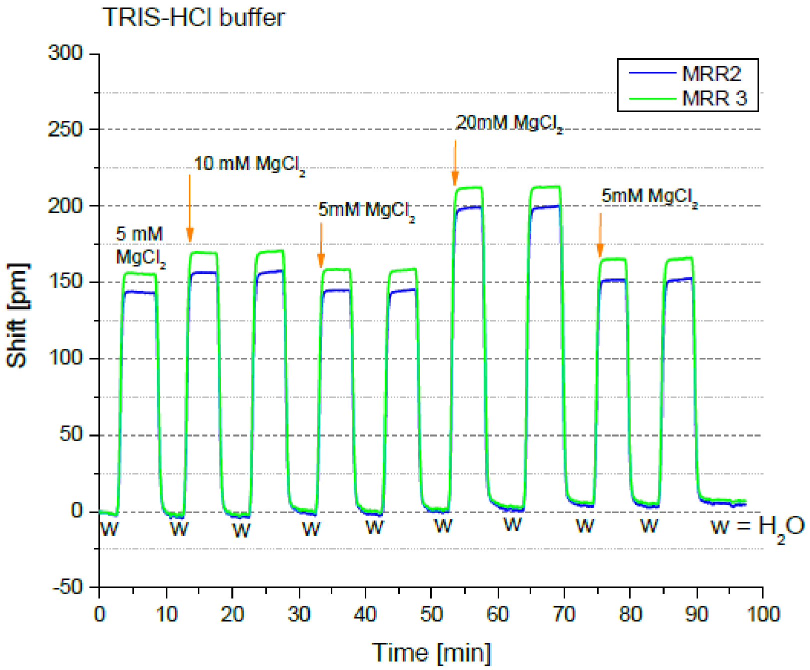

Figure 114: Measurements with buffer solutions with different concentrations of $MgCl_2$ used for the detection of the mycotoxin OTA.

Since the presence of magnesium chloride is essential for the folding of the aptamer and hence for its ability to recognize its target analyte, different buffers that would not form precipitates have been tested. Hence the phosphate was swapped for Tris. The composition of the buffer that was used from then onwards was 10 mM Tris-HCl, 120 mM NaCl, 5 mM KCl (pH 8.0). Tris-HCl does not precipitate in the presence of magnesium chloride. Changing to the Tris-based buffer for the measurements on the MRRs did not interfere significantly with the ability of the aptamers to bind to their target analytes as resulted from assays performed on flat surfaces which performed in parallel with the validation on real MRRs.

In **Figure *114***, it is shown the response of the detection unit on the Tris-HCl buffer solution with small differences in the concentration of $MgCl_2$, presenting the high stability, repeatability and reliability of the measuring system.

For biomodifying the photonic chips with high spatial control and thus being able to immobilize different aptamers on each different MRR of the chip, the sensing surfaces have been modified using the laser-based technique LIFT. In **Figure *116*** and **Figure *117*** is shown the response of the measuring system upon capturing of the Copper ions using aptazymes. The aptamer against copper is unique since it consists of two strands. The first strand (GGTAAGCCTGGGCCTCTTTCTTTTTAAGAAAGAAC) is longer in length, 36nt long and is immobilized onto the surfaces, similarly to the rest of the aptamers. However, the recognition of copper ions does not happen with this immobilized strand alone. A second, shorter strand is hybridized to the immobilized one (AGCTTCTTTCTAATACGGCTTACC, 24nt long) and in the presence of copper this strand gets removed. In essence, the longer strand exerts an enzymatic action on the shorter strand which acts as the substrate. For this reason, the copper aptameric sequence is better described as an aptazyme. Breaking of the substrate strand into two fragments and the subsequent dissociation of both of them from the immobilized strand is what we detect with the MRRs when we expose the aptazyme on the MRR surfaces to copper ions. Since the molecular weight of the substrate strand is quite large (7.500 Da), this makes the detection of copper easier to monitor due to the large shift anticipated and recorded. The following schematic representation (**Figure *115***) outlines the principle of operation of the copper aptazyme.

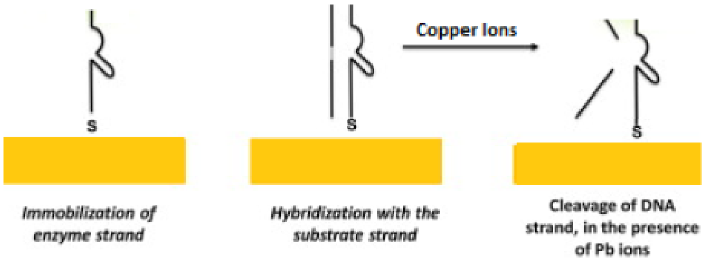

Figure 115: Schematic representation of the copper aptazyme immobilized on the MRR surfaces prior to and upon addition of copper to the system.

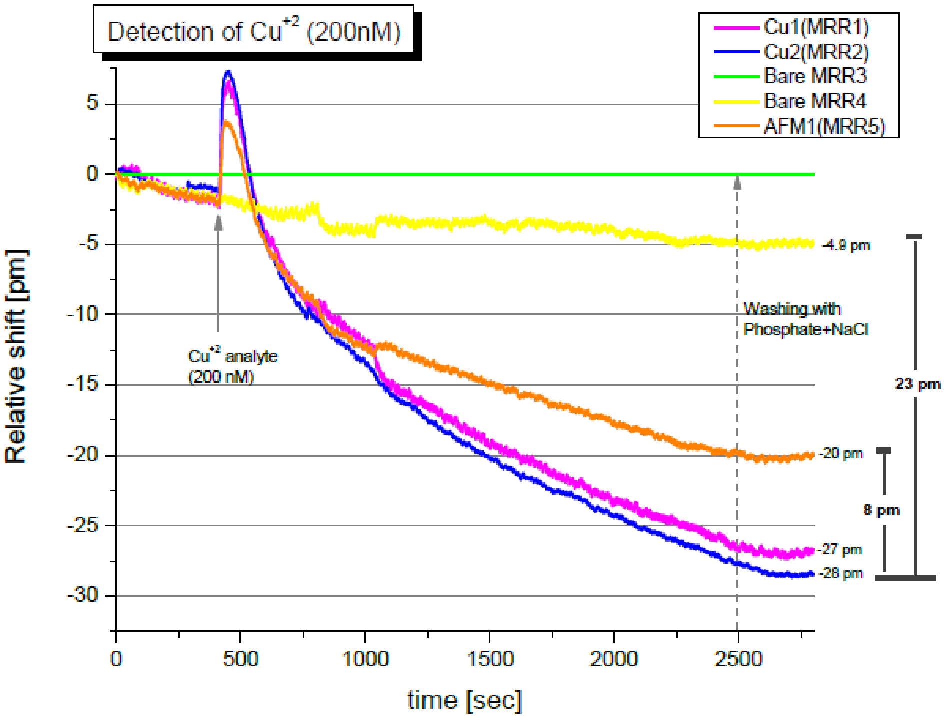

Figure 116: Copper ions detection using the experimental setup in PCRL. Experiment 1.

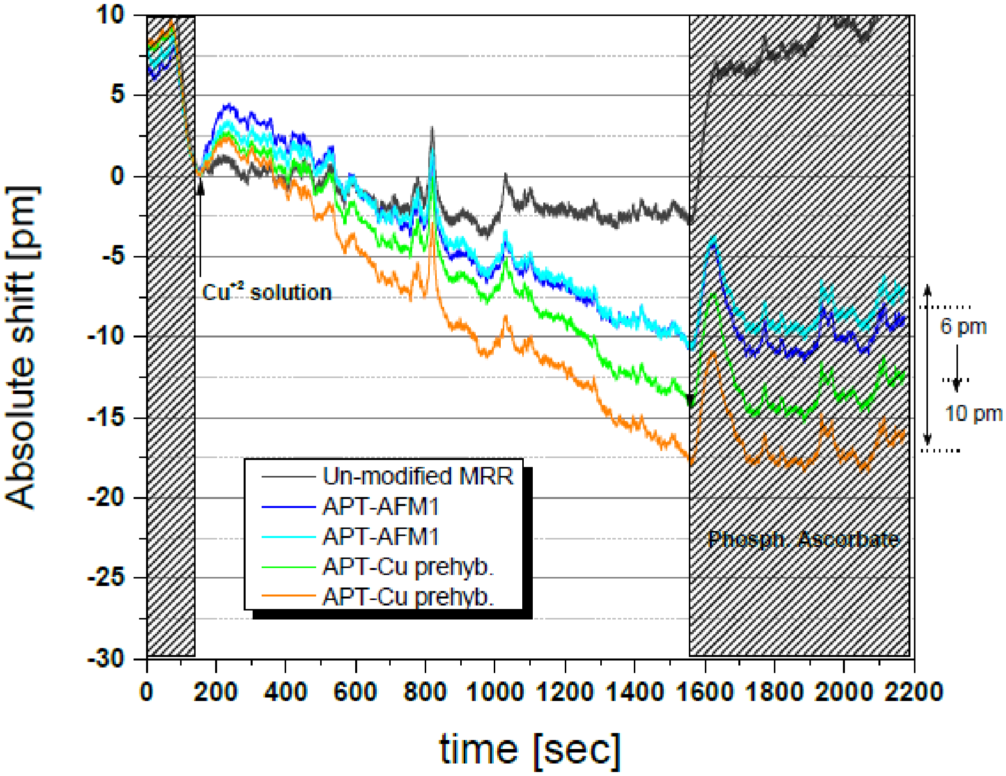

Figure 117: Copper ions detection using the experimental setup in PCRL. Experiment 2.

In conclusion, a measurement system with a microfluidic system have been developed and demonstrated. The photonic part, consisting of MRR-based chips on TriPleX platform with $1.5{\cdot}10^4$ Q-factor has been validated, using sucrose solutions with different concentrations implementing bulk refractive index change experiments, as well as biochemical samples on biomodified MRR surfaces. Using the absolute resonance shifts of the MRRs, we have estimated that their sensitivity is close to 93.7 nm/RIU. Using the relative resonance shifts on the other hand and excluding the noise from the microfluidic part, we have confirmed that the wavelength resolution of the measurement system can be 0.38 pm for a coarse scanning step of 8 pm and only 0.08 pm for a finer step of 0.5 pm. Moreover, the biosensor was successfully validated with good specificity for the case of Copper. The detection was overall good for the detection of the different analytes, mainly using the complementary aptamer approach.

4.4 References of Chapter 4

[Link Minnowboard]
https://software.intel.com/content/www/us/en/develop/topics/iot/hardware/minnow-board-turbot.html

[Link Flotsam Lure] http://www.minnowboard.org/wiki_subdomain/Flotsam_Lure/

[Link BBB] https://beagleboard.org/black

[Link Arduino Mega] https://store.arduino.cc/arduino-mega-2560-rev3

[Link LM317]
https://www.ti.com/lit/ds/symlink/lm317.pdf?ts=1615091335550&ref_url=https%253A%252F%252Fwww.google.ca%252F

[Link sbRIO-9637] https://www.ni.com/en-us/support/model.sbrio-9637.html

[Link XTR111-2EVM] https://www.ti.com/tool/XTR111-2EVM

[Link RHM5K-CH] https://www.teamwavelength.com/product/rhm5k-ch-5-a-unipolar-chassis-mt-temp-controller/

[Link LabVIEW2015] https://www.ni.com/pdf/manuals/374715c.html

[Besselink2016] G.A.J Besselink, R. Heideman, E. Schreuder, L.S. Wevers, F. Falke , and H.H. Van den Vlekkert, “Performance of Arrayed Microring Resonator Sensors with the TriPleX Platform,” J Biosensors and Bioelectronics 7(2), 209, 2016.

[Heideman2012] R. Heideman, M. Hoekman, and E. Schreuder, “TriPleX-based integrated optical ring resonators for lab-on-a- chip and environmental detection,” IEEE J. Sel. Top. Quantum Electron. 18(5), 1583–1596 (2012).

Chapter 5. Conclusions

In this chapter, the work that carried out and presented in this PhD thesis is concluded and a few directions for future work are given.

5.1 General conclusions

Within this thesis, a novel, photonic biosensor based on MRRs, designed on the TriPleX platform has been described. The thesis was focused on three individual sections.

Firstly, in chapter 2, an analytical description of the design of the photonic components that consist the photonic sensor was given. The simulation methods that have been used were extensively presented for each one of the different design stages. Using the appropriate simulation tool, the basic waveguide structure was optimized in terms of propagation losses and compactness towards the hybrid integration and single mode operation at 850 nm. The photonic structures that enable the compact implementation of the photonic circuit without fiber pigtails and external polarization control were presented. These structures include the multimode interference couplers (MMIs) for splitting the optical power into eight equal part that feed the parallel MRRs, grating couplers for the vertical coupling of the VCSEL light into the TriPleX platform. The designs with the best simulation operation have been fabricated, tested, and characterized. These results were in a particularly good agreement with the theoretical values. Moreover, a third photonic structure, the polarization rotator has been designed and simulated. The goal was to take the advantage of the higher penetration depth of the TM propagated mode to the sample, in order to increase the sensor's sensitivity. Nevertheless, due to fabrication limitations and difficulties, it was not feasible to fabricate and thus, experimentally characterize this structure.

Secondly, in chapter 3, a method based on the FFT for the processing of the measurement data in bio-photonic sensors that rely on optical resonant cavities and wavelength scanning lasers was investigated. The FFT method compared the transfer function of the cavity with a reference curve using a large number of samples that lie both inside and outside the resonance spectrum. By this comparison it can provide accurate estimation of the resonance shift in the subsample resolution regime overcoming the fundamental limitation of the peak-search approach. The method can also ensure high performance for practical systems with large scanning steps and cavities with low Q-factor and low round-trip amplitude transmission, and it can provide high tolerance to the amplitude and spectral noise that are always present in the measurement. Using an MRR as the model cavity and appropriate statistical models for the amplitude and spectral noise, we have shown through Monte-Carlo simulations that the FFT method has optimum performance for relatively low Q-factors around 10^4 and that it can result in system resolution improvement by more than two orders of magnitude compared to the peak-search method. This directly translates into an equivalent improvement in the detection limit of the sensor system, which continues to hold true even when the peak-search method is combined with ultra-high Q-factor designs and ultra-short scanning steps, due to the trade-off between the system resolution and the system sensitivity in this type of sensors. Moreover, comparing the FFT method with a more complex variant of the peak-search method with Lorentzian fitting, it was found that it can ensure the same level of error in the estimation of the resonance shift using a wavelength scanning step almost 270 times shorter. Furthermore, the impact of factors like the number of the resonance peaks, the wavelength dependence of the laser power and the asymmetry of the transfer functions have been investigated.

Thirdly, in chapter 4, a detailed description of the electronics has been given as well as validation experimental results have been presented that verify the agreement of the FFT method with the trends of the numerical studies. The hardware comprising the electronic platform has been carefully selected for its compatibility with the programming language. The hardware has been selected after performing a thorough search of the available options and through testing different electronic components in order to choose the most appropriate, having in mind their integration in the complete system. The testing of the components validated their seamless compatibility, functionality and high performance, ensuring a functional bio-photonic sensor. The programming language selected (LabVIEW) offers high flexibility, allowing the developer to focus on the application and easily design user friendly graphical user interfaces. The user interfaces that have been developed, offer a simple environment that would be straightforward to use even by non-experts. The measurement system that was developed for the validation of the FFT-based method consists of the microfluidic and the photonic part. Sucrose solutions with different concentrations were used in these experiments. The MRRs' sensitivity has been estimated close to 93.7 nm/RIU. The resolution of the measurement system was found 0.38 and 0.08 pm for scanning step 8 and 0.5 pm, respectively. The latter led to limit of detection value of $8.5\cdot10^{-7}$ RIU, which is a record performance for this kind of sensors.

5.2 Future work

Based on the photonic component designs for the light manipulation into the photonic integrated circuits, the FFT-based algorithm for the accurate detection of the refractive index changes in liquid samples, the electronic boards and layouts that have been developed and the experimental results that have been presented under the framework of this thesis, a number of actions can be identified for the future.

In the medical diagnostics industry for example, there is an ever-increasing need for the development of robust, reliable, accurate and fast devices for early diagnosis, screening and monitoring diseases allowing for the presently emerging paradigm shift of Personalized Medicine and Companion Diagnostics. In the case of cancer deaths, which in EU, surpassed those from cardiovascular disorders representing the number one cause of death (over 25%) and in the years to come, cancer incidents and deaths are expected to rise, in line with the increase of life expectancy, the World Health Organization (WHO) states that many cancers can be reduced, and patients to have a high chance to be cured if cancer is detected early and treated adequately, through the personalized management of the patients while there is a growing consensus among clinicians and investigators that this is the only viable defense against cancer morbidity. Cancer diagnostic testing is performed mainly in laboratories that are often remotely located from the site of patient care, are equipped with large and complex instruments that typically require highly skilled personnel to operate and are performing batchwise and not delivering immediate results to clinicians after taking the samples.

Therefore, a major challenge in the diagnostics field is the development of robust and reliable companion diagnostic devices that will allow cancer disease markers to be detected accurately in (community) hospitals and in places as diverse as the developing world, community hospitals, the doctor's office, or perhaps even at home in the future.

This photonic refractive index change sensor could be used as a miniaturized, ultra-sensitive and reliable Point-of-Care (PoC) device combining a disposable microfluidic cartridge for the monitoring of cancer biomarkers in whole blood samples. This device would aid primary tumor and metastases detection, as well as monitoring of drug efficacy as a companion diagnostic. It could provide clinicians, caretakers and patients with a more sensitive, robust and selective tool for improved clinical decisions through the early and fast diagnosis of the disease, as well as monitoring of therapeutic response, reducing the cost of the healthcare system. Besides the obvious health benefit for the patient, it could contribute to the sustainability of the European health care system by decreasing the expenditure associated with pharmaceutical treatments and with hospitalization. Such a system could rely on the novel photonic sensor that was developed within the framework of this thesis and combined with the most promising concepts from the nanochemical, biological and fluidic parts of lab-on-a-chip systems, could overcome limitations related to sensitivity, specificity, reliability, compactness and cost issues.

A second example of application could be considered the food industry. Having efficient means to monitor the quality and ensure the safety of food products is a vital need for modern societies. Food contamination has become over the last century much more frequent and dangerous, as it now involves contamination not only by natural toxins and microorganisms, but also by a large variety of chemical agents such as insecticides, herbicides, antibiotics and heavy metals. Therefore, food contamination and related food borne illnesses are today a serious public-health threat and have an enormous economic impact on the public health-care systems with thousands of deaths and hundreds of thousands of hospitalizations in the EU every year. Today, the tools for food quality control during the collection and processing of raw materials, as well as during the production of food products are still based on heavy analytical methods such as high-performance liquid chromatography (HPLC), thin-layer chromatography (TLC) and mass spectrometry (MS). These methods can provide indeed a strict quality control, but they are very complex, expensive, time-consuming with time-to-result up to several days, and appropriate only for well controlled laboratory environments. In order to reduce the number of samples that should be analyzed and to optimize the trade-off between the cost and the reliability of the control procedures, the heavy analytical methods should be combined with the use of low-cost screening tools. However, in many practical cases this is not efficient or even not possible at all due to the unavailability of sensitive enough or reliable enough screening tools.

Same as before, the solution for a reliable, fast, low cost, sensitive and portable for in-situ application could be a similar to the photonic sensor that was described in this thesis, integrated with biological, nanochemical and microfluidic platforms leading to a portable, multi-analyte, reusable, bio-photonic, lab-on-a-chip based sensor for real-time monitoring of food quality.

Another application field in which this refractive index sensor could be applied, could be the monitoring of the air quality inside (public or private) transportation vehicles. Despite the undeniable benefits of diesel technology in terms of use and CO_2 emissions, it is becoming increasingly apparent in the scientific community that diesel technology has serious environmental disadvantages due to the development of other harmful contaminants that were previously ignored or completely overlooked. Due to incomplete combustion of the fuel in the combustion chamber, diesel engines are estimated to emit at least 25 times more particles than petrol engines. While the health risks posed by diesel particle emissions are present for anyone living and breathing in an urban environment with diesel vehicles on the road, these risks are amplified and magnified for people who are inside a vehicle surrounded by others. It is almost certain that the fresh air carried into the cabin through the vehicle's ventilation system would contain large concentrations of these hazardous particles emitted by the diesel engines of the surrounding vehicles in such a situation.

So, the RI sensor that described in this thesis, could be part of a disruptive sensing system for the detection of these nanoparticles inside the vehicle’s cabin environment, and the transmission of the relevant information to the climate control system of the vehicle in order to take actions and counteract the contamination. The selectivity of the RI sensing system to these particles could be based on the use of a thin layer of enzymes, antibodies, aptamers or imprinted polymer films on top of the waveguiding core that can serve as the transduction layer for the recognition and the selective binding of the molecules near the surface of the sensor.

Finally, another application field on which the use of a similar to the already described refractive index sensor could have an impact, is the safety and the security of the drinking water. The concept of clean and safe water has evolved over the centuries and there are new clear standards, namely a long list of substances that above a certain concentration level become a health hazard. There is a wide range of both chemical and microbial contaminants that may be found in drinking-water, some of which can have adverse effects on health’s consumers. Thus, the understanding of the nature of contamination sources and how these may enter and pollute the water supply networks is critical for ensuring water safety and consequently to the public health.

At the moment for the most part, samples are taken and analyzed in laboratories associated with the water utilities. In the last few years, a number of optical spectroscopy-based sensors have been developed, which can detect these substances, provide almost real-time results but remain highly expensive. The use of the photonic sensor that is presented in this thesis, could be used in both ways. Firstly, it could be used as a first alarm since it is capable to detect events happening to the water composition with high precision. Secondly, in combination with the biochemistry technology it could strengthen its operation by adding the specificity ability, and thus, detect and identify the substances that are responsible for the change in the water composition. In both cases, the proposed photonic sensor could be used for the detection of real threats and not only harmless changes in water composition and provide warning signals in the case any of the targets is detected above the safe concentration, aiming to be a low-cost, real-time with high sensitivity and accuracy solution.

Appendix I

More information about the characterization results of the MMIs is provided in this section.

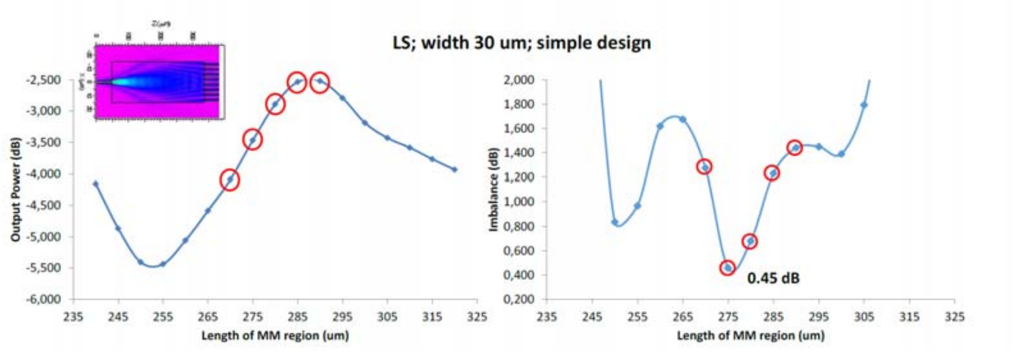

Figure 118: Insertion loss and power imbalance results for simple design LS, width 30 um.

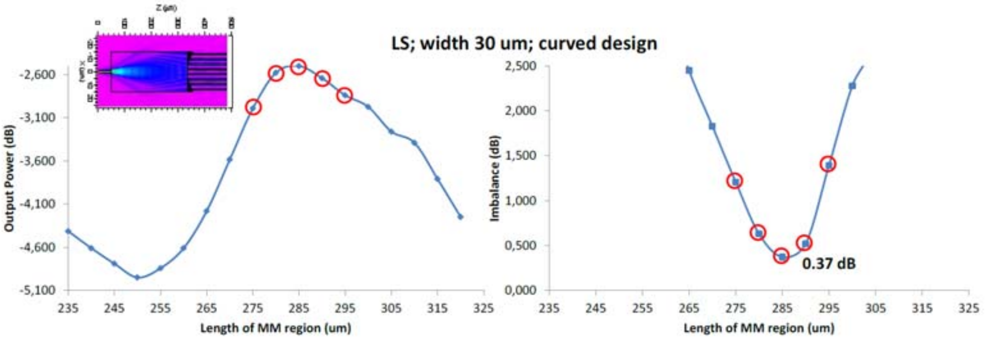

Figure 119: Insertion loss and power imbalance results for curved design LS, width 30 um.

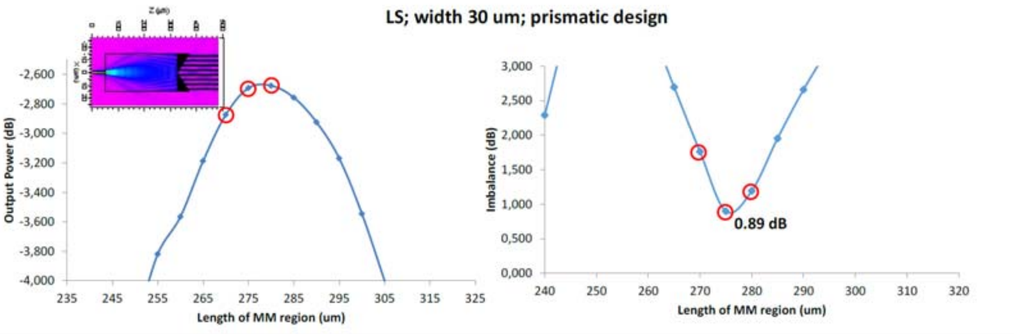

Figure 120: Insertion loss and power imbalance results for prismatic design LS, width 30 um.

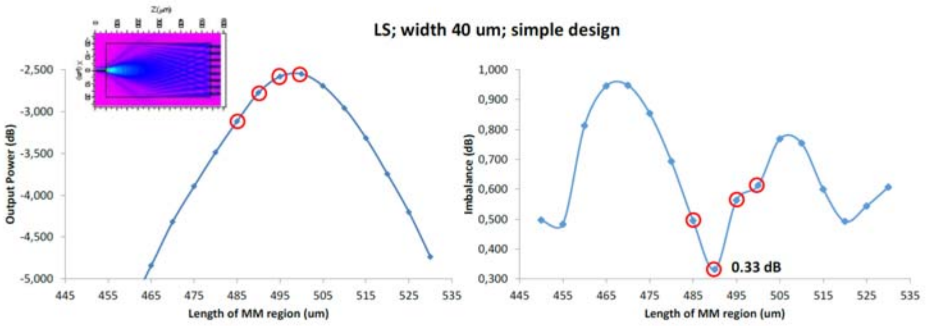

Figure 121: Insertion loss and power imbalance results for simple design LS, width 40 um.

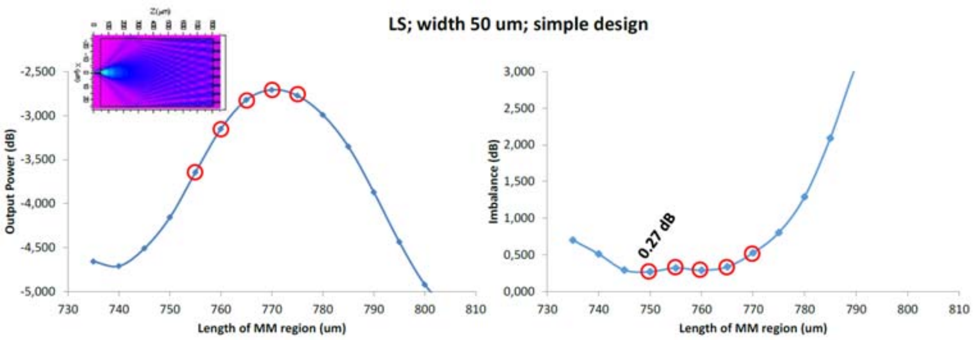

Figure 122: Insertion loss and power imbalance results for simple design LS, width 50 um.

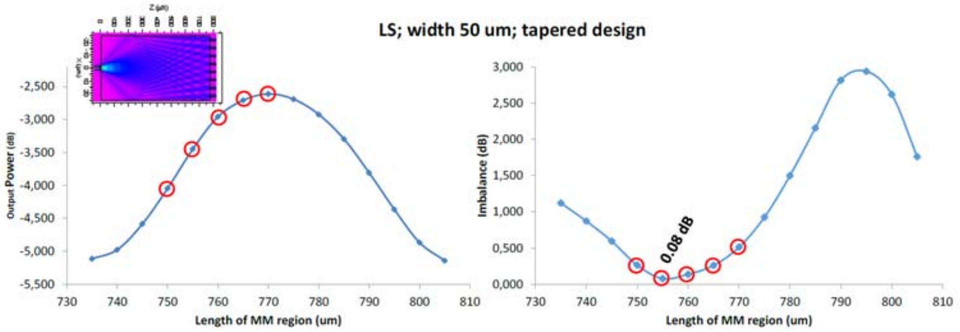

Figure 123: Insertion loss and power imbalance results for tapered design LS, width 50 um.

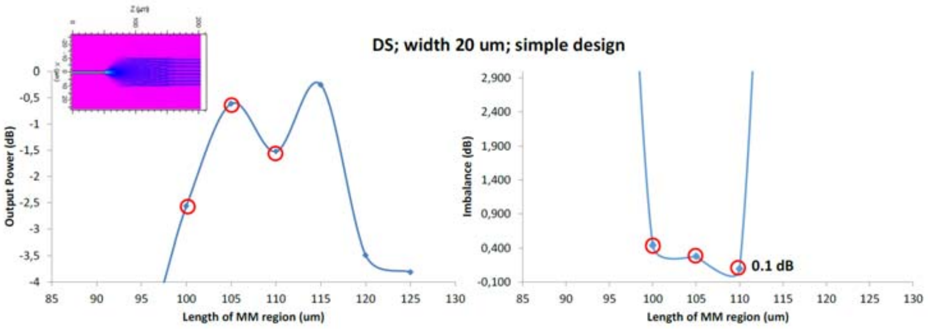

Figure 124: Insertion loss and power imbalance results for simple design DS, width 20 um.

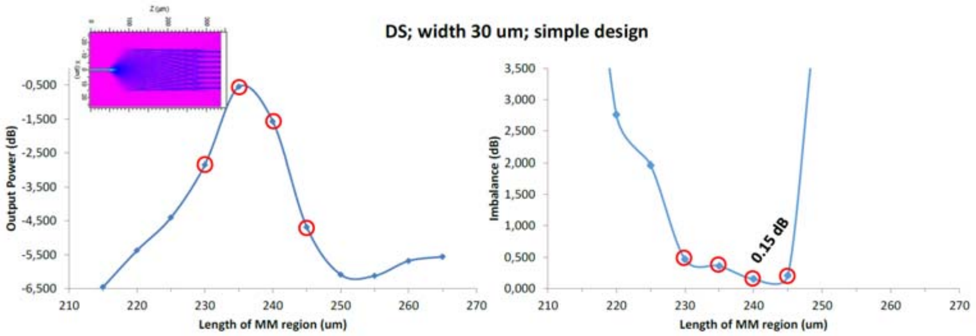

Figure 125: Insertion loss and power imbalance results for simple design DS, width 30 um.

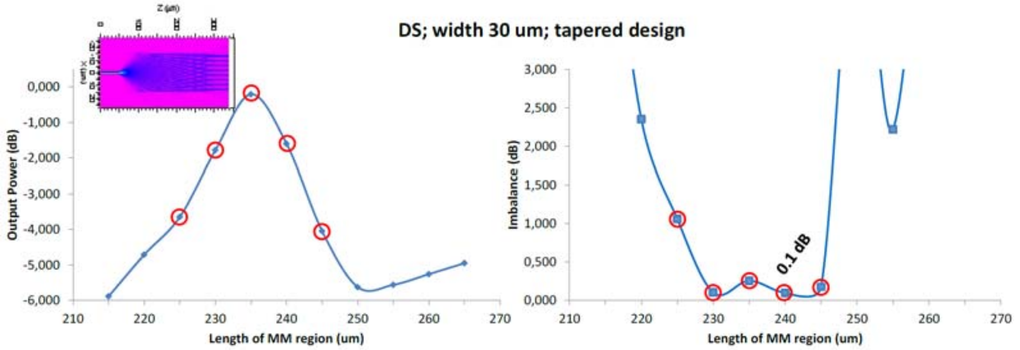

Figure 126: Insertion loss and power imbalance results for tapered design DS, width 30 um.

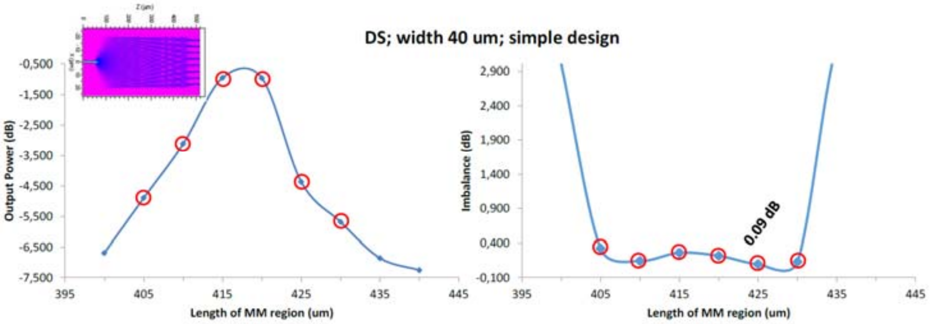

Figure 127: Insertion loss and power imbalance results for simple design DS, width 40 um.

Table 6: Parameters of the 51 1x8 MMI couplers, delivered to LioniX

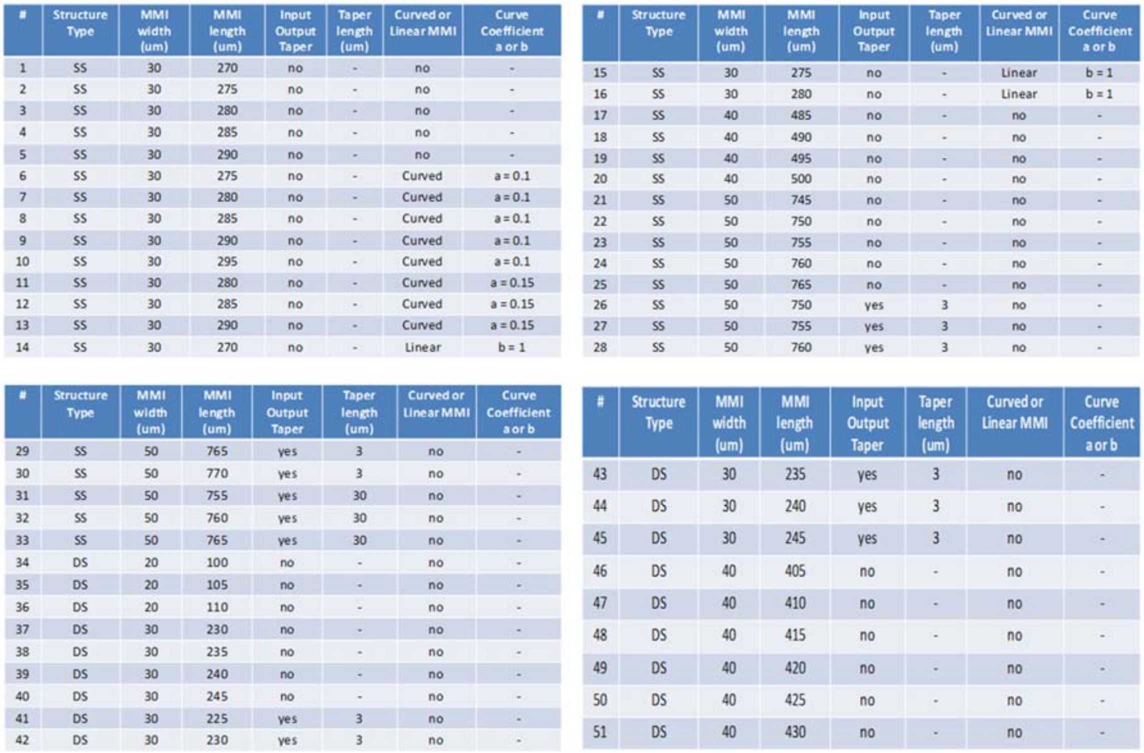

#	Structure Type	MMI width (um)	MMI length (um)	Input Output Taper	Taper length (um)	Curved or Linear MMI	Curve Coefficient a or b
1	SS	30	270	no	-	no	-
2	SS	30	275	no	-	no	-
3	SS	30	280	no	-	no	-
4	SS	30	285	no	-	no	-
5	SS	30	290	no	-	no	-
6	SS	30	275	no	-	Curved	a = 0.1
7	SS	30	280	no	-	Curved	a = 0.1
8	SS	30	285	no	-	Curved	a = 0.1
9	SS	30	290	no	-	Curved	a = 0.1
10	SS	30	295	no	-	Curved	a = 0.1
11	SS	30	280	no	-	Curved	a = 0.15
12	SS	30	285	no	-	Curved	a = 0.15
13	SS	30	290	no	-	Curved	a = 0.15
14	SS	30	270	no	-	Linear	b = 1
15	SS	30	275	no	-	Linear	b = 1
16	SS	30	280	no	-	Linear	b = 1
17	SS	40	485	no	-	no	-
18	SS	40	490	no	-	no	-
19	SS	40	495	no	-	no	-
20	SS	40	500	no	-	no	-
21	SS	50	745	no	-	no	-
22	SS	50	750	no	-	no	-
23	SS	50	755	no	-	no	-
24	SS	50	760	no	-	no	-
25	SS	50	765	no	-	no	-
26	SS	50	750	yes	3	no	-
27	SS	50	755	yes	3	no	-
28	SS	50	760	yes	3	no	-
29	SS	50	765	yes	3	no	-
30	SS	50	770	yes	3	no	-
31	SS	50	755	yes	30	no	-
32	SS	50	760	yes	30	no	-
33	SS	50	765	yes	30	no	-
34	DS	20	100	no	-	no	-
35	DS	20	105	no	-	no	-
36	DS	20	110	no	-	no	-
37	DS	30	230	no	-	no	-
38	DS	30	235	no	-	no	-
39	DS	30	240	no	-	no	-
40	DS	30	245	no	-	no	-
41	DS	30	225	yes	3	no	-
42	DS	30	230	yes	3	no	-
43	DS	30	235	yes	3	no	-
44	DS	30	240	yes	3	no	-
45	DS	30	245	yes	3	no	-
46	DS	40	405	no	-	no	-
47	DS	40	410	no	-	no	-
48	DS	40	415	no	-	no	-
49	DS	40	420	no	-	no	-
50	DS	40	425	no	-	no	-
51	DS	40	430	no	-	no	-

In the next table, the measurement results of the MMI structures of the 1st simulation run, are presented.

Table 7: Measurement results of the 1G 1x8 MMIs.

		Wafer			
		102		201	
		λ = 853.96 nm	λ = 855.77 nm	λ = 853.96 nm	λ = 855.77 nm
	L (µm)	Imbalance (dB)			
SS A0.1 W30	275	4.98	3.45	4.66	5.47
	280	3.41	11.73	2.64	8.51
	285	3.63	5.78	7.76	7.91
	290	4.97	3.27	4.93	7.77
	295	4.19	4.48	18.63	14.94
SS A0.15 W30	280	4.91	3.35	4.91	5.39
	285	5.22	5.61	6.77	4.48
	290	10.35	7.36	9.98	9.56
SS B1 W30	270	9.65	7.36	15.06	10.02
	275	7.15	4.47	6.77	7.30
	280	11.65	8.62	7.19	9.09
SS W30	270	16.22	8.51	10.28	10.54
	275	13.79	8.93	9.33	10.55

	280	9.46	7.16	12.38	9.90
	285	17.13	14.63	9.05	8.51
	290	9.74	9.49	9.74	8.78
SS T3 W50	750	15.55	15.30	15.16	14.81
	755	13.64	9.61	11.94	9.13
	760	7.85	11.15	11.50	11.46
	765	9.02	9.04	12.01	12.28
	770	10.40	11.55	15.51	12.53
SS T30 W50	755	10.18	11.36	17.35	13.37
	760	16.86	14.69	13.42	14.22
	765	10.95	13.45	16.10	16.48
SS W40	485	9.61	9.50	14.79	8.92
	490	15.67	11.93	11.06	11.53
	495	11.79	11.73	7.60	13.13
	500	4.98	7.02	12.85	9.49
SS W50	745	4.30	9.63	11.33	11.24
	750	9.63	11.70	6.72	14.00
	755	9.03	11.35	5.53	11.09
	760	16.03	12.49	5.07	12.84
	765	16.43	11.69	9.12	10.17
DS T3 W30	225	2.78	1.10	8.14	7.63
	230	8.68	8.22	15.19	13.76
	235	15.92	16.89	14.15	15.65
	240	16.75	16.47	16.67	13.62
	245	9.05	9.21	6.97	6.70
DS W20	100	4.90	4.73	3.63	9.52
	105	10.34	10.45	14.47	17.70
	110	8.14	8.46	10.21	12.31
DS W30	230	7.32	7.35	8.40	11.47
	235	18.56	16.64	11.86	16.53
	240	19.63	15.98	16.72	12.04
	245	10.49	8.81	10.41	9.48
DS W40	405	5.37	7.90	14.71	11.03
	410	18.70	10.94	8.99	16.18
	415	15.94	15.16	25.28	19.01
	420	20.30	15.02	15.01	19.54
	425	18.79	17.93	-	-
	430	11.07	10.46	6.25	8.10
DS Splitter 1x4		8.50	2.25	8.50	2.25
DS Splitter 1x8		6.50	2.88	6.50	2.88

		Wafer			
		102		201	
		λ = 853.96 nm	λ = 855.77 nm	λ = 853.96 nm	λ = 855.77 nm
	L (μm)	Insertion loss (dB)			
SS A0.1 W30	275	4.63	1.84	5.41	2.22
	280	5.07	4.79	7.86	0.79
	285	6.51	0.68	5.82	1.94
	290	6.11	4.72	9.54	1.02
	295	6.48	4.04	6.57	4.02
SS A0.15 W30	280	10.16	3.42	9.24	6.38
	285	6.99	1.93	8.34	7.90
	290	1.75	3.32	3.17	2.20
SS B1 W30	270	1.87	4.72	10.47	0.32
	275	0.82	4.72	10.85	0.25
	280	2.33	5.04	2.68	3.27
SS W30	270	2.48	3.95	4.92	1.98
	275	8.13	4.43	0.63	1.65
	280	4.03	5.54	3.74	5.15
	285	9.18	3.24	6.02	1.44
	290	5.93	3.65	5.93	7.09
SS T3 W50	750	1.27	1.21	7.63	6.82
	755	7.08	5.85	8.18	7.05
	760	10.91	6.03	6.83	6.98
	765	5.25	2.18	5.57	0.25
	770	3.45	0.50	5.95	3.49
SS T30 W50	755	0.56	0.02	8.30	6.22
	760	3.75	2.75	8.12	5.34
	765	5.70	1.45	8.14	5.79
SS W40	485	3.64	0.32	7.98	8.41
	490	3.57	0.59	7.55	8.93
	495	0.66	4.05	5.49	8.31
	500	12.54	11.89	8.75	8.71
SS W50	745	4.71	0.83	9.19	2.66
	750	3.11	4.03	0.12	7.32
	755	4.81	3.85	0.59	7.90
	760	2.60	0.46	2.06	6.22
	765	1.05	3.26	8.33	7.01
DS T3 W30	225	4.11	4.81	1.67	5.33
	230	5.77	5.68	7.38	5.31

	235	5.50	4.42	3.79	5.46
	240	4.18	3.47	8.09	6.54
	245	4.93	3.61	9.39	4.86
DS W20	100	8.98	7.83	7.98	7.68
	105	8.71	7.34	3.52	8.00
	110	7.10	7.50	3.24	8.17
DS W30	230	6.72	5.02	2.43	5.72
	235	5.56	5.86	0.93	6.86
	240	2.34	3.56	0.16	6.52
	245	3.77	4.83	6.61	5.48
DS W40	405	4.73	1.08	3.41	4.43
	410	4.74	0.06	0.01	2.29
	415	5.34	1.11	8.67	6.01
	420	5.11	1.35	6.56	4.42
	425	5.16	1.22	5.16	1.22
	430	5.30	0.33	2.45	4.59
DS Splitter 1x4		9.07	1.49	9.08	1.49
DS Splitter 1x8		5.64	5.73	5.64	5.73

In the next table, the 2nd generation of the 1x8 MMI which has been sent for fabrication are presented:

Table 8: Simulation results of the 2G 1x8 MMI couplers.

#	Structure Type	Width of MMI (um)	Length of MMI (um)	Imbalance (dB)	Total Power (dB)
1	DS	20	94	0.20	-0.53
2	DS	20	95	0.08	-0.76
3	DS	30	207	0.56	-0.52
4	DS	30	208	0.49	-0.60
5	DS	40	364	0.21	-0.88
6	DS	40	365	0.37	-0.66
7	SS	20	94	0.11	-0.43
8	SS	20	95	0.04	-0.54
9	SS	30	208	0.44	-0.61
10	SS	30	209	0.36	-0.56
11	SS	40	367	0.39	-0.94
12	SS	40	369	0.44	-0.51
13	SS	50	573	0.26	-0.93
14	SS	50	575	0.37	-0.64

Table 9: Simulation results of the 1G 1x4 MMI couplers.

#	Structure Type	Width of MMI (um)	Length of MMI (um)	Imbalance (dB)	Total Power (dB)
1	DS	20	186	0.16	-0.59
2	DS	20	187	0.29	-0.53
3	DS	30	414	0.12	-0.74
4	DS	30	415	0.12	-0.78
5	DS	40	731	0.17	-0.78
6	DS	40	732	0.23	-0.77
7	SS	20	188	0.27	-0.44
8	SS	20	189	0.20	-0.59
9	SS	30	417	0.08	-0.63
10	SS	30	418	0.18	-0.58
11	SS	40	737	0.19	-0.83
12	SS	40	738	0.12	-0.76

In the next figures, a summary of characterization results of the 1G 1x8 MMIs are presented.

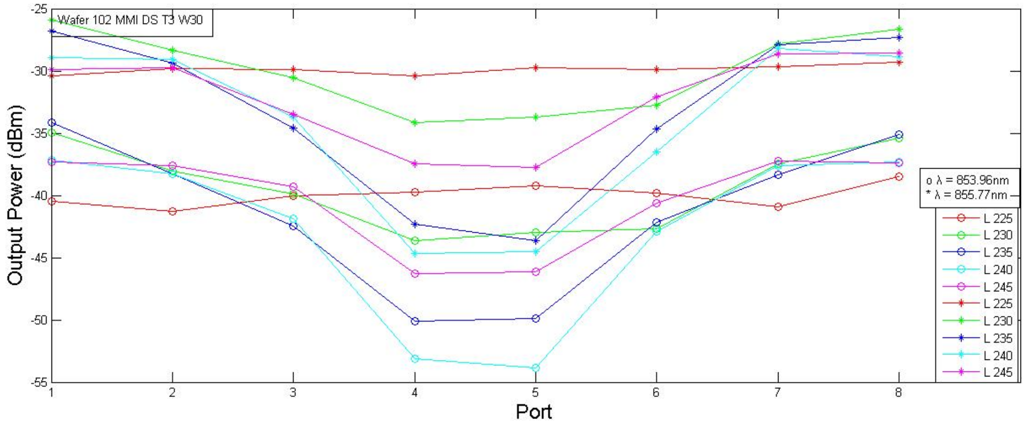

Figure 128: MMI output ports power vs MMI length (with 3 um tapers) for width 30 um.

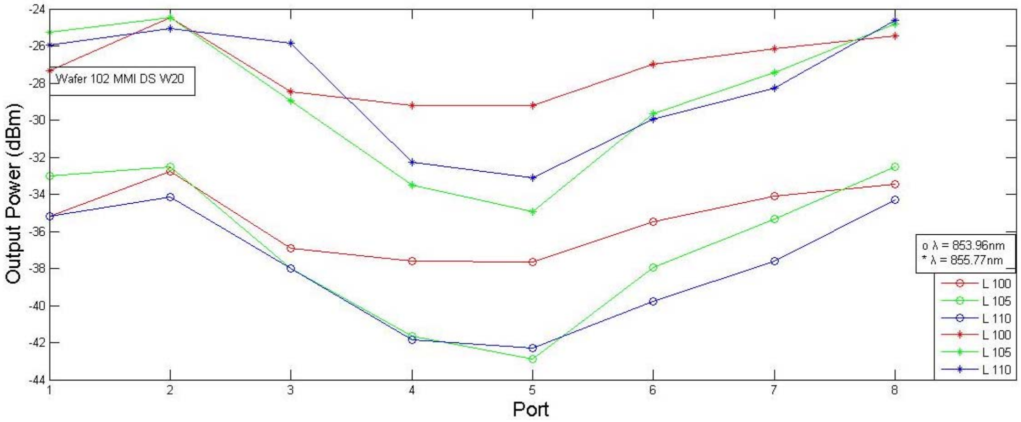

Figure 129: MMI output ports power vs MMI length for width 20 um.

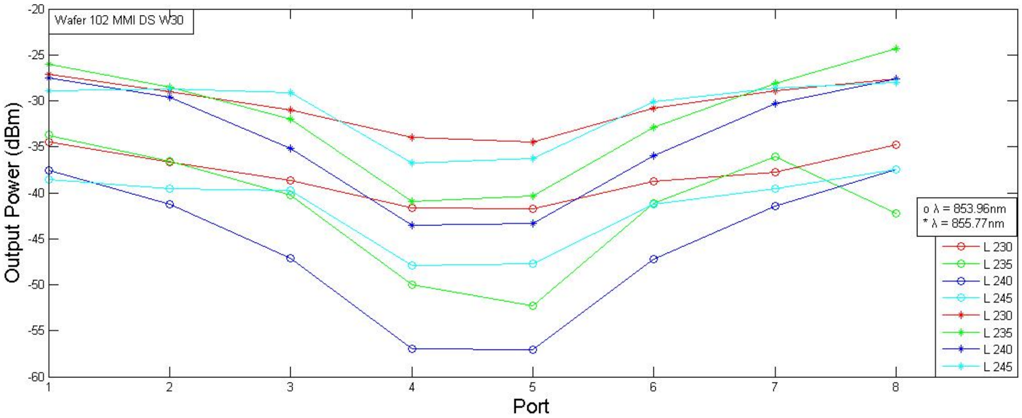

Figure 130: MMI output ports power vs MMI length for width 30 um.

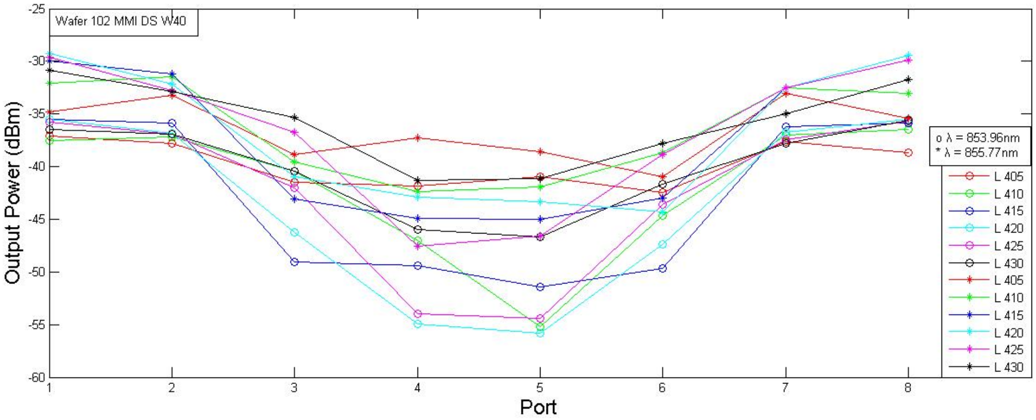

Figure 131: MMI output ports power vs MMI length for width 40 um.

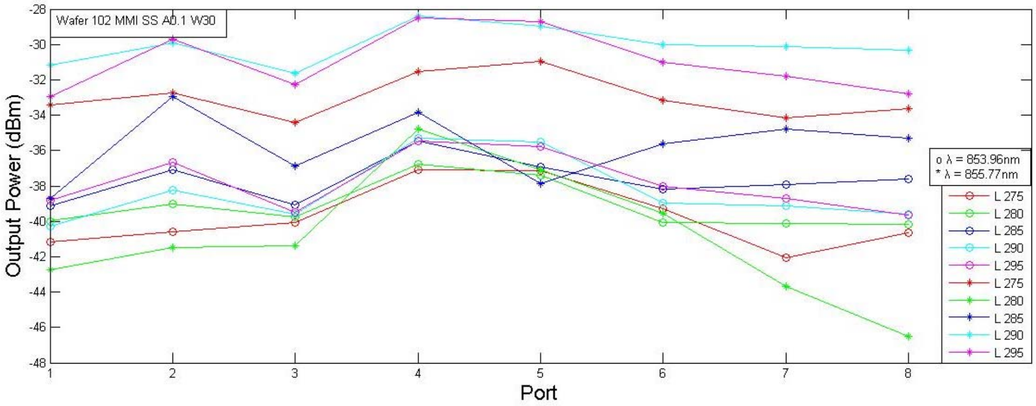

Figure 132: MMI output ports power vs MMI length for width 30 um (curved design).

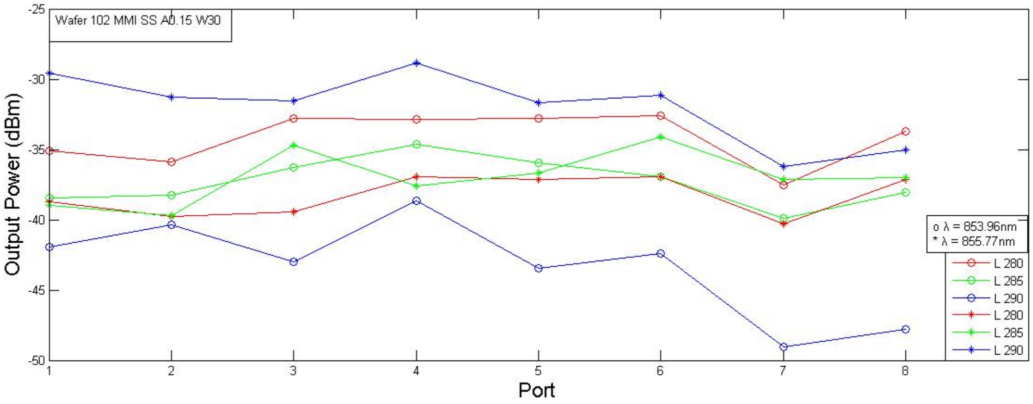

Figure 133: MMI output ports power vs MMI length for width 30 um (curved design).

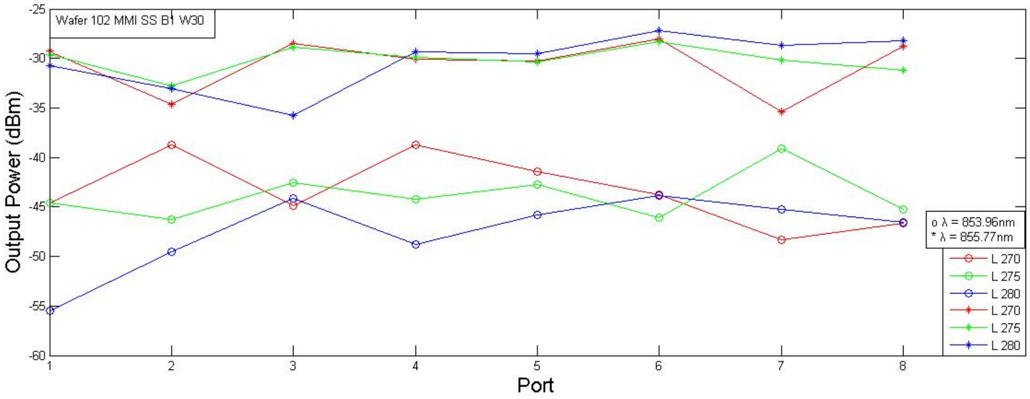

Figure 134: MMI output ports power vs MMI length for width 30 um.

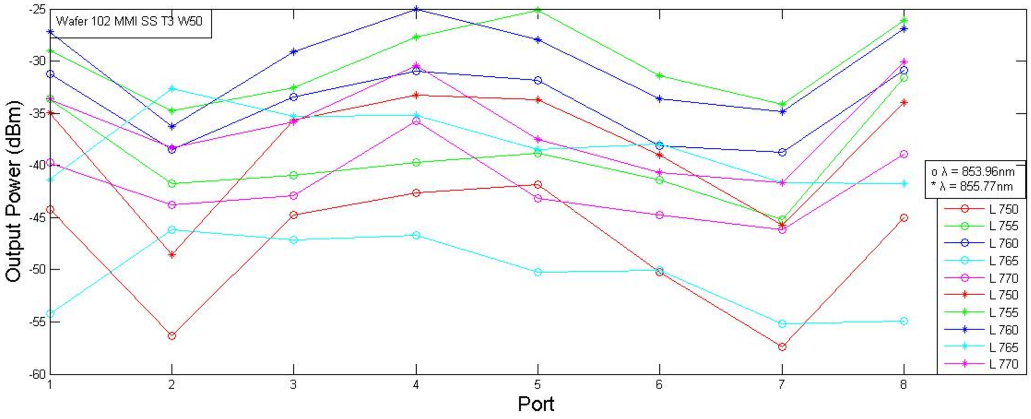

Figure 135: MMI output ports power vs MMI length for width 50 um.

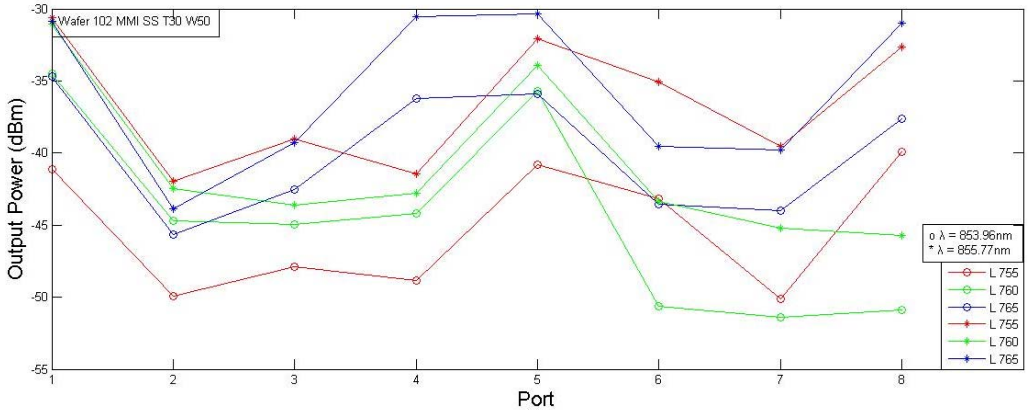

Figure 136: MMI output ports power vs MMI length (with 30 um tapers) for width 50 um.

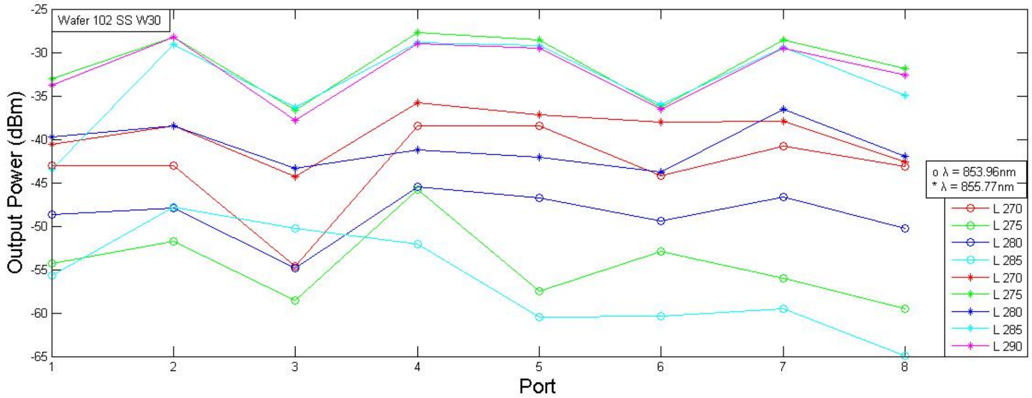

Figure 137: MMI output ports power vs MMI length for width 30 um.

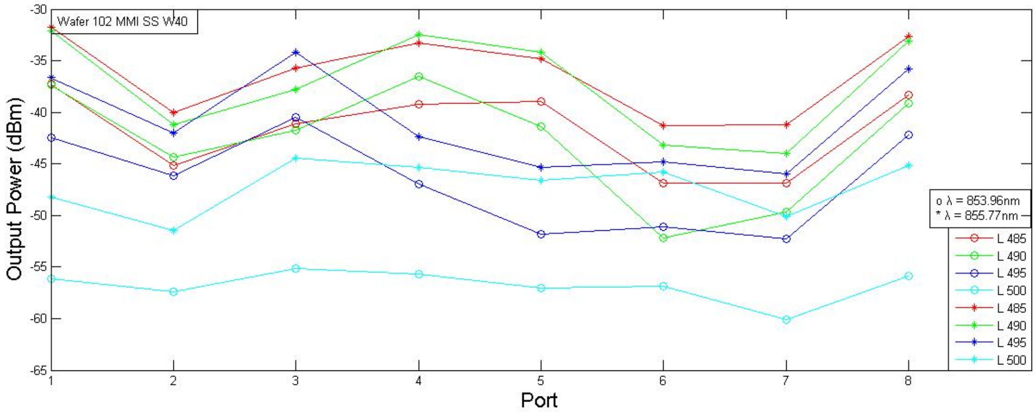

Figure 138: MMI output ports power vs MMI length for width 40 um.

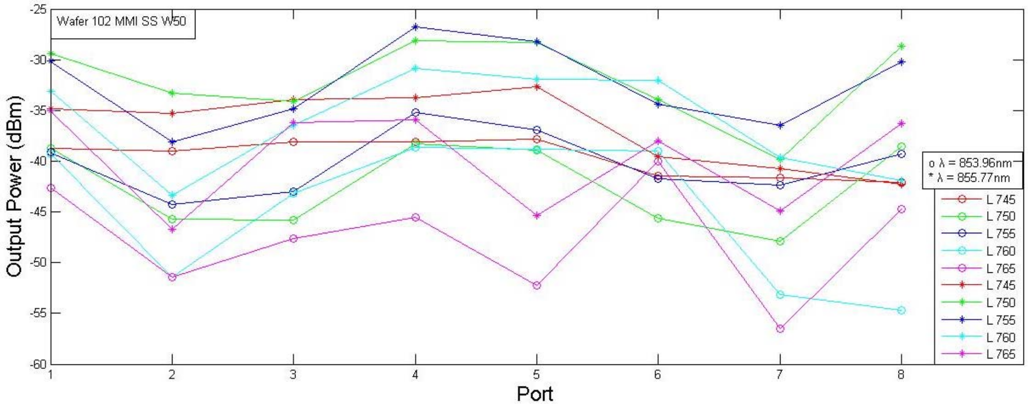

Figure 139: MMI output ports power vs MMI length for width 50 um.

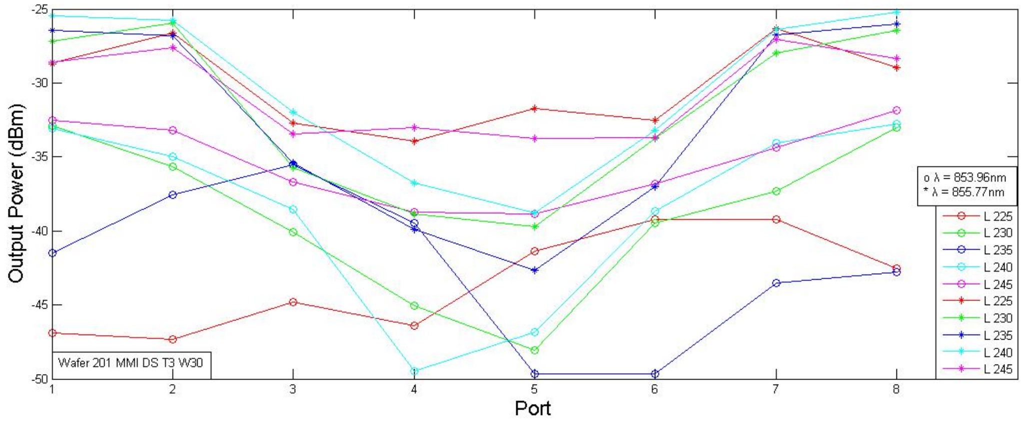

Figure 140: MMI output ports power vs MMI length for width 30 um.

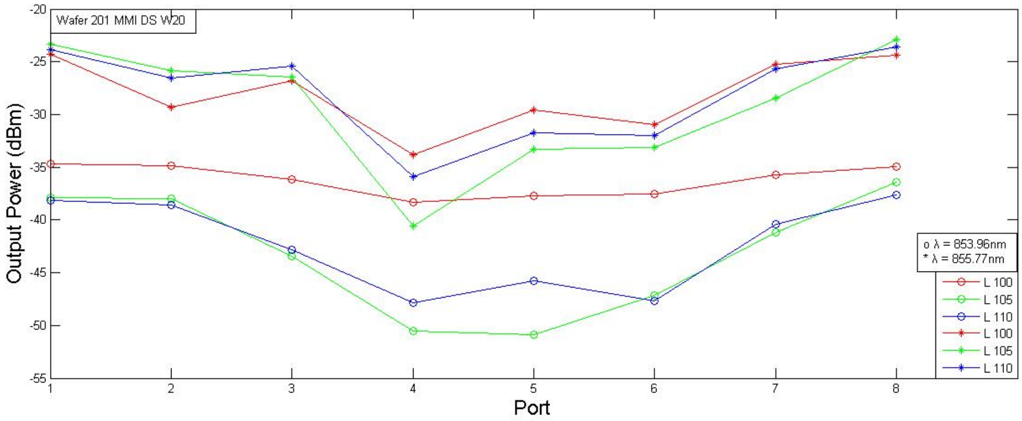

Figure 141: MMI output ports power vs MMI length for width 20 um.

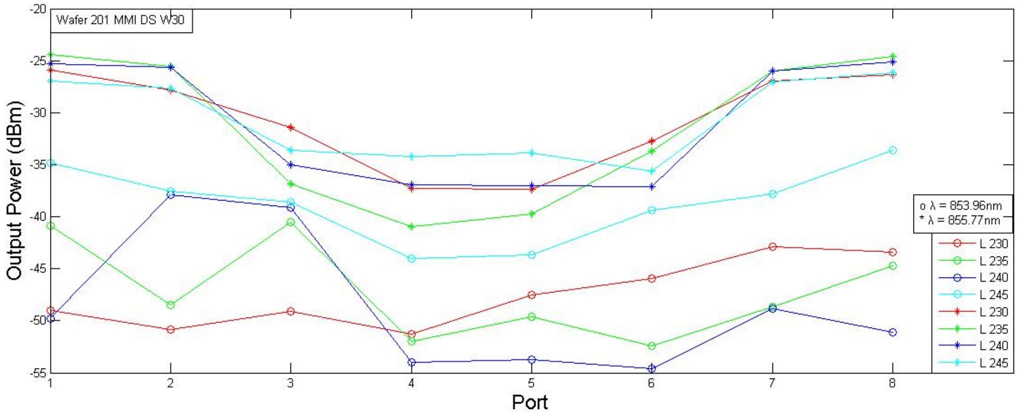

Figure 142: MMI output ports power vs MMI length for width 30 um.

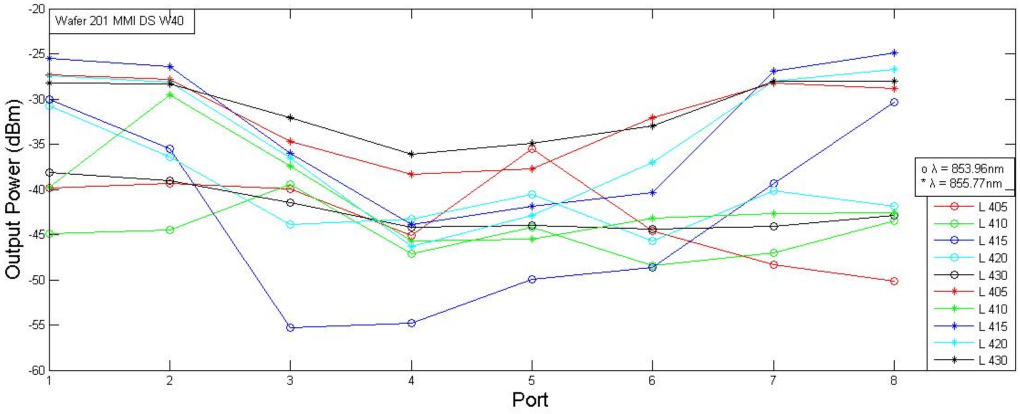

Figure 143: MMI output ports power vs MMI length for width 40 um.

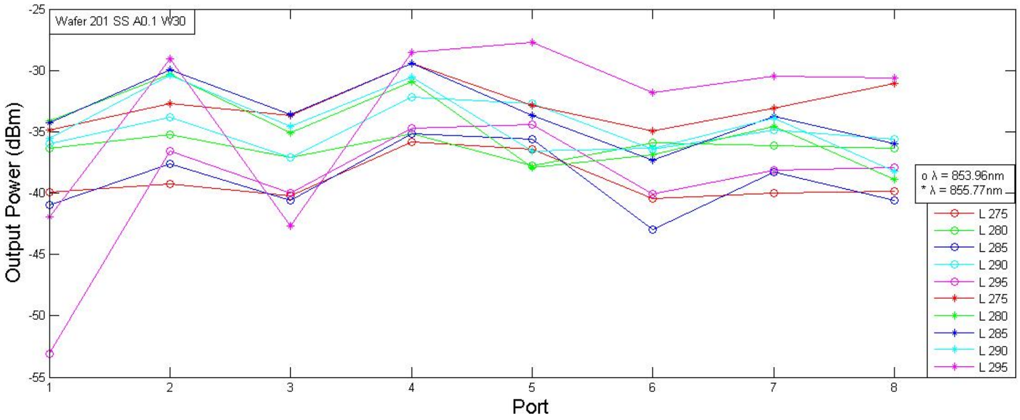

Figure 144: MMI output ports power vs MMI length for width 30 um (curved design).

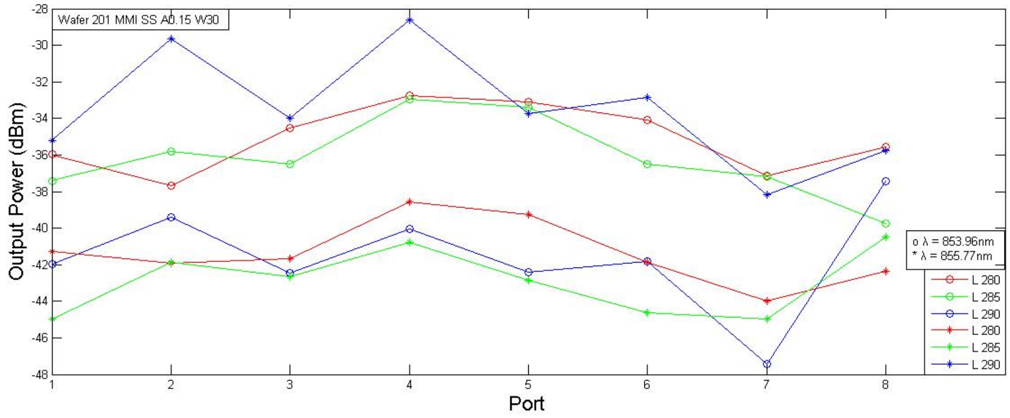

Figure 145: MMI output ports power vs MMI length for width 30 um (curved design).

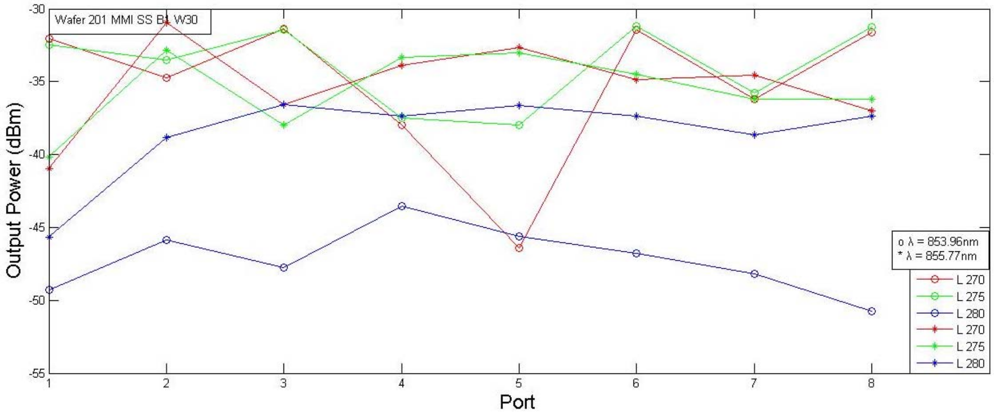

Figure 146: MMI output ports power vs MMI length for width 30 um.

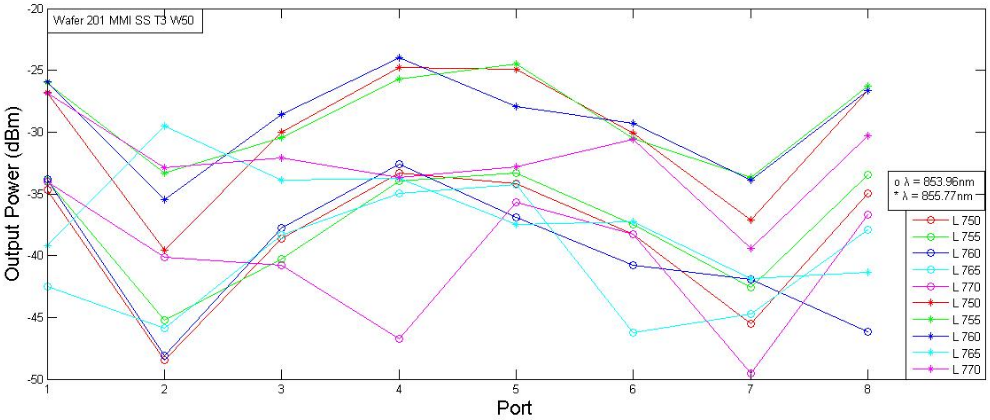

Figure 147: MMI output ports power vs MMI length for width 50 um.

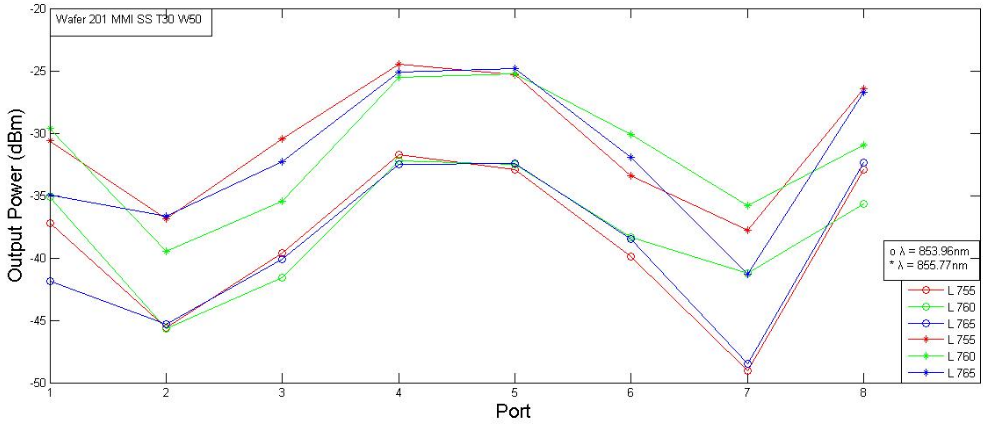

Figure 148: MMI output ports power vs MMI length for width 50 um.

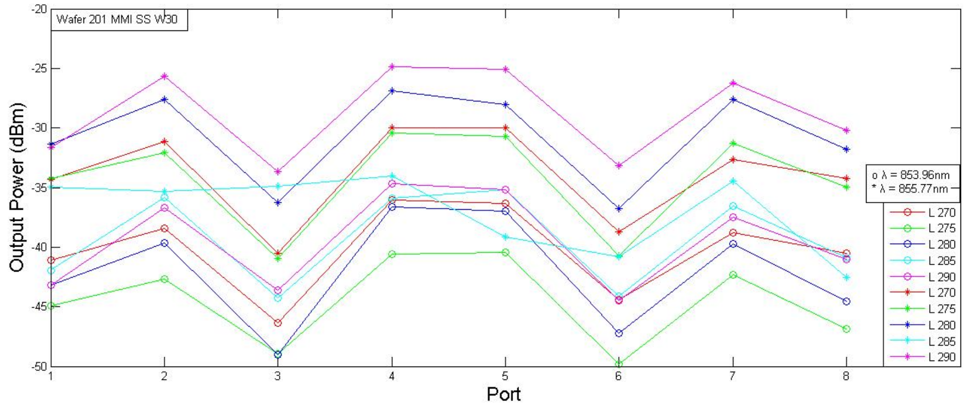

Figure 149: MMI output ports power vs MMI length for width 30 um.

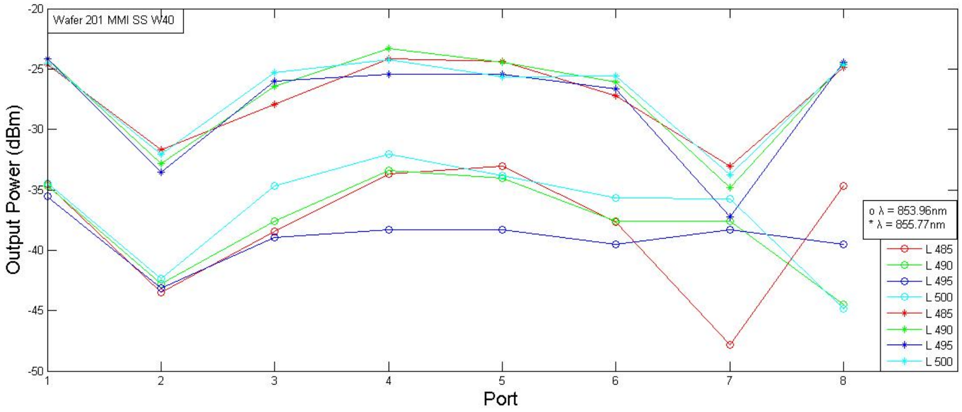

Figure 150: MMI output ports power vs MMI length for width 40 um.

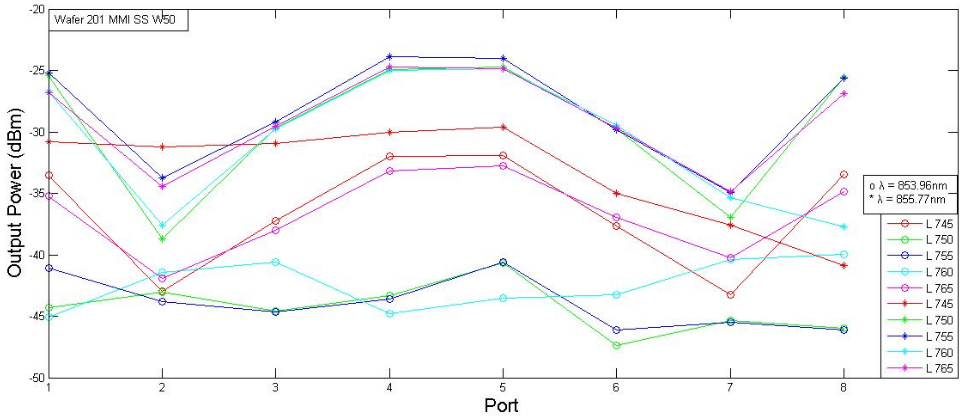

Figure 151: MMI output ports power vs MMI length for width 50 um.

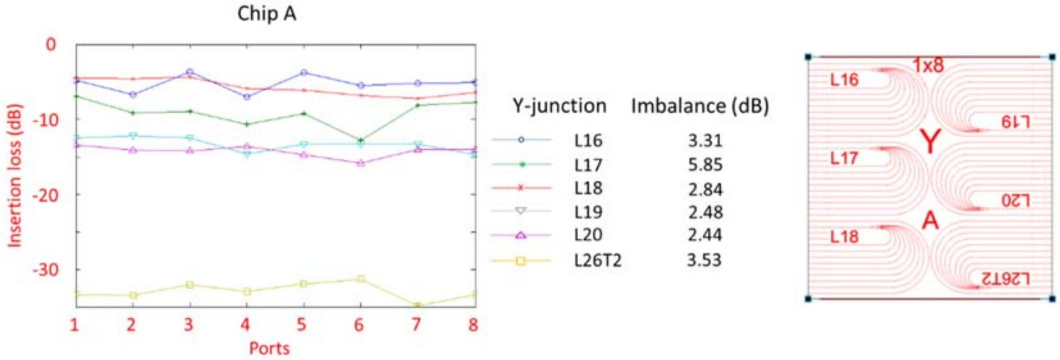

Figure 152: Experiment results of Y-junctions in chip-A.

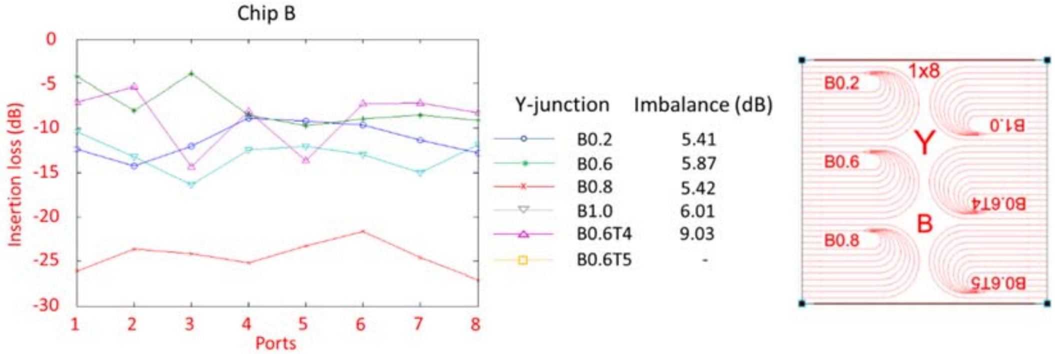

Figure 153: Experiment results of Y-junctions in chip-B.

Appendix II

The simulation results regarding the polarization rotator are presented in this section.

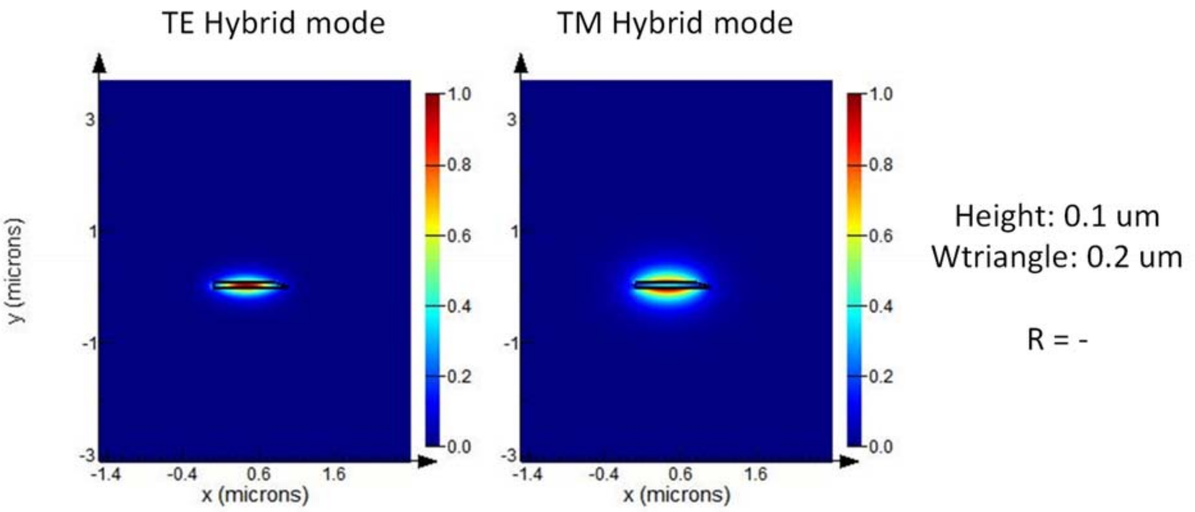

Height: 0.1 um
Wtriangle: 0.2 um

R = -

Figure 154: Polarization partial rotator with Height= 0.1 um and $W_{triangle}$= 0.2 um.

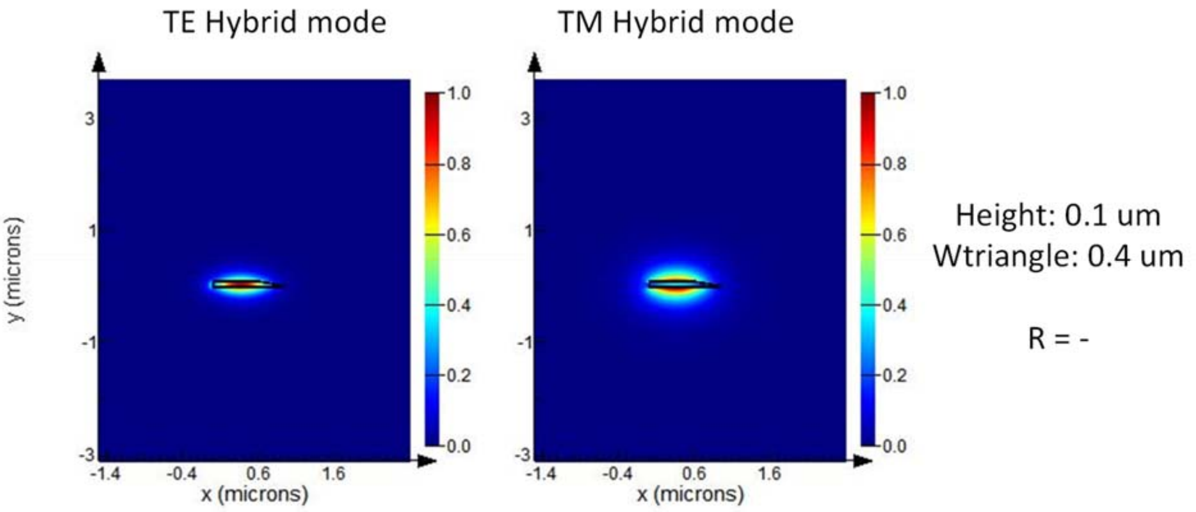

Height: 0.1 um
Wtriangle: 0.4 um

R = -

Figure 155: Polarization partial rotator with Height= 0.1 um and $W_{triangle}$= 0.4 um.

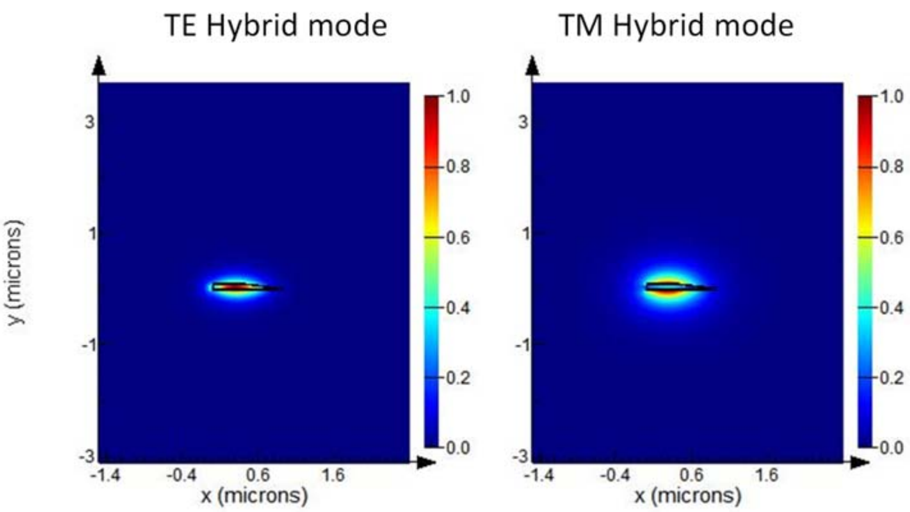

TE Hybrid mode

TM Hybrid mode

Height: 0.1 um
Wtriangle: 0.6 um

R = -

Figure 156: Polarization partial rotator with Height= 0.1 um and $W_{triangle}$= 0.6 um.

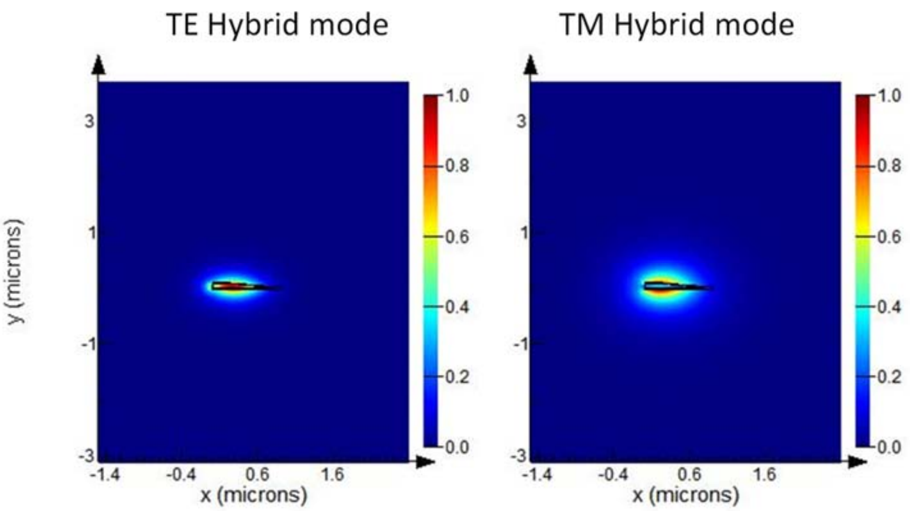

TE Hybrid mode

TM Hybrid mode

Height: 0.1 um
Wtriangle: 0.8 um

R = -

Figure 157: Polarization partial rotator with Height= 0.1 um and $W_{triangle}$= 0.8 um.

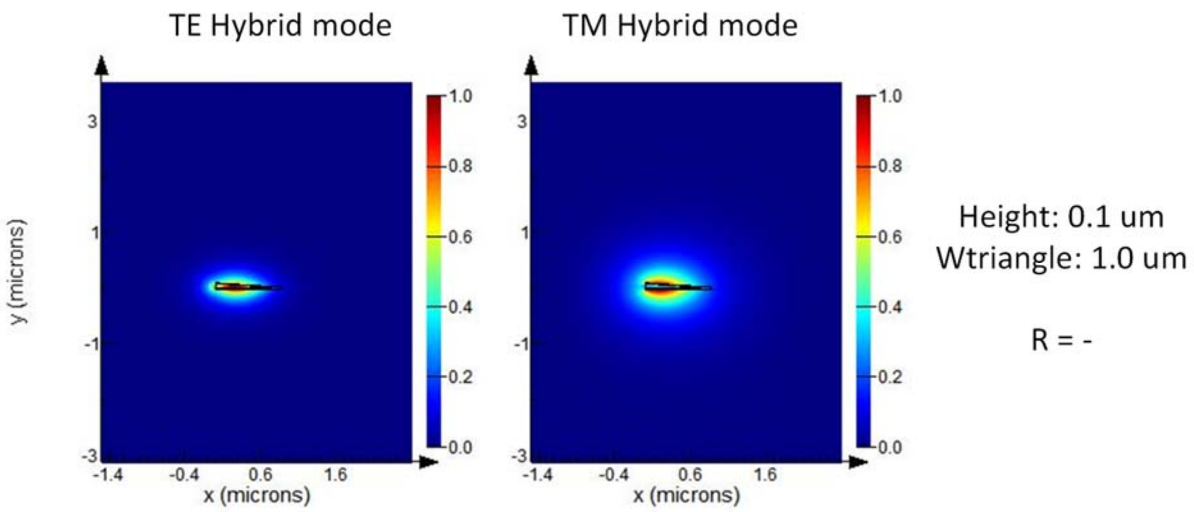

Figure 158: Polarization partial rotator with Height= 0.1 um and $W_{triangle}$= 1.0 um.

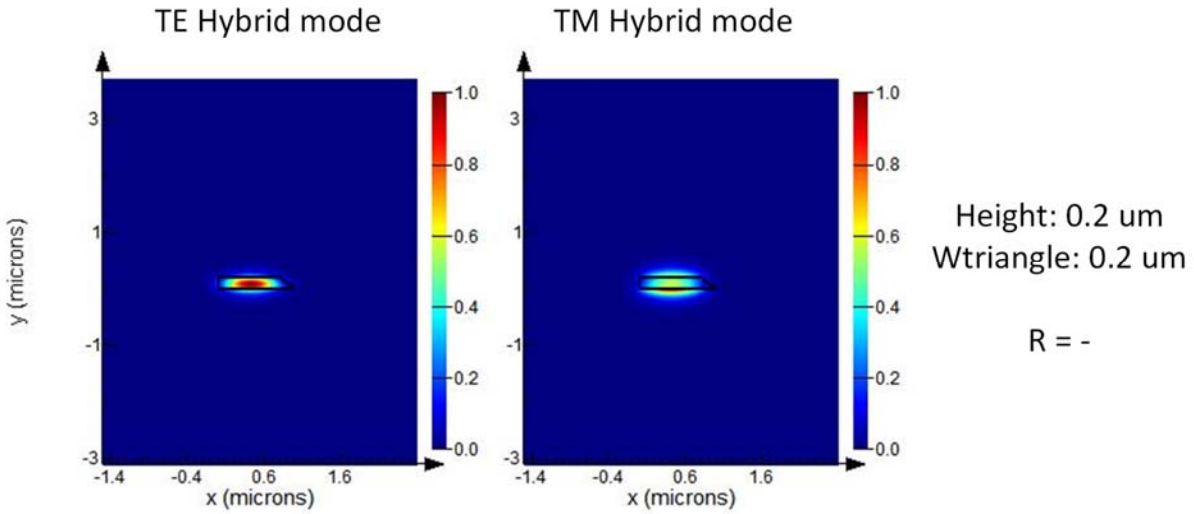

Figure 159: Polarization partial rotator with Height= 0.2 um and $W_{triangle}$= 0.2 um.

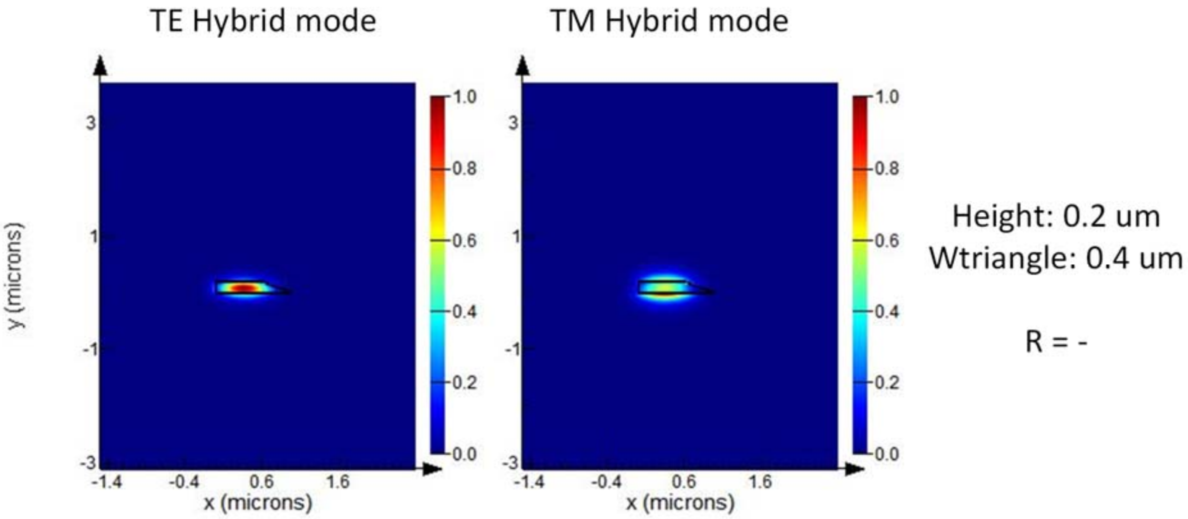

Figure 160: Polarization partial rotator with Height= 0.2 um and $W_{triangle}$= 0.4 um.

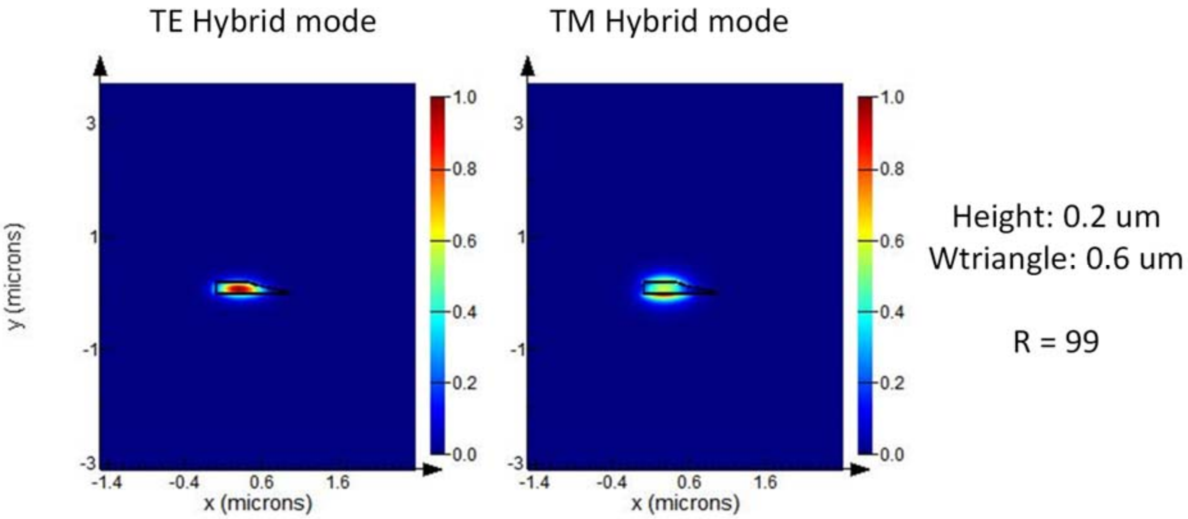

Figure 161: Polarization partial rotator with Height= 0.2 um and $W_{triangle}$= 0.6 um.

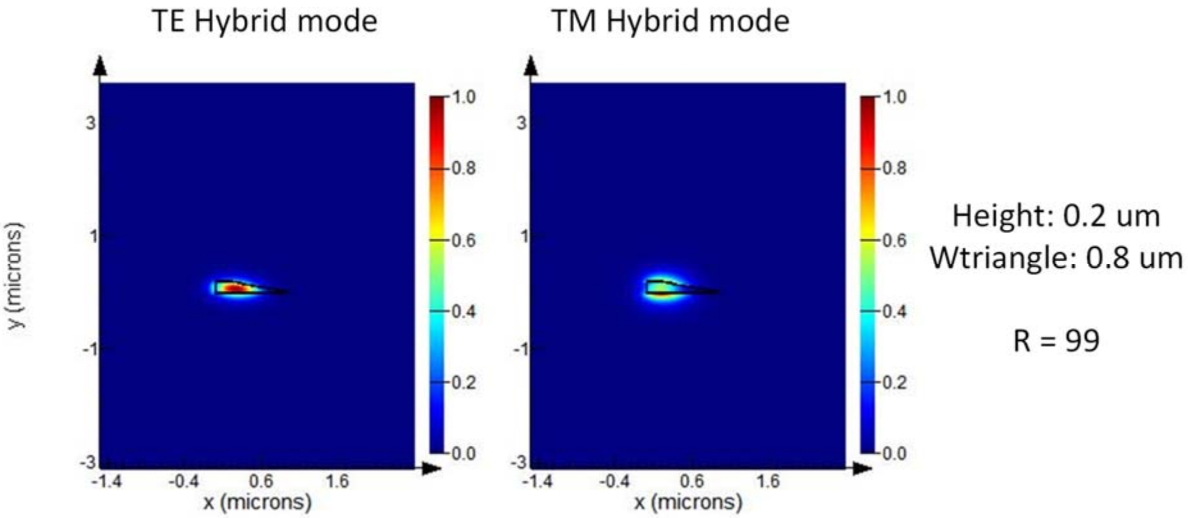

Figure 162: Polarization partial rotator with Height= 0.2 um and $W_{triangle}$= 0.8 um.

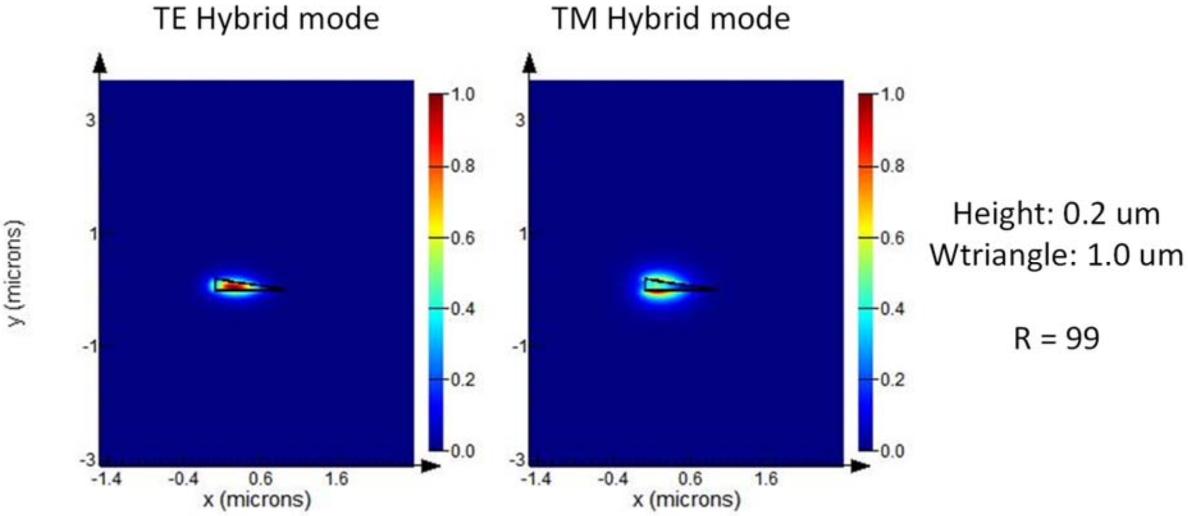

Figure 163: Polarization partial rotator with Height= 0.2 um and $W_{triangle}$= 1.0 um.

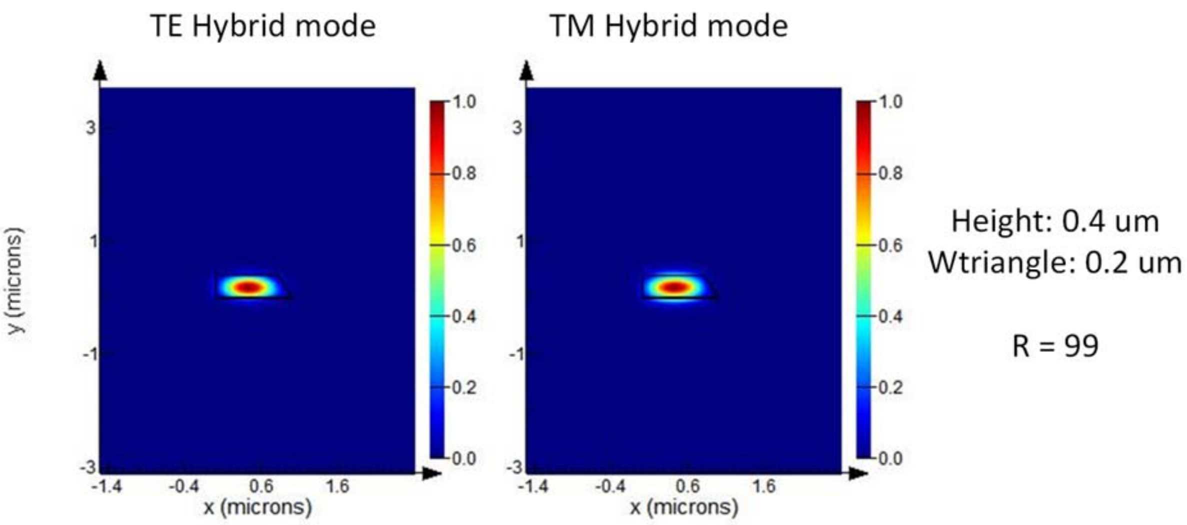

Figure 164: Polarization partial rotator with Height= 0.4 um and $W_{triangle}$= 0.2 um.

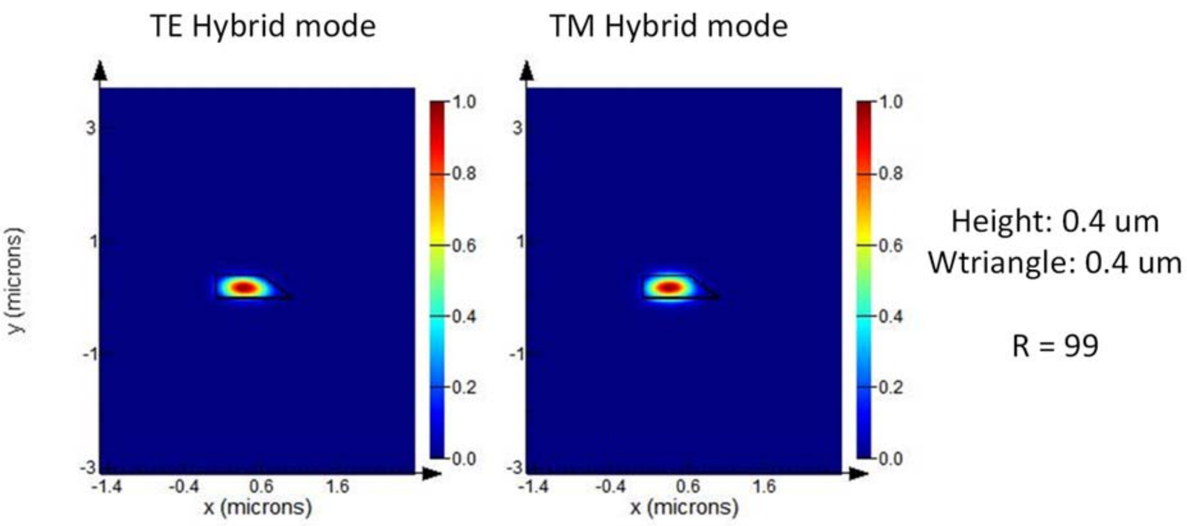

Figure 165: Polarization partial rotator with Height= 0.4 um and $W_{triangle}$= 0.4 um.

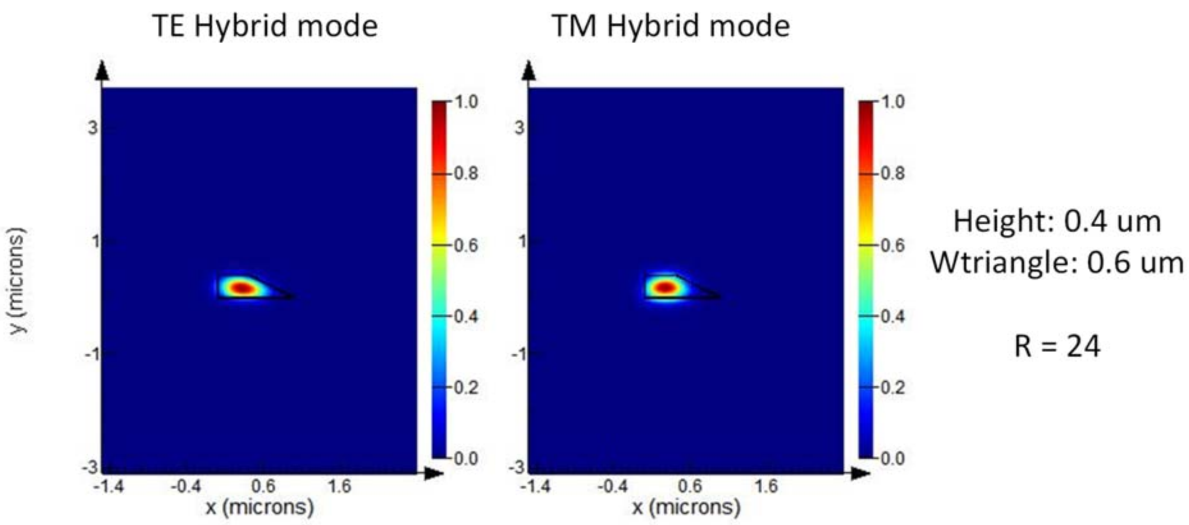

Figure 166: Polarization partial rotator with Height= 0.4 um and $W_{triangle}$= 0.6 um.

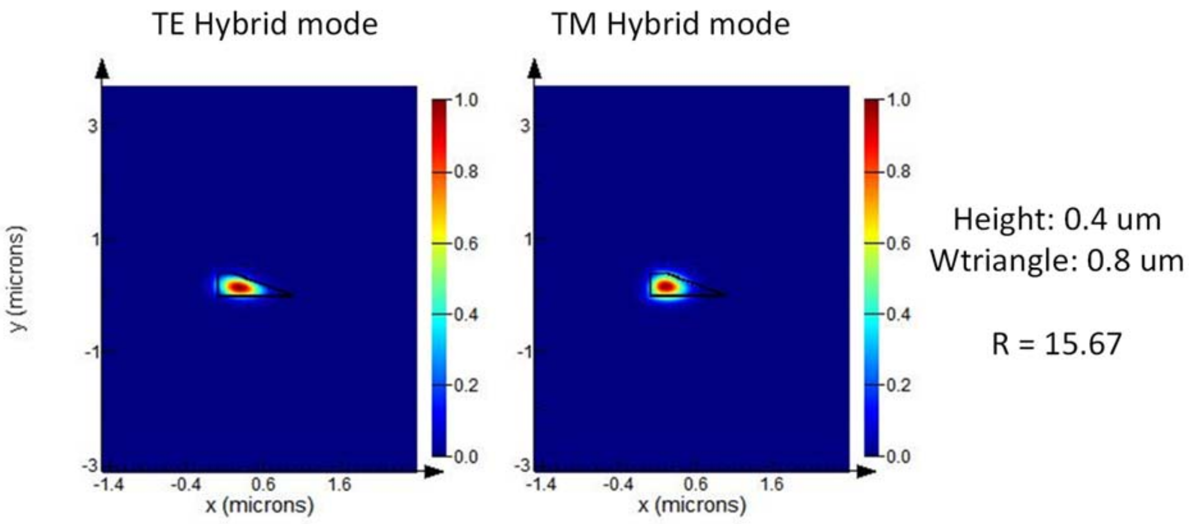

Figure 167: Polarization partial rotator with Height= 0.4 um and $W_{triangle}$= 0.8 um.

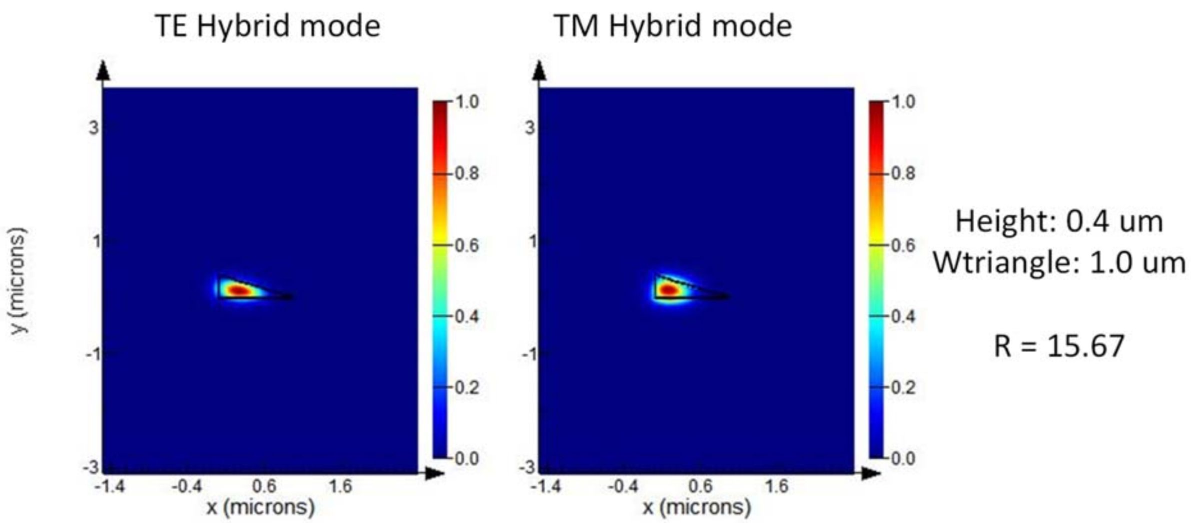

Figure 168: Polarization partial rotator with Height= 0.4 um and $W_{triangle}$= 1.0 um.

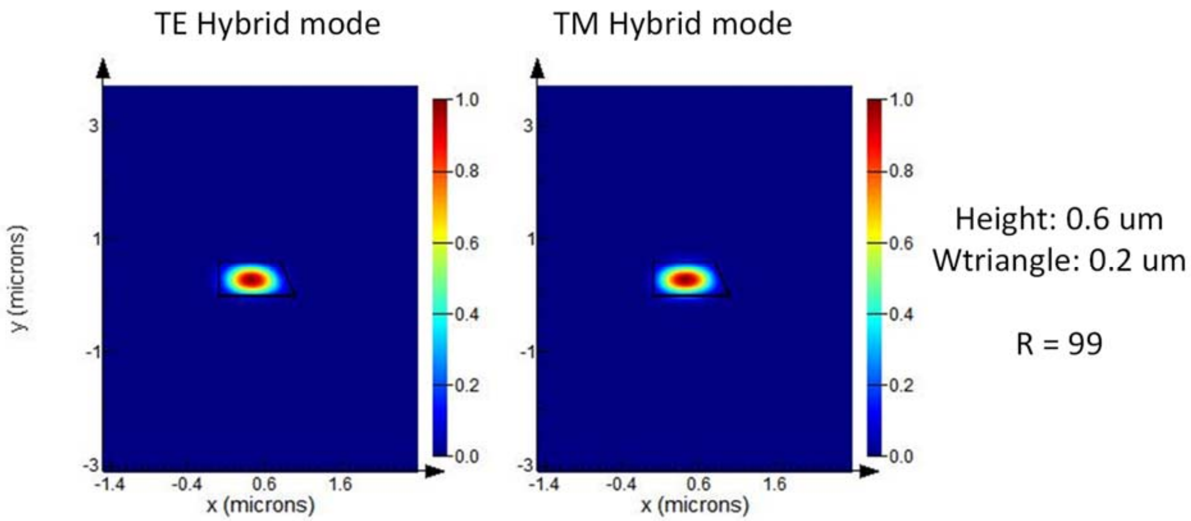

Figure 169: Polarization partial rotator with Height= 0.6 um and $W_{triangle}$= 0.2 um.

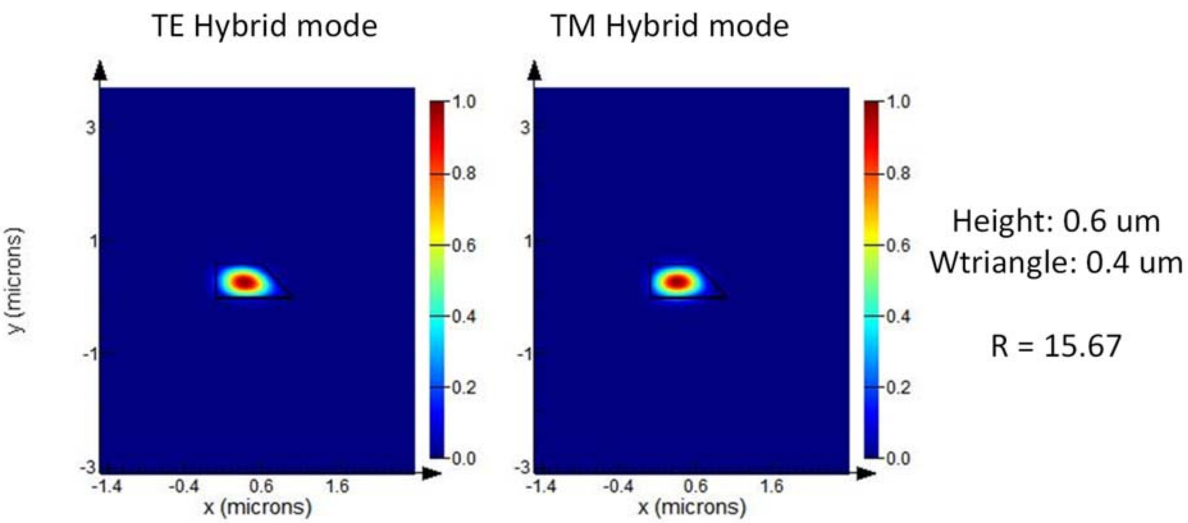
TE Hybrid mode

TM Hybrid mode

Height: 0.6 um
Wtriangle: 0.4 um

R = 15.67

Figure 170: Polarization partial rotator with Height= 0.6 um and $W_{triangle}$= 0.4 um.

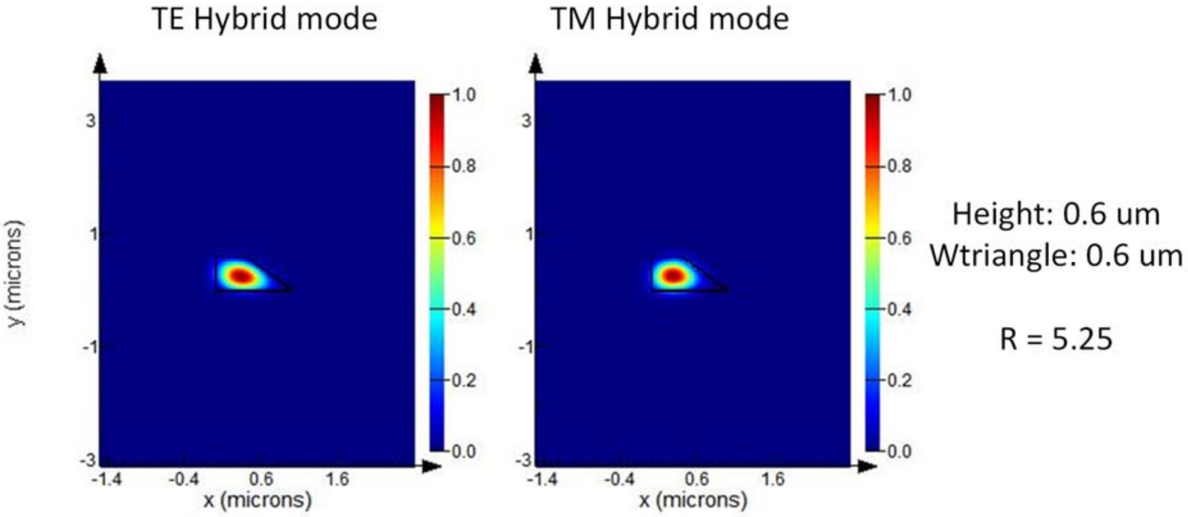
TE Hybrid mode

TM Hybrid mode

Height: 0.6 um
Wtriangle: 0.6 um

R = 5.25

Figure 171: Polarization partial rotator with Height= 0.6 um and $W_{triangle}$= 0.6 um.

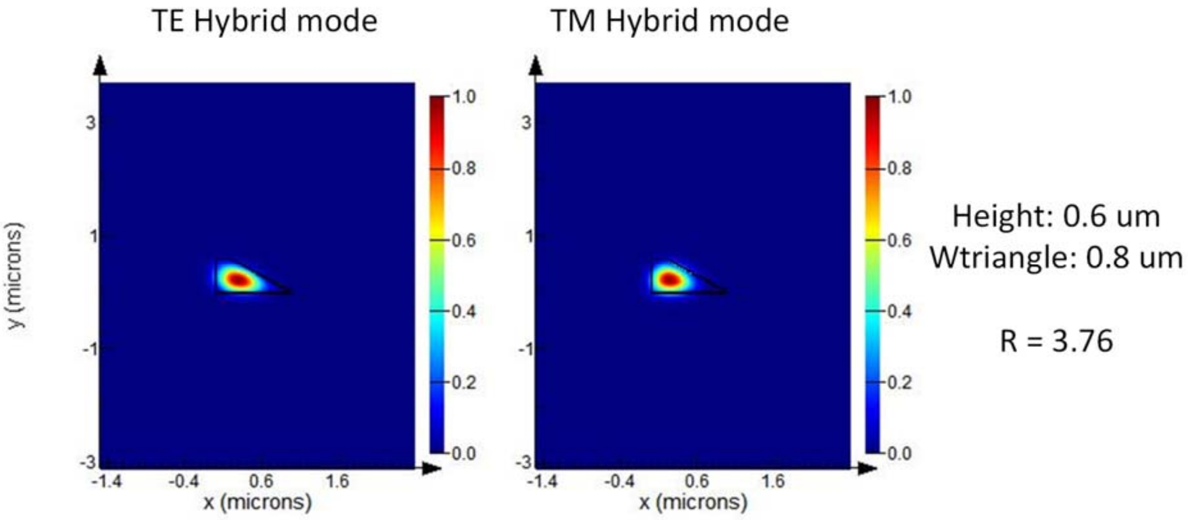

Figure 172: Polarization partial rotator with Height= 0.6 um and $W_{triangle}$= 0.8 um.

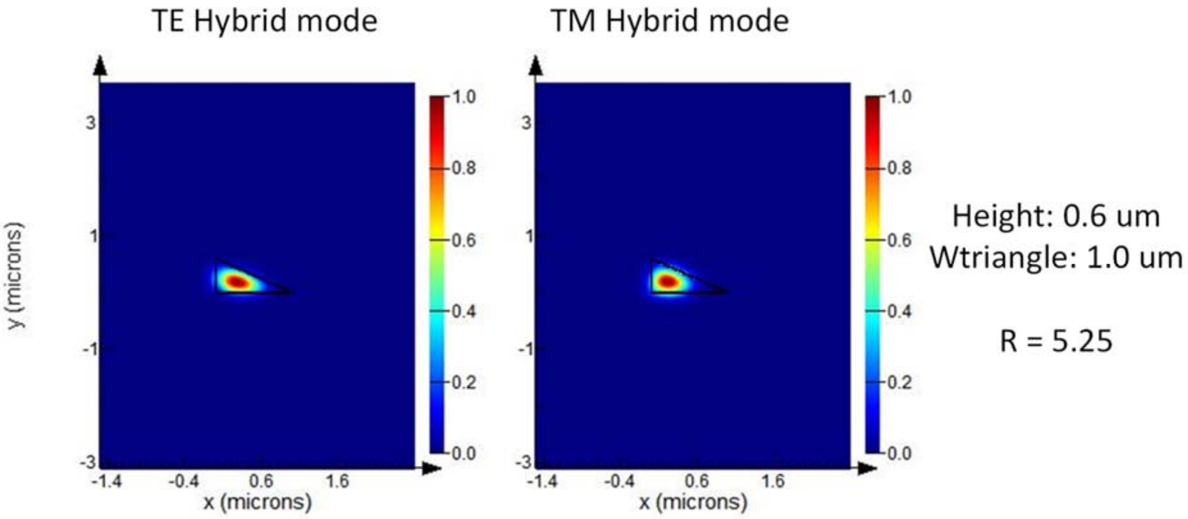

Figure 173: Polarization partial rotator with Height= 0.6 um and $W_{triangle}$= 1.0 um.

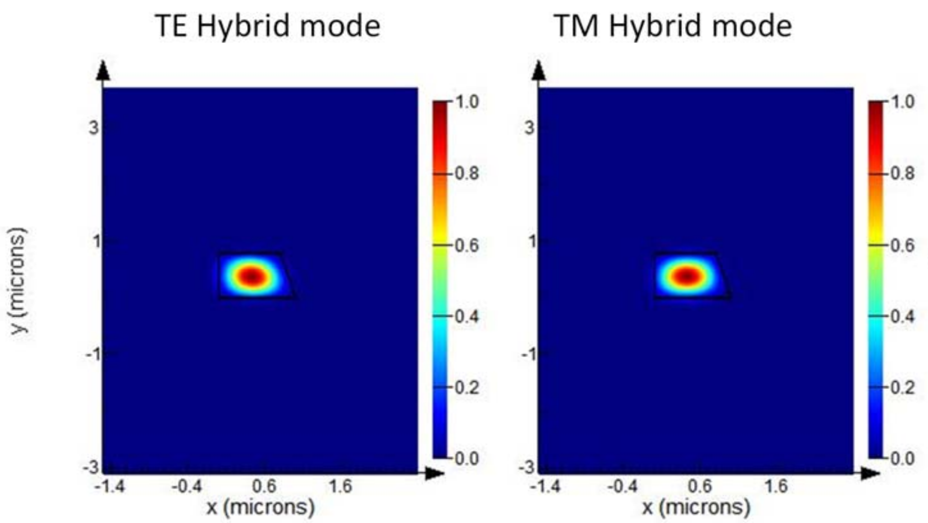
TE Hybrid mode

TM Hybrid mode

Height: 0.8 um
Wtriangle: 0.2 um

R = 11.5

Figure 174: Polarization partial rotator with Height= 0.8 um and $W_{triangle}$= 0.2 um.

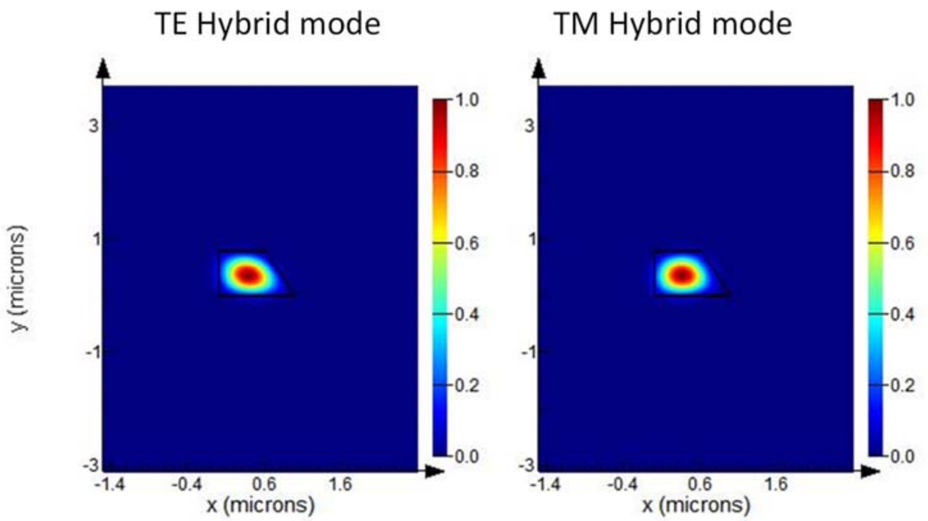
TE Hybrid mode

TM Hybrid mode

Height: 0.8 um
Wtriangle: 0.4 um

R = 1.5

Figure 175: Polarization partial rotator with Height= 0.8 um and $W_{triangle}$= 0.4 um.

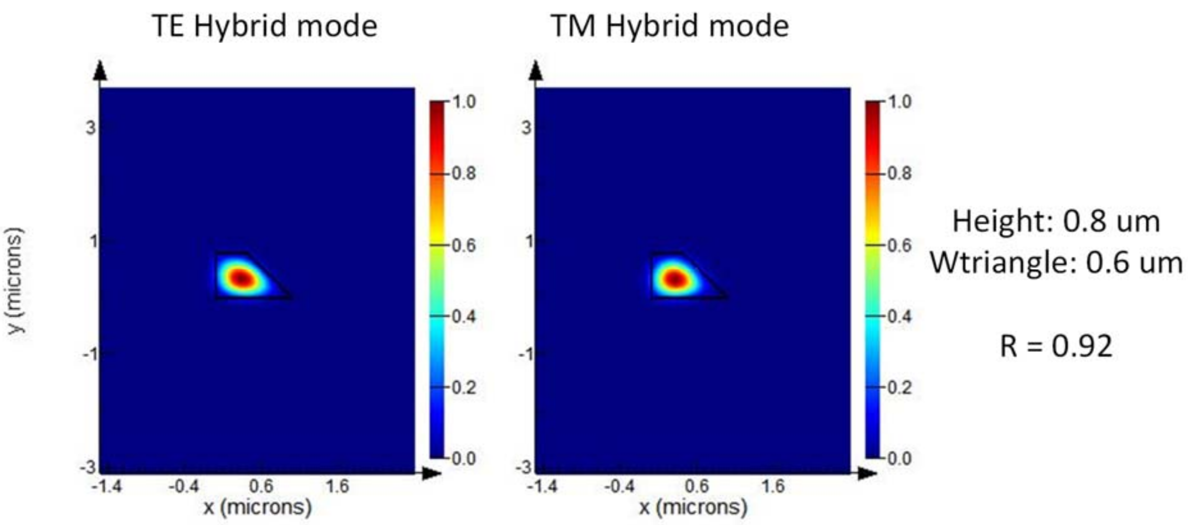

Height: 0.8 um
Wtriangle: 0.6 um

R = 0.92

Figure 176: Polarization partial rotator with Height= 0.8 um and W$_{triangle}$= 0.6 um.

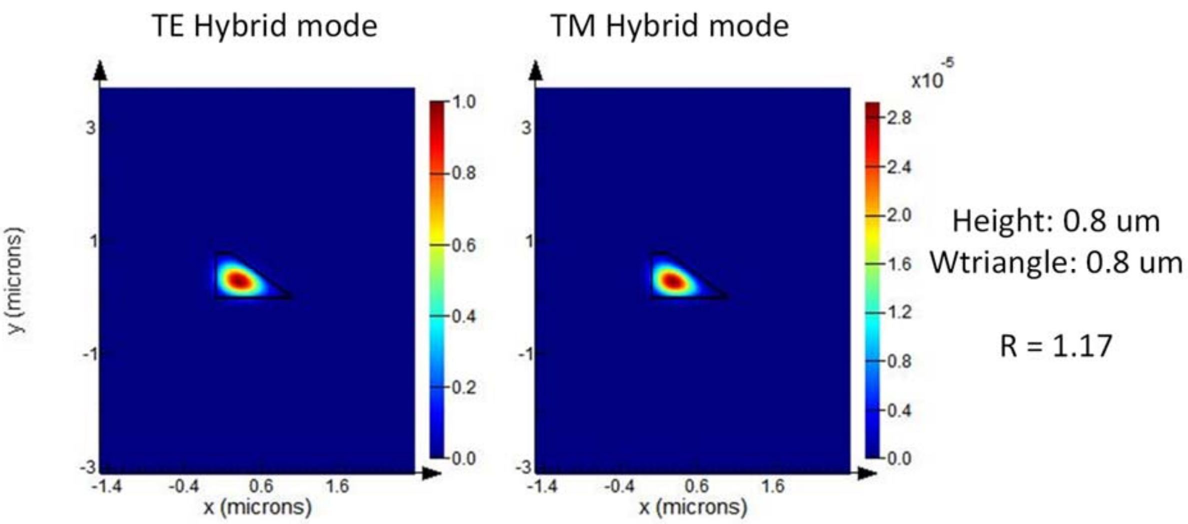

Height: 0.8 um
Wtriangle: 0.8 um

R = 1.17

Figure 177: Polarization partial rotator with Height= 0.8 um and W$_{triangle}$= 0.8 um.

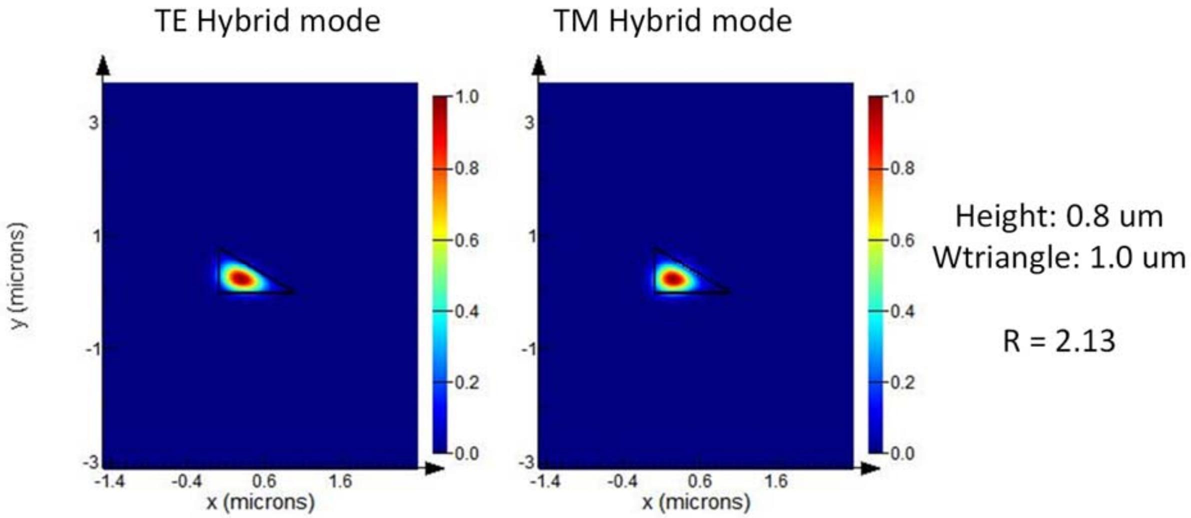

Figure 178: *Polarization partial rotator with Height= 0.8 um and $W_{triangle}$= 1.0 um.*

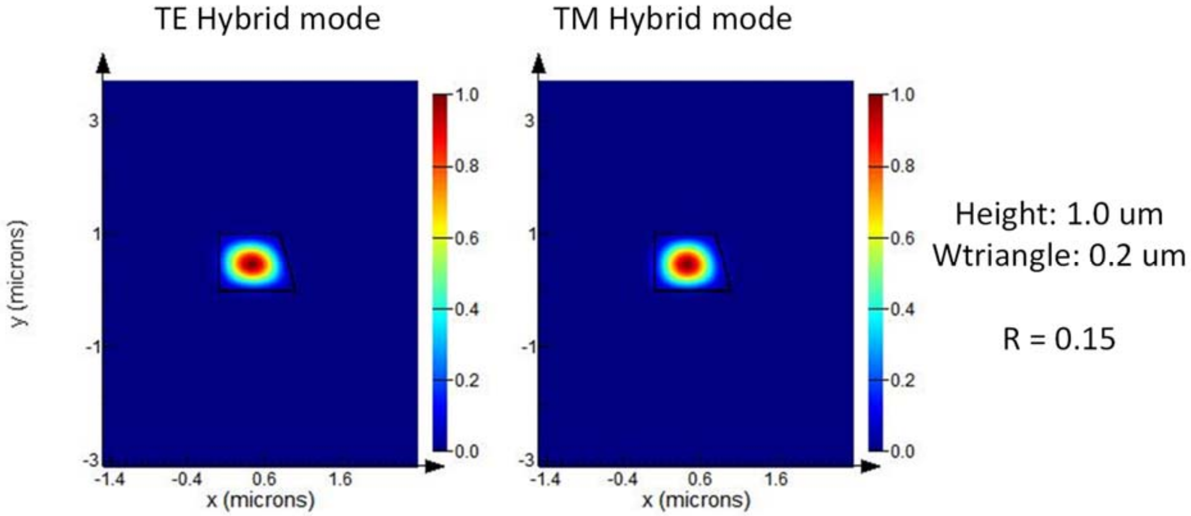

Figure 179: *Polarization partial rotator with Height= 1.0 um and $W_{triangle}$= 0.2 um.*

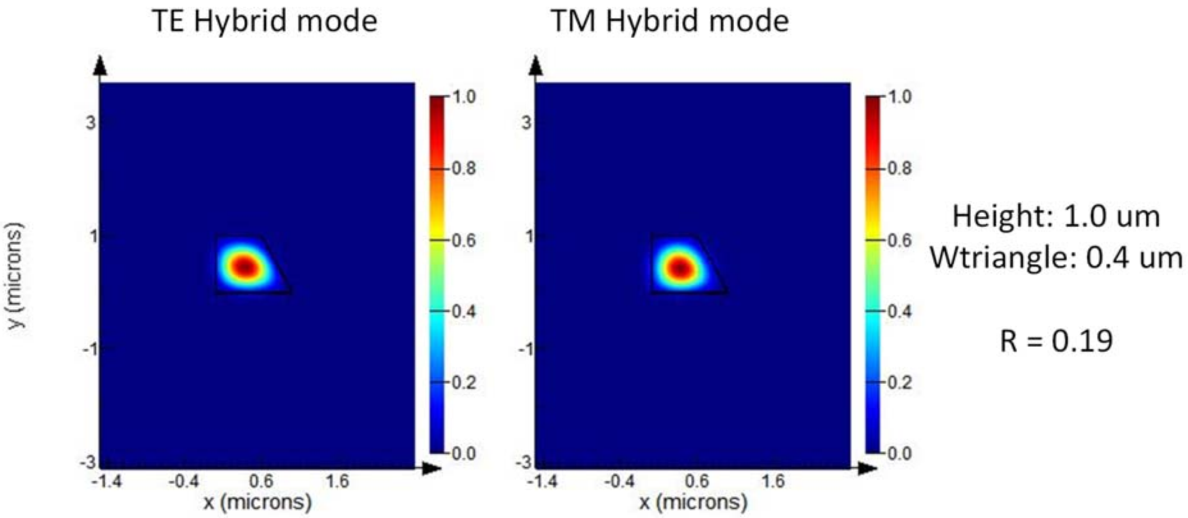

Figure 180: Polarization partial rotator with Height= 1.0 um and $W_{triangle}$= 0.4 um.

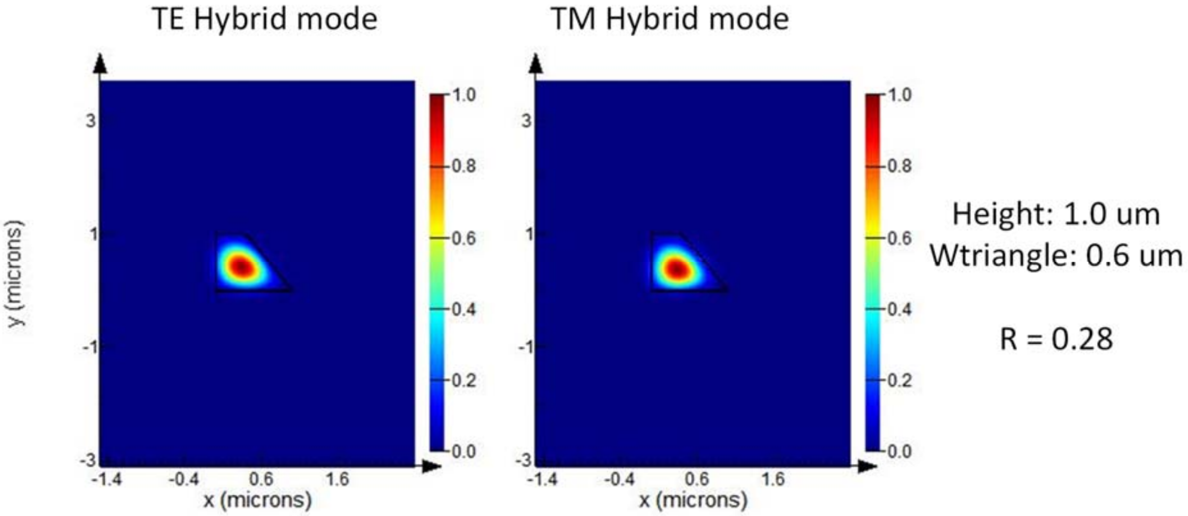

Figure 181: Polarization partial rotator with Height= 1.0 um and $W_{triangle}$= 0.6 um.

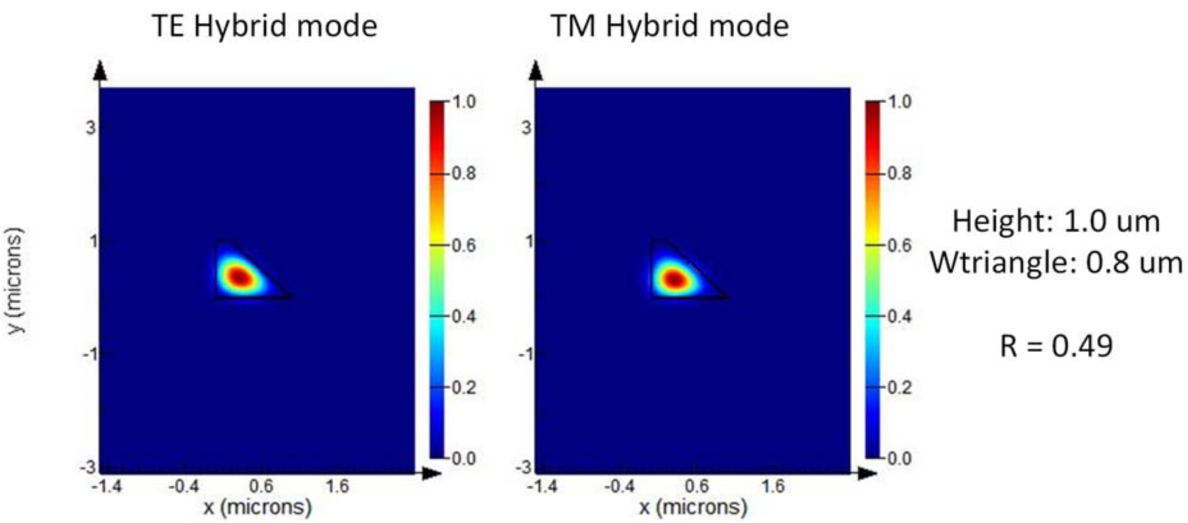

Figure 182: Polarization partial rotator with Height= 1.0 um and $W_{triangle}$= 0.8 um.

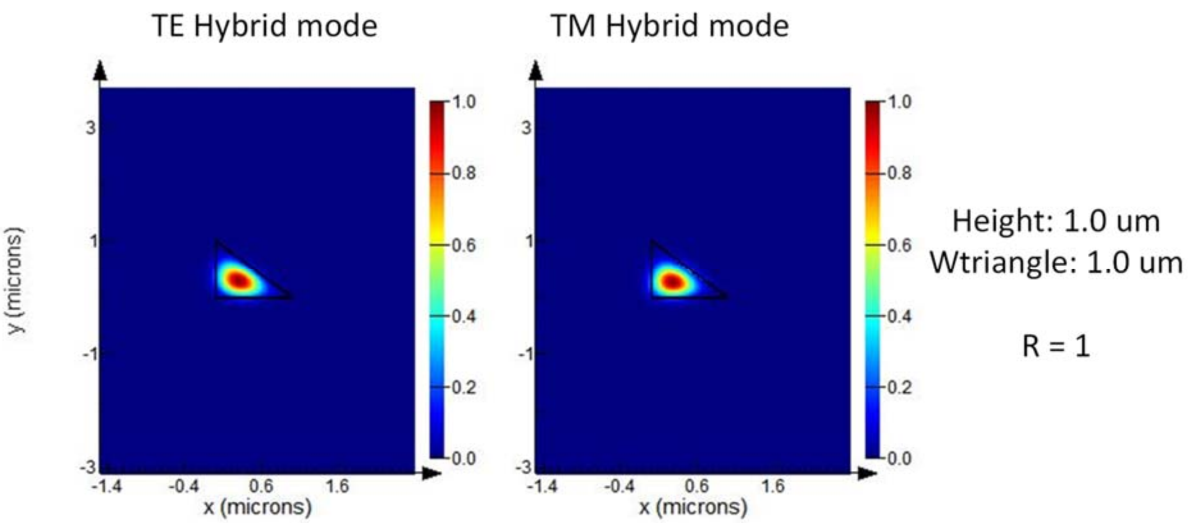

Figure 183: Polarization partial rotator with Height= 1.0 um and $W_{triangle}$= 1.0 um.

List of figures

List of tables

List of publications

1. H. Avramopoulos, V. Katopodis, P. Groumas, L. Gounaridis, A. Konczykowska, Z. Zhang, G. De Valicourt, R. Dinu, A. Vannucci, T. Keinicke Johansen, A. Pagano, C. Kouloumentas, “Passive and electro-optic polymer photonics and InP electronics integration for multi-flow terabit transceivers at edge SDN switches and data-center gateways,” 16th International Conference on Transparent Optical Networks (ICTON), 2014.
2. V. Katopodis, P. Groumas, Z. Zhang, J. Dupuy, E. Miller, A. Beretta, L. Gounaridis, J. H. Choi, D. Pech, F. Jorge, V. Nodjiadjim, R. Dinu, G. Cangini, A. Dede, A. Vannucci, A. Konczykowska, N. Keil, H. G. Bach, N. Grote, C. Kouloumentas, H. Avramopoulos, “2x100-Gb/s NRZ-OOK Integrated Transmitter for Intradata Center Connectivity,” IEEE Photonics Technology Letters, 2014.
3. P. Groumas, V. Katopodis, J. H. Choi, H.-G. Bach, J.-Y. Dupuy, A. Konczykowska, Z. Zhang, P. Harati, E. Miller, A. Beretta, L. Gounaridis, F. Jorge, V. Nodjiadjim, A. Dede, A. Vannucci, G. Cangini, R. Dinu, N. Keil, N. Grote, H. Avramopoulos, C. Kouloumentas, “Multi-100 GbE and 400 GbE interfaces for intra-data center networks based on arrayed transceivers with serial 100 Gb/s operation,” Journal of Lightwave Technology, 2015.
4. L. Gounaridis, P. Groumas, E. Schreuder, R. Heideman, V. Katopodis, C. Kouloumentas, H. Avramopoulos,” Design of grating couplers and MMI couplers on the TriPleX platform enabling ultra-compact photonic-based biosensors,” Sensors and Actuators B: Chemical, 2015.
5. L. Gounaridis, P. Groumas, E. Schreuder, R. Heideman, H. Avramopoulos, C. Kouloumentas, “New set of design rules for resonant refractive index sensors enabled by FFT based processing of the measurement data,” Optics express, 2016.
6. L. Gounaridis, P. Groumas, E. Schreuder, G. Tsekenis, A. Marousis, R. Heideman, H. Avramopoulos, C. Kouloumentas, “High performance refractive index sensor based on low Q-factor ring resonators and FFT processing of wavelength scanning data,” Optics express, 2017.
7. L. Gounaridis, P. Groumas, E. Schreuder, G. Tsekenis, R. Heideman, H. Avramopoulos, C. Kouloumentas, “Low Q-factor ring resonators with ultra-low limit of detection based on FFT processing of spectral scanning data,” CLEO: Science and Innovations, 2017.
8. P. Groumas, C. Tsokos, M. Kleinert, D. Marchenko, V. Katopodis, M. Dekkers, M. Falcucci, R.B. Timens, L. Gounaridis, C.G. Roeloffzen, A. Vannucci, R.G. Heideman, N. Keil, C. Kouloumentas, H. Avramopoulos, “Photonic integration technology for the interface between the optical and wireless part in 5G networks: The H2020-ICT-HAMLET approach,” IEEE Photonics Society Summer Topical Meeting Series (SUM), 2017.
9. C. Tsokos, E. Mylonas, P. Groumas, V. Katopodis, L. Gounaridis, R. B. Timens, R. M Oldenbeuving, C. G.H. Roeloffzen, H. Avramopoulos, C. Kouloumentas, “Analysis of a multibeam optical beamforming network based on Blass matrix architecture,” Journal of Lightwave Technology, 2018.
10. V. Katopodis, H. Mardoyan, C. Tsokos, D. Felipe, A. Konczykowska, P. Groumas, M. Spyropoulou, L. Gounaridis, P. Jennevé, F. Boitier, F. Jorge, T. K. Johansen, M. Tienforti, J. Y. Dupuy, A. Vannucci, N. Keil, H. Avramopoulos, C. Kouloumentas, “Multiflow Transmitter With Full Format and Rate Flexibility for Next Generation Networks,” Journal of Lightwave Technology, 2018.
11. C. Tsokos, E. Mylonas, P. Groumas, L. Gounaridis, H. Avramopoulos, C. Kouloumentas, “Optical beamforming network for multi-beam operation with continuous angle selection,” IEEE Photonics Technology Letters, 2018.

12. L. Gounaridis, P. Groumas, E. Schreuder, C. Tsokos, E. Mylonas, A. Raptakis, R. Heideman, H. Avramopoulos, C. Kouloumentas, “Design of ultra-compact multimode interference (MMI) couplers and high efficiency grating couplers in TriPleX platform as part of a photonic-based sensor,” Integrated Optics: Devices, Materials, and Technologies XXIII, SPIE, 2019.
13. P. Groumas, C. Tsokos, D. Felipe, U. Troppenz, R. Hersent, P. Bakopoulos, B. Atias, J.Y. Dupuy, A. Pagano, A. Chiado Piat, S. Kibben, L. Gounaridis, A. Raptakis, M. Seyfried, M. Moehrle, C. Kouloumentas, N. Keil, H. Avramopoulos, “Enabling low-cost high-volume production compatible terabit transceivers with up to 1.6 Tbps capacity and 100Gbps per lane PAM-4 modulation for intra-data center optical interconnects up to 2km: The TERIPHIC project approach,” Metro and Data Center Optical Networks and Short-Reach Links III, SPIE, 2020.
14. C. Tsokos, E. Andrianopoulos, A. Raptakis, N. Lyras, L. Gounaridis, P. Groumas, H. Avramopoulos, C. Kouloumentas, “Optical Beamforming Networks Supporting Multibeam and Multicast Operation,” 22nd International Conference on Transparent Optical Networks, ICTON, 2020.
15. C. Kouloumentas, C. Tsokos, P. Groumas, L. Gounaridis, A. Raptakis, E. Mylonas, E. Andrianopoulos, K. Wörhoff, K. Ławniczuk, A. Leinse, H. Avramopoulos, “Multi-Rate and Multi-Channel Optical Equalizer Based on Photonic Integration,” IEEE Photonics Technology Letters, 2020.
16. M. Chatzipetrou, L. Gounaridis, G. Tsekenis, M. Dimadi, R. Vestering-Stenger, E. F. Schreuder, A. Trilling, G. Besselink, L. Scheres, A. van der Meer, E. Lindhout, R. G. Heideman, H. Leeuwis, S. Graf, T. Volden, M. Ningler, C. Kouloumentas, C. Strehle, V. Revol, A. Klinakis, H. Avramopoulos and I. Zergioti, “A miniature Bio-photonics Companion Diagnostics platform for reliable cancer treatment monitoring in blood fluids,” Sensors, Nanosensors for Biomedical Applications, 2021.
17. E. Maltezos, L. Karagiannidis, A. Dadoukis, K. Petousakis, F. Misixchroni, E. Ouzounoglou, L. Gounaridis, D. Gounaridis, C. Kouloumentas, A. Amditis, “Public safety in smart cities under the edge computing concept,” IEEE, MeditCom, Hybrid on-line conference, July 2021. (under review)
18. A. Raptakis, L. Gounaridis, M. Weigel, M. Kleinert, M. Georgiopoulos, E. Mylonas, P. Groumas, C. Tsokos, N. Keil, H. Avramopoulos, C. Kouloumentas, “2D Optical Phased Arrays for Laser Beam Steering Based on 3D Polymer Photonic Integration Circuits,” IEEE, Journal of Lightwave Technology, April 2021. (under review)
19. D. Gounaridis, L. Gounaridis, S. Giannikou, P. Groumas, C. Tsokos, A. Raptakis, E. Ouzounoglou, H. Avramopoulos, C. Kouloumentas, “High performance refractive index sensor for real time monitoring of water composition change,” SimHydro: Models for complex and global water issues - Practices and expectations, France, June 2021. (under review)
20. D. Gounaridis, L. Gounaridis, S. Giannikou, P. Groumas, C. Tsokos, A. Raptakis, E. Ouzounoglou, H. Avramopoulos, C. Kouloumentas, “Photonic integrated refractive index sensor for real time evaluation of water composition,” AQUA≈360: Water for All - Emerging Issues and Innovations, United Kingdom, September 2021. (under review)